6-9-2016

On Cross-Anisotropy of Flexible Pavement Layer Materials for Improved Pavement Responses

Mesbah Ahmed

Student Name: Mesbah U. Ahmed

Candidate

Graduate Unit (Department): Civil Engineering

Department

This dissertation is approved, and it is acceptable in quality and form for publication:

Approved by the Dissertation Committee:

Rafiqul A. Tarefder, Chairperson

Tang-Tat Ng, Member

Arup K. Maji, Member

Yu-Lin Shen, Member

ON CROSS-ANISOTROPY OF FLEXIBLE PAVEMENT LAYER MATERIALS FOR IMPROVED PAVEMENT RESPONSES

By

MESBAH U. AHMED

B.Sc. in Civil Engineering (2007)
Bangladesh University of Engineering and Technology (BUET), Dhaka, Bangladesh

M.Sc. in Civil Engineering (2010)
University of New Mexico (UNM), Albuquerque, New Mexico, USA

DISSERTATION
Submitted in Partial Fulfillment of the
Requirements for the Degree of

Doctor of Philosophy

Engineering

The University of New Mexico
Albuquerque, New Mexico, USA
May 2016

DEDICATION

To my parents for their love, encouragement & trust

ACKNOWLEDGEMENT

I would like to thank Dr. Rafiqul Tarefder, my supervisor and dissertation committee chair, for his time and support during the entire course of my Ph.D. research. I express my sincere gratitude for giving me the freedom of thoughts, research and access to any kind of resources required for this study. To me, he is not just a mentor; he is a friend from whom I learnt a lot. His guidance and professional style will remain with me as I continue my future career.

I would like to thank my dissertation committee members: Dr. Tang-Tat Ng, Dr. Arup Maji, and Dr. Yu-Lin Shen for their time and valuable suggestions pertaining to this study. Through the journey of my PhD, they taught me the way to focus and persistence to solve different problems related to research. I would like to acknowledge Dr. Howard Schreyer, Professor Emeritus, UNM; Dr. John Foster, Assistant Professor, UT Austin; and Bill Scherzinger, Sandia National Laboratory, for sharing their knowledge on constitutive modeling and computational mechanics.

I would like to thank Jeff Mann, Pavement Design and Virgil Valdez, Research Bureau, New Mexico Department of Transportation (NMDOT) for their assistance in field data and material collection. Effort of the Field Exploration Team, NMDOT for the field coring and testing is also highly appreciated.

Special thanks are due to Asif, Tahmid, Zafrul, and Rashad for their assistance during the laboratory and field tests. Review and constructive criticism by Mohi and Amina are also appreciated. Co-operation and encouragement from the team members of my research group are

greatly acknowledged. At this point, I want to remember my friends, Late Minhaz Mahdi and Yi Huang, for their encouraging and motivational words.

I would like to acknowledge the Department of Civil Engineering, UNM for providing facilities to expedite my research and study. I appreciate the assistance and encouragement provided the departmental staff, especially, Josie, Yolanda, Rebekah, and Hope.

Finally, I would like to express my love & gratitude to my wife and daughter for their endless patience, support, and encouragement during difficult times and conducting my research.

On Cross-Anisotropy of Flexible Pavement Layer Materials for Improved Pavement Responses

By

Mesbah Ahmed

B.Sc., Civil Engineering, Bangladesh University of Engineering and Technology, 2007

M.Sc., Civil Engineering, University of New Mexico, 2010

Ph.D., Engineering, University of New Mexico, 2016

ABSTRACT

Pavement layer materials are typically assumed to be isotropic in determining pavement responses, such as stress and strain. The main benefit of the isotropic assumption is that stiffness[1] defined by modulus of elasticity (*E*-value) is equal in all directions. In reality, stiffness along vertical and horizontal (i.e., E_v and E_h) may vary due to density gradients in compacted layer materials caused by vertical compaction during construction. Therefore, pavement layer materials with different vertical and horizontal modulus (i.e., $E_v \neq E_h$) are cross-anisotropic. Past studies have reported that degree of cross-anisotropy, ($n = E_h / E_v$) ranges from 0.2 to 0.85 in Asphalt Concrete (AC) layers. Yet, the presence of cross-anisotropy is not considered in pavement layers for determining stress and strains, which are used for prediction of pavement distresses such as rutting and fatigue cracking. Ignoring the presence of AC cross-anisotropy may lead to an error in stress-strain calculations, and in pavement distress value predictions. To this end, this study examines the effects of cross-anisotropy on pavement stress-strain and thereby, evaluates the importance of cross-anisotropy in pavement design.

[1] Stiffness and modulus are synonymous; therefore, both terms are used interchangeably in this study.

In addition to cross-anisotropy, AC modulus is temperature and frequency dependent. Pavement temperature varies not only at different times over a day but also at different seasons over a year. Also, temperature is not constant over the depth of an AC layer which leads to a non-homogenous distribution of AC stiffness. AC modulus varies due to different loading frequencies caused by variable speed of moving vehicles. Unbound layers such as base and subbase are stress-dependent. The stiffness of an unbound layer differs at different months over a year due to varying moisture contents. This study considers all of these factors such as temperature, frequency, and moisture with material cross-anisotropy through laboratory testing and finite element modeling.

In this study, a dynamic Finite Element Model (FEM) is developed based on the geometry of an instrumented pavement section at Milepost (MP) 141 on I-40, Rio Puerco, New Mexico and deflections, stress, and strains are predicted under truck tire pressure. Two different material models are employed: (i) generalized cross-anisotropic and temperature dependent viscoelastic model, and (ii) nonlinear elastic and stress-dependent model. The first one is for the AC layer whereas the second one is for unbound layers such as base and subbase courses.

In this study, dynamic modulus tests were conducted in the laboratory on field-compacted vertical and horizontal AC cores to determine the parameters required for developing the generalized cross-anisotropic viscoelastic model. Resilient modulus tests were conducted on granular aggregates collected from the base and subbase layers to develop nonlinear elastic and stress-dependent material model. After integrating these material models, the dynamic FEM is simulated under a Falling Weight Deflectometer (FWD) test type load (79.6 psi over a circular

area with 6 inch radius) for model validation. The simulated responses are compared to in-situ deflections, stress, and strains under a FWD test. It is observed that the simulated pavement responses are close to in-situ responses.

Using the validated model under non-uniform vertical tire-pavement contact stress, FEM simulations are run at varying *n*-values and temperatures to determine tensile strain at the bottom of AC layer and vertical compressive strains in all layers. It is observed that strains are sensitive to material cross-anisotropy and strains with cross-anisotropy assumption are greater than those with isotropy assumption. In particular, both horizontal tensile and vertical compressive strains increased in case of AC cross-anisotropy, whereas only vertical strains increase in case of unbound layer cross-anisotropy. These strain variations due to cross-anisotropy increase at high temperature and in presence of stress-dependent unbound layer.

In order to determine pavement distresses, simulated strains are used to determine damage due to fatigue and permanent deformation using Miner's rule. In case of AC cross-anisotropy, damage decreases as *n*-value increases towards isotropy ($n = 1$). However, unbound layer cross-anisotropy leads to an increase in fatigue damage as *n*-value increases towards isotropy. It is also observed that damage due to AC cross-anisotropy is very high compared to unbound layer cross-anisotropy. It indicates that earlier pavement damage is mostly caused by the AC cross-anisotropy. That is, AC cross-anisotropy is more important than the unbound layer cross-anisotropy when considering rutting and fatigue damage only. This study recommends to incorporate the AC cross-anisotropy, at a minimum, in pavement analysis and design.

Table of Content

CHAPTER 1 1
INTRODUCTION 1
1.1 General 1
1.2 Background 1
1.3 Previous Studies 3
1.4 Research Need 7
1.5 Hypothesis 8
1.6 Objectives 8
1.7 Outline 9
CHAPTER 2 10
LITERATURE REVIEW 10
2.1 General 10
2.2 Material Cross-Anisotropy 10
2.3 Viscoelasticity of AC 16
2.4 Past Studies AC Cross-Anisotropy 24
2.5 Dynamic Modulus of Field-compacted AC 28
2.6 Depth-Temperature Variation and Effect on AC 29
2.7 Unbound Layer Stress-Dependency 30
CHAPTER 3 35
DYNAMIC FEM DEVELOPMENT 35
3.1 General 35
3.2 Outline of Model Development 35
3.3 Instrumented Pavement Section 36
3.4 Model Geometry 38
3.5 Boundary Condition 40
3.6 Mesh Generation 43
3.7 Material Properties 44
3.7.1 OGFC 46
3.7.2 Asphalt Concrete 49

3.7.3 Unbound layers 63
3.8 Loading Type 69
3.9 Dynamic FEM Analysis 72
3.10 FEM vs. Field 75
3.11 Distribution of Pavement Response 77
3.11.1 Contour of vertical deflection 77
3.11.2 Contour of vertical stress 79
3.11.3 Contour of vertical strain 80
3.11.4 Contour of longitudinal horizontal stress 82
3.11.5 Contour of longitudinal horizontal strain 83
3.11.6 Contour of transverse horizontal stress 85
3.11.7 Contour of transverse horizontal strain 86
3.12 Summary 88
CHAPTER 4 89
AC CROSS-ANISOTROPY 89
4.1 General 89
4.2 Outline 89
4.3 Phase: I 90
4.3.1 Model Description 90
4.3.2 Results and Discussion 93
4.3.3 Summary of Phase I 95
4.4 Phase: II 96
4.4.1 Model Description 96
4.4.2 Pavement Performance Indicator 99
4.4.3 Results and Discussion 101
4.5 Summary of parametric study 112
4.6 Summary 114
CHAPTER 5 116
UNBOUND LAYER CROSS-ANISOTROPY 116
5.1 General 116
5.2 Outline 116

5.3 Model Description 117
5.4 Analysis and Discussion 120
5.4.2 Vertical Strain 124
5.5 Summary of parametric study 135
5.5 Summary 137
CHAPTER 6 138
CROSS-ANISOTROPY AND STRESS-DEPENDENCY 138
6.1 General 138
6.2 Outline 138
6.3 Model Description 139
6.4 Analysis and Discussion 149
6.4.1 Depth-Temperature Variation 149
6.4.2 Base Isotropy vs. Cross-anisotropy 157
6.4.3 Linear vs. Nonlinear Elastic 164
6.4.4 Loading Duration 169
6.5 Summary of parametric study 173
6.5 Summary 176
CHAPTER 7 178
CONCLUSIONS AND RECOMMENDATIONS 178
7.1 General 178
7.2 Conclusions 178
7.3 Recommendations 181
REFERENCES 183
APPENDIX A 193

List of Tables

Table 2.1 Number of independent components in elasticity matrix 14
Table 3.1 Prony Series Coefficient (vertical & horizontal AC cores) 56
Table 3.2 Summary of base and subbase resilient modulus 65
Table 3.3 Mesh assignment for tire imprint area 71
Table 3.4 Comparison of pavement responses (Field vs. FEM) 76
Table 4.1 Material of Pavement Layers 91
Table 4.2 Prony Series for AC viscoelasticity (Al-Qadi et al. 2010) 92
Table 4.3 Analysis matrix of FEM simulation 93
Table 4.4 Prony series coefficient 97
Table 4.5 Backcalculated moduli of the unbound layers 97
Table 4.6 Analysis matrix of FEM simulation under wheel load 99
Table 4.7 Comparison of horizontal tensile strain (transverse vs. longitudinal) 111
Table 4.8 Comparison of vertical strain in pavement layers 112
Table 4.9: Summary of parametric study (AC cross-anisotropy) 113
Table 5.1 Instantaneous modulus at different temperatures 118
Table 5.2 Prony series coefficient (unbound layer cross-anisotropy) 118
Table 5.3 Backcalculated moduli of the unbound layers 119
Table 5.4 Analysis matrix of FEM simulation under wheel load 120
Table 5.5: Summary of parametric study (Unbound layer cross-anisotropy) 136
Table 6.1 Prony series coefficients (OGFC & AC) 140
Table 6.2 Strain at varying shear modulus 142
Table 6.3 Summary of regression coefficients 144
Table 6.4 Adjusted regression coefficients 146
Table 6.5: Summary of parametric study (AC cross-anisotropy & stress-dependency) 174

List of Figures

Figure 1.1 Cross-anisotropy in pavement materials 2
Figure 1.2 Temperature variation over depth in AC of a pavement section 6
Figure 1.3 Research needs 7
Figure 1.4 Outline of dissertation 9
Figure 2.1 State of stresses 11
Figure 2.2 Elasticity and viscosity 17
Figure 2.3 Maxwell model 19
Figure 2.4 Kelvin model 20
Figure 2.5 Generalized Maxwell Model 21
Figure 2.6 Relaxation modulus test 23
Figure 2.7 Dynamic modulus test for viscoelasticity 24
Figure 2.8 Nonlinearity of unbound layer materials 31
Figure 2.9: State of stresses in unbound material under resilient modulus test 32
Figure 2.10 Incorporation of stress-dependency in a pavement model 34
Figure 3.1 Flowchart of FEM modeling and validation 36
Figure 3.2 Instrumented Pavement Section (I-40, MP 141) 37
Figure 3.3 Plan View of Instrumented Pavement Section (I-40) 38
Figure 3.4 Multilayered structure of pavement section at MP 141, I-40 40
Figure 3.5 Preliminary boundary condition of the model (BC: 1) 41
Figure 3.6 Modified boundary condition of the model (BC: 2) 42
Figure 3.7 Mesh sensitivity analysis 44
Figure 3.8 Flow diagram of tests for material characterization 45
Figure 3.9 Dynamic modulus test 47
Figure 3.10 Dynamic modulus values of OGFC 48
Figure 3.11 Relaxation modulus of OGFC 49
Figure 3.12 Schematic of laboratory test to determine the degree of cross-anisotropy 50
Figure 3.13 Extraction of field-compacted AC core 51
Figure 3.14 Preparation of vertical test specimen for laboratory tests 52
Figure 3.15 Preparation of horizontal test specimen for laboratory tests 53

Figure 3.16 Dynamic and relaxation modulus of vertical AC core 54
Figure 3.17 Dynamic and relaxation modulus of horizontal AC core 55
Figure 3.18 Laboratory tests for Poisson's ratio 58
Figure 3.19 Depth-temperature variation in AC layer 60
Figure 3.20 Creep and relaxation after integration of subroutine 62
Figure 3.21 Vertical and horizontal relaxation modulus variation 63
Figure 3.22 Laboratory resilient modulus tests 64
Figure 3.23 Stress-dependency in a single element analysis 68
Figure 3.24 Variation of load over time during a FWD test 69
Figure 3.25 Wheel load variation over time and shapes of tire imrpint area 70
Figure 3.26 Contact stress distribution and loading duration 71
Figure 3.27 Validation of pavement FEM model 75
Figure 3.28 Comparison of pavement surface deflections (FEM vs. Field) 76
Figure 3.29 Vertical deflection 79
Figure 3.30 Vertical stress 80
Figure 3.31 Vertical strain 82
Figure 3.32 Horizontal stress in AC (longitudinal) 83
Figure 3.33 Horizontal strain in AC (longitudinal) 85
Figure 3.34 Horizontal stress in AC (transverse) 86
Figure 3.35 Horizontal strain in AC (transverse) 87
Figure 4.1 Outline of the study 90
Figure 4.2 Effect of AC cross-anisotropy on horizontal tensile strain 94
Figure 4.3 Effect of AC cross-anisotropy on vertical strain 95
Figure 4.4 Temperature variation over depth in AC layer 98
Figure 4.5 Effect of AC cross-anisotropy on tensile strain at bottom of the AC layer 102
Figure 4.6 Effect of AC cross-anisotropy on tensile strain ratio and damage 103
Figure 4.7 Effect of AC cross-anisotropy on vertical strain in pavement layers 105
Figure 4.8 Effect of AC cross-anisotropy on vertical strain ratios and damage 107
Figure 4.9 Effect of AC cross-anisotropy on vertical stress in unbound layers 109
Figure 4.10 Variation of AC modulus with pavement temperature 111
Figure 5.1 Outline of the study 117

Figure 5.2 Effect of cross-anisotropy on tensile strain at the bottom of AC 122
Figure 5.3 Tensile strain ratios and damage in AC 123
Figure 5.4 Effect of cross-anisotropy on vertical strain in AC 125
Figure 5.5 Vertical strain ratios and damage in AC 126
Figure 5.6 Effect of cross-anisotropy on vertical strain in base 128
Figure 5.7 Vertical strain ratios and damage in base 129
Figure 5.8 Effect of cross-anisotropy on vertical strain in subbase 130
Figure 5.9 Vertical strain ratios and damage in subbase 131
Figure 5.10 Effect of cross-anisotropy on vertical strain in subgrade 133
Figure 5.11 Vertical strain ratios and damage in subgrade 134
Figure 6.1 Outline of the study 139
Figure 6.2 Deflection and stress at varying shear modulus (G_{vh}) 142
Figure 6.3 Flow chart of stress-dependency determination in different months 143
Figure 6.4 Flow chart of stress-dependency determination in different months 145
Figure 6.5 Base and subbase modular ratios in different months 146
Figure 6.6 Flow chart of material models in UMAT, ABAQUS 148
Figure 6.7 Horizontal tensile strain in AC (Temperature variation) 150
Figure 6.8 Tensile strain ratio and damage in AC 151
Figure 6.9 Vertical strain in pavement layers (Temperature variation) 153
Figure 6.10 Vertical nonlinear modulus in unbound layers 154
Figure 6.11 Vertical strain ratio and damage in pavement layers 156
Figure 6.12 Horizontal tensile strain in AC (isotropic vs. cross-anisotropic base) 157
Figure 6.13 Tensile strain ratio and damage in AC 159
Figure 6.14 Vertical strain in pavement layers (isotropic vs. cross-anisotropic base) 160
Figure 6.15 Vertical stress and modulus in unbound layers 161
Figure 6.16 Vertical strain ratio and damage in pavement layers 163
Figure 6.17 Tensile strain in AC layer (Linear vs. nonlinear elastic) 164
Figure 6.18 Tensile strain ratio and damage (Linear vs. nonlinear elastic) 165
Figure 6.19 Vertical strains in pavement layers (Linear vs. nonlinear elastic) 167
Figure 6.20 Vertical strain ratios in pavement layers (Linear vs. nonlinear elastic) 168
Figure 6.21 Damage in pavement layers (Linear vs. nonlinear elastic) 169

Figure 6.22 Tensile strain in AC layer at varying loading duration 170
Figure 6.23 Tensile strain ratio and damage at varying loading duration 171
Figure 6.24 Vertical strain in pavement layers at varying loading duration..... 172
Figure 6.25 Vertical strain ratio and damage at varying loading duration 173

CHAPTER 1

INTRODUCTION

1.1 General

A flexible pavement is a multilayered structure that comprises the stiffest material, i.e., Asphalt Concrete (AC), in top layer and gradually lesser stiff material, i.e., aggregates and soil, in bottom layers. Fatigue and rutting performances of AC pavements are related to stress-strain responses of pavements under load as imposed by traffic. Generally, stress and strain are predicted assuming isotropic material in different layers. Isotropic means each pavement layer material has identical stiffness along 3-directions, during a pavement analysis. However, stress-strain may be different due to consideration of cross-anisotropic materials, i.e., unequal stiffness in horizontal and vertical directions, in pavement layers. Consequently, cross-anisotropy influences the pavement performance. This study investigates the effect of AC layer cross-anisotropy on pavement response. Base, subbase, and subgrade layer anisotropies are outside the scope of this study.

1.2 Background

A flexible pavement section is constructed by compacting different layers or lifts using repeated load by a roller wheel (see Figure 1.1(a)). Due to the lack of confinement in horizontal direction, the compaction forces are not same in horizontal and vertical direction. Therefore, materials stiffness, i.e., defined by the modulus of elasticity, E, vary along these two orthogonal directions as shown in Figure 1.1(b). Therefore, pavement layers have two different E-values in horizontal and vertical direction (Tutumluer 1998). A material is said to be isotropic if its property, i.e., E-

value, is same in all three directions and if not, it is anisotropic (Tutumluer and Seyhan 1999). A special type of material anisotropy is cross-anisotropy where properties along any two directions are the same, however, property in third direction varies. A core is extracted from a layer or lift to show the orientation of E-values in a 3D reference system (see Figure 1.1(c)). It shows that *E*-values in horizontal plane, i.e., E_x and E_z, are the same whereas these are not equal to the vertical *E*-value, i.e., E_y. It indicates that the layer material is cross-anisotropic. Mathematically, cross-anisotropy of AC can be defined as a ratio of horizontal and vertical modulus of elasticity (E_x/E_y) where, $E_x = E_z$. In this study, it will be denoted by a factor, n $(= E_x/E_y = E_h/E_v$, where, $E_v =$ modulus along vertical direction, and $E_h =$ modulus along horizontal direction).

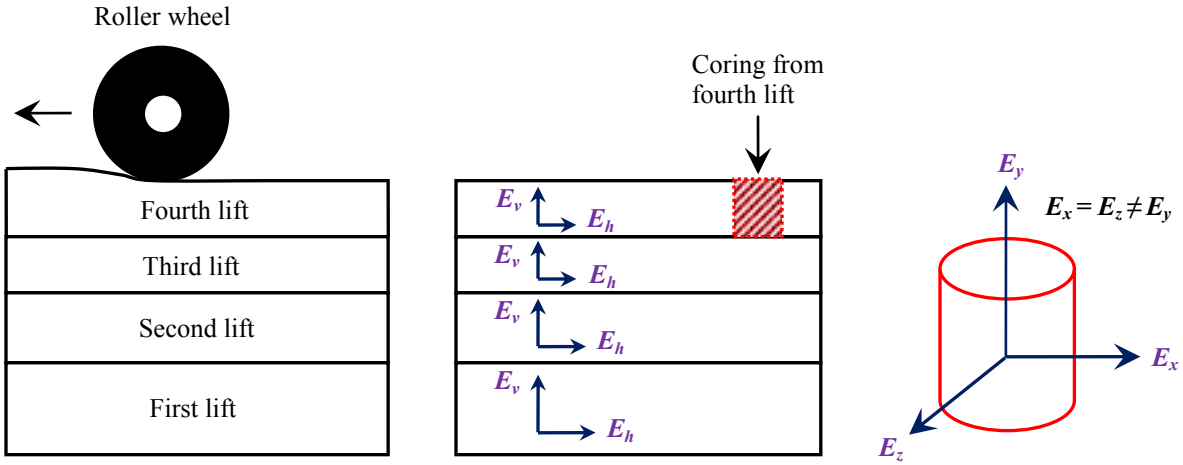

(a) Compaction of pavement (b) *E*-values after compaction (c) Cross-anisotropy in core

Figure 1.1 Cross-anisotropy in pavement materials

Pavement performance and damage are mostly influenced by a pavement's response, such as stress-strain, due to traffic induced repeated load. Pavement response is directly related to the stiffness, *E*-value, of layer materials. Recently, presence of cross-anisotropy in AC layer is observed in some studies (Masad et al. 2002, Wang et al. 2005, and Motola and Uzan 2007).

Therefore, consideration of AC layer cross-anisotropy may have effect on stress-strain in pavement layers.

1.3 Previous Studies

Cross-anisotropy of unbound granular aggregate base layer of an instrumented pavement section was observed by Barksdale et al. (1989). They proposed a linear elastic cross-anisotropic model for this unbound layer. Anisotropy was also observed in granular aggregate during an experimental effort by Lo and Lee (1990). Based on the experimental results, this study proposed cross-anisotropy model for elastic granular aggregate. Later, Tutumluer and Barksdale (1995) performed a study on the same instrumented pavement section in Barksdale et al. (1989). They proposed a nonlinear cross-anisotropic model for granular aggregate. It was in good agreement with the pavement response.

Tutumluer et al. (2001) conducted triaxial test to determine the cross-anisotropic parameters of Unbound Aggregate Base (UAB) layer. For the validation of their study, pavement response data were collected from the test sections in both Texas Transportation Institute (TTI) and Georgia Tech. Based on the laboratory test results, they developed a nonlinear elastic cross-anisotropic model for the UAB. Later, this model was validated by the collected pavement response. They compared the pavement analysis results for both cross-anisotropic and isotropic material model. It was observed the analysis results for these two different models are not the same.

Before 2000, study of cross-anisotropy was mostly concentrated to the unbound granular aggregate layer. Attention was paid to cross-anisotropy of bound layer, i.e., AC layer, by Masad

et al. (2002). This study investigated the anisotropy of AC using micromechanics-based model. The degree of anisotropy was predicted by quantifying the anisotropy of internal structure of an AC cylinder sample as compacted by the Superpave gyratory compactor in laboratory, i.e., orientation of the longest axes and contact normal of aggregates. These orientations were captured by image analysis technique. They observed that the vertical and horizontal stiffness were not the same. In some cases, horizontal stiffness was even 30% greater than the vertical stiffness. In the same year, a research work by Mamlouk et al. (2002) stated that the anisotropic effect of AC, compacted by Superpave Gyratory Compactor in laboratory, might be ignored as they observed small difference in stiffness along horizontal, vertical, and diagonal direction from compressive and tensile properties of AC.

Later, Wang et al. (2005) performed a study to determine the degree of cross-anisotropy of field collected AC sample. The conducted the Triaxial test on 4-inch cube specimen. This cube specimen was extracted from a block that was cored from WesTrack project, i.e., a pavement test section. Asphalt content and air void content of this sample were 5.7% and 8% respectively. They conducted both Triaxial compression, extension, and simple shear test on this cube specimen at room temperature (20 °C). Variation of temperature and loading frequency were out of the scope of this study. This study reported that the vertical stiffness were 2-5 times greater than horizontal modulus. Finally, they recommended further investigation on characterization and modeling of anisotropic properties of asphalt concrete.

Presence of cross-anisotropy in AC is also studied by Motola and Uzan (2007). Goal of this study was to investigate the presence of initial compaction induced anisotropy in field AC layer

and to determine the degree of anisotropy at different frequencies. AC slabs were cut from the thin asphalt pavement section. A number of test cube specimens of 8 in. x 3.2 in. x 3.2 in. were cored from these AC slabs. Therefore, each cube specimen had one long (horizontal) and one short (vertical) axis. The asphalt content and air void content of these cube specimens were 4.8% and 9.8%. The nominal maximum aggregate size was 0.5 inch (12.7 mm). Dynamic modulus test were conducted on these test cube specimens at different frequencies, between 0.2 and 20 Hz, along both short and long axes. This test was conducted only at 40 °C. It was observed that the AC is cross-anisotropic. In addition, the degree of cross-anisotropy, i.e., ratio of horizontal and vertical modulus, was 40%.

To this day, several studies to predict pavement responses have been performed considering pavement materials as isotropic under dynamic load (Kuo and Chou 2004, Uddin and Garza 2010, and Tarefder and Ahmed 2013). A study by Masad et al. (2006) covered both isotropic and anisotropic material model for unbound layers, such as granular aggregate in base layer, to determine the pavement response. In their study, an axi-symmteric Finite Element Model (FEM) was developed that was subjected to a static load to simulate Benkelman beam load. Cross-anisotropy was also investigated by Oh et al. (2006) for unbound layer material. They developed four different cross-anisotropy material models based on laboratory tests. These material models were then implemented in a static FEM to predict pavement response under Falling Weight Deflectometer (FWD) test. Later, Al-Qadi et al. (2010) considered cross-anisotropy for the unbound layers, such as base and subgrade, in a 3D dynamic FEM to predict pavement responses under a FWD test load. In addition, nonlinear elasticity was incorporated for granular aggregate in base layer. It is evident that these studies ignored the presence of the AC cross-anisotropy.

Temperature is an important factor that affects stiffness of the AC. It is known that the AC modulus is high at low temperature and vice versa (Appea 2003, Robbins 2009, and Bayat et al. 2011). Previous studies also documents that a pavement temperature varies over the depth (Diefenderfer 2002, and Herb et al. 2006). A qualitative variation of temperature over the depth of an AC layer is shown in Figure 1.2. During a day, temperature at a pavement surface is greater than its bottom, i.e., bottom of an AC layer. This trend may change at different times over a day.

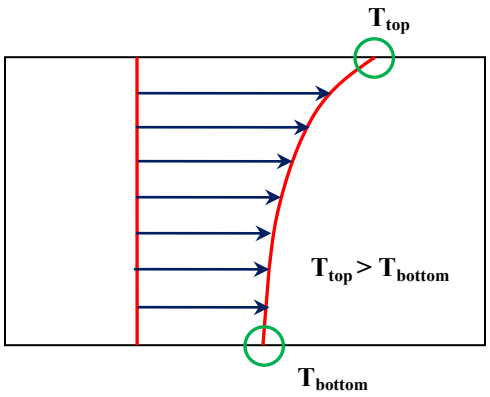

Figure 1.2 Temperature variation over depth in AC of a pavement section

In response to this temperature variation, AC modulus may also vary over the depth. The modulus variation may affect the stress and strain of a pavement structure. In a study by Dave et al. (2011), a graded FEM was developed to incorporate non-uniform distribution of stiffness in an AC layer. It was observed that the non-uniformity of the stiffness over the depth affects the stress-strain. At this point, it was recommended to incorporate the non-uniform distribution of AC stiffness due to depth-temperature variation. Later, Wang and Al-Qadi (2013) developed a 3D FEM to evaluate the effect of unbound layer cross-anisotropy where it was assumed that temperature remains constant over the depth of an AC layer.

On a pavement surface, vehicles move at different speeds that cause different loading durations, i.e., in other words, loading rates or frequencies. Stress-strain in a pavement may be affected by these varying loading durations since the AC is a frequency dependent material (Papazian 1962, Witczack and Root 1974, and Witczak and Fonseca 1996). It generates a need to study the effect of cross-anisotropy of AC on pavement stress-strain at different loading durations. It is mentioned earlier that the unbound layers were considered as nonlinear (stress-dependent) elastic in different studies (Hicks and Monismith 1971 and Uzan 1985). It was observed that presence of nonlinearity affects the pavement responses. Therefore, effect of cross-anisotropy of AC on pavement response needs to be studied in presence linear or nonlinear elastic base layer.

1.4 Research Need

The above mentioned literature survey related to AC cross-anisotropy has figured out some research needs. These are outlined in Figure 1.3. It shows that the major research need is to investigate the pavement response such as stress-strain due to the variation of AC cross-anisotropy. The effect AC cross-anisotropy needs to be addressed with the three other different phenomena and material characteristics as shown in Figure 1.3.

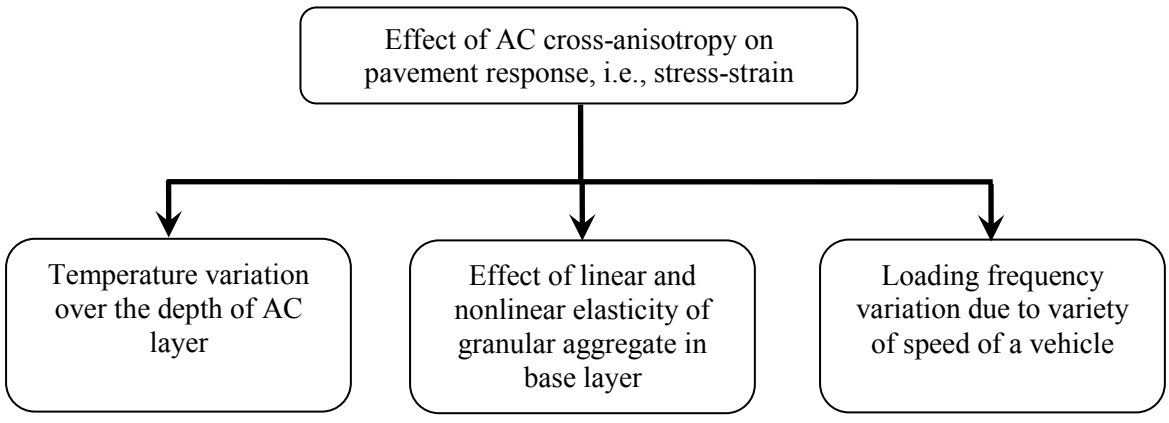

Figure 1.3 Research needs

1.5 Hypothesis

AC is the top most layer of a multi-layered asphalt pavement. A high amount of traffic induced stress is distributed in this layer. Till today, effect of cross-anisotropy of AC on pavement such as stress-strain is not studied yet. It is hypothesized that incorporation of cross-anisotropy of AC layer in pavement will have significant effect on pavement stress-strain. This effect can be investigated by a numerical method such as dynamic Finite Element Method (FEM) considering AC layer depth-temperature variation, loading duration, and linear or nonlinear elastic base layer.

1.6 Objectives

Main goal of this study is to investigate the effect of the AC cross-anisotropy on pavement stress-strain through the dynamic FEM. Specific objectives are as below:

- Develop a temperature-dependent and cross-anisotropic linear viscoelastic AC model based on both laboratory and field tests of the field-compacted AC cores.
- Develop a stress-dependent and cross-anisotropic nonlinear elastic model for unbound layers based on both laboratory and field tests.
- Incorporate the developed material models of the AC and unbound layers into the dynamic FEM to determine pavement stress-strain under dynamic load.
- Perform the parametric study based on specific pavement responses, such as tensile strain at the bottom of the AC layer and vertical compressive strains in pavement layers, at varying degree of cross-anisotropy (n-values).
- Incorporate the simulated strains into the Miner's damage formula to investigate the effect of the AC cross-anisotropy on the pavement damage.

1.7 Outline

Outline of this dissertation is shown in Figure 1.4. The entire dissertation is divided in a total of seven chapters which describe the research need and proposed hypothesis, development of the model and required laboratory as well as field testing, and parametric study based on pavement responses simulated by the dynamic FEM.

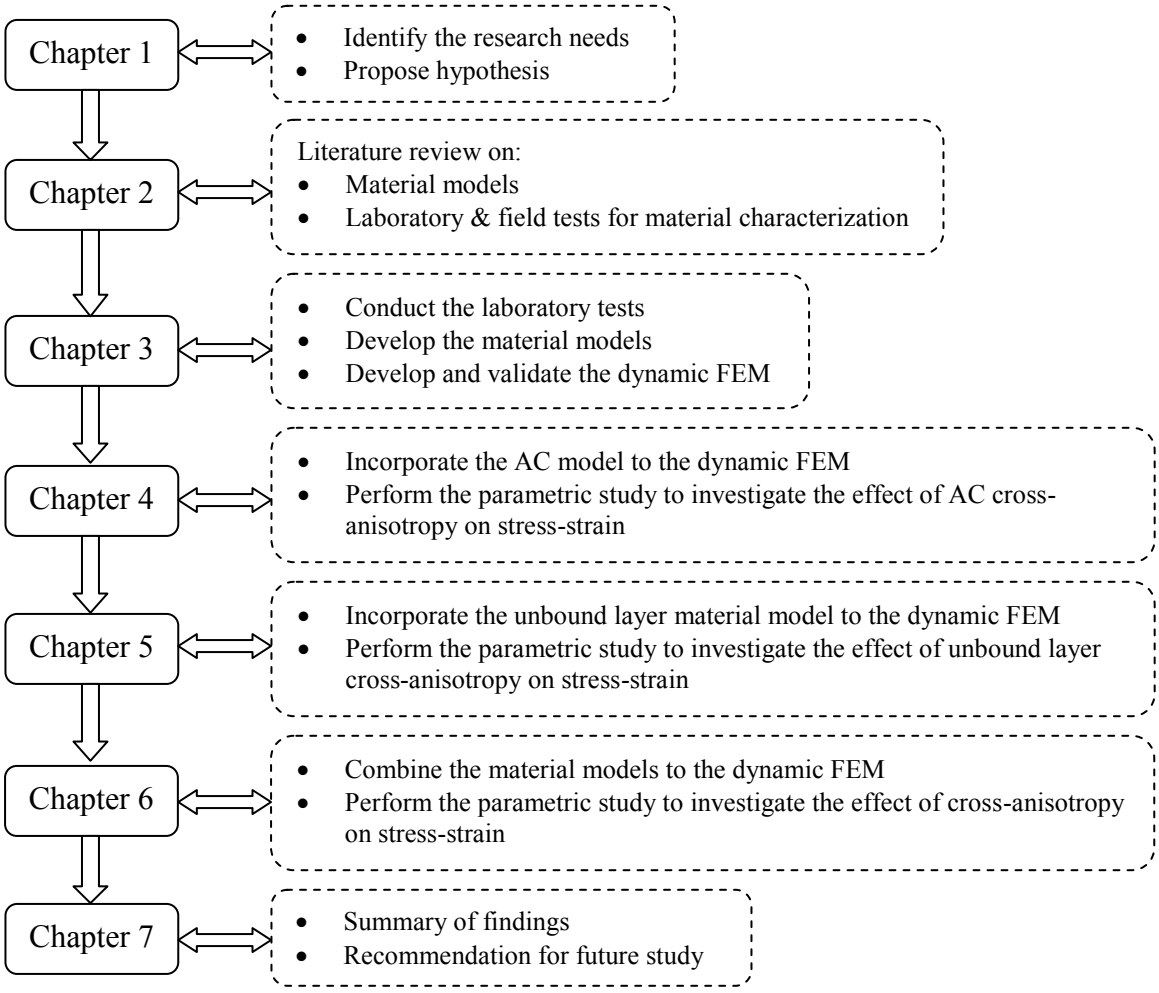

Figure 1.4 Outline of dissertation

CHAPTER 2

LITERATURE REVIEW

2.1 General

A number of researches have been performed on different aspects of pavement modeling or analysis such as analysis technique, characterization of material properties, types of load, climatic factors which affects material behavior and so on. A literature review is performed to explore the findings, limitations and/or recommendations based on the earlier researches related to the objectives of this study. Summary of this literature review is documented in this chapter.

2.2 Material Cross-Anisotropy

A vertical load is applied on a solid medium which generates both normal and shear stresses on a rectangle element in a 2-D plane (Figure 2.1). In a 3-D Cartesian reference system, there are total of nine stress components (σ_{ij}, $i, j = 1$, 2, and 3) on a cube element. The first subscript, *i*, denotes an axis which is perpendicular to a specific surface of stresses. The second subscript, *j*, denotes an axis which is along the stress direction. Among these components, three are normal stresses (σ_{ij} where $i = j$) and the rest are shear stresses (σ_{ij} where $i \neq j$). Strains (ε_{ij}) related to each of the earlier mentioned stresses are also shown in Figure 2.1.

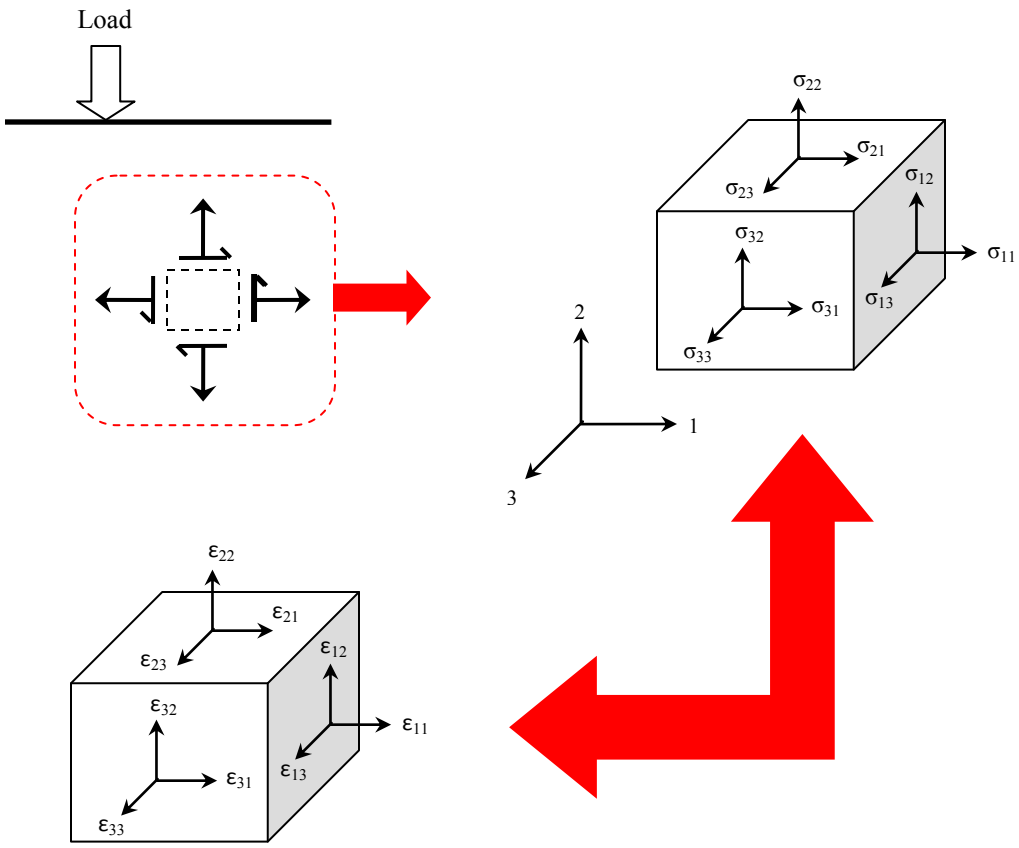

Figure 2.1 State of stresses

It is known that stresses and strains are correlated by the Hooke's law (Sadd et al. 2009). According to this law, stress is equal to product of strain and modulus of elasticity, i.e., $\sigma = E\varepsilon$, where $E =$ modulus of elasticity. This expression is a basic relationship between stress and strain. In case of the earlier mentioned state of stresses, the generalized form will be: $\sigma_{ij} = C_{ijkl}\varepsilon_{kl}$, where $C_{ijkl} =$ modulus of elasticity along different directions and $i, j, k, l = 1, 2,$ and 3. This generalized form is expanded in a matrix form as shown in eqn. (2.1). It is observed that nine components of stresses are related to strains based on a total of 81 components of modulus of elasticity.

$$\begin{Bmatrix}\sigma_{11}\\ \sigma_{22}\\ \sigma_{33}\\ \sigma_{23}\\ \sigma_{31}\\ \sigma_{12}\\ \sigma_{32}\\ \sigma_{13}\\ \sigma_{21}\end{Bmatrix}=\begin{bmatrix}C_{1111} & C_{1122} & C_{1133} & C_{1123} & C_{1131} & C_{1112} & C_{1132} & C_{1113} & C_{1121}\\ C_{2211} & C_{2222} & C_{2233} & C_{2223} & C_{2231} & C_{2212} & C_{2232} & C_{2213} & C_{2221}\\ C_{3311} & C_{3322} & C_{3333} & C_{3323} & C_{3331} & C_{3312} & C_{3332} & C_{3313} & C_{3321}\\ C_{2311} & C_{2322} & C_{2333} & C_{2323} & C_{2331} & C_{2312} & C_{2332} & C_{2313} & C_{2321}\\ C_{3111} & C_{3122} & C_{3133} & C_{3123} & C_{3131} & C_{3112} & C_{3132} & C_{3113} & C_{3121}\\ C_{1211} & C_{1222} & C_{1233} & C_{1223} & C_{1231} & C_{1212} & C_{1232} & C_{1213} & C_{1221}\\ C_{3211} & C_{3222} & C_{3233} & C_{3223} & C_{3231} & C_{3212} & C_{3232} & C_{3213} & C_{3221}\\ C_{1311} & C_{1322} & C_{1333} & C_{1323} & C_{1331} & C_{1312} & C_{1332} & C_{1313} & C_{1321}\\ C_{2111} & C_{2122} & C_{2133} & C_{2123} & C_{2131} & C_{2112} & C_{2132} & C_{2113} & C_{2121}\end{bmatrix}\begin{Bmatrix}\varepsilon_{11}\\ \varepsilon_{22}\\ \varepsilon_{33}\\ \varepsilon_{23}\\ \varepsilon_{31}\\ \varepsilon_{12}\\ \varepsilon_{32}\\ \varepsilon_{13}\\ \varepsilon_{21}\end{Bmatrix} \tag{2.1}$$

There is symmetry in stress and strain tensor, i.e., $\sigma_{ij}=\sigma_{ji}$ and $\varepsilon_{kl}=\varepsilon_{lk}$, which reduces 81 components to 36. The reduced form of the eqn. (2.1) is shown in eqn. (2.2). Three normal stress components are: σ_i where $i=1$, 2, and 3 whereas three shear stress components are: τ_i where $j=4$, 5, and 6. In case of strains, ε_i where $i=1$, 2, and 3 are normal and γ_i where $j=4$, 5, and 6 are shear components. In addition, the C_{ijkl}-matrix reduces to C_{ij}-matrix which comprises 36 independent components.

$$\begin{Bmatrix}\sigma_1\\ \sigma_2\\ \sigma_3\\ \tau_4\\ \tau_5\\ \tau_6\end{Bmatrix}=\begin{bmatrix}C_{11} & C_{12} & C_{13} & C_{14} & C_{15} & C_{16}\\ C_{21} & C_{22} & C_{23} & C_{24} & C_{25} & C_{26}\\ C_{31} & C_{32} & C_{33} & C_{34} & C_{35} & C_{36}\\ C_{41} & C_{42} & C_{43} & C_{44} & C_{45} & C_{46}\\ C_{51} & C_{52} & C_{53} & C_{54} & C_{55} & C_{56}\\ C_{61} & C_{62} & C_{63} & C_{64} & C_{65} & C_{66}\end{bmatrix}\begin{Bmatrix}\varepsilon_1\\ \varepsilon_2\\ \varepsilon_3\\ \gamma_4\\ \gamma_5\\ \gamma_6\end{Bmatrix} \tag{2.2}$$

These 36 independent components are further reduced to 21 components due to energy based symmetry. The modified form of the eqn. (2.2) is shown in eqn. (2.3). Therefore, it can be said that 21 independent components are necessary to define an anisotropic material.

$$\begin{Bmatrix}\sigma_1\\ \sigma_2\\ \sigma_3\\ \tau_4\\ \tau_5\\ \tau_6\end{Bmatrix}=\begin{bmatrix}C_{11} & C_{12} & C_{13} & C_{14} & C_{15} & C_{16}\\ & C_{22} & C_{23} & C_{24} & C_{25} & C_{26}\\ & & C_{33} & C_{34} & C_{35} & C_{36}\\ & & & C_{44} & C_{45} & C_{46}\\ & & & & C_{55} & C_{56}\\ & & & & & C_{66}\end{bmatrix}\begin{Bmatrix}\varepsilon_1\\ \varepsilon_2\\ \varepsilon_3\\ \gamma_4\\ \gamma_5\\ \gamma_6\end{Bmatrix} \tag{2.3}$$

A material is orthotropic whenever it has three orthogonal axes of symmetry. Due to presence of these axes of symmetry, number of components in eqn. (2.3) will reduce to 9 independent components and the modified form is eqn. (2.4).

$$\begin{Bmatrix}\sigma_1\\ \sigma_2\\ \sigma_3\\ \tau_4\\ \tau_5\\ \tau_6\end{Bmatrix}=\begin{bmatrix}C_{11} & C_{12} & C_{13} & 0 & 0 & 0\\ & C_{22} & C_{23} & 0 & 0 & 0\\ & & C_{33} & 0 & 0 & 0\\ & & & C_{44} & 0 & 0\\ & & & & C_{55} & 0\\ & & & & & C_{66}\end{bmatrix}\begin{Bmatrix}\varepsilon_1\\ \varepsilon_2\\ \varepsilon_3\\ \gamma_4\\ \gamma_5\\ \gamma_6\end{Bmatrix} \tag{2.4}$$

A material is called cross-anisotropic or transversely isotropic whenever modulus of elasticity along two orthogonal axes (on a plane) is same and differs from that along an axis normal to that plane, i.e., $E_2 = E_1 \neq E_3$. In this type of anisotropy, number of independent components is reduced to 5, i.e., $C_{11}, C_{22}, C_{12}, C_{13}, C_{44}$.

$$\begin{Bmatrix}\sigma_1\\ \sigma_2\\ \sigma_3\\ \tau_4\\ \tau_5\\ \tau_6\end{Bmatrix}=\begin{bmatrix}C_{11} & C_{12} & C_{13} & 0 & 0 & 0\\ & C_{22} & C_{12} & 0 & 0 & 0\\ & & C_{11} & 0 & 0 & 0\\ & & & C_{44} & 0 & 0\\ & & & & \dfrac{C_{11}-C_{12}}{2} & 0\\ & & & & & C_{44}\end{bmatrix}\begin{Bmatrix}\varepsilon_1\\ \varepsilon_2\\ \varepsilon_3\\ \gamma_4\\ \gamma_5\\ \gamma_6\end{Bmatrix} \tag{2.5}$$

The material is isotropic whenever the modulus of elasticity is same in every direction. Therefore, the 5 independent components are finally reduced to 2 components and the eqn. (2.6) is simple form for isotropic elasticity.

$$\begin{Bmatrix} \sigma_1 \\ \sigma_2 \\ \sigma_3 \\ \tau_4 \\ \tau_5 \\ \tau_6 \end{Bmatrix} = \begin{bmatrix} C_{11} & C_{12} & C_{12} & 0 & 0 & 0 \\ & C_{11} & C_{12} & 0 & 0 & 0 \\ & & C_{11} & 0 & 0 & 0 \\ & & & \frac{C_{11}-C_{12}}{2} & 0 & 0 \\ & & & & \frac{C_{11}-C_{12}}{2} & 0 \\ & & & & & \frac{C_{11}-C_{12}}{2} \end{bmatrix} \begin{Bmatrix} \varepsilon_1 \\ \varepsilon_2 \\ \varepsilon_3 \\ \gamma_4 \\ \gamma_5 \\ \gamma_6 \end{Bmatrix} \tag{2.6}$$

Based on the above mentioned discussion, it is evident that different types of anisotropy comprise different number of independent components in the elasticity matrix, i.e., *C* or *E*-matrix. Number of these components is summarized in Table 2.1. In a typical isotropic material, 2 independent components are required whereas 5 independent components are required to define cross-anisotropy.

Table 2.1 Number of independent components in elasticity matrix

Material type	Independent constants
General anisotropy	81
Anisotropy (symmetry of stress & strain tensor)	36
Anisotropy (with elastic energy)	21
Orthotropic	9
Cross-anisotropy (Transverse isotropy)	5
Isotropy	2

During the stress-strain calculation, it is necessary to determine the values of independent components. These independent components are function of some basic mechanical parameters, such as Elastic modulus (E), Shear modulus (G) and Poisson's ratio (ν) in different directions or planes. Components of the C-matrix in terms of these mechanical parameters are complicated. For this reason, the Compliance (D-matrix), i.e., reciprocal of the elastic modulus, is introduced to understand the simplest form the independent components. Eqn. (2.7) is the D-matrix for orthotropic material which comprises three E-values, three G-values and three $\nu-$values respectively.

$$[D]=\begin{bmatrix} \frac{1}{E_1} & -\frac{\nu_{21}}{E_2} & -\frac{\nu_{31}}{E_3} & 0 & 0 & 0 \\ -\frac{\nu_{12}}{E_1} & \frac{1}{E_2} & -\frac{\nu_{32}}{E_3} & 0 & 0 & 0 \\ -\frac{\nu_{13}}{E_1} & -\frac{\nu_{23}}{E_2} & \frac{1}{E_3} & 0 & 0 & 0 \\ & & & \frac{1}{G_{23}} & 0 & 0 \\ & & & & \frac{1}{G_{31}} & 0 \\ & & & & & \frac{1}{G_{12}} \end{bmatrix} \tag{2.7}$$

If the axis-*1*, *2* and *3* (in Figure 2.1) is expressed as *v*, *h* and *v*-directions where '*h*' is horizontal and '*v*' is vertical, eqn. (2.7) will become eqn. (2.8). It is observed that eqn. (2.8) has 5 independent components, i.e., E_v, E_h, G_{vh}, ν_{vh} and ν_{hh}, which is true for cross-anisotropy or transverse isotropy. Therefore, during analysis, these five mechanical parameters need to be determined to assign material cross-anisotropy.

$$[D]=\begin{bmatrix} \frac{1}{E_h} & -\frac{\nu_{vh}}{E_v} & -\frac{\nu_{hh}}{E_h} & 0 & 0 & 0 \\ & \frac{1}{E_v} & -\frac{\nu_{vh}}{E_v} & 0 & 0 & 0 \\ & & \frac{1}{E_h} & 0 & 0 & 0 \\ & & & \frac{1}{G_{vh}} & 0 & 0 \\ & & & & \frac{2(1+\nu_{hh})}{E_h} & 0 \\ & & & & & \frac{1}{G_{hv}} \end{bmatrix} \tag{2.8}$$

A material becomes isotropy whenever the E and ν -values are same in every direction. The eqn. (2.8) becomes (2.9). It is evident that only two independent mechanical parameters, i.e., E and ν , are needed to assign the material isotropy.

$$[D]=\begin{bmatrix} \frac{1}{E} & -\frac{\nu}{E} & -\frac{\nu}{E} & 0 & 0 & 0 \\ & \frac{1}{E} & -\frac{\nu}{E} & 0 & 0 & 0 \\ & & \frac{1}{E} & 0 & 0 & 0 \\ & & & \frac{2(1+\nu)}{E} & 0 & 0 \\ & & & & \frac{2(1+\nu)}{E} & 0 \\ & & & & & \frac{2(1+\nu)}{E} \end{bmatrix} \tag{2.9}$$

2.3 Viscoelasticity of AC

It is known that the AC is a viscoelastic material (Papazian 1962, Haddad 1995, and Lee 1996). A viscoelastic material exhibits both elasticity and viscosity. Basic feature of an elastic material is to store energy whenever it is deformed due to an external load and release this energy

completely upon removal of the load. In brief, there are zero deformation and energy dissipation after a complete cycle of loading-unloading. In case of viscosity, energy is continuously dissipated with none stored. In reality, a number of engineering materials including the AC stores and dissipates in varying degrees during a loading-unloading cycle.

In discussion under the earlier section, it is mentioned that stress (σ) is equal to product of the modulus of elasticity (E) and strain (ε). The E-value can be determined from the slope of a stress-strain variation of a linear elastic material (see Figure 2.2(a)). Mechanical behavior of a linear elastic material can be expressed by a spring which shows instantaneous response during both loading and unloading. In case of a viscous material, energy dissipates due to resistance to flow or deformation and stress is equal to product of viscosity (η) and strain variation over time ($\dot{\varepsilon}$). Mechanical behavior of a viscous material can be expressed by a dashpot (see Figure 2.2(b)).

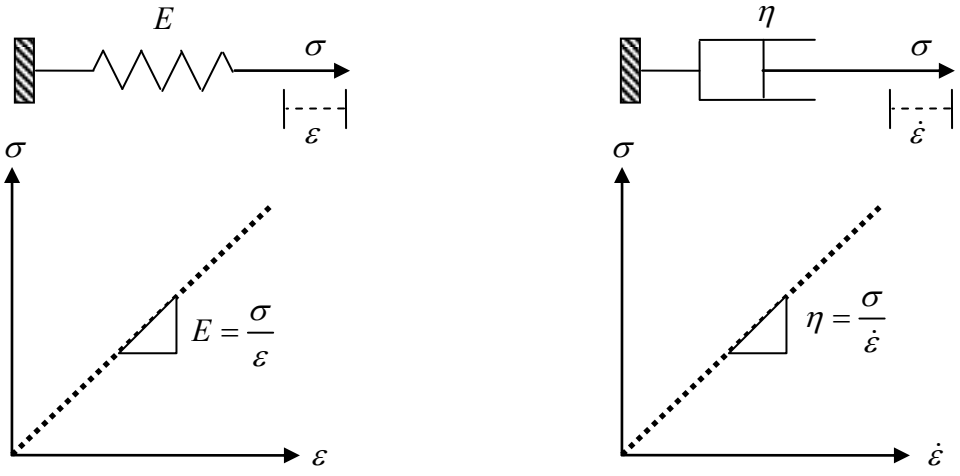

(a) Elasticity (b) Viscosity

Figure 2.2 Elasticity and viscosity

The above mentioned discussion indicates that mechanical behavior of a viscoelastic material can be expressed as combinations of spring and dashpot. Many different combinations can be used for this purpose. There are two basic mechanical models available for viscoelasticity and these are: Maxwell and Kelvin models respectively (Huang 2004).

Maxwell Model

It is a combination of a spring and a dashpot in series (Figure 2.3). Let, this model is subjected to a instantaneous strain which is constant over a certain span of time, i.e., $\varepsilon(t) = \varepsilon$. Total strain is summation of strains in spring (ε_s) and dashpot (ε_d) as below:

$$\varepsilon = \varepsilon_s + \varepsilon_d = \frac{\sigma}{E} + \frac{\sigma t}{\eta} = \frac{\sigma}{E}\left(1 + \frac{t}{T_{relax}}\right) \tag{2.10}$$

where T_{relax} = relaxation time = η / E. Figure 2.3 shows stress gradually decreases over time due constant strain. This behavior is known as relaxation. Eqn. (2.10) can be re-written as follows:

$$\frac{\partial \varepsilon}{\partial t} = \frac{1}{E}\frac{\partial \sigma}{\partial t} + \frac{\sigma}{\eta} \Rightarrow 0 = \frac{1}{E}\frac{\partial \sigma}{\partial t} + \frac{\sigma}{\eta} \Rightarrow -\frac{1}{E}\frac{\partial \sigma}{\partial t} = \frac{\sigma}{\eta} \Rightarrow -\frac{1}{E}\int_{\sigma_0}^{\sigma}\frac{d\sigma}{\sigma} = \frac{1}{\eta}\int_0^t dt \Rightarrow \sigma = \sigma_0 e^{-tE/\eta} \tag{2.11}$$

Special cases:

(a) $t = 0;\ \sigma = \sigma_0$

(b) $t = \infty;\ \sigma = 0$

(c) $t = T_{relax};\ \sigma = 0.368\sigma_0$

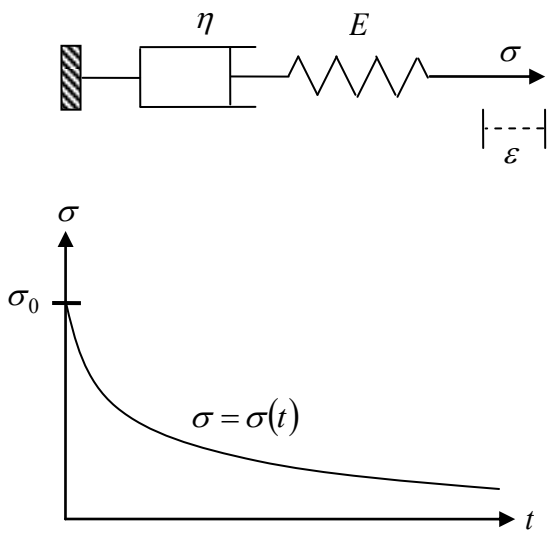

Figure 2.3 Maxwell model

Kelvin Model

It is a combination of a spring and a dashpot in parallel (Figure 2.4). Let, this model is subjected to an instantaneous stress which is constant over a certain span of time, i.e., $\sigma(t) = \sigma$. Total stress is summation of stresses in spring (ε_s) and dashpot (ε_d) as below:

$$\sigma = \sigma_s + \sigma_d = E\varepsilon + \eta \frac{\partial \varepsilon}{\partial t} \tag{2.12}$$

$$\int_0^{\varepsilon} \frac{d\varepsilon}{\sigma - E\varepsilon} = \int_0^{t} \frac{dt}{\eta} \Rightarrow -\frac{1}{E} \ln\left(\frac{\sigma - E\varepsilon}{\sigma}\right) = \frac{t}{\eta} \Rightarrow \varepsilon = \frac{\sigma}{E}\left(1 - e^{-tE/\eta}\right) \Rightarrow \varepsilon = \varepsilon_0\left(1 - e^{-t/T_{retard}}\right) \tag{2.13}$$

where T_{retard} = retardation time = η/E. Figure 2.4 shows strain gradually increases over time due constant stress. This behavior is known as retardation.

Special cases:

(a) $t = 0;\ \varepsilon = 0$

(b) $t = \infty;\ \varepsilon = \varepsilon_0$

(c) $t = T_{retard}$; $\varepsilon = 0.368\varepsilon_0$

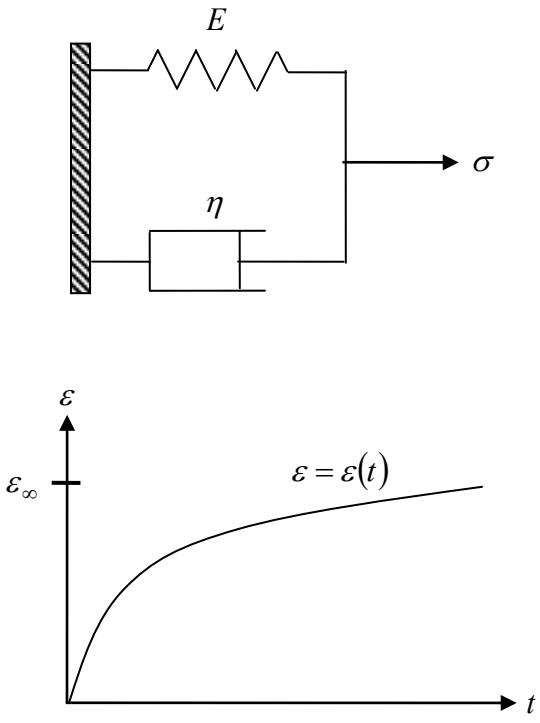

Figure 2.4 Kelvin model

Generalized Maxwell Model (GMM)

It is a model which includes *n*-number of Maxwell models/elements in parallel with a constant spring as shown in Figure 2.5 (Mase and Mase 1999, and Buechlar 2012). The spring has an elastic modulus (E_∞) which is known as long term modulus. The Maxwell elements have both modulus (E_i) and viscosity (η_i) and each of these elements has individual relaxation time ($\tau_i = \eta_i / E_i$). Stress calculation based on this model will be described under this subsection. Prior to the derivation, derivative of the eqn. (2.10) respect to time is as follows:

$$\dot{\varepsilon} = \dot{\varepsilon}_s + \dot{\varepsilon}_d = \frac{\dot{\sigma}}{E} + \frac{\sigma}{\eta} \tag{2.14}$$

It is mentioned earlier that the relaxation time is ratio of viscosity and modulus of elasticity for single Maxwell element. Here, it is denoted by τ and $\tau = \eta / E$. Now, eqn. (2.13) becomes:

$$\dot{\sigma} = E\dot{\varepsilon} - \frac{\sigma}{\tau} \tag{2.15}$$

Laplace transformation of eqn. (2.15) leads to:

$$s\sigma(s) = sE\varepsilon(s) - \frac{\sigma(s)}{\tau} \Rightarrow \sigma(s) = \frac{sE}{s + \frac{1}{\tau}}\varepsilon(s) \tag{2.16}$$

Now, the inverse Laplace transform of eqn. (2.16) back to time domain yields the following form:

$$\sigma(t) = \int_{t'=0}^{t'=t} Ee^{\left[-(t-t')/\tau\right]}\dot{\varepsilon}dt' \tag{2.17}$$

It is the most basic integral form of the Maxwell model for stress-strain calculation. This equation is used later to derive general integral form for the GMM.

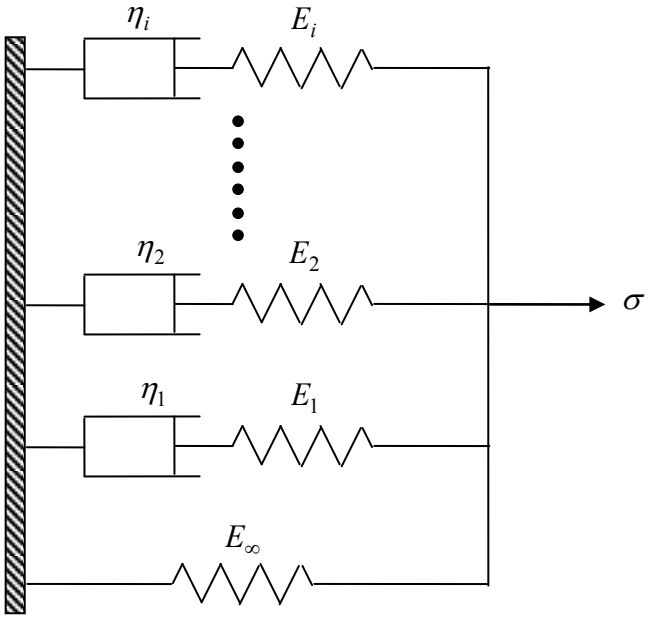

Figure 2.5 Generalized Maxwell Model

Summing up the spring and the Maxwell elements using the eqn. (2.16), the generalized form is as below:

$$\sigma(s) = \left(E_\infty + \sum_{i=1}^{n} \frac{sE_i}{s + 1/\tau_i} \right) \varepsilon(s) \tag{2.18}$$

Inverse Laplace transformation of eqn. (2.18) leads to:

$$\sigma(t) = \int_{t'=0}^{t'=t} \left\{ E_\infty + \sum_{i=1}^{n} E_i e^{\left[-(t-t')/\tau_i \right]} \right\} \dot{\varepsilon} dt' \tag{2.19}$$

Simplest form of eqn. (2.19) is as follows:

$$\sigma(t) = \int_{t'=0}^{t'=t} E(t-t') \dot{\varepsilon} dt' \tag{2.20}$$

where $E(t) = E_\infty + \sum_{i=1}^{n} E_i e^{\left(-t/\tau_i \right)}$ and this can be further modified to:

$$E(t) = E_0 \left[1 - \sum_{i=1}^{n} e_i \left\{ 1 - \exp^{\left(-t/\tau_i \right)} \right\} \right] \tag{2.21}$$

In this study, eqn. (2.21) will be adopted to assign AC viscoelasticity to the dynamic FEM of pavement. This equation is typically known as Prony series.

The above mentioned summarizes the theoretical background of viscoelasticity. Based on the nature of the eqn. (2.21), it is understood that the relaxation modulus test of a specific material is sufficient for assignment of viscoelasticity. In a relaxation modulus test, a constant strain (tensile or compression based on material type) is applied over a certain duration (Figure 2.6). In response to applied strain, an instantaneous stress is developed which gradually attenuates over time. Later, ratio of stress and strain at different time steps yields the relaxation modulus.

Finally, laboratory determined relaxation modulus values are fitted against eqn. (2.21) to determine the instantaneous modulus (E_0) and Prony series parameters, i.e., e_i and τ_i .

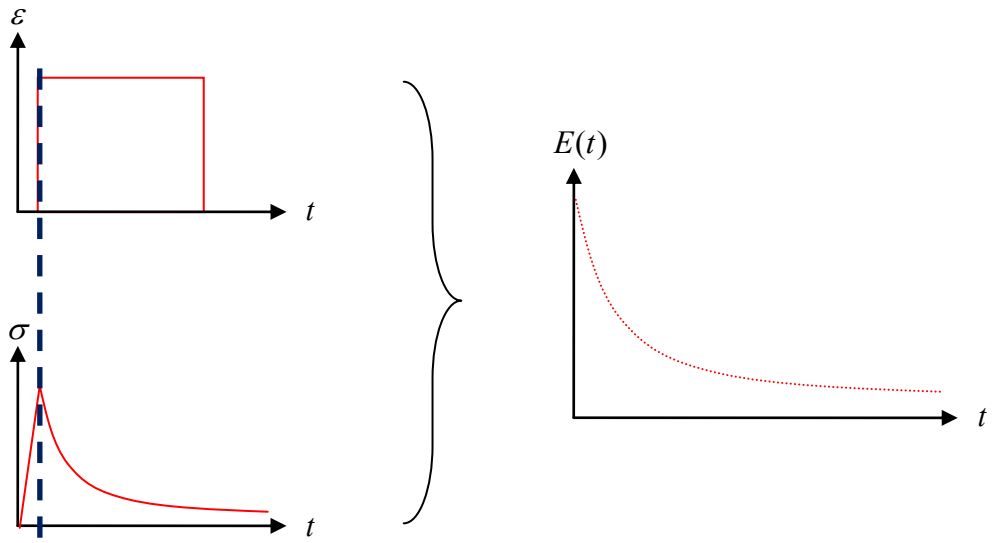

Figure 2.6 Relaxation modulus test

AC is a temperature- and frequency-dependent material which cannot be characterized by this simple type of test. Dynamic modulus test determines the modulus of AC at varying frequencies and temperatures. In this test, an AC cylinder is subjected to a uniaxial compressive cyclic stress at frequencies: 0.1, 0.5, 1.0, 5.0, 10, and 25 Hz respectively. Dynamic modulus (E^*) is determined from the ratio of applied stress (σ) and resulted strain (ε). Frequency varying dynamic modulus test is also repeated at varying temperatures. Time-Temperature-Superposition (TTSP) is applied to generate the dynamic modulus master curve at a reference temperature (Gurp and Palmen 1998, Schwartz et al. 2002, and Dealy and Plazek 2009). The relaxation modulus variation over time is determined from the dynamic modulus master curve. Details of the dynamic modulus test and related analysis will be discussed in Chapter 3.

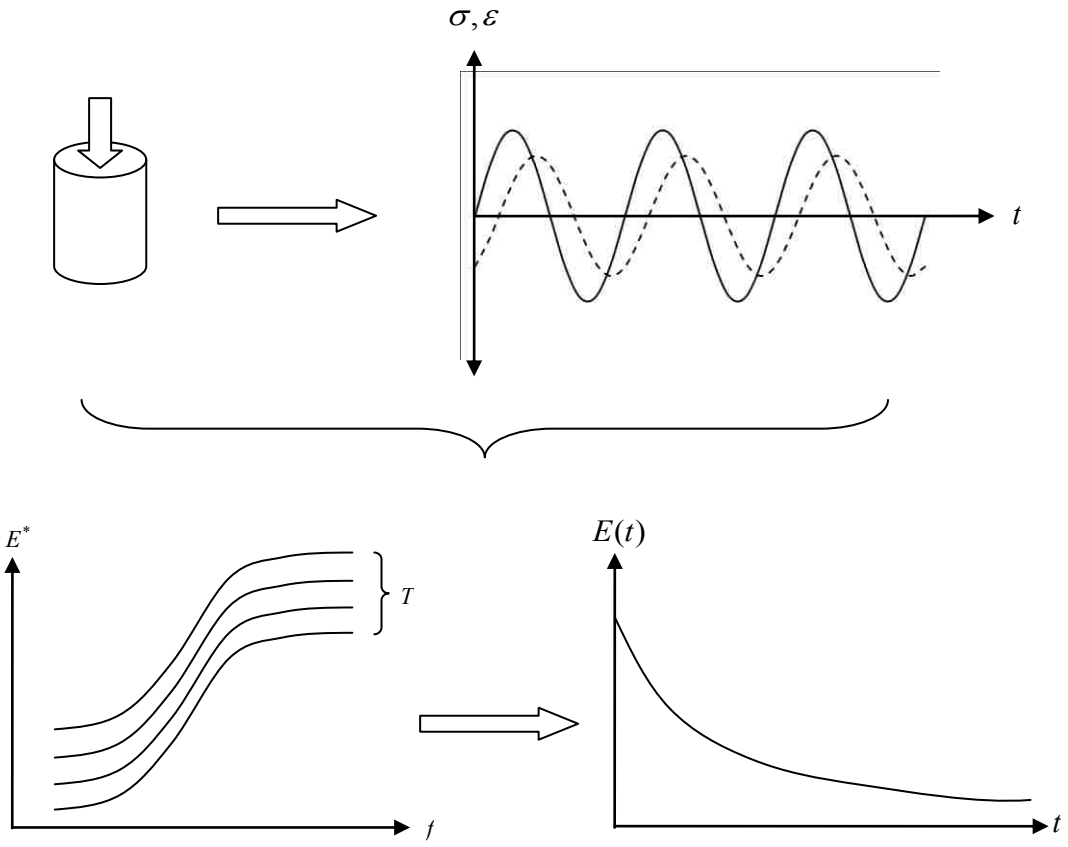

Figure 2.7 Dynamic modulus test for viscoelasticity

Finally, the Prony series parameters are determined by fitting the relaxation modulus curve against the eqn. (2.21).

2.4 Past Studies AC Cross-Anisotropy

A cross-anisotropic viscoelastic model will be developed for the AC which will be incorporated to the dynamic FEM. Later, a parametric study will be performed to investigate the effect of the AC cross-anisotropy on pavement stress-strain. For this reason, it is necessary to explore the previous researches to get the following information:

- Method to determine the AC cross-anisotropy

- Findings and/or recommendation
- Limitation(s)

The studies related to the AC cross-anisotropy are summarized as below:

Masad et al. (2002)

Method: This study investigated the presence of anisotropy in the AC using a micromechanics-based model. The test specimen was prepared by compacting loose AC mix in a Superpave Gyratory Compactor (SGC) in laboratory. The degree of anisotropy was predicted by quantifying the anisotropy of internal structure of the laboratory compacted AC test specimen, i.e., orientation of the longest axes and contact normal of aggregates. These orientations were captured by image analysis technique.

Findings: The stiffness along the vertical and horizontal stiffness was not the same which indicated that the AC possesses the anisotropy. In some cases, horizontal stiffness was even 30% greater than the vertical stiffness.

Limitations: The outcomes of this study cannot be used for viscoelastic modeling of the AC.

Mamlouk et al. (2002)

This study determined the anisotropy of AC test specimens which were also compacted by a SGC in laboratory. These test specimens were extracted along vertical, horizontal, and diagonal directions from the laboratory compacted AC cylinder. The dynamic modulus test was conducted to evaluate the presence of anisotropy.

Findings: It was observed that the ratio of the horizontal and vertical stiffness was as high as 0.85. It was concluded that the anisotropy in the laboratory compacted AC is insignificant due to small difference (15%) between vertical and horizontal direction stiffness.

Limitations: This study did not conduct any laboratory test on field-compacted AC core. Therefore, the outcomes are not the field representative.

Wang et al. (2005)

This study determined the degree of cross-anisotropy of field-compacted AC test specimens the laboratory Triaxial tests. A number of 4 inch AC cube test specimens were used for the tests. These cube specimens were extracted from a block which was cored earlier from the WesTrack project, i.e., a pavement test section. Asphalt content and air void content of this sample were 5.7% and 8% respectively. The Triaxial tests were conducted in compression, extension, and simple shear test mode on this cube specimen at the room temperature (20 °C).

Findings: The ratios of the horizontal and vertical stiffness were 0.2~0.5. Finally, it was recommended to perform further investigation on characterization and modeling of anisotropic properties of asphalt concrete.

Limitations: Variation of temperature and loading frequency were out of the scope of this study. In addition, the outcomes cannot be used for the viscoelastic modeling of the AC.

Motola and Uzan (2007)

Goal of this study was to investigate the presence of initial compaction induced anisotropy in field-compacted AC test specimen and to determine the degree of anisotropy at different frequencies. For this purpose, AC slabs were cut from the thin asphalt pavement section. A

number of test cube specimens of 8 in. x 3.2 in. x 3.2 in. were cored from these AC slabs. The asphalt content and air void content of these cube specimens were 4.8% and 9.8%. A Dynamic modulus type test was conducted on these test cube specimens at different frequencies, between 0.2 and 20 Hz.

Findings: The AC was observed as cross-anisotropic. In addition, the degree of cross-anisotropy was as high as 0.4.

Limitations: The tests were conducted on a specific type of AC mix which had nominal maximum aggregate size was 0.5 inch (12.7 mm). This test was conducted only at 40 °C. Degree of cross-anisotropy at other temperature is unknown. Therefore, proper viscoelastic modeling of the AC is not possible with these test outcomes.

Jurado (2008)

This study determined the presence of cross-anisotropy in laboratory-compacted AC test specimen using an ultrasonic method. Five independent material constants to define the cross-anisotropy were determined based on the interpretation of velocity measurements in different configurations.

Findings: This study also observed that the vertical and horizontal stiffness of the laboratory-compacted AC are not the same.

Limitations: Outcomes of this study cannot be used for viscoelastic modeling of the AC.

Summary of the above mentioned studies are is as below:

- Presence of cross-anisotropy in AC is observed in both laboratory and field-compacted AC.

- Degree of cross-anisotropy varies from 0.2 to 0.85 in the past studies. The field-compacted AC typically shows smaller horizontal modulus compared to laboratory-compacted AC.
- Dynamic modulus tests were conducted on both laboratory-compacted vertical and horizontal cores, i.e., cylinder shaped test specimens, to determine the degree of cross-anisotropy. However, rectangle test specimens were used in case of field-compacted AC and conventional dynamic modulus test was not conducted. Therefore, it was not possible to determine the viscoelasticity or Prony series parameters of the field-compacted AC.

2.5 Dynamic Modulus of Field-compacted AC

A conventional dynamic modulus test requires an AC cylinder of 4 inch diameter and 6 inch height so that the slenderness ratio can be at least or above 1.5. An AC cylinder is preferred over a rectangle specimen to avoid corner stiffness. Gauge length of the strain gauge for measuring strain needs to be greater than 2-3 times the Nominal Maximum Aggregate Size (NMAS). In addition, clearance between end of strain gauge and edge of AC test specimen needs to be at least 1 inch to avoid stress concentration. It is difficult to get an AC cylinder with required dimensions from an asphalt pavement. This is because a pavement typically constructed by compacting multiple thin AC lifts.

Efforts were made to determine the dynamic modulus of thin AC in past studies (Kaloush 2001 and Pellinen et al. 2002). In the study by Kaloush (2001), disk-shaped thin layers of AC were collected from selected pavement sections. A total of three disks were stacked vertically and glued together to prepare an AC cylinder with required dimensions. Two different types of glues were used and these are: binder and epoxy. The strain gauges were installed at the mid-AC disk

within the interfaces to measure the strain under the cyclic loading. It was observed that the AC cylinder with binder at the interfaces of the disks shows more reasonable values compared to that using epoxy. In other study by Pellinen (2002), rectangle blocks are cut from AC cores and stacked along both vertical and horizontal directions. These are glued together to prepare a block. Finally, dynamic modulus test was conducted on the AC blocks. However, there is possibility of corner stiffness which may affect the dynamic modulus values severely.

The above mentioned discussion indicates that the dynamic modulus test on thin AC can be conducted according to the methodology proposed by Kaloush (2001). However, research needs to be performed to explore a better testing configuration where the dynamic modulus test can be conducted on a full sized AC cylinder collected from a pavement section.

2.6 Depth-Temperature Variation and Effect on AC

It is mentioned earlier that pavement temperature affects stiffness (*E*-value) of AC (Chapuis and Gatien 1995, Robbins 2009, and Bayat et al. 2011). Generally, at high temperature shear stiffness (*G*-value) of asphalt binder is low which eventually leads to an overall reduction in AC mix and vice versa (Appea 2003). In a pavement section, temperature varies over depth. Typically, during daytime, pavement surface temperature is high and gradually decreases towards the bottom (Islam 2015). Diefenderfer (2002) performed a study on this issue where temperatures were measured by the thermocouples installed at different depths of a pavement section in the Virginia Smart Road. It was observed that temperature varies linearly with depth. Based on this observation, linear depth-temperature model was proposed under the scope of this study. Herb et

al. (2006) also performed a study on depth-temperature variation. This study stated that the temperature varies nonlinearly over depth of a pavement section.

The above mentioned studies show that temperature is not constant over pavement depth. Due to the temperature variation, AC modulus should also vary over depth. A study by Wang and Al-Qadi (2013) incorporated temperature dependency of the AC modulus in a dynamic FEM of pavement to simulate stress-strain under truck. The FEM were simulated at two different temperatures such as 25 °C and 47 °C and these temperatures were constant over the AC layer. However, considering average temperature in a pavement model which is constant over depth may lead to an error in simulated stress-strain. Before this study, Dave et al. (2011) applied graded FEM to incorporate non-homogeneous distribution of mechanical properties over depth, especially non uniform distribution of *E*-values in AC layer. In this method, *E*-value is defined to vary over the AC depth. It was recommended to perform further research to incorporate the variation of *E*-value over the AC depth based on depth-temperature profile.

2.7 Unbound Layer Stress-Dependency

In a pavement structure, base, subbase, and subgrade comprise granular aggregates and fine soil which are called unbound materials due to little to no cohesion. Past studies show that these materials are nonlinear elastic (Hicks and Monismith 1971, and Uzan 1985). In case of nonlinear elasticity, material undergoes deformation during loading and regains its original shape after removal of load similar to linear elasticity. However, the entire trend is nonlinear instead of linear as observed in linear elasticity (Figure 2.8(a)). Unbound materials are also stress-dependent. Typically, an unbound material exhibits very little to no stiffness without confining

pressure. In presence of confining pressure and imposed traffic stress, stiffness may vary. A material exhibits stress-hardening whenever the stiffness increases with increase in the earlier mentioned stresses (Figure 2.8(b)). Generally, this behavior is observed in granular aggregates.

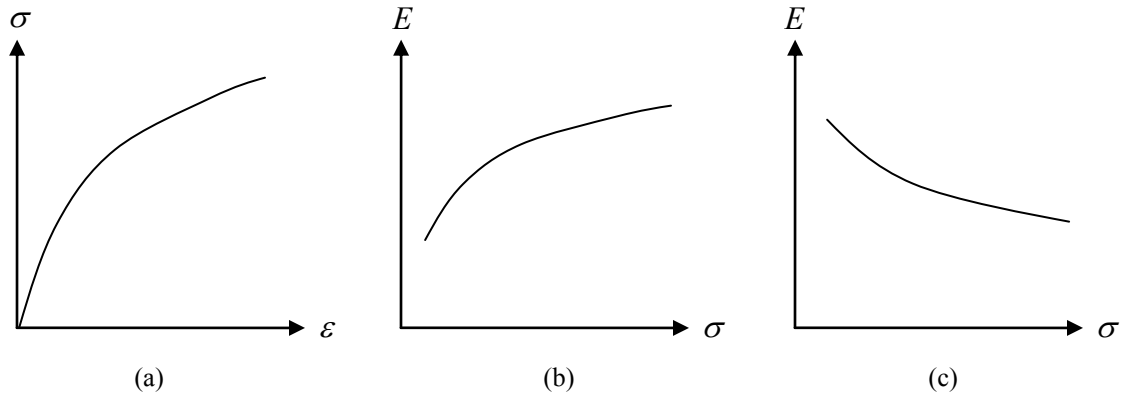

Figure 2.8 Nonlinearity of unbound layer materials

In some other materials, stiffness decreases as the stress increases (Figure 2.8(c)). This behavior is stress-softening. This behavior is typically observed in fine soils. In reality, a number of unbound materials show both of stress-hardening and softening.

In these studies, resilient modulus tests were conducted on unbound materials in triaxial chambers. During the test, resilient modulus (M_R), i.e., ratio of axial stress (σ_a) and resilient strain (ε_r), was determined at varying confining pressure (σ_c) and deviator stress (σ_d). In the field of pavement engineering, this was first addressed by Hicks and Monismith (1971). This study observed that M_R of unbound material is mainly dependent on bulk stress, i.e., $\theta = \sigma_a + 2\sigma_r$ where σ_r = radial stress (Figure 2.9). They proposed the $K-\theta$ model to correlate M_R and θ of unbound materials. This model is as follows:

$$M_R = K(\theta)^n \tag{2.22}$$

where K, n = regression coefficients. This model is good for coarse aggregate where the normal stresses at particle contact interfaces are dominant. However, in case of fine soil, this model has a shortcoming since it fails to adequately distinguish the effect of shear behavior.

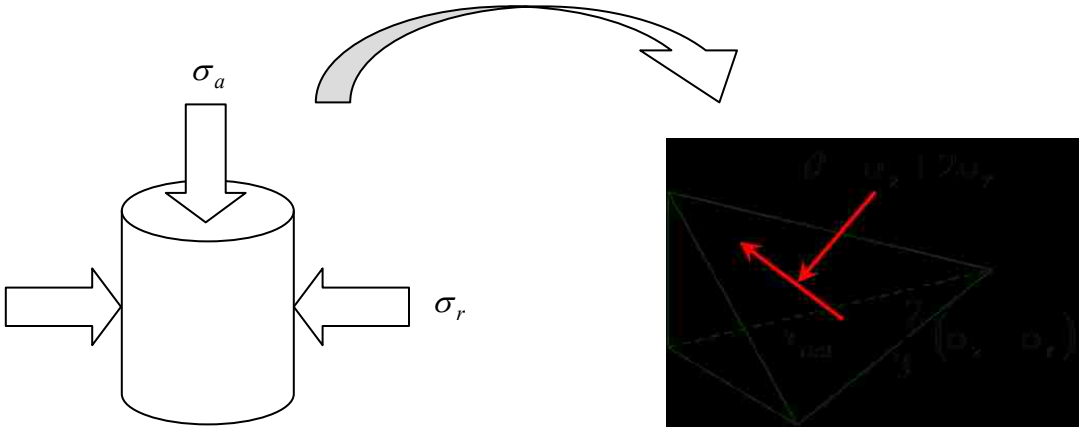

Figure 2.9: State of stresses in unbound material under resilient modulus test

Later, Uzan (1985) modified this model to address the shear behavior. The modified model is as below:

$$M_R = k_1(\theta)^{k_2}(\sigma_d)^{k_3} \tag{2.23}$$

where σ_d = deviatoric stress $(= \sigma_a - \sigma_r)$, and k_1, k_2, k_3 = regression coefficients. It is known that the normal and shear stresses, i.e., θ and τ_{oct} = octahedral shear stress, along octahedral plane are greater than any other stresses. In addition, these stresses are function of all the principal stresses. Therefore, it is more reasonable to use these specific stresses to incorporate the stress-dependency. Later, this model was also modified by replacing σ_d by τ_{oct}. The modified

model is known as universal octahedral shear stress model (Wiczack and Uzan 1988). This model is as follows:

$$M_R = k_1 p_a \left(\frac{\theta}{p_a} \right)^{k_2} \left(\frac{\tau_{oct}}{p_a} \right)^{k_3} \tag{2.24}$$

where p_a =atmospheric pressure. In eqn. (23), M_R will be surprisingly small if τ_{oct} tends to very small even though θ is not small. Therefore, this model was also modified which is known as MEPDG model for unbound layers (ARA 2004). This model is as follows:

$$M_R = k_1 p_a \left(\frac{\theta}{p_a} \right)^{k_2} \left(\frac{\tau_{oct}}{p_a} + 1 \right)^{k_3} \tag{2.25}$$

This model can be used for different types of unbound materials which may exhibit only stress-hardening or softening or both of them. During unbound layer modeling, especially in pavement, this model is implemented in some steps (Figure 2.10). At the beginning, initial stiffness or tangent modulus is assigned based on the nature of resilient modulus variation at varying stress. Strains are calculated using the tangent modulus under a load/stress through an analysis technique such as FEM. Stresses at different locations of a continuum are then determined as 'Output Stresses' at an analysis step from these strains incorporating the tangent modulus. Principal stresses ($\sigma_1, \sigma_2, \sigma_3$) are also calculated from the earlier determined state of stresses which are later used during determination of M_R. This M_R is fed back to the main module of the analysis technique as the tangent modulus and the analysis till the end of analysis duration.

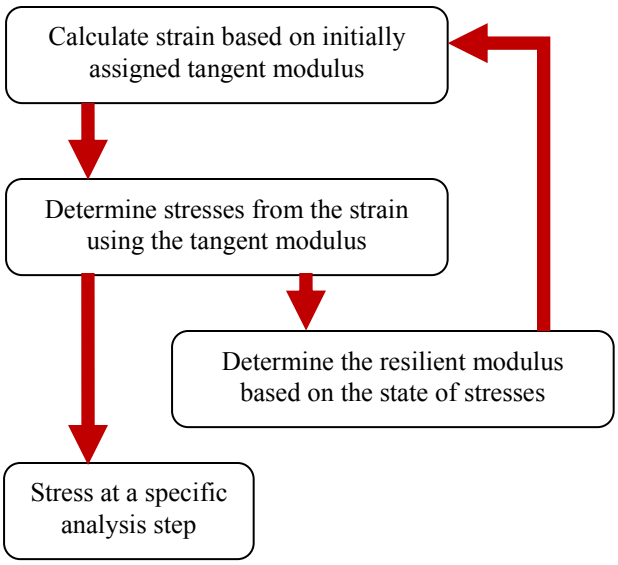

Figure 2.10 Incorporation of stress-dependency in a pavement model

CHAPTER 3

DYNAMIC FEM DEVELOPMENT

3.1 General

The dynamic Finite Element Model (FEM) of the instrumented pavement section is developed to evaluate the effect pavement layer cross-anisotropy. In this chapter, steps during development of the dynamic FEM, such as geometry and mesh generation, material models, boundary conditions, loading types and so on, are described in details.

3.2 Outline of Model Development

Development of the dynamic FEM to study the effect of cross-anisotropy on pavement response, such as stress-strain, requires a set of basic steps. These steps are outlined in Figure 3.1. The procedure begins with the development of a multi-layered 3D geometry of a selected pavement section. Different material models need to be developed based on laboratory and/or field tests which will later be incorporated to these layers. Temperature variation over pavement depth will be assigned to address temperature-dependency of AC. The dynamic, i.e., time-varying load, will be assigned on the model which will mimic field test load and wheel load imposed by moving traffic. The model geometry will be discretized with small elements which are known as mesh. Once the mesh generation is completed, boundary will be imposed on the model. Finally, the dynamic FEM will be simulated for validation and parametric to study the effect of cross-anisotropy on pavement stress-strain and thereby, performance.

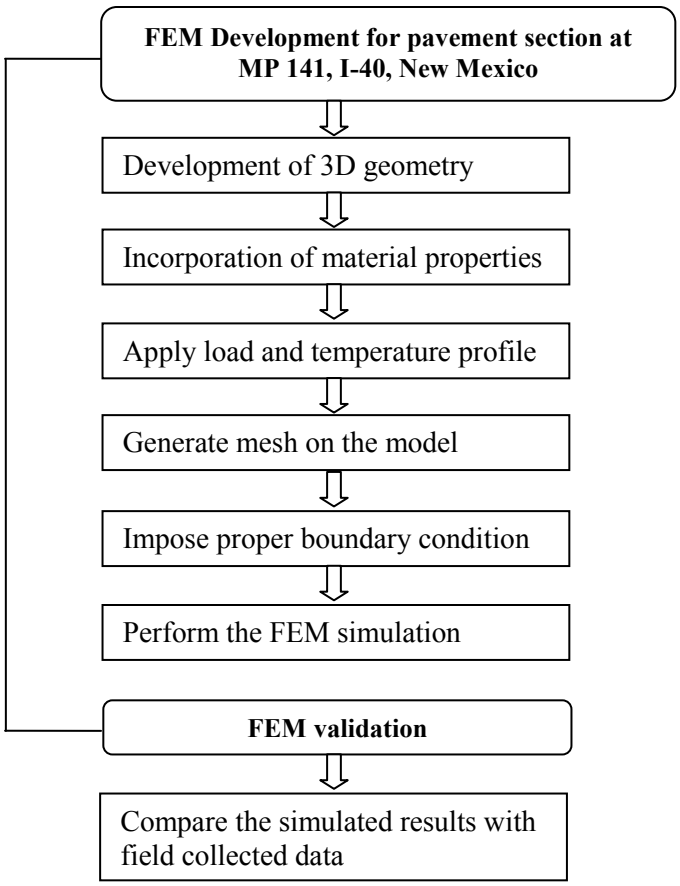

Figure 3.1 Flowchart of FEM modeling and validation

3.3 Instrumented Pavement Section

The cross-section of instrumented section (I-40, MP 141) that is used for FEM geometry is shown in Figure 3.2. The instrumented pavement consists of four major structural layers such as AC at the top, granular aggregate layer at the base, Process-Place and Compacted (PPC) aggregates in subbase, and engineered soil in subgrade. PPC layer is prepared by mixing of Reclaimed Asphalt Pavement (RAP) from surface as well as aggregate from base layer and then, compacting it in place. The elevation of strain gauges and pressure cells from the surface are shown. Total thickness of AC layer is 26.67 cm (10.5 in). This AC layer consists of three lifts each with a thickness of 8.89 cm (3.5 in). Thickness of the base is 15.24 cm (6 in) and the PPC layer is 20.32 cm (8 in).

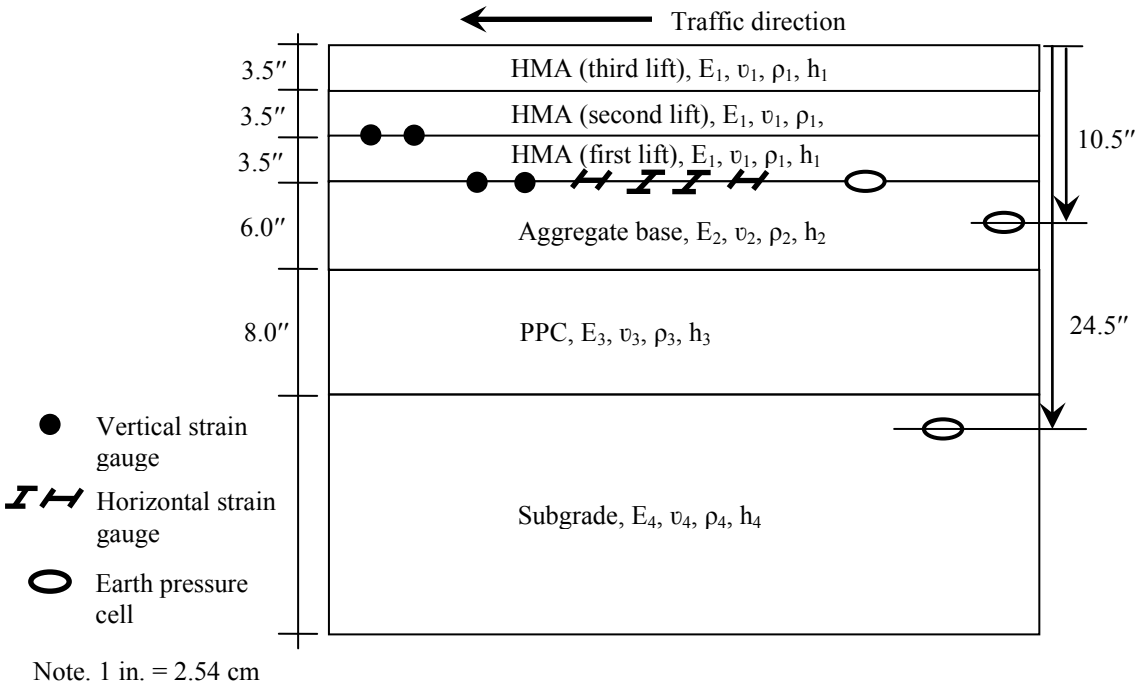

Note. 1 in. = 2.54 cm

Figure 3.2 Instrumented Pavement Section (I-40, MP 141)

Plan view of the instrumentation section is shown in Figure 3.3. A total of fourteen horizontal asphalt strain gauges have been installed at the bottom of AC layer (Tarefder and Islam 2015). Seven strain gauges have been placed along longitudinal direction and seven other placed in the transverse direction of traffic. Four earth pressure cells have been installed at different depths to measure the vertical stress.

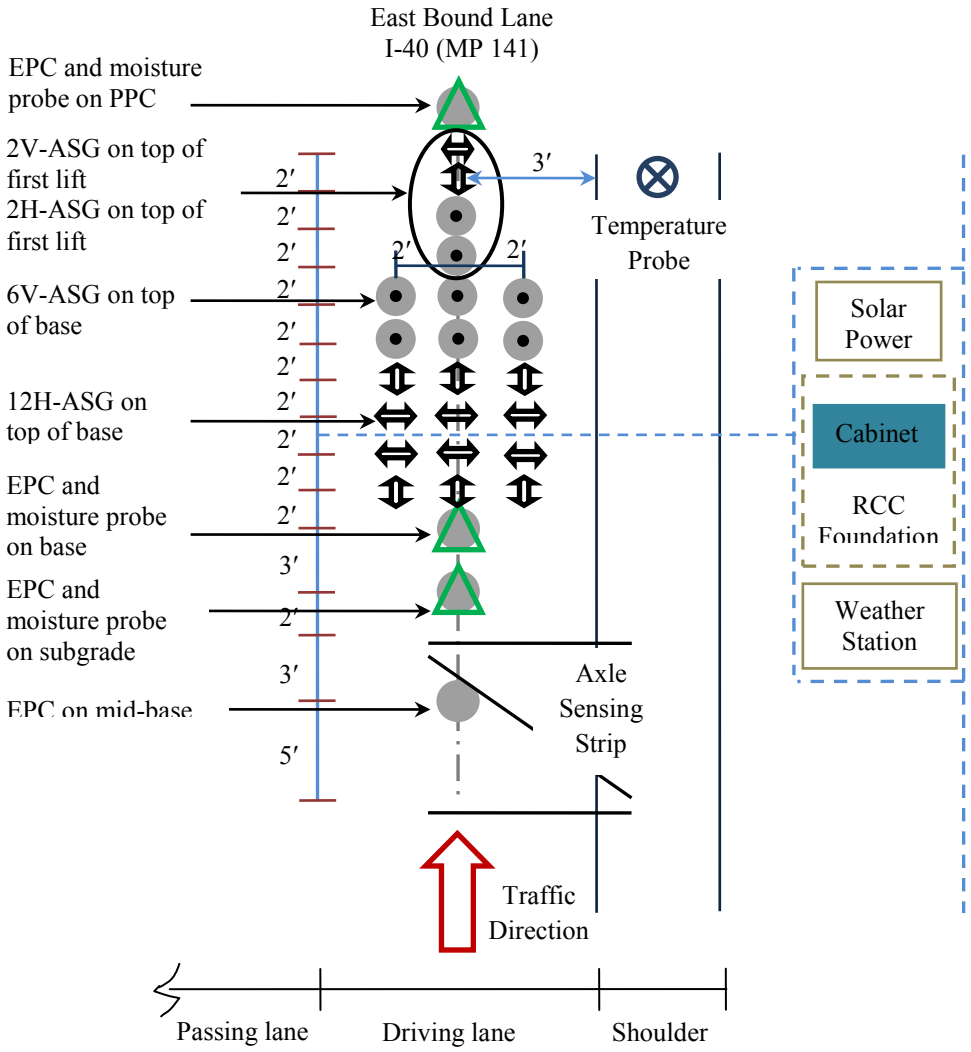

Note. 1 ft. = 30.48 cm

Figure 3.3 Plan View of Instrumented Pavement Section (I-40)

3.4 Model Geometry

A pavement section can be idealized by 2D or 3D geometry in FEM (Abu-Farsakh et al. 2007, and Al-Qadi et al. 2010). FEM with 2D geometry is not compatible with different types of loading area. For an example, 2D axi-symmetric model is convenient to be loaded by circular plate, whereas 2D plane strain model is convenient for rectangular load. On the other hand, FEM with 3D geometry is convenient for any arbitrary shape of loading area.

The quarter cube geometry was selected to develop the model due to its two axis of symmetry (Figure 3.4). The depth and horizontal length of a model were selected to diminish the effect of stress near the boundary according to Duncan et al. (1968). In this study, the depth of the model was taken 50 times the loading radius and horizontal length was taken more than 12 times the loading radius. Wave reflection by the boundary is one of the major concerns in a dynamic analysis, which may occur due to the insufficient distance to the boundary (Petyt 1990). Therefore, the final dimensions, i.e., length, width, and depth, of this entire model were selected to be 300 in. x 300 in. x 300 in. (7.62 m x 7.62 m x 7.62 m). The numbers of layers as well as thicknesses of every layer were assigned according to the instrumented section described earlier.

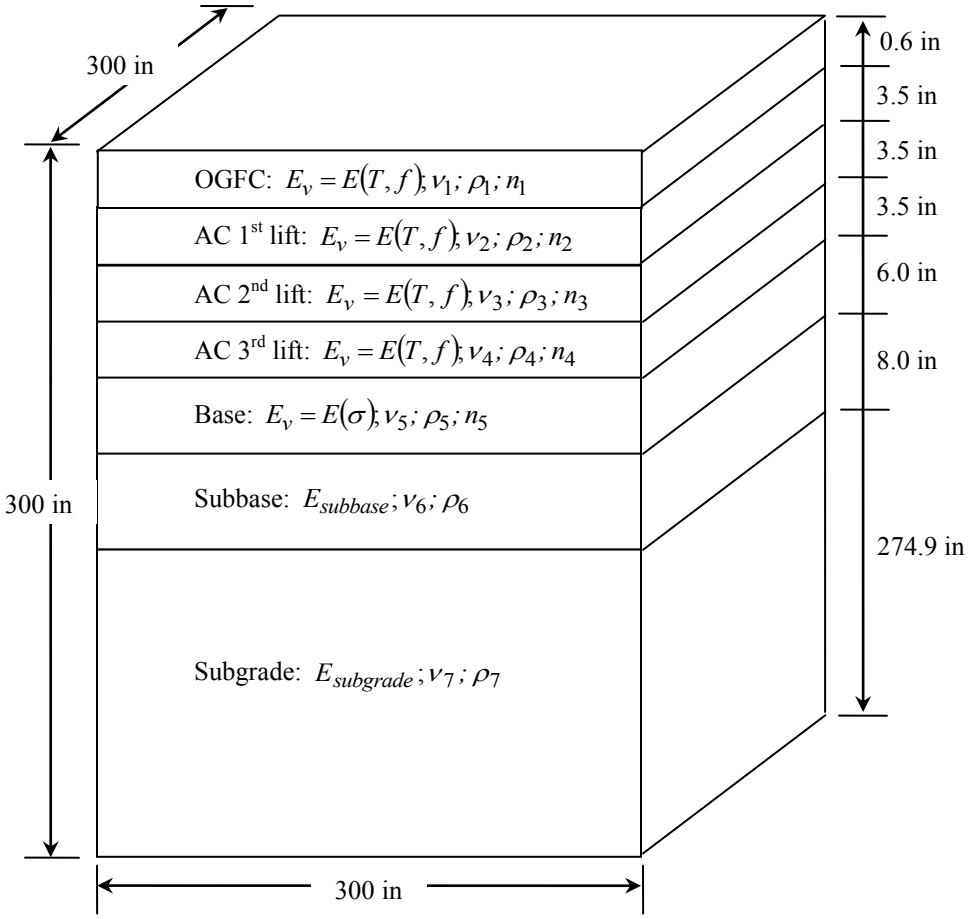

Figure 3.4 Multilayered structure of pavement section at MP 141, I-40

3.5 Boundary Condition

Boundary conditions are assigned differently in different phases of this study. At the preliminary stage of model development, the bottom boundary is restrained to move along the three mutually orthogonal directions (see Figure 3.5). Therefore, there will be no deflection in horizontal and vertical directions in this plane. Movements of the vertical boundaries are restrained only in the horizontal directions.

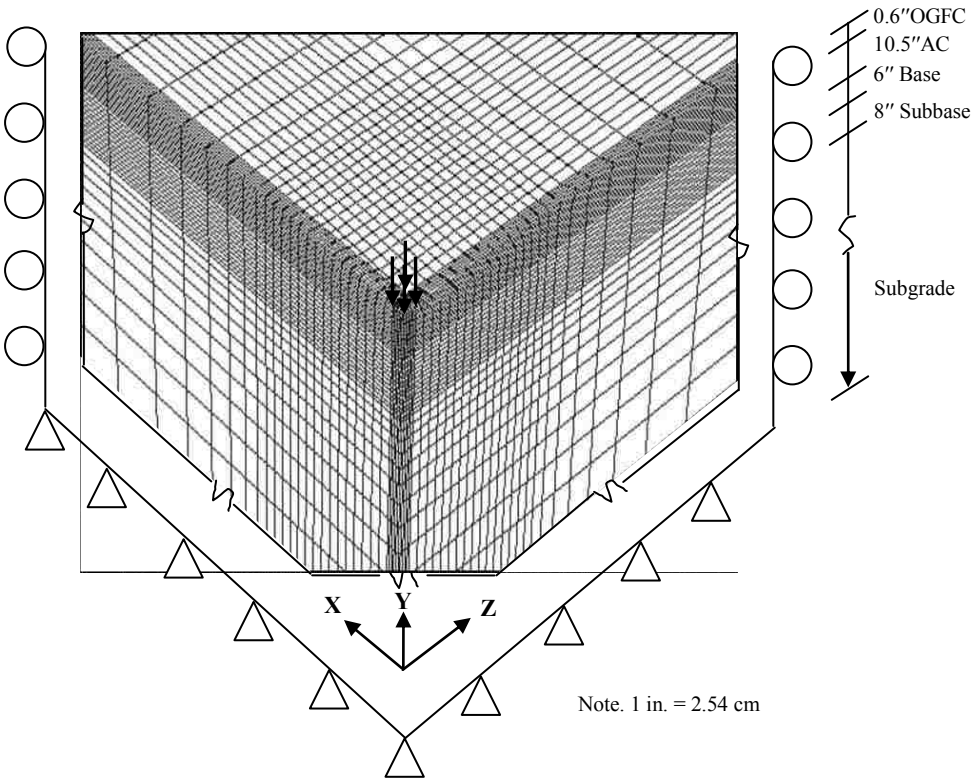

Figure 3.5 Preliminary boundary condition of the model (BC: 1)

Later, the boundary condition is improved by incorporation of the so-called spring-dashpots along the boundaries in the two mutually orthogonal directions considering the future application of this model under repeated load as shown in Figure 3.6 (Lysmer and Kuhlemeyer 1969, Novak et al. 1978, and Gazetas 1991). It is expected that stresses due to the repeated load will not be reflected back from the boundary due to the use of spring-dashpots.

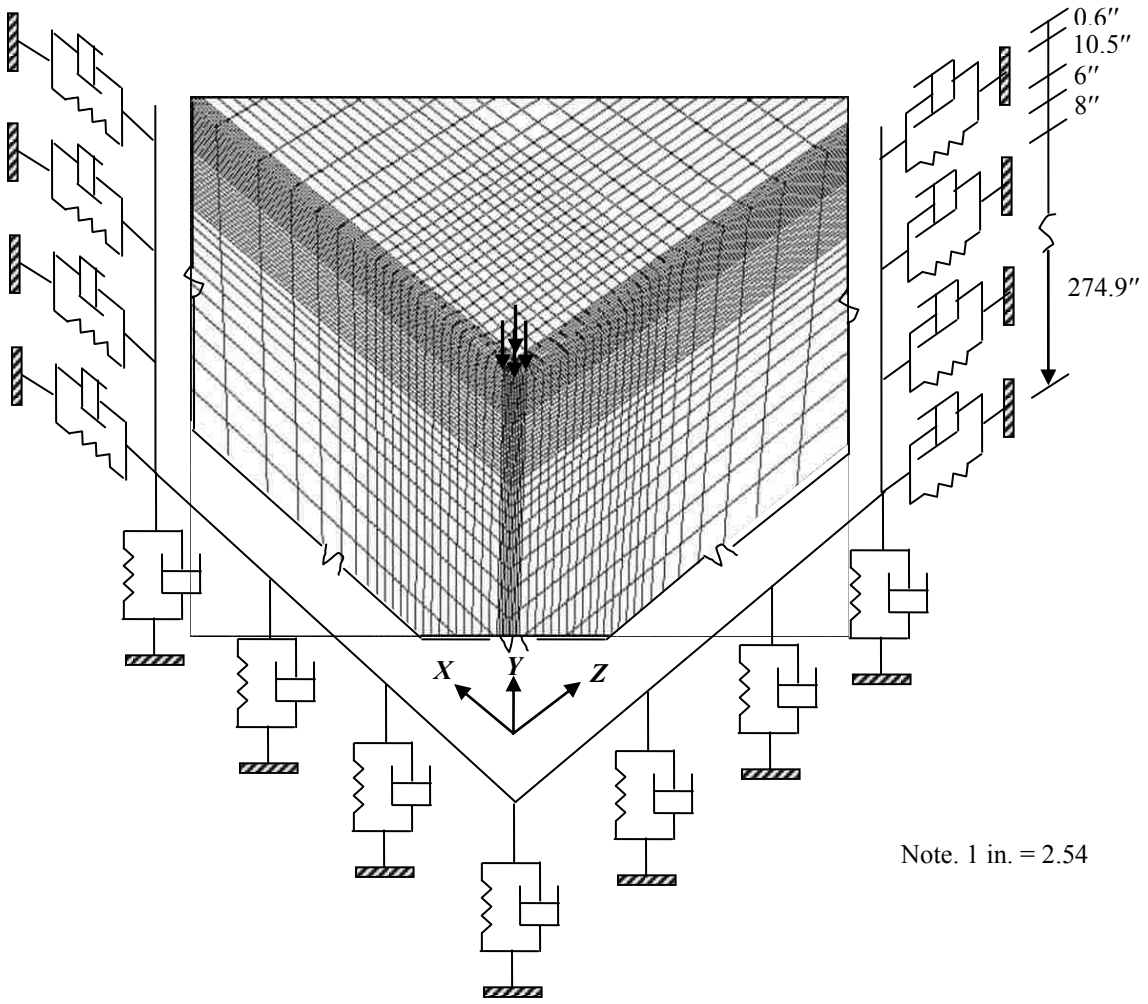

Figure 3.6 Modified boundary condition of the model (BC: 2)

It is known that the pavement layer interfaces are typically partially-bonded which affects the pavement responses (Shahin et al. 1986, and Mehta 2007). In this study, conditions of layer interfaces were evaluated to assign proper contact properties in the FEM. Based on the visual inspection from coring, most of the layer interfaces were in good condition except the interface between the first and second lifts of the AC layer. Therefore, only this interface was considered as partially-bonded whereas the rest of the layer interfaces were considered as fully-bonded. The coulomb friction law was used to model the contact along the layer interfaces (Molinari et al.

2012). According to this law, $\tau = \mu\sigma_N$, where $\tau =$ shear stress, $\sigma_N =$ normal stress, and $\mu =$ friction coefficient. Friction coefficients required to define this contact model at different layer interfaces were collected from the literature (Romanoschi and Metcalf 2001). The friction coefficient along partially-bonded interfaces in AC is 0.7 and that along the other interfaces is 1.0 (fully-bonded). The Penalty method, available in ABAQUS 6.10-EF2, is adapted to implement this contact behavior (King and Richards 2013).

3.6 Mesh Generation

An 8-noded brick element (C3D8) was used for the mesh generation. The size of the element during the mesh generation is selected after a number of trial analyses during a mesh-sensitivity analysis (Figure 3.7). The mesh-sensitivity analysis is performed by simulating the dynamic FEM for varying sizes of elements. The element size near the loading area is varied due to the influence of these elements on the stress gradient. In essence, a number of simulations were performed by reducing the depth of elements in AC layer from 89 mm (3.5 in.) to 13 mm (0.5 in.). In each of the simulations, vertical surface deflection is determined at the node that coincides with the center of the load. The effect of the element size variation on the vertical surface deflection shows that the deflection diminishes with gradual reduction of the depth of this element. The trend of vertical deflection with element depth variation begins to be constant from the simulation with the element depth of 18 mm (0.7 in.). Based on the consideration of accuracy, analysis time and memory storage for the dynamic simulations, the optimum depth of the smallest element is found to be 18 mm (0.7 in.). The largest dimension of this model is 1049.25 mm (41.97 in) at the bottom.

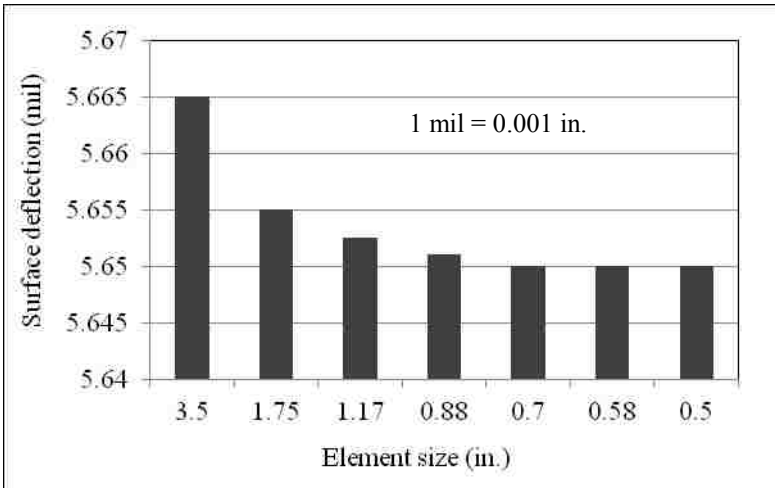

Figure 3.7 Mesh sensitivity analysis

3.7 Material Properties

There is a need to input the material properties of different layers in to the dynamic FEM. These properties are determined by both laboratory and field tests. These tests are selected based on material types. Generally, OGFC and AC are assigned as viscoelastic whereas unbound materials, such as base, subbase and subgrade, are assigned as nonlinear elastic stress-dependent materials. In a simple case, unbound layers are sometimes assumed as linear elastic. Specific properties of the layer materials in the FEM are summarized below:

- OGFC: Viscoelastic and temperature dependent
- AC: Viscoelastic, temperature dependent, and cross-anisotropic
- Base: Nonlinear elastic and stress-dependent
- Subbase: Nonlinear elastic and stress-dependent
- Subgrade: Linear elastic

In this study, cross-anisotropy is also incorporated to the unbound layers as a limited scope. The subgrade is assumed is considered linear elastic due to very small stress variation caused by

traffic. Several different types of laboratory and field tests are required to determine the material properties. These tests are mentioned in the flow diagram (see Figure 3.8). In case of the OGFC, the dynamic modulus test is conducted to determine the frequency-dependent modulus which is later converted to relaxation modulus variation over time as viscoelastic behavior into the FEM. This test is also conducted for the AC for the same purpose. However, dynamic modulus test for the AC is conducted on both vertical and horizontal cores to determine the modulus along those orthogonal directions. Indirect tensile tests are conducted to determine Poisson's ratio in a horizontal plane.

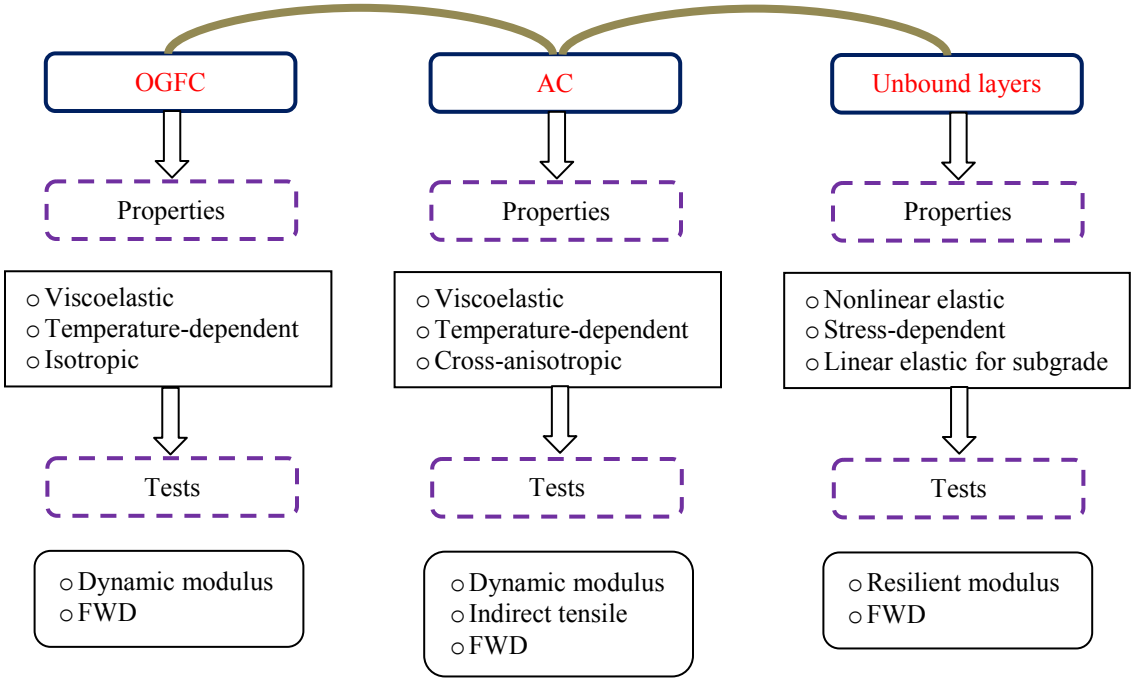

Figure 3.8 Flow diagram of tests for material characterization

Resilient modulus tests are conducted on granular aggregates and PPC from base and subbase respectively to determine the nonlinear elasticity and stress-dependency. FWD test is conducted

to determine the temperature-dependency of AC modulus and predict the unbound layer moduli. Details of these tests for different layer materials are discussed in the following sections:

3.7.1 OGFC

The OGFC layer is mainly used in a pavement as a wearing surface which provides sufficient skid resistance to vehicle tires and expedites drainage of water due to rainfall (Huber 2000, and Putman 2012). A uniform gradation of aggregates mixed with asphalt binder is typically used to construct this thin layer. It is considered as a non-structural layer; however, it possesses stiffness even though it may be smaller than the AC layer underneath (Putman 2012). In addition, it withstands the tire pressure and helps to reduce this pressure on the AC layer at a small extent. Based on these facts, the OGFC is assumed as linear viscoelastic, temperature dependent, and isotropic as mentioned in the earlier section (Stempihar and Kaloush 2010, and Wang et al. 2013).

Viscoelasticity of the OGFC is modeled using the GMM for the dynamic FEM. The relaxation modulus variation required to determine the GMM parameters is converted from the dynamic modulus test of the OGFC. Prior to the dynamic modulus test, material is collected from the field mix during the construction. A test specimen with 4 inch diameter and 6 inch height is prepared using the Superpave Gyratory compactor to conduct the test according to AASHTO TP 62-07 (2007). Figure 3.9 shows the test setup where the test specimen is subjected a repeated uniaxial load. Three LVDTs are attached vertically to the specimen measure the deformation under the repeated load. According to the guideline, the tests are conducted at different frequencies and

temperatures. These frequencies are: 0.1, 0.5, 1, 5, 10 and 25 Hz and temperatures are: -10, 4, 21, 37, and 54 °C.

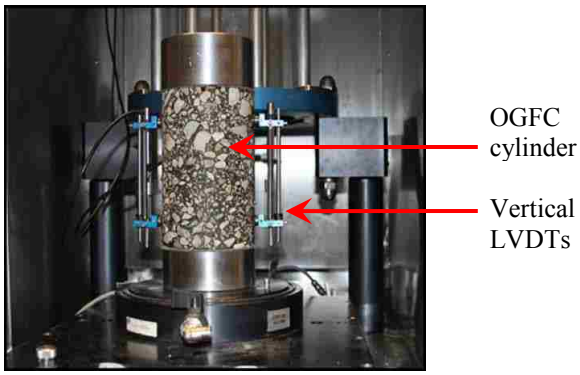

Figure 3.9 Dynamic modulus test

The dynamic modulus values at different frequencies and temperatures are plotted in Figure 3.10(a). These values are high at higher frequency and lower temperature regime which was expected as a typical observation. A dynamic modulus master curve is generated by converting the modulus values to the frequencies at a reference temperature of 21 °C using the William-Lande-Ferry (WLF) method as proposed by Williams et al. 1955 (see Figure 3.10). This master curve is later converted to the relaxation modulus variation over time (Park and Schapery 1999, and Underwood and Kim 2009).

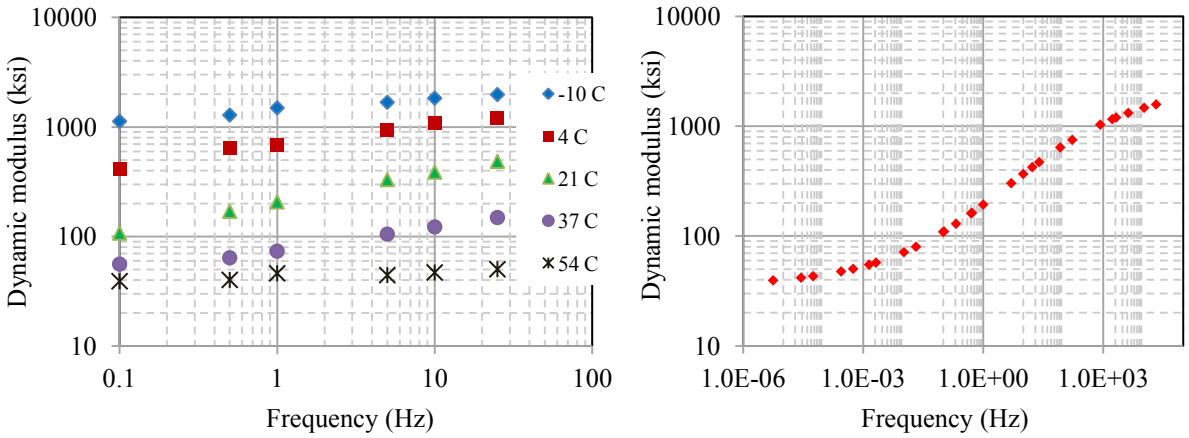

(a) Dynamic modulus (b) Master curve

Figure 3.10 Dynamic modulus values of OGFC

The converted relaxation modulus variation of the OGFC is shown in Figure 3.11. The instantaneous and long term modulus values are 1500 and 33 ksi respectively. Parameters of the GMM are determined based on this relaxation modulus variation which is summarized in the table on the right side of Figure 3.11. These parameters are later given as input to the dynamic FEM as OGFC material property. Determination of temperature dependency of this layer in field will be documented later.

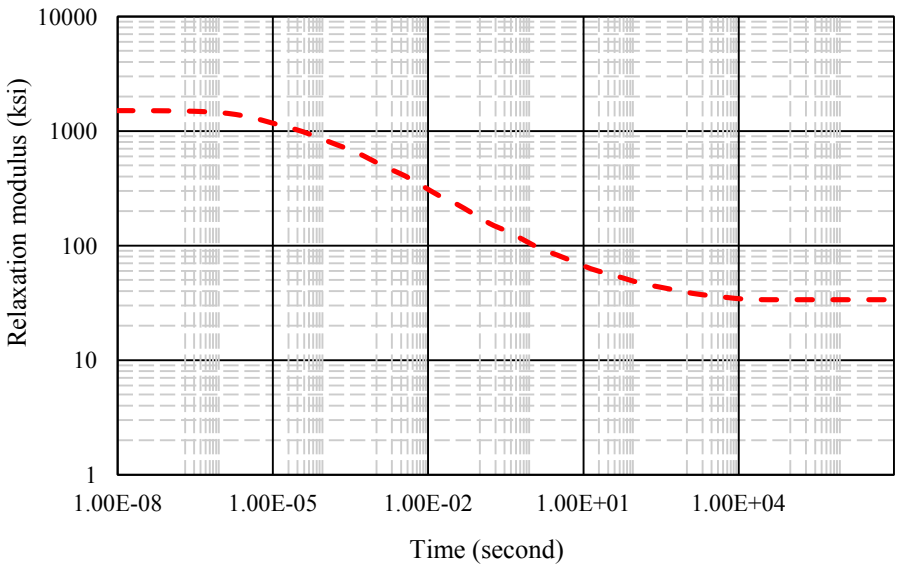

i	e_i	τ_i
1	0.2	1.1
2	0.2	4.7
3	0.15	9.75
4	0.15	100
5	0.1	250
6	0.1	470

Figure 3.11 Relaxation modulus of OGFC

3.7.2 Asphalt Concrete

The dynamic modulus test is also conducted on the AC to determine the GMM parameters to assign viscoelasticity similar to the OGFC. In addition, there is a need to determine the five independent parameters (E_v, E_h, G_{vh}, ν_{vh}, and ν_{hh}) of the AC which is considered as cross-anisotropic. The dynamic modulus tests are conducted on vertical AC core to determine the vertical modulus, E_v, and Poisson's ratio on vertical plane, ν_{vh}, respectively (see Figure 3.12). The Indirect Tensile Test is conducted to determine the horizontal modulus, E_h, and Poisson's ratio on horizontal plane, ν_{hh} (see Figure 3.12). Later, the dynamic modulus test is also conducted on the horizontal AC core to determine the E_h and ν_{hh} which will be discussed later under this section. Value of the G_{vh}, i.e., shear modulus on a vertical plane, is collected from literatures.

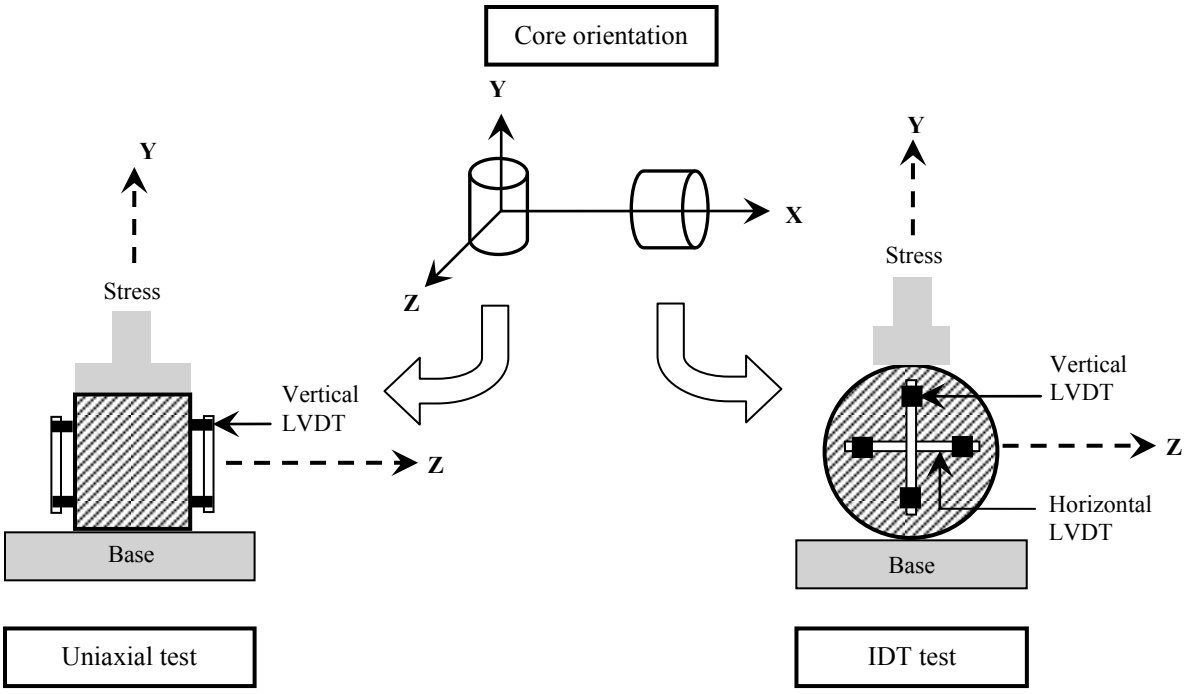

Figure 3.12 Schematic of laboratory test to determine the degree of cross-anisotropy

Goal of this study is to investigate the effect of the AC cross-anisotropy which is resulted from field-compaction. For this reason, the laboratory tests to characterize the AC properties need to be conducted on field-compacted AC cores. Cores are collected from the same instrumented pavement section using a portable 6 inch diameter core drill bit (see Figure 3.13). The AC layer has three lifts each with a similar thickness of 3.5 inch. During the coring, it is observed that the top layer interface is partially bonded and the bottom layer interface is fully bonded. This partial de-bonding may be due to intrusion of water into this interface from the top. Several cores are collected from the same pavement section for the earlier mentioned laboratory tests.

Figure 3.13 Extraction of field-compacted AC core

Both vertical and horizontal AC cores are required for laboratory tests to determine the viscoelastic and cross-anisotropic parameters. The proposed dynamic modulus and indirect tensile tests require specific dimension for test specimen. The criteria for the dimension are as below (Uzan and Motola 2007):

- Gauge length should be equal or greater than 3 times the nominal aggregate size
- Difference between the end of a LVDT and edge of a test specimen should be fairly 1 inch to avoid possible presence of stress-concentration
- Any interface, such as partially-bonded interface, should be outside the gauge length

It is already mentioned that the field-compacted AC lift has the maximum thickness of 3.5 inch. It indicates that the vertical test specimen may not satisfy the above mentioned criteria if this core is directly used for the test. This may result if the AC core is split at the interface which leads to a height and diameter ratio of less than 1.5. Based on the possibility of this issue, two

different types of dynamic modulus test specimen are prepared (see Figure 3.14). The fist one is a core with 3.5 and 3 inch height and diameter respectively from the mid-lift and two more cores with 1 and 3 inch height and diameter respectively. These cores are arranged, as shown in Figure 3.14, and glued with asphalt binder at the interfaces. The entire task is conducted according to the guideline of Kaloush (2000). The second one is a core with 4.5 and 3 inch height and diameter respectively where one of the layer interfaces is partially-bonded. The dynamic modulus tests are conducted on both of these test specimens.

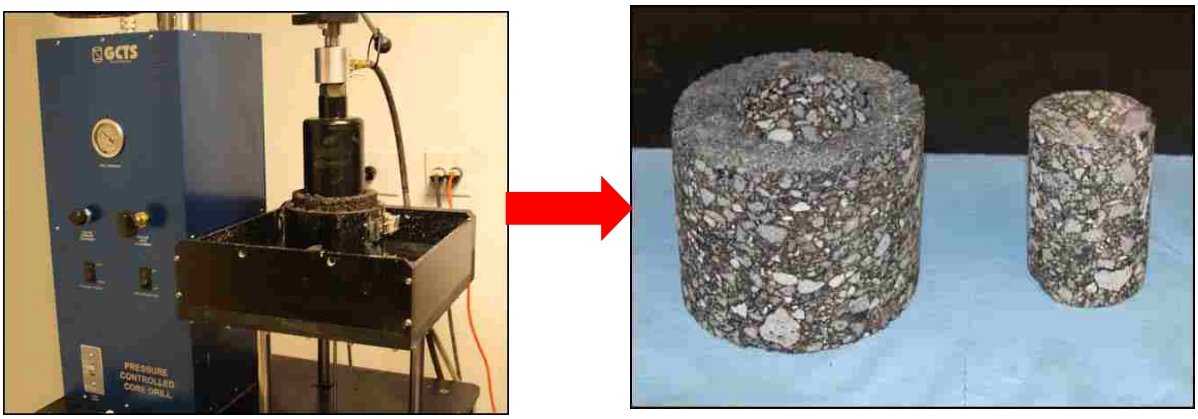

Figure 3.14 Preparation of vertical test specimen for laboratory tests

Figure 3.15 shows the sample preparation for horizontal AC core. The field-compacted core is first cut on two sides by a saw so that it can be placed inside a casing of the core drill. Once the two edges are cut, the core is placed inside the casing for drilling. A 3 inch diameter core drill is used to extract the core. The 3 inch diameter extracted core is gain cut at the two ends to make 4.5 inch height test specimen with smooth surfaces.

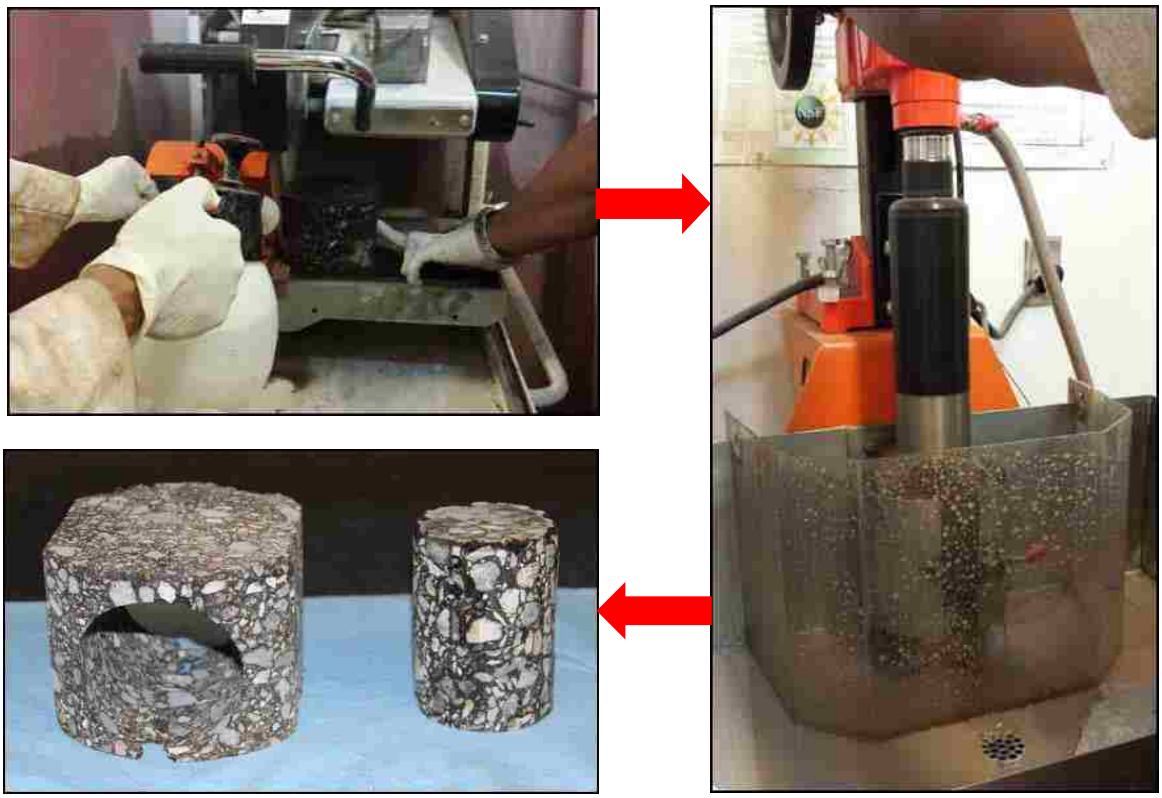

Figure 3.15 Preparation of horizontal test specimen for laboratory tests

Test specimen with 6 inch diameter and 2 inch thickness is also prepared for the indirect tensile test. During the sample preparation, the field-compacted AC core is simply cut at the two ends to make a test specimen with required dimension.

The dynamic modulus tests are conducted on both vertical and horizontal AC cores (see Figure 3.16). The entire test procedure, i.e., guideline, temperatures, and frequencies, is similar to the OGFC, except, the test specimen dimension. Dynamic modulus of the vertical AC core at pre-selected frequencies and temperatures are shown in Figure 3.16(a). Based on these values, a dynamic modulus master curve is generated using the Time-Temperature Superposition (TTSP).

The master curve is shown in Figure 3.16(b). Relaxation modulus values are determined from the dynamic modulus master curve which is shown in Figure 3.16(c).

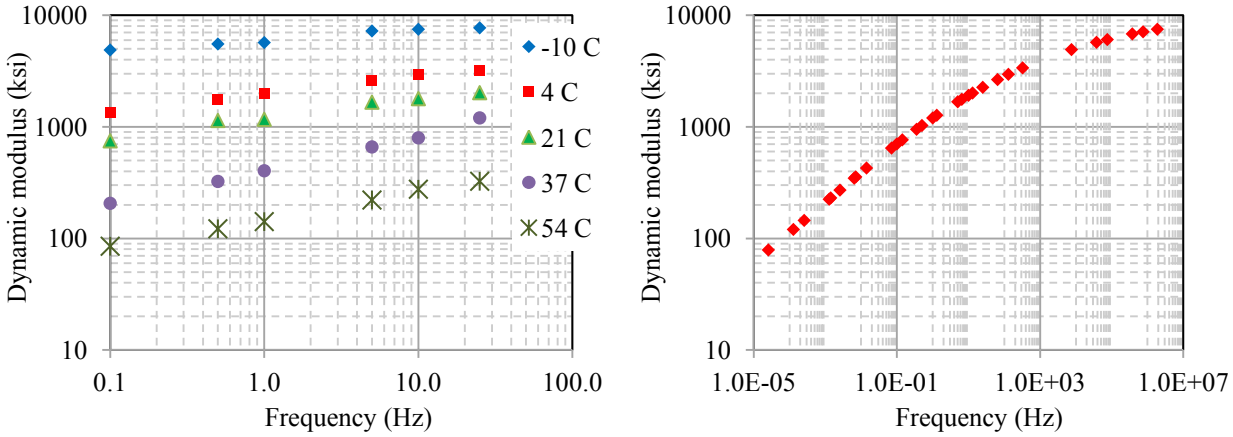

(a) Dynamic modulus

(b) Master curve

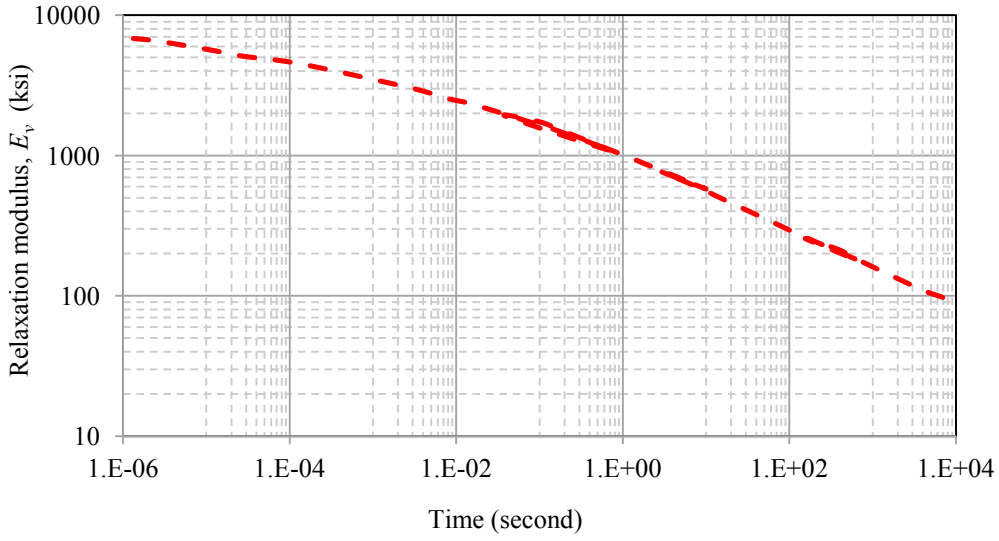

(c) Relaxation modulus

Figure 3.16 Dynamic and relaxation modulus of vertical AC core

Dynamic modulus of the horizontal AC core at pre-selected frequencies and temperatures are shown in Figure 3.17(a). Based on these values, a dynamic modulus master curve is generated

using the TTSP. The master curve is shown in Figure 3.17(b). Relaxation modulus values are determined from the dynamic modulus master curve which is shown in Figure 3.17(c).

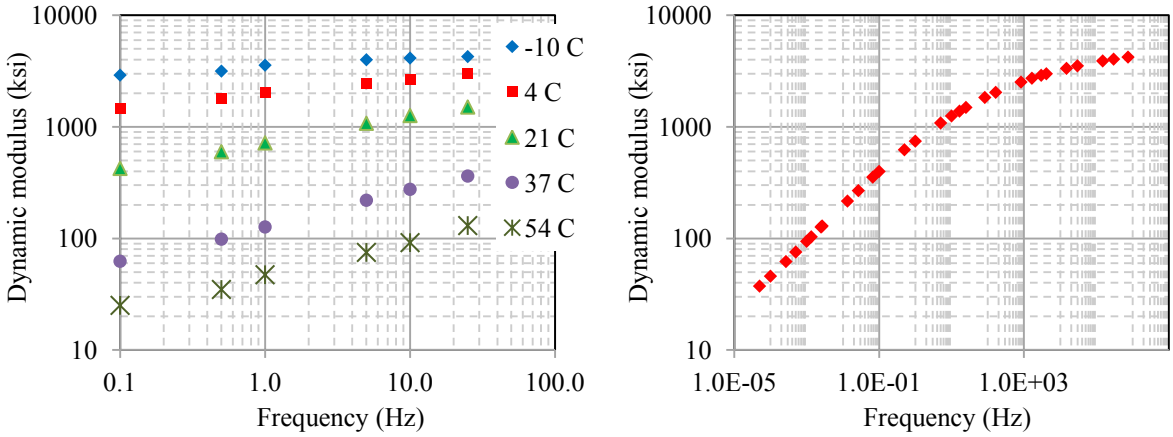

(a) Dynamic modulus

(b) Master curve

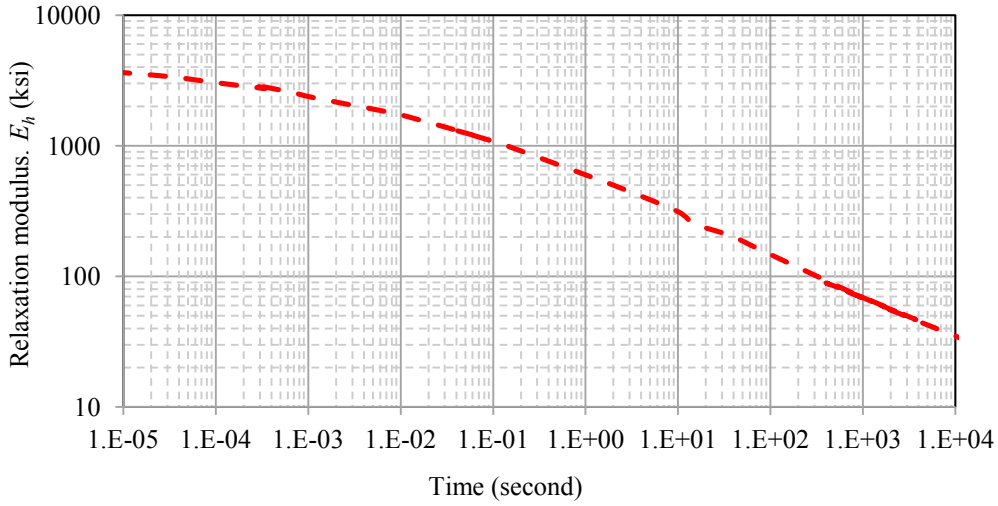

(c) Relaxation modulus

Figure 3.17 Dynamic and relaxation modulus of horizontal AC core

The relaxation modulus values are used to determine the Prony series coefficients using the following equations:

Vertical AC core: $$E_v(t) = E_{v,0}\left[1 - \sum e_{v,i}\left\{1 - \exp\left(-t/\tau_{v,i}\right)\right\}\right] \quad (3.1)$$

Horizontal AC core: $$E_h(t) = E_{h,0}\left[1 - \sum e_{h,i}\left\{1 - \exp\left(-t/\tau_{h,i}\right)\right\}\right] \quad (3.2)$$

where $E_{v,0}, E_{h,0}$ = instantaneous modulus of vertical and horizontal AC cores, $e_{v,i}, e_{h,i}$ = coefficients of vertical and horizontal AC cores, and $\tau_{v,i}, \tau_{h,i}$ = relaxation time of vertical and horizontal AC cores. The instantaneous modulus values of the vertical and horizontal AC are 7037 and 3795 ksi respectively. Therefore, the resulting degree of cross-anisotropy ($n = E_{h,0}/E_{v,0}$): 0.54. Coefficients of Prony series as viscoelasticity parameters of the two mutually orthogonal cores are summarized in Table 3.1. The instantaneous moduli as well as the Prony series coefficients for both of the cores are assigned as input to the dynamic FEM so that the cross-anisotropic viscoelasticity of the AC can be implemented.

Table 3.1 Prony Series Coefficient (vertical & horizontal AC cores)

i	$e_{v,i}$	$\tau_{v,i}$	$e_{h,i}$	$\tau_{h,i}$
1	0.277	1.04E-05	0.292	0.001
2	0.2	0.018	0.2	0.056
3	0.15	0.0011	0.15	15.64
4	0.13	0.00019	0.19	0.0001
5	0.13	0.68	0.1	0.61
6	0.09	22.99	0.054	0.02

The Poisson's ratio on a vertical plane, ν_{vh}, is determined from the ratio of horizontal and vertical strain. The horizontal strain is measured using two LVDTs placed along the diameter of the test specimen subjected to a uniaxial load. During the measurement of horizontal strain, a

vertical LVDT is also connected to the specimen along the loading axis to simultaneously measure the vertical strain. Finally, the vertical Poisson's ratio (ν_{vh}) is 0.35 which is in typical range. The Poisson's ratio on a horizontal plane, ν_{hh}, is determined from the ratio strains along two orthogonal directions. These strains are measured by an Indirect Tensile Test as shown in Figure 3.18(a). The vertical strain is measured by the LVDT along loading axis whereas the horizontal strain is measured by the LVDT along transverse to the loading axis. Finally, the Poisson's ratio (ν_{hh}) is 0.3. One more test is conducted to determine Poisson's ratio for cross-validation. In this test, a cube shaped AC test specimen is prepared from the field-compacted core (Figure 3.18(b)). The specimen is subjected to uniaxial load along the horizontal axis and two LVDTs along, which are attached both vertical and horizontal directions, measure the strains. Based on the measured strains, Poisson's ratio is 0.32 which is close the earlier one. In the FEM, Poisson's ratio 0.3 from the first test method since this method is commonly accepted in the field of pavement engineering (Lee and Kim 2009).

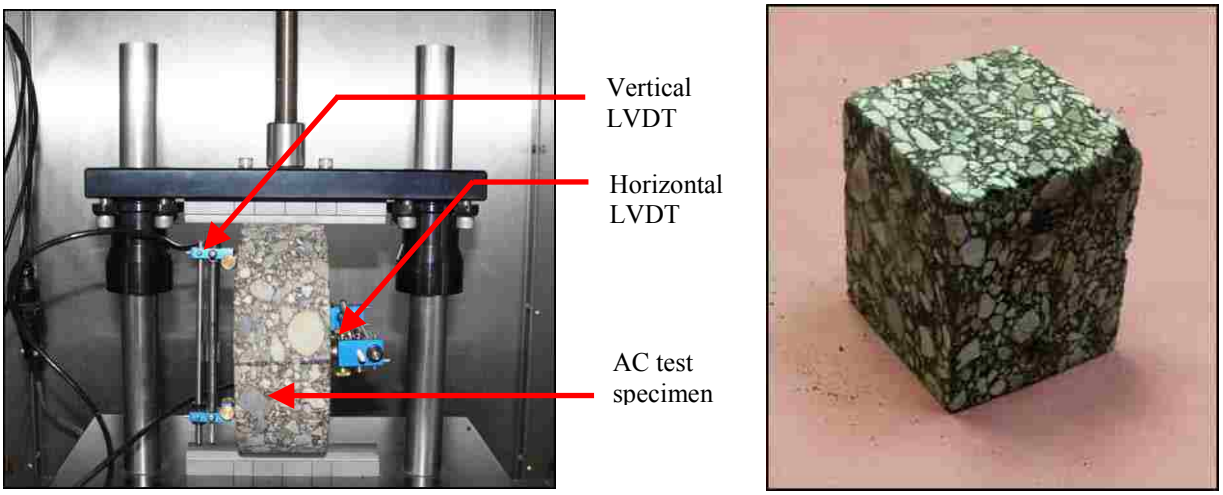

(a) Indirect tensile test

(b) Cube test specimen

Figure 3.18 Laboratory tests for Poisson's ratio

In the dynamic FEM, shear modulus of AC needs to assign in both horizontal and vertical planes. The shear modulus on horizontal plane can be assigned as follows:

$$G_{hh}(t) = \frac{E_h(t)}{2(1+\nu_{hh})} \tag{3.3}$$

The shear modulus of the field-compacted AC on vertical plane cannot be determined since the required laboratory test equipment is not available. In this case, a parametric study is performed by a number of FEM simulations at varying shear modulus to investigate the effect of this variation on pavement responses. It is found that shear modulus variation has little effect which can be reasonably ignored. This parametric study will be discussed in detail in Chapter 6. Finally, this value (G_{vh}) is assigned according to the literature as follows:

$$G_{vh}(t) = m \times E_v(t) \tag{3.4}$$

where the *m*-value is assigned equal to 0.38 (Kim 2004).

It is mentioned earlier that the AC is temperature dependent material. In addition, pavement temperature varies over a depth as well as in different seasons over a year. Therefore, this temperature-dependency of the AC modulus needs to be incorporated to the dynamic FEM. A model was proposed by Appea (2003) to correlate pavement temperature and modulus which is as below:

$$\frac{E_{25}}{E_T} = e^{-0.031(25-T)} \tag{3.5}$$

where E_{25} = modulus of the AC at 25 °C, E_T = modulus of the AC at T °C, and T = temperature of the AC (°C). This model was developed for specific AC mix in Virginia smart road. This model may not be applicable to the instrumented pavement section in New Mexico. It indicates that a similar type of model can be developed if the AC modulus at different temperatures is available.

A test program was then initiated to conduct routine FWD test on the instrumented section on I-40. In this program, FWD tests were conducted at 20 different locations on the pavement at different temperatures over a day. Temperatures in pavement were measured by temperature probes which were installed at different depths. Generally, tests were conducted in morning, noon, and afternoon to incorporate significant temperature variations. This strategy was repeated every month over a year. The AC modulus is then backcalculated from the FWD test data at those temperatures to populate a database. A regression analysis is then performed to develop the following relationship:

$$\frac{E_{21}}{E_T} = e^{-0.0342(25-T)} \tag{3.6}$$

It is also known that pavement temperature varies over the depth which indicates that the AC modulus should also vary over the depth. In this study, this temperature dependency of AC modulus is incorporated based on an assumption of linear depth-temperature variation. Therefore, the equation for the temperature variations is as follows:

$$T_z = T_{surface} - \frac{\left(T_{surafce} - T_{bottom}\right) \times z}{D} \tag{3.7}$$

where T_z = temperature of the AC at depth, z (°C), $T_{surface}$ = surface temperature (°C), T_{bottom} = temperature at bottom of the AC layer (°C), and D = thickness of the AC layer (in.). In this relationship, 21 °C is the reference temperature since the relaxation modulus variation is determined that temperature. The surface and bottom temperatures are measured by the temperature probe installed at specific depths of the AC layer. Figure 3.19 shows the qualitative trend of AC modulus over the depth due to incorporation of this temperature dependency. In most of the time, surface and bottom temperatures are not the same. Therefore, AC modulus at the surface and bottom will also be different.

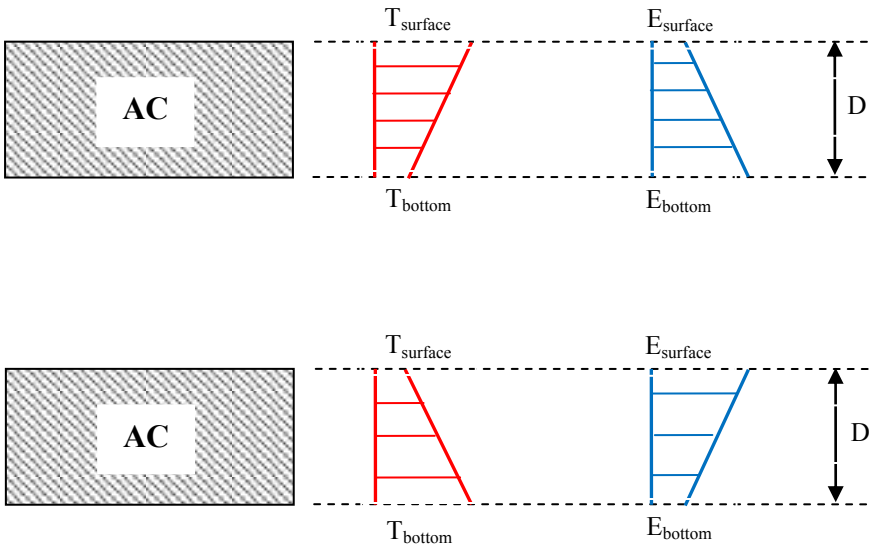

Figure 3.19 Depth-temperature variation in AC layer

The temperature dependency of AC moduli for both vertical and horizontal directions is incorporated as follows:

$$\frac{E_{v,0(T=21°C)}}{E_{v,0}(z)} = e^{-0.0342(25-T)} \tag{3.8}$$

$$\frac{E_{h,0(T=21°C)}}{E_{h,0}(z)} = e^{-0.0342(25-T)} \tag{3.9}$$

A subroutine is developed in FORTRAN to implement the temperature dependent and cross-anisotropic viscoelastic model of the AC layer. Later, this subroutine is integrated to the dynamic FEM in ABAQUS using the User Defined Material (UMAT) interface.

Prior to the integration of a subroutine to any FEM, it is common practice to investigate whether it can re-produce the similar material behavior as expected by applying a load or displacement (stress or strain) on simple element. The subroutine developed for temperature-dependent and cross-anisotropic viscoelasticity also needs to be evaluated. As mentioned earlier, a viscoelastic material has two major behaviors: creep and relaxation. In this step, a constant vertical stress of 1 psi is applied on a single element of unit dimension to investigate creep behavior (Figure 3.20). The top 4-nodes are free whereas the bottom 4-nodes are restrained to move along three orthogonal directions. The subroutine is integrated to this element and the simulations are performed at two different temperatures such as 9.9 and 35.1 ºC respectively. These temperatures are assigned constant over the depth of the element. Figure 3.20 shows that there is an instantaneous vertical strain at the initial time and later, it gradually increases. Initially, the strain increase rate is high and it diminishes slowly. It indicates that the subroutine is able to mimic the creep behavior. It is also observed that vertical strain at smaller at low temperature which follows typical trend.

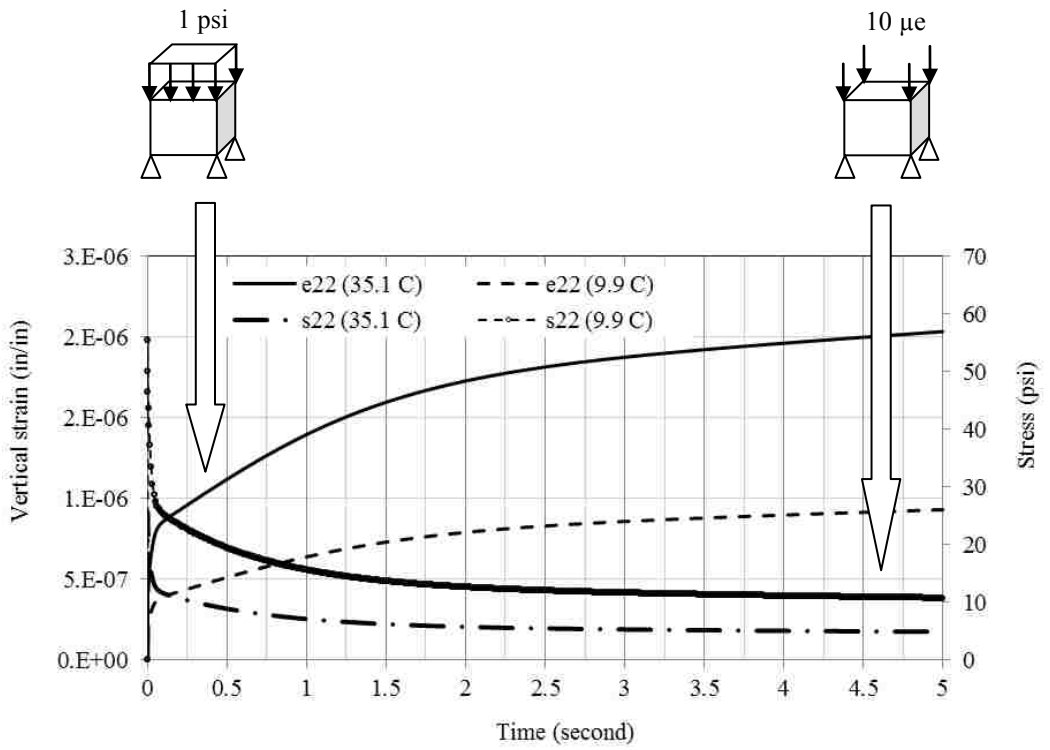

Figure 3.20 Creep and relaxation after integration of subroutine

Now, constant vertical strain 10 microstrain (με) is applied on top 4-nodes to investigate the relaxation behavior. It is observed that there is an instantaneous stress at the initial analysis time step and it gradually attenuates with time (Figure 3.20). This behavior is observed at both high and low temperatures. Opposite to the trend of strain variation, stress is small at high temperatures and vice versa. Based on the observations, this subroutine is also able to incorporate both relaxation and temperature-dependency.

It is observed earlier that the element under constant a stress and strain exhibits creep and relaxation respectively. However, it is necessary to understand the reason behind it. For this reason, both vertical and horizontal relaxation modulus variations against time are plotted in Figure 3.21. It is observed that the both of the moduli attenuate with time which is compatible

with eqns. 3.1 and3.2. In addition, horizontal modulus is smaller than vertical modulus. Both of the vertical and horizontal moduli are temperature-dependent, i.e., modulus is small at high temperature and vice versa.

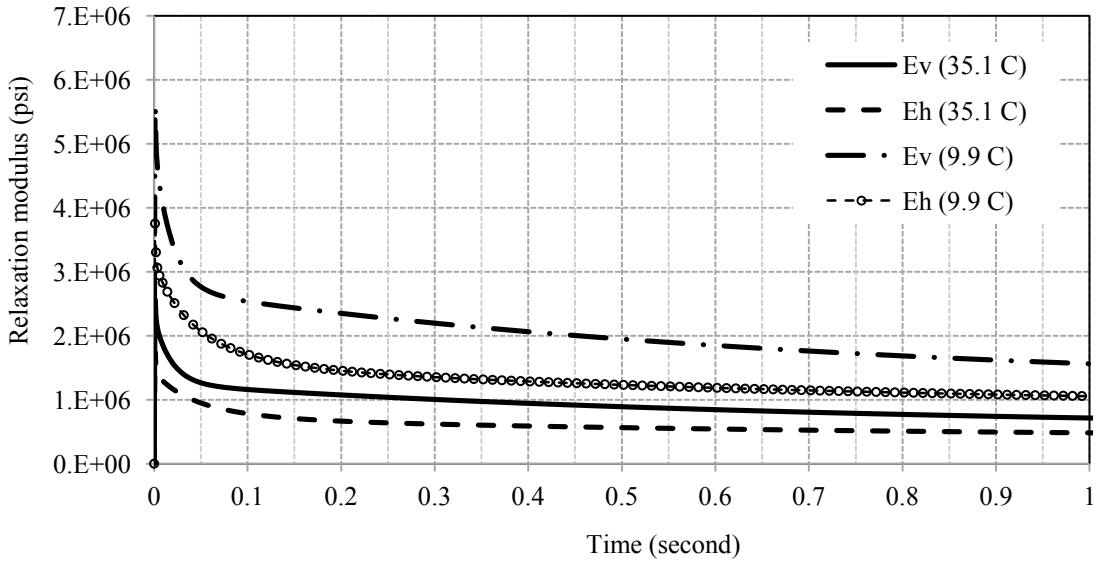

Figure 3.21 Vertical and horizontal relaxation modulus variation

In summary, the above mentioned observations indicate that the developed subroutine successfully implements the temperature-dependency and cross-anisotropic viscoelasticity. Therefore, this subroutine can be incorporated to the dynamic FEM of pavement.

3.7.3 Unbound layers

The dynamic FEM in this study is developed in three different phases as mentioned earlier. In the first phase, the unbound layers are assumed as linear elastic which are determined from the backcalculation of FWD tests. In the second phase, nonlinear elastic and stress-dependency is incorporated to the base layer while the other unbound layers are still linear elastic. In the third

phase, the two unbound layers, i.e., base and subbase, are considered nonlinear elastic and stress-dependent materials whereas the subgrade is linear elastic. The reason is that stress variation in base and subbase is significantly higher compared to subgrade since those layers are at relatively shallow depths.

Stress-dependencies of these layers were determined based on the laboratory tests such as resilient modulus test. Granular aggregates from these layers were collected from the pavement section during the construction for the resilient modulus tests. This test was conducted on granular aggregates collected from both of these layers to determine the stress-dependencies according to the AASHTO T307-99 (2003). Figure 3.22 shows that a cylinder test specimen of unbound material with 4 in. diameter and 8 in. height was prepared for a resilient modulus test. The specimen was kept inside a triaxial cell to apply confining stress by compressed air. A load cell (capacity of 5000 lbs) was used to apply repeated axial load. External LVDTs were used to measure the vertical deformation under this repeated load.

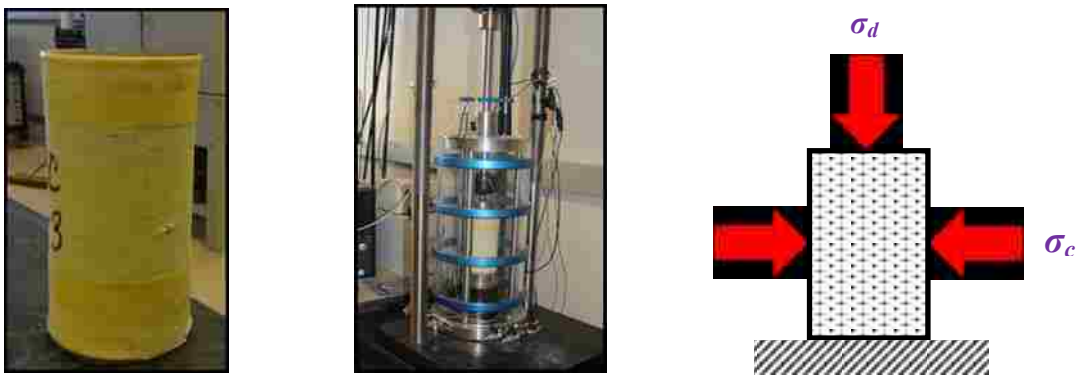

(a) Test specimen (b) Resilient modulus (c) State of stresses

Figure 3.22 Laboratory resilient modulus tests

During the test, the test sample was subjected to a confined pressure (σ_c), i.e., cell pressure applied through compressed air. Once the sample was confined to cell pressure, the deviatoric pressure (σ_d) was applied on the flat surface of the sample along the vertical direction by the load cell. The 10% of this deviatoric pressure was applied in static mode and the rest 90% was applied in cyclic mode. The sample was subjected to a total of 5000 loading cycles. The resilient modulus (M_r) was calculated using the deviatoric stress (σ_d) and the average irrecoverable strain (ε_r) from the last five cycles. The resilient modulus was determined for each of the loading sequences using the following formula:

$$M_r = \frac{\sigma_d}{\varepsilon_r} \tag{3.10}$$

A stress-sequence as defined by the AASHTO T307-99, for granular aggregates, was applied on both of the base and subbase test specimen. Resilient modulus (M_r) values were determined at each of these stress-sequences. Results are summarized in Table 3.2. It is evident that the resilient modulus values of both base and subbase increase as both of the cell and deviatoric stress increase. Therefore, aggregates from both of these layers are stress-dependent.

Table 3.2 Summary of base and subbase resilient modulus

Cell pressure (psi)	Deviator stress (psi)	Max Cyclic stress (psi)	Base resilient modulus, M_r (ksi)	Subbase resilient modulus, M_r (ksi)
3	3	2.7	64.5	22.1
3	6	5.4	87.8	21.2
3	9	8.1	109.8	22.6
5	5	4.5	88.3	21.3
5	10	9	120.5	23.1
5	15	13.5	140.4	25.4
10	10	9	124.8	22.6
10	20	18	157.6	27.7

Stress-dependencies of both base and subbase need to be incorporated to the dynamic FEM. The generalized model as adopted in the newly developed Mechanistic Empirical Pavement Design Guide (MEPDG) was used in this study to incorporate base and subbase stress-dependency (ARA 2004):

$$M_r = k_1 p_a \left(\frac{\theta}{p_a} \right)^{k_2} \left(\frac{\tau_{oct}}{p_a} + 1 \right)^{k_3} \tag{3.11}$$

where $\theta =$ bulk stress $(= \sigma_d + 2\sigma_c)$, $\tau_{oct} =$ octahedral shear stress, $p_a =$ atmospheric pressure, and $k_1, k_2, k_3 =$ regression coefficients that need to be determined from laboratory resilient modulus test. The octahedral shear stress (τ_{oct}) is determined according to the following formula:

$$\tau_{oct} = \frac{1}{3} \sqrt{(\sigma_1 - \sigma_2)^2 + (\sigma_2 - \sigma_3)^2 + (\sigma_1 - \sigma_3)^2} \tag{3.12}$$

where, $\sigma_1, \sigma_2, \sigma_3 =$ principal stresses along three mutually orthogonal directions. In this study, $\sigma_2 =$ major principal stress along vertical direction $(= \sigma_c + \sigma_d)$, and $\sigma_1 = \sigma_3 =$ principal stresses along horizontal plane. Therefore, equation (3.12) can be rewritten as follows:

$$\tau_{oct} = \frac{\sqrt{2}}{3} \sigma_d \tag{3.13}$$

The regression coefficients based on the resilient modulus test on granular aggregate fromt eh base layer at moisture content of 6%, are 6385, 0.15 and 0.75 respectively. A FORTRAN subroutine is also developed for nonlinear elasticity and stress-dependency which will be incorporated to the FEM via UMAT in ABAQUS.

This subroutine is also evaluated by applying 10 psi, ramp over time, on a single element similar to the previous step. Figure 3.23 shows that both bulk and octahedral shear stress vary linearly with vertical stress. This is because, the bulk stress is summation of three orthogonal stress components, i.e., $\theta = \sigma_1 + \sigma_2 + \sigma_3$, and the octahedral shear stress is: $\tau_{oct} = \sqrt{2}/3(\sigma_2 - \sigma_1)$ since $\sigma_1 \approx \sigma_3$. Resilient modulus ($M_R$) is a nonlinear function of both bulk and octahedral shear stress. In addition, there is no negative regression coefficient. It leads to gradual increase in M_R with vertical stress which is the example of stress-hardening. At the stress of 10 psi, the maximum of M_R is about 90,000 psi. At the end, it is observed that the nonlinear modulus results in nonlinear variation in vertical strain even after the application of linear varying vertical stress. At 10 psi, the vertical strain is 150 με.

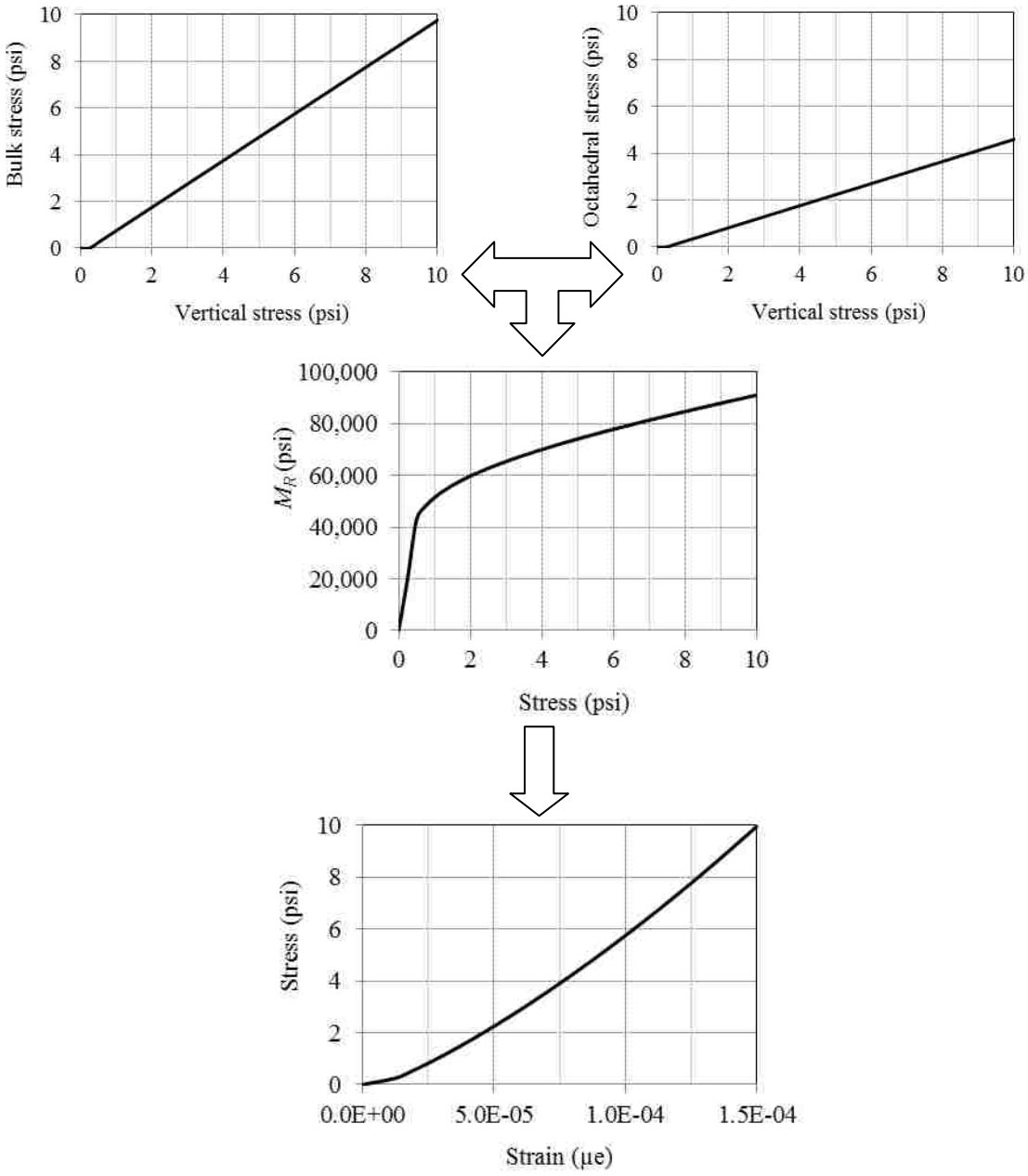

Figure 3.23 Stress-dependency in a single element analysis

In summary, the above mentioned observations indicate that the developed subroutine successfully implements the stress-dependency and nonlinear elasticity. Therefore, this subroutine can be incorporated to the dynamic FEM of pavement.

3.8 Loading Type

In this study, two major types of loading types are used and these are: FWD test load and truck wheel load. The FWD load is mainly used to develop and validate the model whereas the pavement response and following parametric studies are performed based on the FEM incorporating the wheel load. Figure 3.24 shows variation of loading magnitude over time during a FWD test. The peak value of this load is 40 kN (9 kip) with a duration of 25 milliseconds (Tarefder et al. 2014). This load is applied over a circular area with a radius of 15.24 cm (6 in.) which applies the maximum vertical stress of 548.82 kPa (79.6 psi).

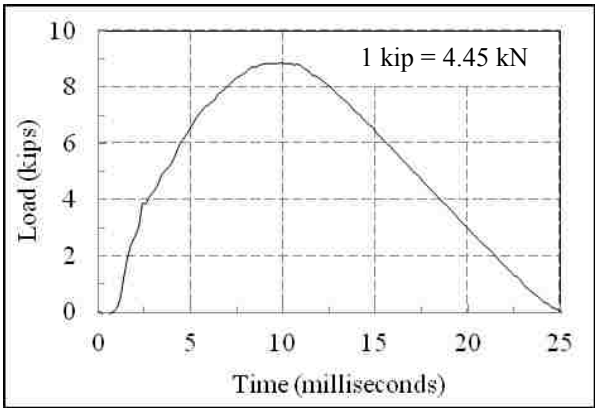

Figure 3.24 Variation of load over time during a FWD test

The wheel load is applied differently during different phases of this study. In the preliminary phases of the model development, tire imprint areas were idealized by both rectangle and rectangle-semicircle shapes. In addition, vertical tire contact stress is assumed uniformly distributed over the imprint areas. Figure 3.25 shows the variation of loading amplitude of wheel of a 18 kip truck over time as well as the tire imprint area. Loading duration is 22.5 milliseconds with the maximum vertical contact stress of 120 psi (MEPDG 2008). In case of tire imprint areas, the longer dimensions are aligned with the traffic direction.

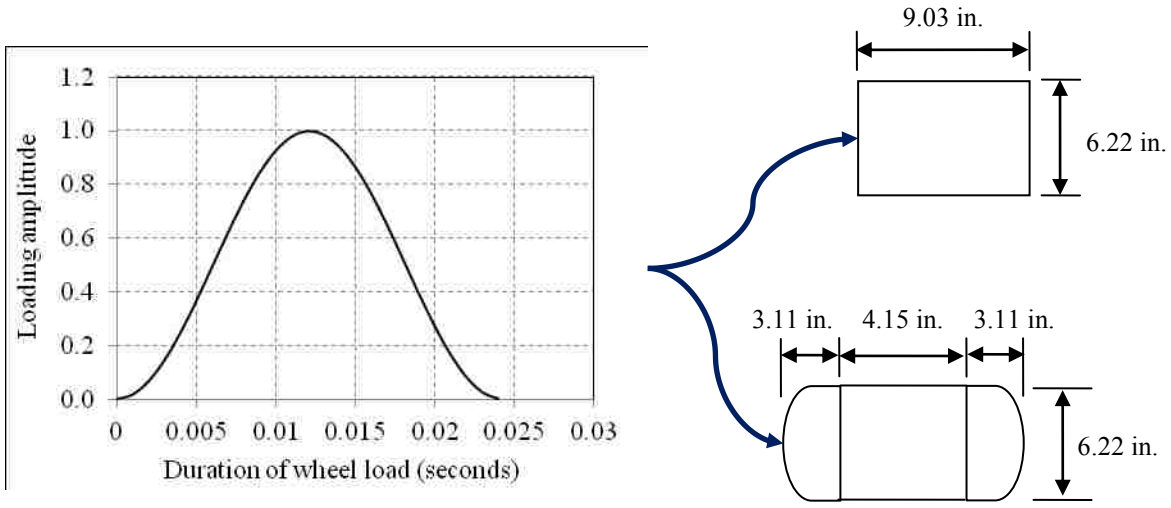

Figure 3.25 Wheel load variation over time and shapes of tire imrpint area

Researchers showed that tire contact stress is not uniform over a tire imprint area (Siddharthan et al. 2002, Al-Qadi and Wang 2009, and Roque et al. 2000). Therefore, the dynamic FEM is updated by applying the non-uniform vertical tire contact stresses over the tire imprint area as the wheel load. Figure 3.26(a) shows the dimension of ribs of a single radial tire from the arrangement of a dual tire 275/80R22.5 as well as the distribution of vertical contact stress over the ribs based on the literatures (Al-Qadi and Wang 2009). The hot-inflated tire pressure is 104.4 psi (720 kPa). There are about five ribs in this tire. The ribs are numbered according to the similar stress magnitudes. Figure 3.26(b) shows the loading duration of the single tire at 96.5 km/hr (60 mph). The loading duration for each of the ribs is assumed to be the same and the duration is 0.03 second. In addition, the peak stresses of the ribs are assumed to be attained at the same time, i.e., 0.015 second.

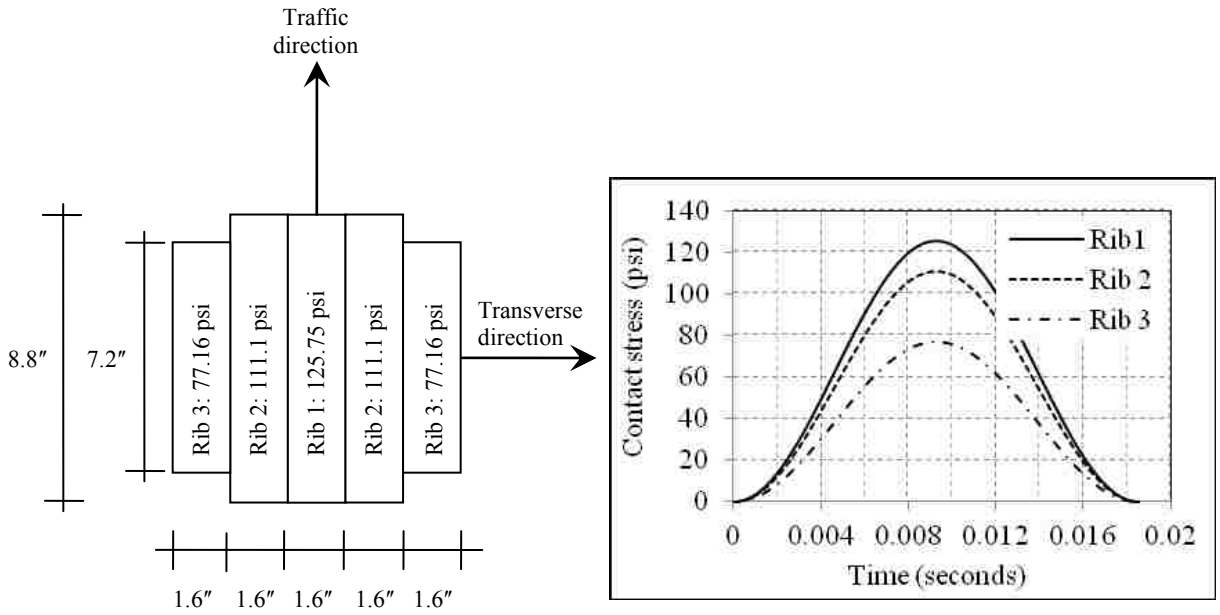

(a) Contact stress distribution (b) Loading duration

Figure 3.26 Contact stress distribution and loading duration

The non-uniform tire contact stress is applied on a quarter of this tire imprint area to generate a truck wheel load on the quarter cube model. Pattern of the mesh on the tire imprint area is summarized in Table 3.3. Dimension of these elements varies from 0.4 to 0.5 in (10.2 to 12.7 mm).

Table 3.3 Mesh assignment for tire imprint area

Ribs of Tire	Number of elements	
	Longitudinal direction	Transverse direction
Rib 1	9	2
Rib 2	9	3
Rib 3	7	3

3.9 Dynamic FEM Analysis

The general equation of a dynamic system can be written as:

$$[M]\{\ddot{u}\}+[C]\{\dot{u}\}+[K]\{u\}=\{F(t)\} \tag{3.14}$$

where $[M]=$ mass matrix of the system, $[C]=$ matrix of damping coefficient, $[K]=$ stiffness matrix of the system, and $\{u\},\{\dot{u}\},\{\ddot{u}\}=$ matrix of nodal displacement, velocity, and acceleration respectively. Mass of the system, i.e., each element, is determined based on product of the density and dimensions. Stiffness of the system, i.e., each element, is calculated based on the matrix of the modulus of elasticity. Generally, mass and stiffness matrices remain constant over time during a typical dynamic analysis. However, a stiffness matrix is not constant over time if the system is considered as viscoelastic. It is known that the relaxation modulus of a viscoelastic material attenuates with time, i.e., $K=K(t)$. Details of damping will be discussed at the end of this section.

There are two algorithms used to solve the above differential equation are implicit and explicit algorithms (Serdaroglu 2010). Explicit algorithm solves the equation at a later time from the state of the system at the current time. On the other hand, implicit algorithm solves the above equation using both current and later state. Among the advantages of explicit algorithm: there is no needs to generate large matrices since the equations are decoupled; no matrix inversion is required since *M* and *C* is diagonal; and no iteration is required. Therefore analysis time is short but algorithm is conditionally stable. Implicit algorithm is unconditionally stable. However implicit algorithm demands long analysis time. This is because, it requires assembling of stiffness matrices and matrix inversion to solve equation (3.14).

In the preliminary stage of the model development whenever the unbound layers was linear elastic, explicit algorithm is used in ABAQUS. Stability of the solution from explicit algorithm is achieved by controlling the time step during analysis. Time step is determined from length of the smallest element and the wave velocity as follows (Cook et al. 2002):

$$\Delta t_{stable} \approx \frac{L_{\min}}{c_d} \tag{3.15}$$

where $L_{\min}$ = length of smallest element and c_d = wave velocity defined as (Kramer 1996):

$$c_d = \sqrt{\frac{E}{\rho}} \tag{3.16}$$

where E = bulk modulus, and ρ = density. Time step used as ABAQUS input is kept smaller than the value determined from equation (3.16) to assure the stability of solution. Later, the implicit algorithm is used in this study due to its unconditional stability.

Damping is an important phenomenon during the dynamic analysis of structure, specially, a pavement system (Samali and Kwok 1995, and El-Ayadi et al. 2012). In a pavement structure, the AC is considered as high frequency layer since the high speed vehicle move on the top of this layer whereas the unbound layers are typically low frequency layers since it is underneath the AC layer and thereby, the loading duration gets higher (Ulloa et al. 2013). Damping assignment on a pavement system is dependent on this frequency magnitude. There are two major types of damping and these are: stiffness or viscous damping and Rayleigh damping (El-Ayadi et al. 2012).

The stiffness damping is applied on a high frequency layer, i.e., AC layer. In this study, the AC is a viscoelastic layer where the stiffness or relaxation modulus deceases with time which leads

to a gradual attenuation of pavement response after unloading. As described earlier, the relaxation modulus is determined from the dynamic modulus values and phase angles at different loading frequencies. These phase angles relate to damping ratios at different loading frequencies, i.e., $\zeta = \tan(\delta)$, where, $\delta =$ phase angle (Tschoegl 1989). The phase angles are summarized in APPENDIX A. This phenomenon indicates that it is not necessary assign additional damping to this layer.

The Rayleigh scheme is typically assigned to the layer where the frequency is not high (El-Ayadi 2012). At moderately low frequencies mass damping is more significant than stiffness or viscous damping. The Rayleigh scheme is as follows (Spears and Jensen 2009):

$$[C] = \alpha[M] + \beta[K] \tag{3.17}$$

where $[C] =$ damping matrix, $[M] =$ mass matrix, $[K] =$ stiffness matrix, and $\alpha, \beta =$ constants for specific damping ratio. These constants are determined using the following relationship:

$$\zeta = \frac{\alpha}{2\omega} + \frac{\beta\omega}{2} \tag{3.18}$$

where $\zeta =$ damping ratio, and $\omega =$ angular frequency of the system.

The damping ratio of 5% is typically suggested for unbound layer materials (Wang and Al-Qadi 2013). Incorporation of damping with the selected damping ratio using the Rayleigh damping scheme is complex since the frequency is unknown (Fekadu 2010). Serdaroglu (2010) approach is used to determine the frequencies from the dynamic analysis. In essence, Fast Fourier Transformation (FFT) was performed on the time history of velocity at the furthest node to determine the frequencies. The time history of velocity has been extracted at the furthest node

right before the support, i.e., 106.7 cm (42.0 in.) above the bottom or support. Incorporating the frequencies and $\zeta = 0.05$ into the Eq. (8), the values of α and β are 10.0 (1/s) and 0.00025 (s) respectively.

3.10 FEM vs. Field

The FEM is simulated under FWD load to predict the surface deflection, horizontal strain in AC layer and vertical stress at different depths. The simulated responses are compared with the field collected pavement responses for the validation (see Figure 3.27). The FWD test was conducted on the instrumented pavement section (MP 141 on I-40) where the HASG and EPC were installed. Deflections, stress, and strains are measured at 9 kip test load.

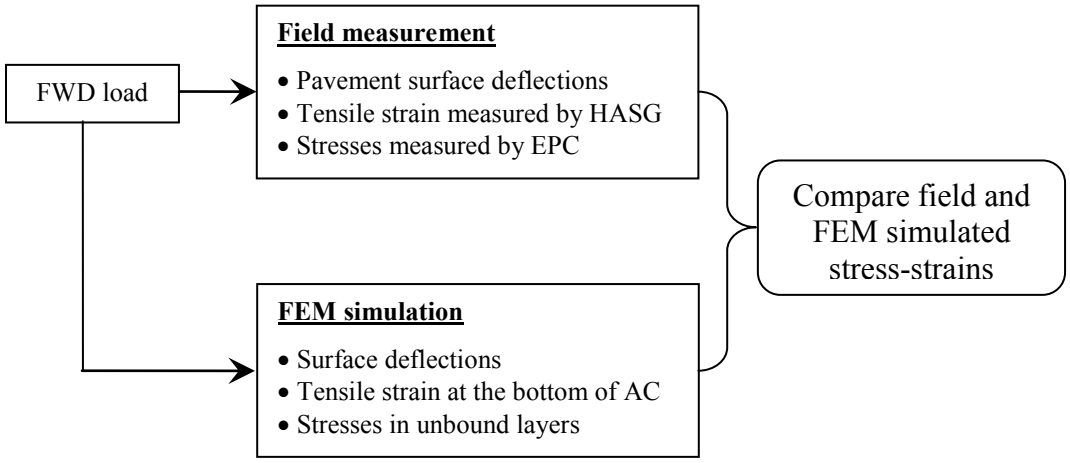

Figure 3.27 Validation of pavement FEM model

Figure 3.28 shows the comparison between field measured and FEM simulated pavement surface deflections. In Figure 3.28(a), the time-deflection history at center of the loading area from the FEM simulation is fairly close to that from the field measurement, i.e., FWD test. The peak deflections from at five different radial distances from FEM simulation and field measurement

are compared in Figure 3.28(b). The field measured deflections are also close to that from the FEM simulation. The RMSE % of the deflections is 7.9%.

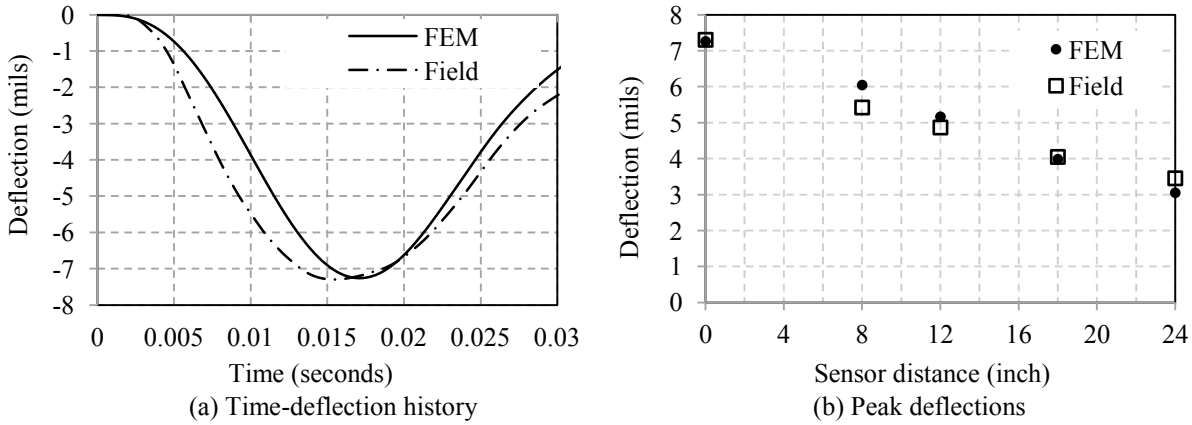

Figure 3.28 Comparison of pavement surface deflections (FEM vs. Field)

Table 3.4 summarizes both of the field measured and FEM predicted stresses and strain. The minimum (%) difference is 2.1, which is in case of horizontal tensile strain at the bottom of the AC layer. The vertical stresses were measured in middle of the base, top of the subbase, and 4 in. below from the subbase-subgrade interface in the subgrade. The stresses simulated by the FEM are fairly close to the field measured stresses with maximum (%) difference of 13.4.

Table 3.4 Comparison of pavement responses (Field vs. FEM)

Response	Field	FEM	(%) Difference
Tensile strain in AC (με)	75.4	73.8	2.1
Vertical stress in base (psi)	14.10	12.6	10.6
Vertical stress in subbase (psi)	10.85	9.4	13.4
Vertical stress in subgrade (psi)	5.28	4.84	8.3

Based on the comparison of time-deflection histories, peak deflections, and stress-strain at depths, it is observed that the FEM simulated pavement response is close to the field responses. Therefore, it can be claimed that the model is validated and ready for further parametric study.

3.11 Distribution of Pavement Response

In this step, the FEM is simulated under the non-uniform vertical tire-pavement contact stress (as shown in Figure 3.26) to observe the distribution of deflections, stress, and strain over the FEM domain. The simulation is performed at two different pavement surface temperatures and these are 9.9 and 35.1 °C. At these pavement surface temperatures, the bottom temperatures are 5.4 and 27.4 °C respectively. After the FEM simulations at these two temperatures, contour of the following pavement responses are plotted:

- Vertical deflection (U2)
- Vertical strain (E22)
- Vertical stress (S22)
- Horizontal stress along traffic direction or longitudinal strain (S33)
- Horizontal stress transverse to traffic direction or transverse strain (S11)
- Horizontal strain along traffic direction or longitudinal strain (E33)
- Horizontal strain transverse to traffic direction or transverse strain (E11)

3.11.1 Contour of vertical deflection

Distributions of vertical deflections over the pavement at two different temperatures are shown in Figure 3.29(a) and (b). Unit of deflection in this figure is in ‘mil’, i.e., 1 mil = 0.001 inch. Figure 3.29(a) shows the distribution of deflections at 9.9 °C. The tire stress is compressive in

nature which leads compressive deflection underneath the loading area. In this contour, compressive deflection has negative sign where color variation from red to blue represents the deflection variation from zero to the maximum limit. It is observed that the deflection is the maximum at the tip of the pavement near the loading area. It diminishes gradually along both vertical and horizontal direction. The qualitative distributions of deflections are almost similar at two different temperatures. However, the deflection values are not equal. AC modulus is high at 9.9 ºC whereas small at 35.1 ºC which results smaller deflection at low temperature and vice versa.

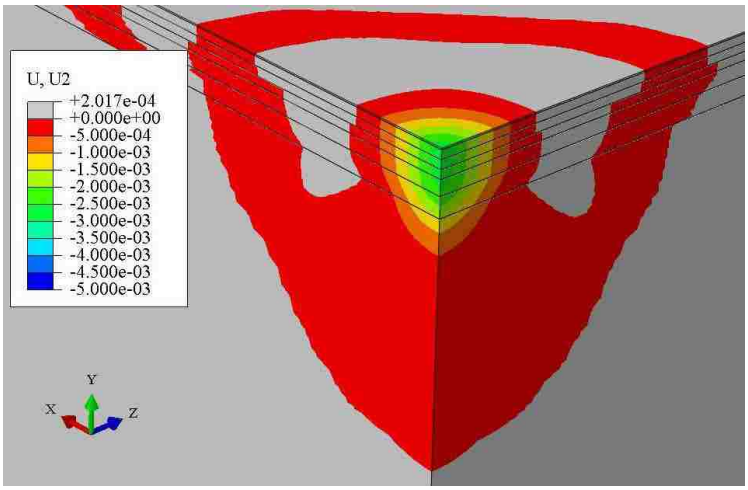

(a) Temperature: 9.9 ºC

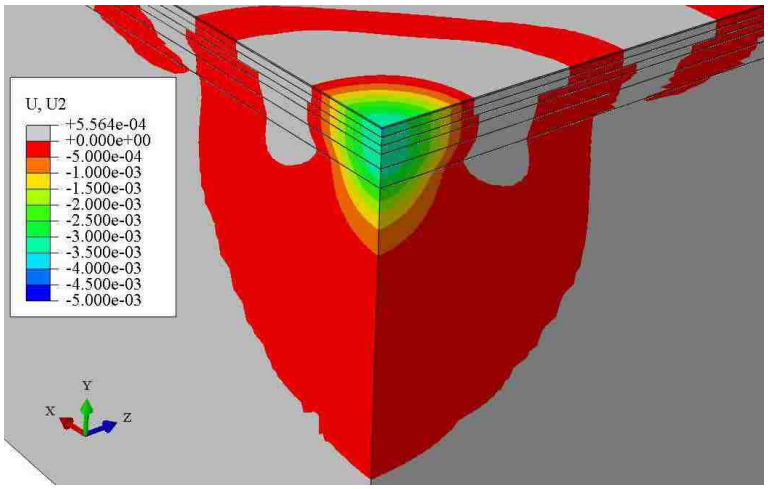

(b) Temperature: 35.1 °C

Figure 3.29 Vertical deflection

3.11.2 Contour of vertical stress

In this step, contours of vertical stresses at 9.9 and 35.1 °C are plotted in Figure 3.30(a) and (b). Similar to the vertical deflection, vertical stress is also in compressive in nature which has nrgative sign. The color variation also follows the earlier trend. These contours show that higher amount of stress is distributed in AC layer and in the unbound layers, i.e., base, subbase, and subgrade, stress falls below 20 psi. Stresses at high temperature are slightly greater than that at low temperature due to temperature-dependency of AC modulus.

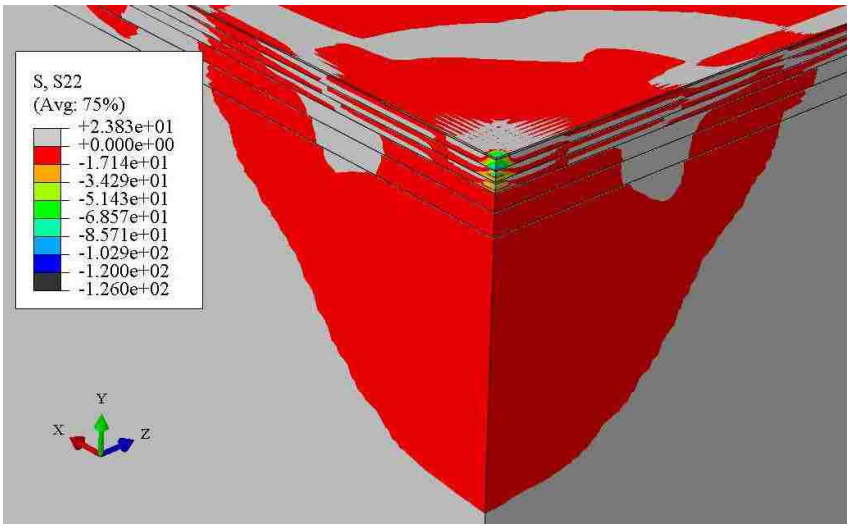

(a) Temperature: 9.9 °C

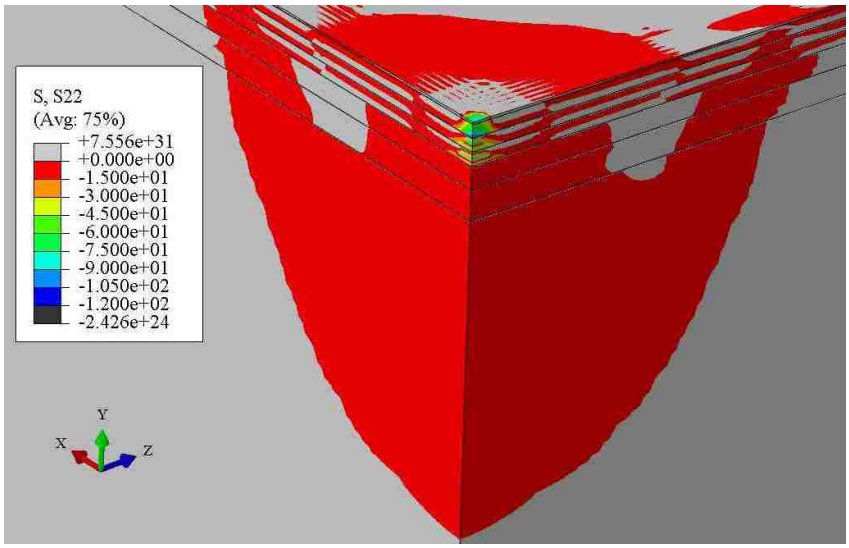

(b) Temperature: 35.1 °C

Figure 3.30 Vertical stress

3.11.3 Contour of vertical strain

In this step, contours of vertical strains at 9.9 and 35.1 °C are plotted in Figure 3.31(a) and (b). Vertical strains are compressive in nature due to compressive tire-pavement contact stress and have –ve sign in the contours. Strain variation over depth is not similar to the previous trends as

observed in stress and deflection. Vertical strain in the AC layer is small even after the presence of high stress. This is due to greater magnitude of AC modulus. Underneath the AC layer, vertical strains are high in the unbound layers. The reason is that the unbound layer is very small compared to the AC modulus and thereby, vertical strain is high due vertical stress even below 20 psi. In every unbound layer, vertical strain is high at the top of a specific layer gradually diminishes with depth. It is also observed that there is a sudden strain variation at the layer interfaces which is due to change in material stiffness/modulus. Finally, at low AC temperature (9.9 °C), vertical strains are also small which is not only due to the temperature variation. A this temperature, unbound layers have the minimum moisture content which leads to higher base and subbase moduli.

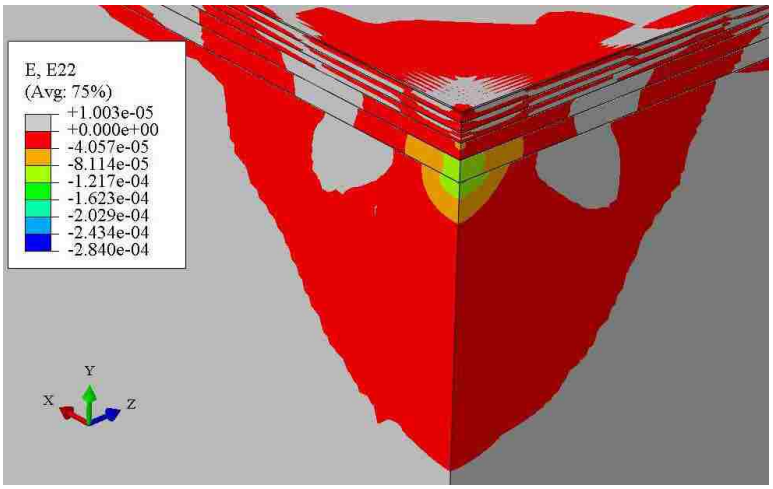

(a) Temperature: 9.9 °C

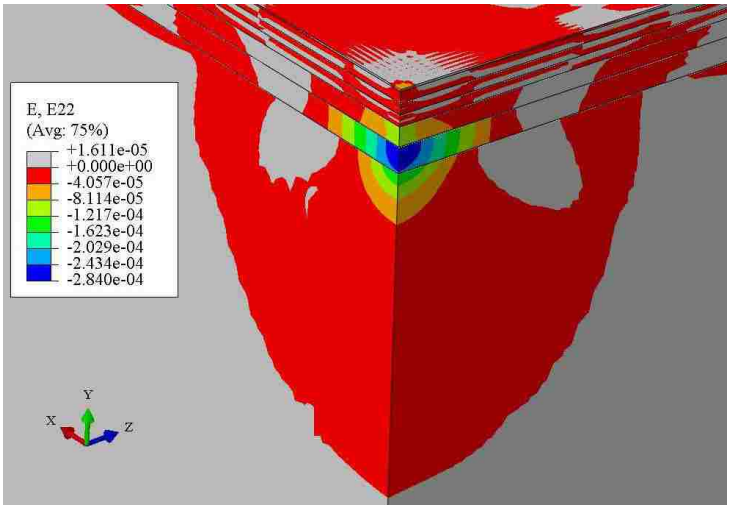

(b) Temperature: 35.1 °C

Figure 3.31 Vertical strain

3.11.4 Contour of longitudinal horizontal stress

In this step, contours of horizontal stress along traffic direction are plotted at 9.9 and 35.1 °C respectively in Figure 3.32(a) and (b). These contours are plotted only for AC layer since the unbound layers cannot withstand tensile stress. Signs of tensile stress are positive in these figures. In both of these contours, longitudinal horizontal stress distribution is discontinuous at the AC-AC layer interfaces due to assignment of partial bonding condition at these interfaces. Tensile stress is developed at the bottom whereas the compressive stress is developed at the top of each of these AC layers/lifts. An interesting observation is that the entire OGFC layer is in compression which is due to its very small thickness. Comparing the two contours, longitudinal horizontal stress at high temperature is slightly greater than that at low temperature.

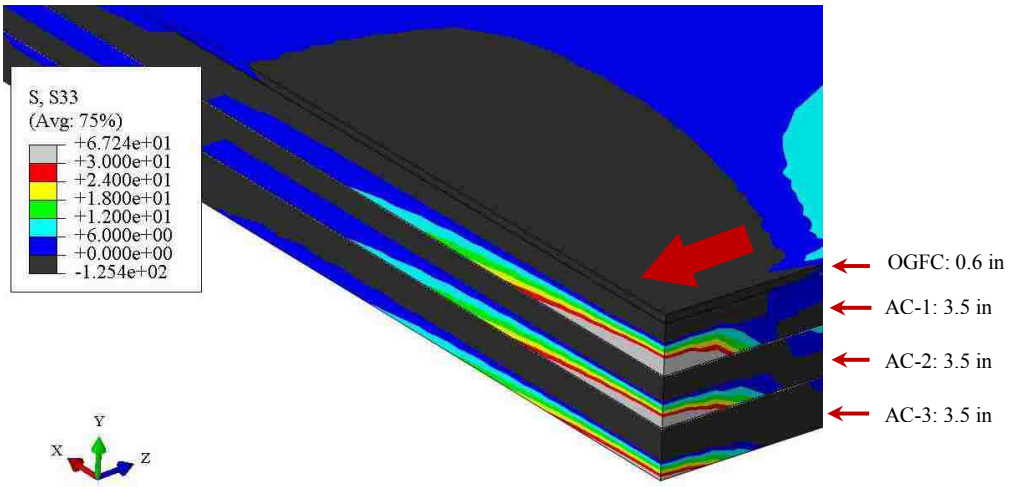

(a) Temperature: 9.9 °C

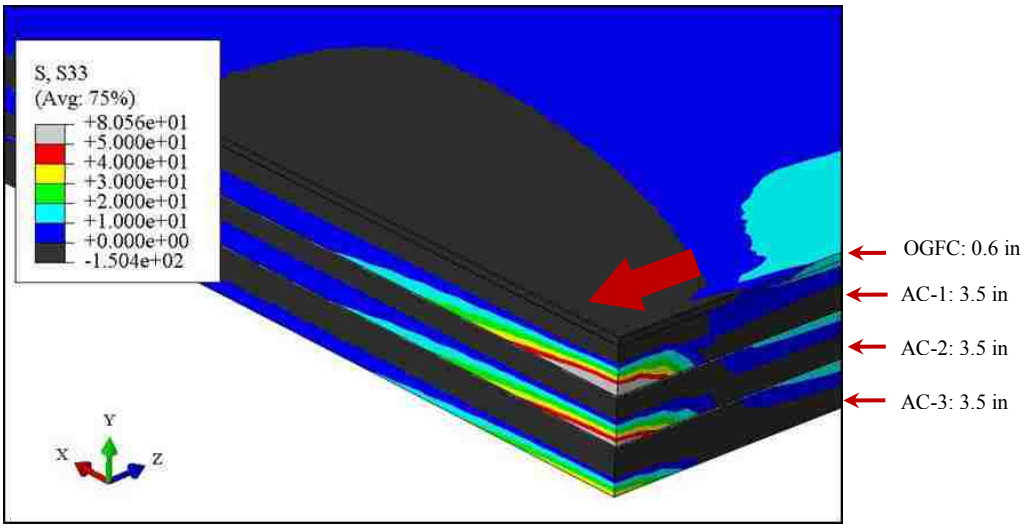

(b) Temperature: 35.1 °C

Figure 3.32 Horizontal stress in AC (longitudinal)

3.11.5 Contour of longitudinal horizontal strain

In this step, contours of horizontal strain in AC along traffic direction are plotted at 9.9 and 35.1 °C respectively in Figure 3.33(a) and (b). Signs of tensile strains are positive in these figures. Similar to the distribution of longitudinal stress, longitudinal strains are also discontinuous at the

AC-AC layer interfaces due to assignment of partial bonding condition at these interfaces. Tensile strain is developed at the bottom whereas the compressive strain is developed at the top of each of these AC layers/lifts. The entire OGFC layer shows compressive strain due to compressive longitudinal stress. Comparing the two contours, longitudinal tensile strain at high temperature is greater than that at low temperature.

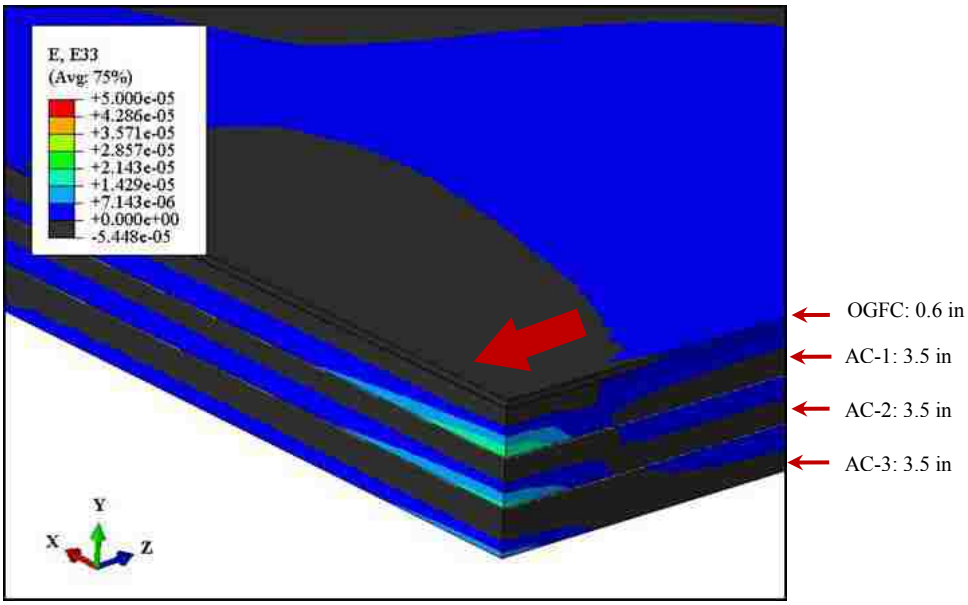

(a) Temperature: 9.9 °C

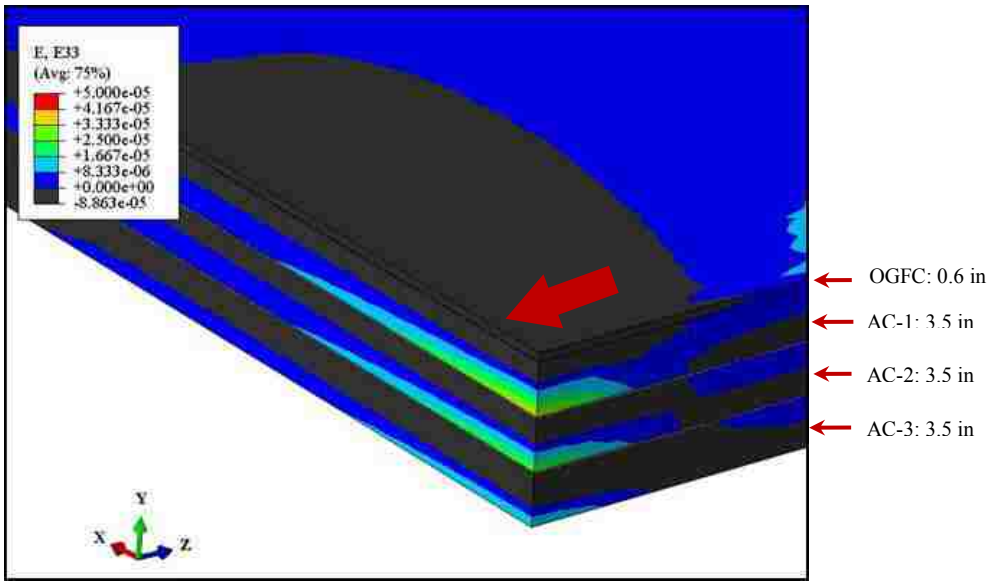

(b) Temperature: 35.1 °C

Figure 3.33 Horizontal strain in AC (longitudinal)

3.11.6 Contour of transverse horizontal stress

In this step, contours of horizontal stress transverse traffic directions are plotted at 9.9 and 35.1 °C respectively in Figure 3.34(a) and (b). In both of these contours, transverse horizontal stress distribution is discontinuous at the AC-AC layer interfaces due to assignment of partial bonding condition at these interfaces as observed in Figure 3.32. Tensile stress is developed at the bottom whereas the compressive stress is developed at the top of each of these AC layers/lifts. Transverse stress at high temperature is slightly greater than that at low temperature. Comparing the transverse and longitudinal horizontal stresses, it is observed that the transverse stress is greater than the longitudinal stress.

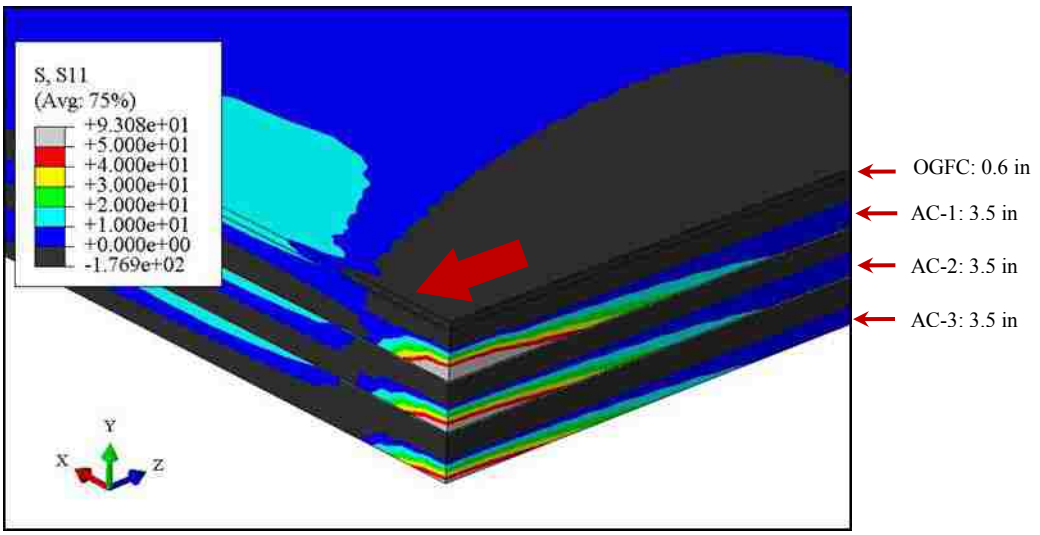

(a) Temperature: 9.9 °C

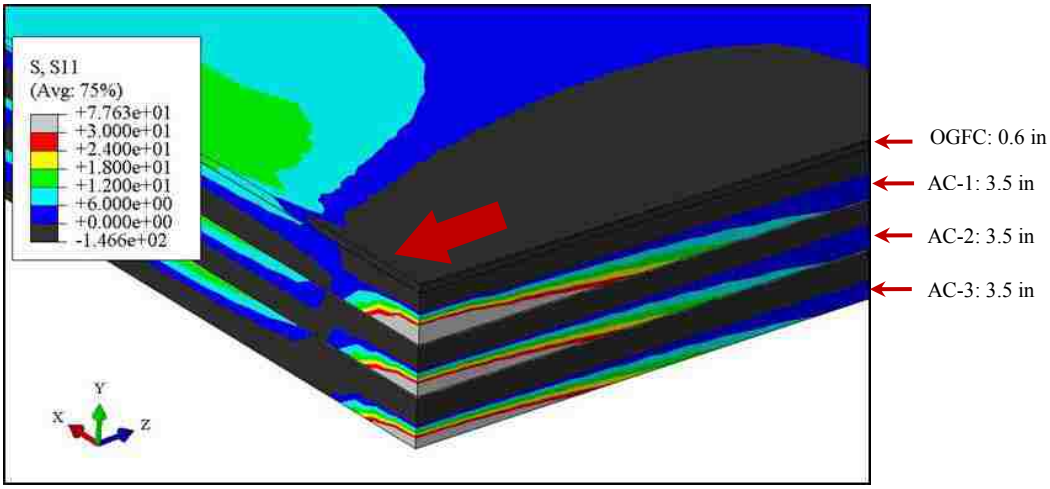

(b) Temperature: 35.1 °C

Figure 3.34 Horizontal stress in AC (transverse)

3.11.7 Contour of transverse horizontal strain

In this step, contours of horizontal strains in AC transverse to traffic direction are plotted at 9.9 and 35.1 °C respectively in Figure 3.35(a) and (b). Similar to the earlier trends, transverse strains are developed at the bottom whereas the compressive strain is developed at the top of each of these AC layers/lifts. The entire OGFC layer shows compressive strain due to compressive

transverse stress. Comparing the two contours, transverse tensile strain at high temperature is greater than that at low temperature.

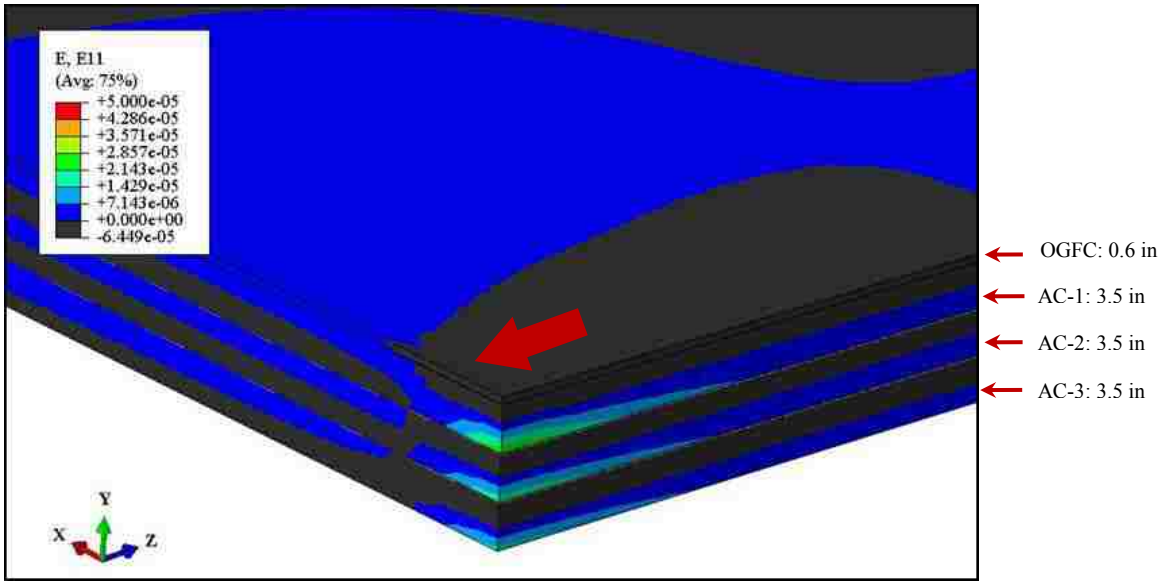

(a) Temperature: 9.9 °C

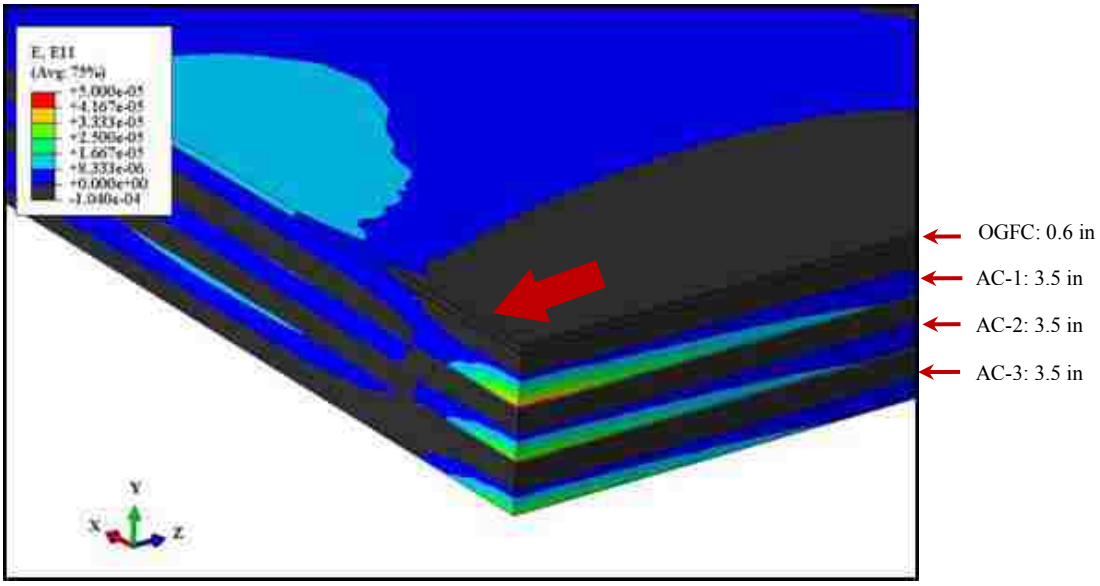

(b) Temperature: 35.1 °C

Figure 3.35 Horizontal strain in AC (transverse)

3.12 Summary

In this phase of the study, details of different steps related FEM developed are documented. These steps are summarized below:

- Dynamic modulus tests were conducted on both vertical and horizontal AC cores to develop the temperature-dependent and cross-anisotropic viscoelastic material model for the AC
- Resilient modulus tests were conducted on granular aggregates from both base and subbase layers to develop nonlinear elastic and stress-dependent material model for unbound layers
- A dynamic FEM is developed integrating the earlier mentioned two different materials to determine pavement responses, such as deflection, stress, and strain, under the FWD test load and non-uniform vertical tire-pavement contact stress
- The developed FEM is validated by comparing the simulated pavement responses and field response under the FWD test load
- The FEM simulation shows that the vertical strains in the unbound layers are greater than that in the AC layer. Each of the AC layers experiences compressive horizontal strain at the top and tensile strain at the bottom.

CHAPTER 4

AC CROSS-ANISOTROPY

4.1 General

Effect of the AC cross-anisotropy on the pavement response, such as stress-strain, is evaluated in this chapter. This study is divided in two phases. In the first phase, effect of AC cross-anisotropy on pavement response is evaluated without considering the temperature dependency of AC layer. In the second phase, temperature dependency is incorporated with further improvement of material model.

4.2 Outline

This study is performed in two different phases as mentioned earlier. Temperature dependency of the AC layer is not incorporated to the dynamic FEM in the first phase whereas it is incorporated in the second phase. However, this is not the only difference between these two phases. The model which is developed in the beginning is replicate of the instrumented pavement section under construction before opening of the traffic. This model has no OGFC layer on the top. In addition, the temperature probes were not installed inside the AC layer at the time of study. In the second phase, the construction was completed, the temperature probes were installed inside the AC layer and the pavement section was open to traffic.

An outline of different phases of this study is shown in Figure 4.1. In the first phase, vertical tire contact stress is assumed uniform. Pavement stress-strain are determined at varying *n*-values by the dynamic FEM simulations, i.e., $n = E_h / E_v$, where E_h = horizontal modulus, and E_v =

vertical modulus. This task is repeated for two different shapes of tire imprint areas as mentioned in the previous chapter. These are: rectangle and rectangle-semi circle. Goal is to determine the imprint shape which determines the pavement with better accuracy. In the second phase, non-uniform tire contact stress is assigned to determine the pavement responses at varying *n*-values and pavement temperatures.

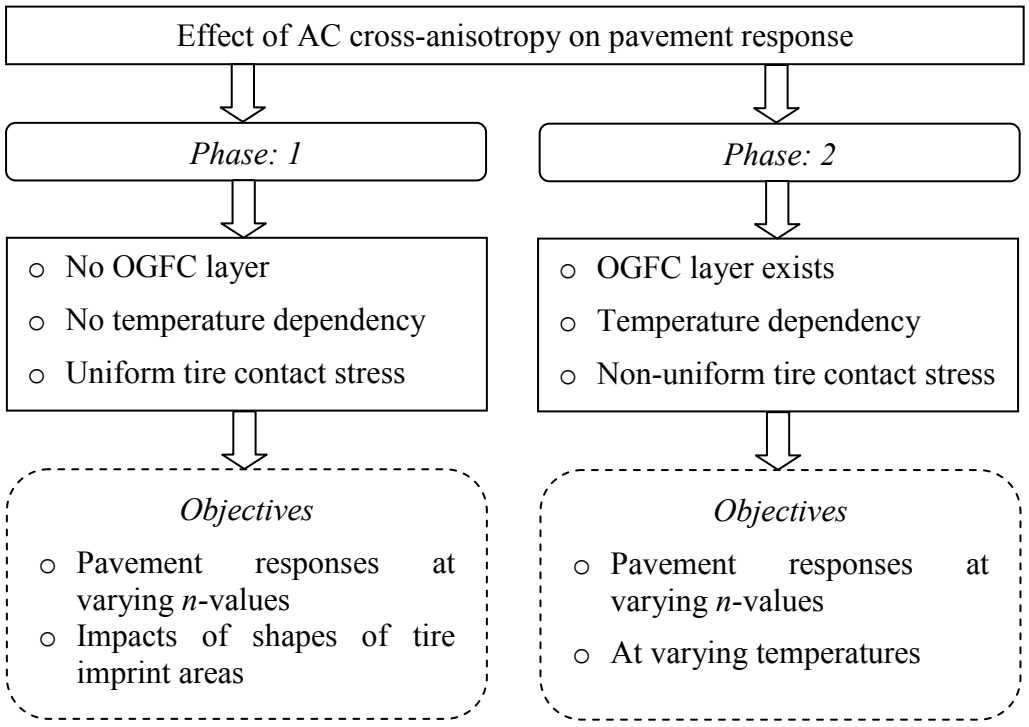

Figure 4.1 Outline of the study

4.3 Phase: I

4.3.1 Model Description

The model geometry is exactly same as the geometry in Figure 3.4, except there is no OGFC layer. Preliminary boundary condition, i.e., BC 1 (see Figure 3.5), is assigned where the bottom of the geometry is restrained to move along both vertical and horizontal directions. In addition,

the vertical planes are restrained to move along horizontal direction. The layer interface is assumed to be fully bonded. Mesh is generated over the geometry according to the method as discussed in section 3.7. The minimum dimension of an element is 0.6 in. Assignment of layer materials to the model is described below:

Three lifts of AC layers on the top of the pavement model are assumed to have identical property. This is due to the fact that these lifts have been constructed using same mix one after another. AC is considered to be visco-elastic material. Elastic modulus of AC as well as rest of the layers is backcalculated from FWD test data. FWD test has been conducted on each layer and lifts sequentially starting from subgrade. FWD deflections data are analyzed using backcalculation software ELMOD. Backcalculated layer moduli, E, as well as density, ρ, and Poisson's ratio, ν, used in backcalculation are summarized in Table 4.1.

Table 4.1 Material of Pavement Layers

Material	E (ksi)	ρ (pcf)	ν
AC	250	145	0.35
Granular aggregate	30	135	0.4
PPC	25	120	0.4
Fine soil	15	110	0.45

Note[1]. 1 ksi = 6.89 MPa
Note[2]. 1 pcf = 16.02 kg/m^3

No laboratory tests are conducted in this study. AC viscous properties are obtained from Al-Qadi et al. (2010) and shown in Table 4.2. These parameters are obtained from Prony series fitting by Al-Qadi et al. (2010).

Table 4.2 Prony Series for AC viscoelasticity (Al-Qadi et al. 2010)

i	e_i	τ_i
1	0.631	0.078
2	0.251	0.816
3	0.0847	5.68
4	0.0267	139

Cross-anisotropy is assigned to materials by varying the magnitude of anisotropy parameters such as *n* and *m* defined as follows:

$$n = \frac{E_{11}}{E_{22}} \tag{4.1}$$

$$m = \frac{G_{12}}{E_{22}} \tag{4.2}$$

where E_{11} = modulus of elasticity on horizontal plane, E_{22} = modulus of elasticity on vertical plane, and G_{12} = shear modulus of elasticity. For cross-anisotropy, $E_{11} = E_{33}$, where E_{33} = modulus of elasticity on horizontal plane along transverse direction. In addition, shear modulus is assumed be the same over three orthogonal planes. That is, $G_{12} = G_{23} = G_{13} = G$.

Layers underneath HMA layer, i.e., base, PPC and subgrade, are assumed to be linear elastic. Backcalculated moduli summarized in Table 4.1 are used as elastic modulus. Cross-anisotropy in modulus of elasticity is assigned to these layers by varying *n*-value.

There are two different types of loading applied to simulate the dynamic FEM. One is FWD test load which is used for comparison between field and simulated pavement response. The other is truck wheel load which is used to determine the pavement stress-strain from the simulations at varying *n*-values. The load is assumed to apply uniform tire contact stress over two different shapes of tire imprint areas: rectangle and rectangle-semi circle. Duration of both of the FWD and wheel load is shown in Figure 3.21. The dynamic simulation is performed in the ABAQUS/Explicit by maintaining the stability criteria. Another important issue related to a dynamic analysis is damping. Damping is assigned to this model according to the method as described in section 3.9. The dynamic FEM simulation of a pavement takes significant amount of time. Therefore, the simulations need to be performed in such a manner that the parametric study can be implemented effectively. Once the model is developed, Table 4.3 is followed as an analysis matrix for the FEM simulations to perform the parametric study. A total of 12 simulations are performed in this stage of the study.

Table 4.3 Analysis matrix of FEM simulation

n-value	FWD load	Wheel load	
		Rectangle	Rectangle-semi circle
0.3	X	X	X
0.5	X	X	X
0.7	X	X	X
1.0	X	X	X

4.3.2 Results and Discussion

The results and related discussion is documented under different sections for both FWD and wheel load as below:

Horizontal Tensile Strain

Horizontal tensile strain in longitudinal at varying *n*-values is plotted in Figure 4.2(a) and (b) for rectangle and rectangle-semi-circle shaped tire imprint areas. In both cases, it is observed that horizontal strain increases with decrease in *n*-values. Decrease in *n*-value means decrease in horizontal *E*-value while vertical *E*-value is constant. Horizontal strain increases as horizontal modulus decreases. It is also observed that the peak strain due to rectangle shaped loading area yields much greater than that due to rectangle-semi-circle loading area. The field measured tensile strain at the bottom of the AC layer is 141 microstrain which is closer to the range of strain due to rectangle-semi-circle shaped loading area.

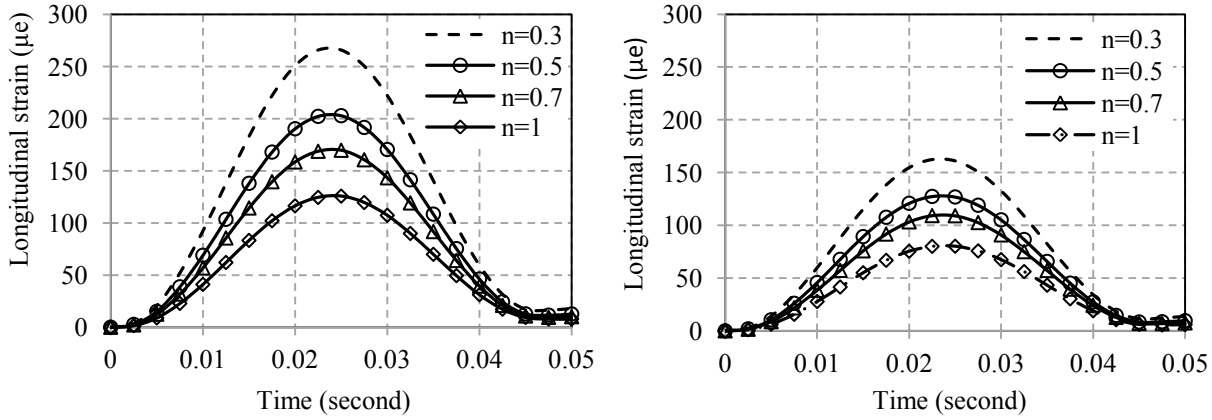

(a) Rectangle (b) Semi-Circle-Rectangle

Figure 4.2 Effect of AC cross-anisotropy on horizontal tensile strain

Vertical Stress

Vertical stress variations are shown in Figure 4.3(a) and (b). Similar to trend of horizontal strain, vertical stress increases as *n*-value decreases. At $n = 0.3$, vertical stress is maximum whereas that is minimum at $n = 1$ (isotropic model). Similar trend is observed in both shapes of the loading

area. It is mentioned earlier that vertical deflection increases as *n*-value decreases for the same amount of vertical load. Increase in vertical deflection causes increase in vertical strain. Therefore, vertical stress increases with vertical strain since the vertical *E*-value remains constant with decrease in *n*-value. Again, FEM simulation with rectangle loading area predicts vertical stress greater than that with semi-circle-rectangle loading area. The field measured vertical stress is 8 psi which is very close to the range of stress with semi-circle-rectangle shaped loading area.

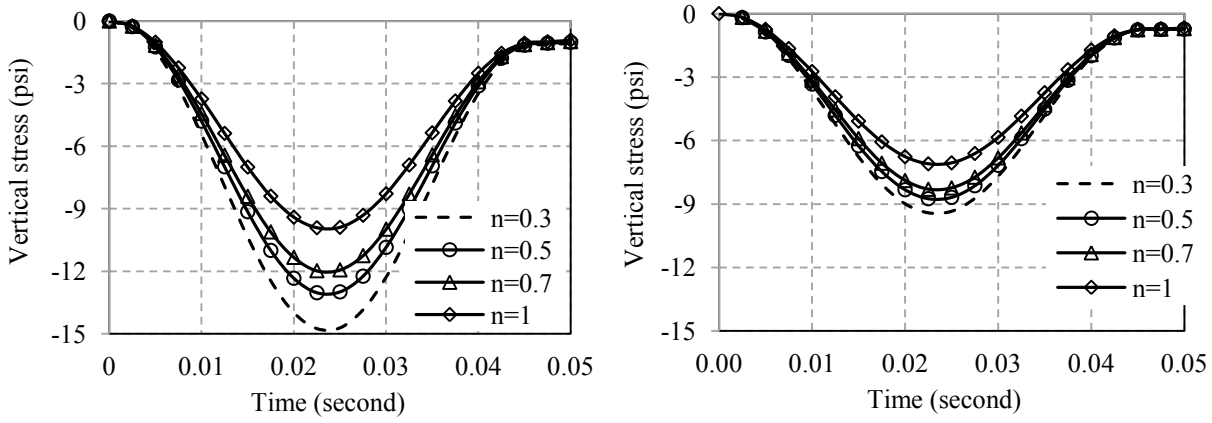

(a) Rectangle (b) Semi-Circle-Rectangle

Figure 4.3 Effect of AC cross-anisotropy on vertical strain

4.3.3 Summary of Phase I

Outcomes of this study are summarized below:

- Pavement response, such as deflection, strain and stress decreases as the *n*-value increases towards 1.0 (isotropy). It indicates consideration of isotropic modulus yields smaller pavement responses. This variation in strain value may significantly influence pavement damage. Therefore, it is recommended to address this issue in the next phase of this study.

- Predicted pavement response due to rectangle shaped loading area is much greater than that due to rectangle-semi-circle shaped loading area. In addition, both field strain and stress are considerably smaller than the predicted response horizontal strain and vertical stress with rectangle shaped loading area. Therefore, it is recommended to apply the uniform vertical contact stress over a rectangle-semi-circle shaped loading area in the next phase.

4.4 Phase: II

4.4.1 Model Description

The model geometry is exactly same as the geometry in Figure 3.4. Preliminary boundary condition, i.e., BC 1 (see Figure 3.5), is assigned where the bottom of the geometry is restrained to move along both vertical and horizontal directions. In addition, the vertical planes are restrained to move along horizontal direction. The layer interfaces are considered partially-bonded and coulomb friction law is used to model the contact between the interfaces. The friction coefficients along layer interfaces in AC are 0.7. Mesh is generated over the geometry according to the method as discussed in section 3.7. The minimum dimension of an element is 0.6 in. Assignment of layer materials to the model is described below:

The AC is viscoelastic and the unbound layers, such as base, subbase, and subgrade are linear elastic which is similar to Phase 1. The main difference lies in determination of cross-anisotropy and viscoelasticity in AC layer. In previous phase, the AC material parameters were collected from the literature, however, laboratory tests were conducted in this phase to determine earlier mentioned parameters. The schematic of laboratory tests are shown in Figure 3.12. The dynamic modulus and relaxation test were conducted to determine the Prony series parameters and

vertical instantaneous modulus (see Figure 3.12). The IDT test was conducted to determine the horizontal instantaneous modulus as well as Poisson's ratio. Based on interpretation of test results, the vertical modulus (E_v) was 1151.87 ksi and the horizontal modulus (E_h) was 345.56 ksi at 21 °C. The resulting degree of cross-anisotropy (n-value) is 0.33. The Poisson's ratio in vertical (ν_{vh}) and horizontal (ν_{hh}) planes are 0.3 and 0.25 respectively. The Prony series coefficients determined from the dynamic modulus values are summarized in Table 4.4.

Table 4.4 Prony series coefficient

i	e_i	τ_i
1	0.2	1.1
2	0.2	4.7
3	0.15	9.75
4	0.15	100
5	0.1	250
6	0.1	470

Moduli of elasticity of unbound layers are predicted from the backcalculation of Falling Weight Deflectometer (FWD) deflection data. The FWD test was conducted on the instrumented pavement section at the selected locations where the sensors were installed. Table 4.5 summarizes the parameters of the unbound layers which are required for the dynamic FEM. Both of the density and Poisson's ratio are summarized in addition to the layer moduli.

Table 4.5 Backcalculated moduli of the unbound layers

Layer	E (ksi)	ρ (pcf)	ν_{vh}
Base	108	135	0.4
Subbase	91	120	0.4
Subgrade	25	110	0.45

The temperature variation over depth of the AC layer at a specific was measured by temperature probes. These temperature probes were installed at different depths of the instrumented pavement section such as 0, 2, 4, 12, 15, and 21 inch from the pavement surface. The depth-temperature variation in the AC layer was interpreted from the linear trend of temperatures**.** Figure 4.4 shows the linear depth-temperature variation based on the temperatures recorded in February and June, 2013 respectively. In both of the cases, the surface temperature is greater than the bottom temperature since the temperatures were recorded during the daytime. The surface temperatures ($T_{surface}$) are 4.1 ºC and 35.1 ºC in February and June, 2013 respectively. The bottom temperatures (T_{bottom}) are 3.6 ºC and 27.4 ºC in February and June, 2013 respectively. The AC modulus is converted to 21 °C using eqn. (5).

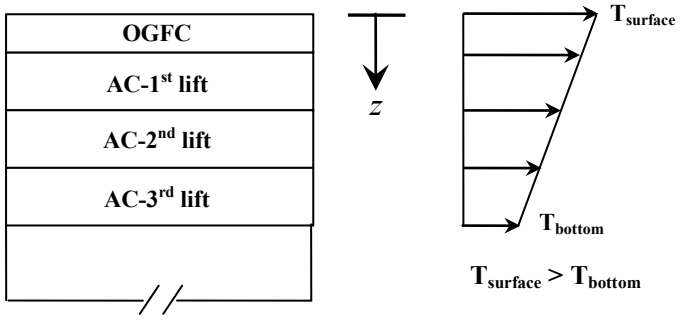

Figure 4.4 Temperature variation over depth in AC layer

In this phase of the study, the previously mentioned two different types of loading applied to simulate the dynamic FEM: FWD and wheel load. The difference lies within the assignment of load distribution over the tire imprint areas as well as shape of tire imprint area. This time wheel load is applied a non-uniform vertical contact stress over different ribs of a tire. Duration of the wheel load is shown and described in Figure 3.23 and related discussion. The dynamic

simulation is performed in the ABAQUS/Implicit to ensure unconditional stability. As mentioned earlier, another important issue related to a dynamic analysis is damping which is assigned to this model according to the method as described in section 3.9. For the parametric study, Table 4.6 is followed as an analysis matrix to perform the FEM simulations. A total of 8 simulations are performed under wheel load. In addition, simulation is performed under FWD test load incorporating *n*-value of 0.33 as well as at temperatures in February and June respectively for validation.

Table 4.6 Analysis matrix of FEM simulation under wheel load

n-value	Pavement surface temperature (°C)	
	February (4.1 °C)	June (35.1 °C)
0.25	X	X
0.5	X	X
0.75	X	X
1.0	X	X

4.4.2 Pavement Performance Indicator

It is a typical practice that pavement performance is evaluated based on accumulated damage which is determined by the Miner's formula incorporating pavement strains (Rajbongshi 1997, Huang 2004, and Ekwulo and Eme 2009). According to this formula, the damage is calculated as follows:

$$D = \sum \frac{n}{N} \tag{4.3}$$

where $D =$ damage factor (0~1), $n =$ actual number of load repetition, and $N =$ number of load repetition till failure. This damage is suggested to calculate based on two major criteria: fatigue

and permanent deformation. In case of fatigue and permanent deformation, eqn. (4.3) will be as follows:

$$D_f = \sum \frac{n}{N_f} \tag{4.4}$$

$$D_d = \sum \frac{n}{N_d} \tag{4.5}$$

where $D_f =$ damage factor due to fatigue, $D_d =$ damage factor due to permanent deformation, $N_f =$number of load repetition till failure due to fatigue, and $N_d =$number of load repetition till failure due to permanent deformation. The Asphalt Institute (Asphalt Institute 1982) proposed the following regression equations to calculate the N_f and N_d:

$$N_f = 0.0796\varepsilon_t^{-3.291} E_h^{-0.854} \tag{4.6}$$

$$N_d = 1.365\varepsilon_c^{-4.477} \tag{4.7}$$

where $\varepsilon_t =$ tensile strain at the bottom of the AC, $E_h =$ modulus of elasticity of AC along horizontal direction, and $\varepsilon_c =$vertical compressive strain. The E_h-value is assumed as isotropic in eqn. (4.6) which indicates that the both vertical and horizontal moduli are assumed to be equal. In this study, $E_h = nE_v$, where $n =$degree of cross-anisotropy. Incorporating the cross-anisotropy, Eqns. (4.4) and (4.5) can be modified as follows for a specific period and loading type:

$$D_{f,anis} = \frac{n}{0.0796n^{-0.854}\varepsilon_{t,anis}^{-3.291} E_v^{-0.854}} \tag{4.8}$$

$$D_{d,anis} = \frac{n}{1.365\varepsilon_{c,anis}^{-4.477}} \tag{4.9}$$

Eqns. (4.8) and (4.9) will be as follows whenever the material is assumed as isotropic:

$$D_{f,iso} = \frac{n}{0.0796\varepsilon_{t,iso}^{-3.291} E_v^{-0.854}} \tag{4.10}$$

$$D_{d,iso} = \frac{n}{1.365\varepsilon_{c,iso}^{-4.477}} \tag{4.11}$$

Now, damage due to single load repetition is defined by ratio of cross-anisotropic damage to isotropic damage for both fatigue and permanent deformation. Relationships of the damages per load repetition are as below:

Fatigue: $$\frac{D_{f,anis}}{D_{f,iso}} = n^{0.854}\left(\frac{\varepsilon_{t,anis}}{\varepsilon_{t,iso}}\right)^{3.291} \tag{4.12}$$

Permanent deformation: $$\frac{D_{d,anis}}{D_{d,iso}} = \left(\frac{\varepsilon_{c,anis}}{\varepsilon_{c,iso}}\right)^{4.477} \tag{4.13}$$

Eqns. (4.12) and (4.13) will be used throughout this study as a pavement performance evaluation indicator to investigate the effect of cross-anisotropy on pavement performance.

4.4.3 Results and Discussion

The results and related discussion is documented under different sections for both FWD and wheel load as below:

Tensile Strain in AC layer

Horizontal tensile strains along both longitudinal and transverse direction at bottom of the AC layer are determined from the dynamic FEM simulation. The tensile strains are determined at different *n*-values by incorporating the depth-temperature variations during the month of February and June. The effect AC cross-anisotropy variation as well as depth-temperature variations on the tensile strains is plotted in Figure 4.5. Figure 4.5(a) shows the effect of AC

cross-anisotropy on the longitudinal tensile strain in February and June. In both of the months, the tensile strain decreases with increase in *n*-value. The strain is the minimum whenever the AC is considered as isotropic, i.e., n=1. In case of smaller *n*-value, horizontal modulus is smaller than vertical modulus. Therefore, strain increases with decrease in horizontal modulus at a constant stress.

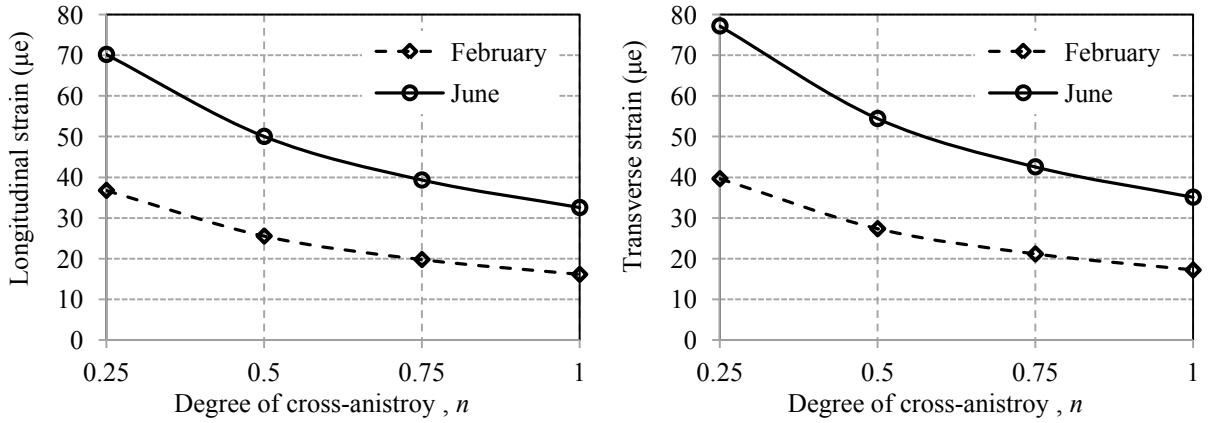

(a) Longitudinal tensile strain (b) Transverse tensile strain

Figure 4.5 Effect of AC cross-anisotropy on tensile strain at bottom of the AC layer

It is also observed that longitudinal tensile strain is greater in June than that in February. Pavement surface temperature is 35.1 °C in June whereas that in February is 4.1 °C. Due to the temperature dependency, the AC modulus is low in June and high in February. Therefore, modulus variation inversely affects the variation in strain. It is also observed that the difference in longitudinal strain, at *n*-value of 0.25 and 1.0, is 20.65 microstrain in February whereas that in June is 37.63 micro-strain. This is due to the temperature difference between top and bottom of the AC layer. This temperature difference in June is 7.7 °C whereas that in February is 0.5 °C. Therefore, the modulus is the maximum in June and minimum in February.

Figure 4.5(b) shows the effect of AC cross-anisotropy on the transverse tensile strain at bottom of the layer. The similar type of trend is evident in case of transverse train. However, the transverse tensile strain is greater than the longitudinal strain. This is due to the distribution of vertical contact stress on single tire imprint area. The average ratio of transverse strain and longitudinal strain are 1.07 and 1.84 in February and June respectively.

The ratio of horizontal tensile strain considering cross-anisotropy and that considering isotropy are calculated for both longitudinal and transverse directions. i.e., e_{anis}/e_{iso} , where e_{anis} = cross-anisotropic strain and e_{iso} = isotropic strain. The strain ratio at varying cross-anisotropy and temperatures are plotted in Figure 4.6. Strain ratio decreases as the *n*-value increases towards isotropy (see Figure 4.6(a)). Strain is not affected significantly if the strain ratio is close 1.0. It is observed that the strain ratio is close to 1.0 at and above *n*-value of 0.75. Temperature effect is high at *n*-value of 0.25 and it diminishes as the *n*-value increases. The strain ratio is high at low temperature and vice versa.

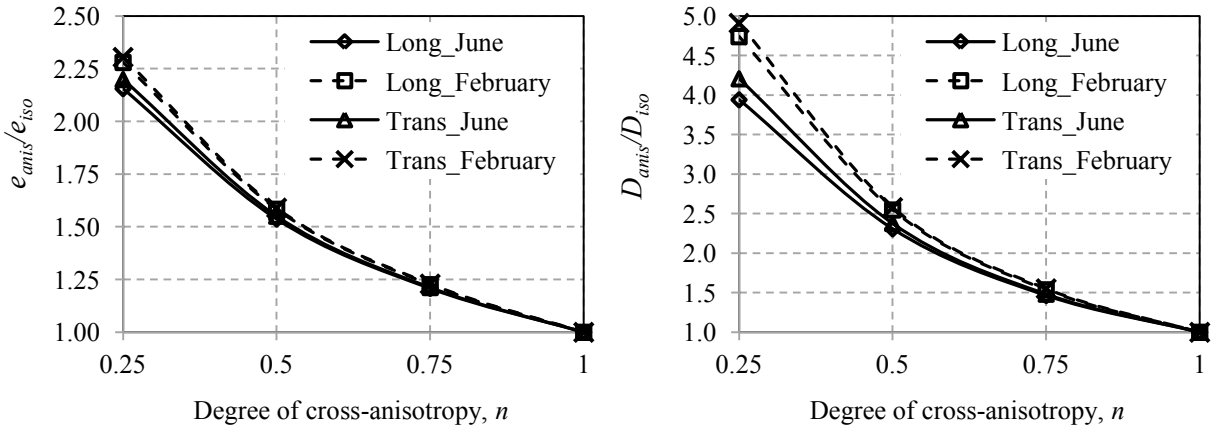

(a) Strain ratio (b) Damage

Figure 4.6 Effect of AC cross-anisotropy on tensile strain ratio and damage

Figure 4.6(b) shows the variation of damage per load repetition at varying cross-anisotropy and temperatures (eqn. 4.12). It is evident that the damage is the maximum at the smallest *n*-value and it drops rapidly with increase in *n*-value. Again, at and above n-value of 0.75, the damage is almost equal to 1.0. It indicates that fatigue damage is affected least whenever *n*-value is or above 0.75. Temperature effect on damage is high at smaller *n*-value which is due to the fact that damage is a function of strain ratio.

Is essence, both of the longitudinal and transverse horizontal tensile strain at bottom of the AC layer increase with the decreases in horizontal modulus of the AC. In addition, the transverse tensile strain is greater than the longitudinal strain. Tensile strain is also highly influenced by temperature variation due to temperature dependency of the AC modulus. Variation of tensile strain is high at high depth-temperature variation and vice versa. Finally, the fatigue damage due to cross-anisotropy is considerably greater than that due to isotropy at *n*-value of 0.25 which decreases rapidly as *n*-value increases and at or above *n*-value of 0.75, fatigue damage is least affected by the AC cross-anisotropy.

Vertical Strain in Pavement Layers

It is known that the rutting, i.e., permanent deformation, on pavement surface results from the vertical strain in pavement layers due to the repeated traffic. The vertical strains are determined on top of pavement layers, such as AC, base, subbase, and subgrade, from the dynamic simulation at varying *n*-values of the AC. Figure 4.7 shows the effect of AC cross-anisotropy on vertical strains in both February and June. Figure 4.7(a) shows that vertical strain on top of the AC layer is the maximum at the *n*-value of 0.25 and minimum at the *n*-value of 1.0 (isotropy).

The vertical strain decreases with increase in *n*-value in both February and June. Strain in June is greater than that in February due to temperature dependency of the AC modulus and the average strain ratio is 2.8. It is also observed that difference in vertical strain, due to *n*-value variation from 0.25 to 1.0, is higher in June than that in February. The vertical strain difference in June is 38.7 micro-strain whereas that in February is 12.3 micro-strain. It indicates that higher vertical strain is resulted from the higher temperature variation in the AC layer.

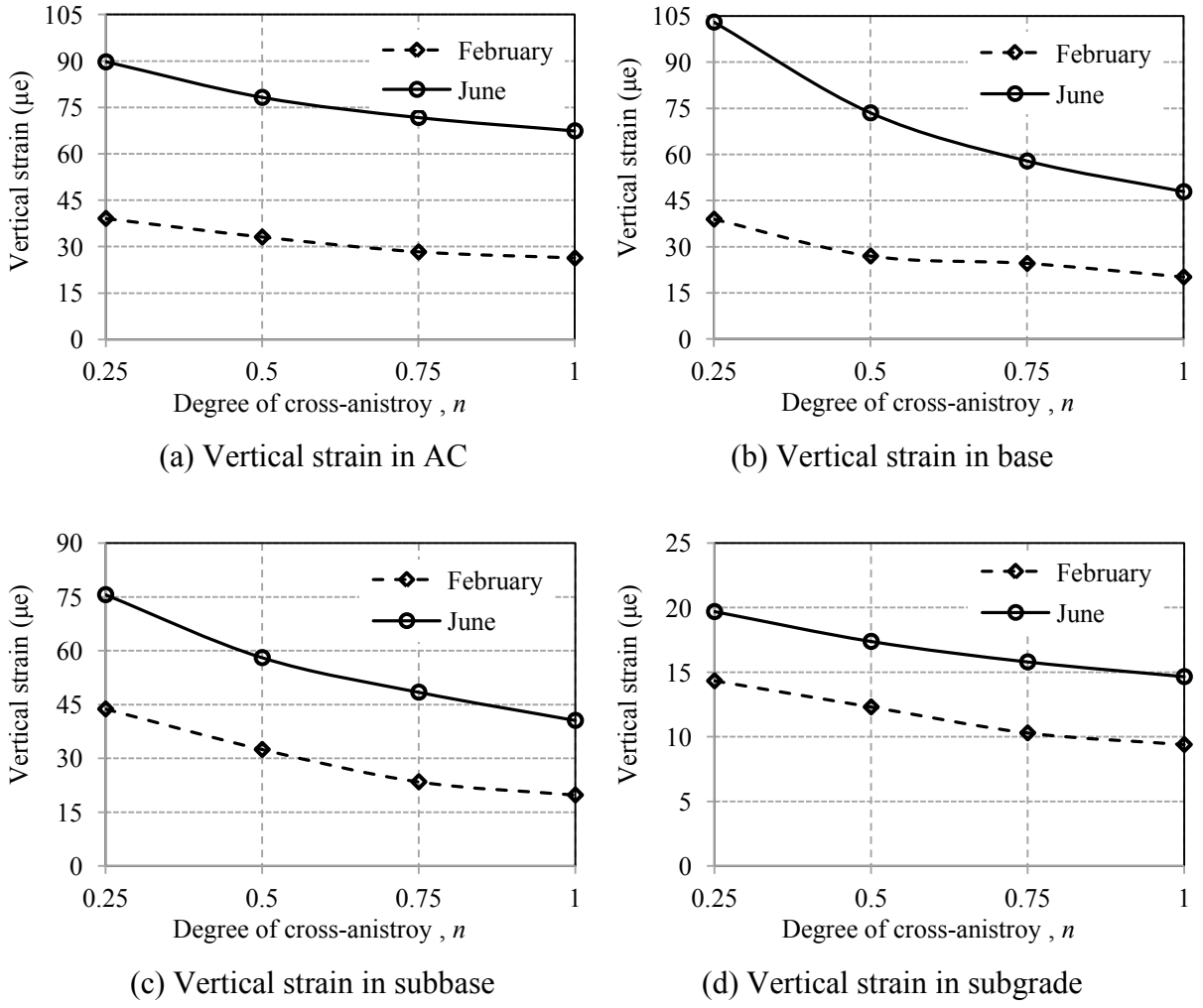

(a) Vertical strain in AC

(b) Vertical strain in base

(c) Vertical strain in subbase

(d) Vertical strain in subgrade

Figure 4.7 Effect of AC cross-anisotropy on vertical strain in pavement layers

Figure 4.7(b) shows the effect of AC cross-anisotropy variation on vertical strain on top of the base layer. The similar type of trend is observed in case of base layer. However, difference in maximum and minimum vertical strain in a specific month is even higher than that on top of the AC layer. The strain differences, due to n-value variation of the AC from 0.25 to 1.0, in June and February are 55.1 and 18.8 micro-strain respectively. This difference is due to the higher temperature variation in June and smaller temperature variation in February. It is also observed that the average ratio of the vertical on top of the base layer due to two different temperatures in June and February is 2.5.

In Figure 4.7(c), vertical strain on top of the subbase decreases with increase in *n*-value of the AC. In this case, differences in vertical strains, due to *n*-value variation from 0.25 to 1.0, in February and June become smaller. These strain differences are 24.0 and 35.0 micro-strain in February and June respectively. It indicates that the effect of temperature difference in top and bottom of the AC layer diminishes in case of vertical strain on top of the subbase. In case of subgrade, the similar effect of AC cross-anisotropy variation is evident on vertical strain (see Figure 4.7(d)). However, difference in vertical strain on top of the subgrade, due to *n*-value variation of the AC from 0.25 to 1.0, is about 5.0 micro-strain in both of the months. It indicates that the difference in vertical strain is not affected by the different depth-temperature variations. It is also observed that the vertical strain on top of the subgrade in June is about 1.5 times that in February.

The ratio of vertical strain considering cross-anisotropy and that considering isotropy are calculated for the pavement layers, namely, AC, base, subbase, and subgrade. The strain ratio at

varying cross-anisotropy and temperatures are plotted in Figure 4.8. Strain ratio decreases as the *n*-value increases towards isotropy (see Figure 4.8(a)). Strain is not affected significantly if the strain ratio is close 1.0. It is observed that the strain ratio is close to 1.0 at and above *n*-value of 0.75. Temperature effect is high at *n*-value of 0.25 and it diminishes as the *n*-value increases. The strain ratio is high at low temperature and vice versa.

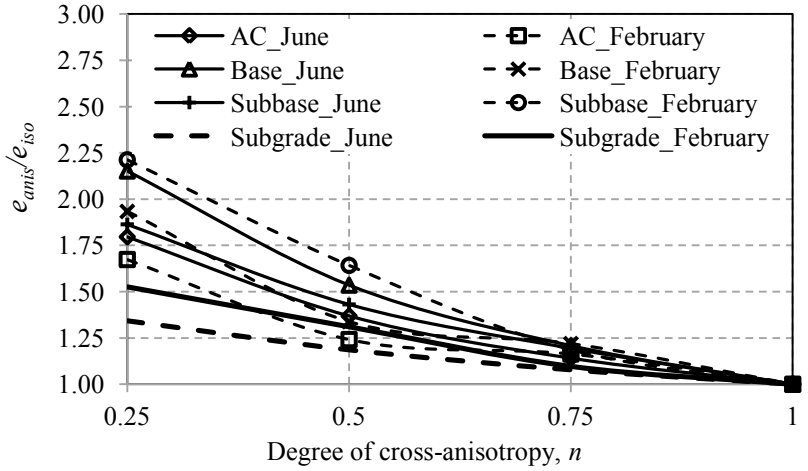

(a) Strain ratio

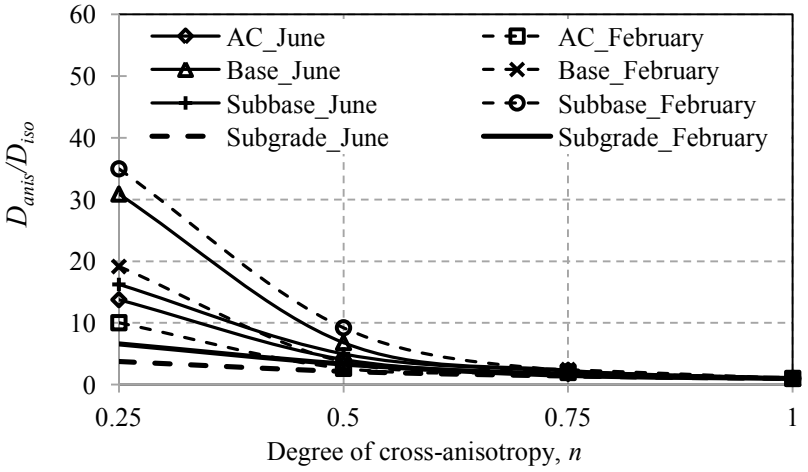

(b) Damage

Figure 4.8 Effect of AC cross-anisotropy on vertical strain ratios and damage

Figure 4.8(b) shows the variation of damage per load repetition at varying cross-anisotropy and temperatures (eqn. 4.13). It is evident that the damage is ratio is the maximum at the smallest *n*-value and it drops rapidly with increase in *n*-value. Again, at and above *n*-value of 0.75, the damage ratio is almost equal to 1.0. It indicates that fatigue damage is affected least whenever *n*-value is or above 0.75. Temperature effect on damage ratio is high at smaller *n*-value which is due to the fact that damage is a function of strain ratio.

Based on the discussion above, the vertical strain on top of the pavement layers increases due to decrease in horizontal AC modulus. The difference in vertical strain on top of the AC and base layer due to cross-anisotropic variation are highly sensitive to the depth-temperature in different months. The vertical strain is the maximum in June due to lower AC modulus and minimum in February due higher AC modulus. Damage ratio (cross-anisotropy vs. isotropy) based on permanent deformation becomes less affected by the AC cross-anisotropy above *n*-value of 0.75.

Vertical Stress in Unbound Layers

Effect of the AC cross-anisotropy on vertical stress on top of the unbound layers is investigated in this step (see Figure 4.9). Figure 4.9(a) shows the variation of vertical stress on top of the subgrade due to variation in *n*-value of the AC. Similar to the strain, vertical stress decreases with increase in *n*-value. The stress is the maximum if the material is considered isotropic, i.e., $n=1$. It is also affected by the temperature dependency of the AC modulus. In February, stress is small at low temperature whereas it is high at high temperature in June. At high temperature, the AC layer experiences greater amount of strain than that at low temperature in response to the

same vertical contact stress as applied by a truck tire. The higher is the vertical strain due to temperature dependency, the higher is the vertical stress on the base layer.

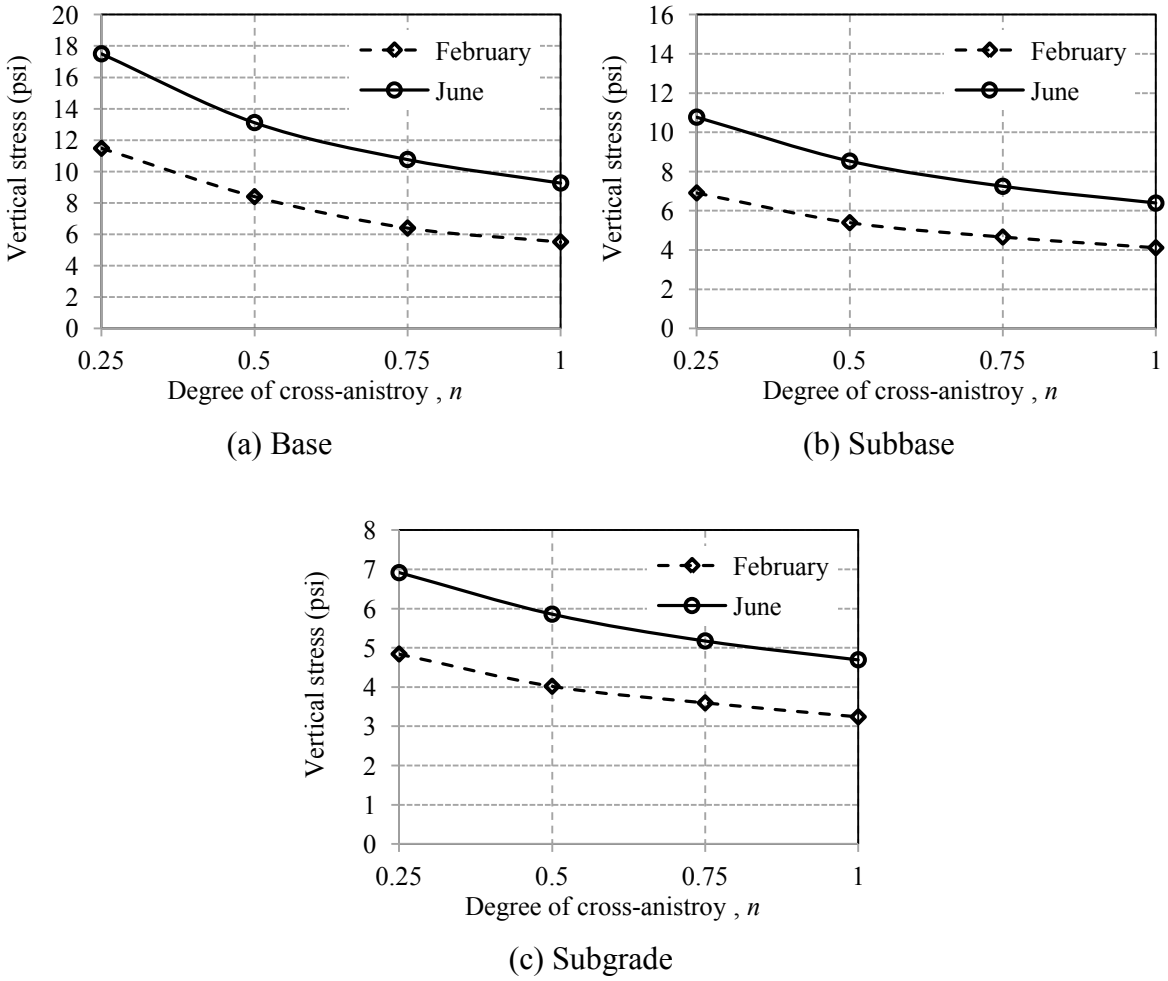

Figure 4.9 Effect of AC cross-anisotropy on vertical stress in unbound layers

Figure 4.9(b) and (c) also shows that vertical stress decrease with increase in *n*-value of the AC. However, difference in the stresses, between *n*-value of 0.25 and 1.0, gradually decreases in subbase and then, subgrade. The effect of temperature dependency on the AC layer also

gradually diminishes in subbase and subgrade. The vertical stress on top of the subbase and subgrade in February and June is smaller compared to the base layer.

The above discussion indicates that vertical stress decreases as the AC modulus is increasing towards the isotropy. In addition, effect of the temperature dependency of the AC on vertical stress in unbound layers diminishes with depth.

Differential vs. Average AC Temperature

In this study, differential temperature is assigned based on linear temperature variation over the depth of the AC layer which was measured in field (see Figure 4.10). Later, temperature dependency of AC modulus over depth is incorporated by integrating the depth-temperature variation and temperature-modulus correlation. However, the constant AC temperature is assigned based on averaging the temperature variation over the depth in the common practices (Wang and Al-Qadi 2013). It leads to a constant AC modulus over the depth. It is necessary to investigate the level of accuracy in pavement responses achieved from the incorporation of differential temperature over the depth. Incorporation of depth-temperature will be strongly recommended if the difference between the FEM simulated strains considering differential and constant temperature over the depth is considerably high.

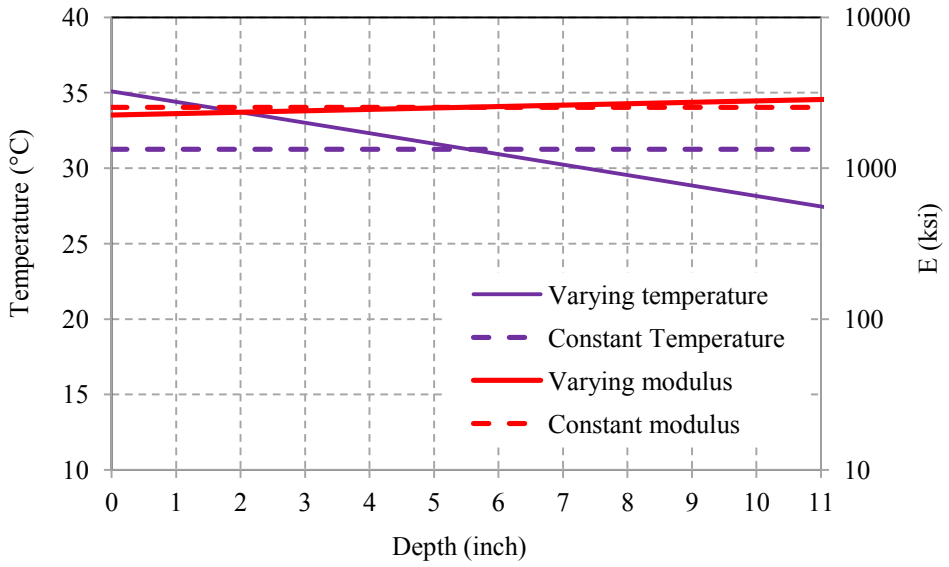

Figure 4.10 Variation of AC modulus with pavement temperature

The dynamic FEM simulation is also performed at average AC temperature of 31.25 °C by varying *n*-values incorporating both of the differential and constant temperature over the depth of the AC layer. Horizontal tensile strains at the bottom of the AC layer in both transverse and longitudinal directions at varying *n*-values are summarized in Table 4.7. The (%) Error is calculated to evaluate the level of accuracy. In both of the cases, (%) error is very low which indicates that incorporation of depth-temperature variation over the AC depth does not enhance accuracy level during prediction of horizontal strains.

Table 4.7 Comparison of horizontal tensile strain (transverse vs. longitudinal)

n-value	Transverse strain			Longitudinal strain		
	T_{diff}	T_{avg}	(%) Error	T_{diff}	T_{avg}	(%) Error
0.25	77.2	76.3	1.23	70.2	69.4	1.19
0.5	54.4	53.8	1.22	50.1	49.4	1.23
0.75	42.6	42.0	1.22	39.3	38.9	1.19
1	35.1	34.7	1.19	32.6	32.2	1.16

The (%) error is also calculated for vertical strains in AC, base, subbase, and subgrade (Table 4.8). It is observed that (%) error is relatively high in AC layer. However, in unbound layers, it is very low. Based on the overall observation, it can be said that considering differential temperature or constant temperature over the depth of the AC layer leads to very close prediction of pavement responses.

Table 4.8 Comparison of vertical strain in pavement layers

Layer	*n*-value	T_{diff}	T_{avg}	(%) Error
AC	0.25	87.4	84.0	3.81
	0.5	66.6	63.3	4.91
	0.75	55.5	52.3	5.78
	1	48.6	45.5	6.52
Base	0.25	103.0	103.2	0.20
	0.5	73.5	73.8	0.34
	0.75	57.8	58.0	0.20
	1	47.9	48.1	0.50
Subbase	0.25	75.6	76.0	0.47
	0.5	58.1	58.6	0.93
	0.75	48.4	48.7	0.59
	1	40.6	41.7	2.83
Subgrade	0.25	19.7	19.7	0.20
	0.5	17.4	17.4	0.17
	0.75	15.8	15.8	0.23
	1	14.7	14.7	0.07

4.5 Summary of parametric study

In the earlier steps, a parametric study is performed to investigate the effect of AC cross-anisotropic variation on pavement responses and damage. In addition, it is investigated whether incorporation of temperature variation over depth can enhance the level of accuracy in pavement analysis. Outcomes of the parametric study are summarized in Table 4.9.

Table 4.9: Summary of parametric study (AC cross-anisotropy)

Response	Parameter variation	Observation	Comment
Tensile strain at the bottom of the AC	• AC temperature: 4.1 °C • n_{AC} : 0.25-1.0 • AC temperature: 35.1 °C • n_{AC} : 0.25-1.0	• Strain is the maximum at *n*-value of 0.25 • Strain decreases as *n*-value increases towards isotropy (*n*=1.0) • Transverse strain is greater than longitudinal strain • Strain is high at high temperature and small at low temperature	• Tensile strain at the bottom of the AC layer is high whenever AC is cross-anisotropic • Strain is sensitive to AC temperature variation
Fatigue damage (D_{anis}/D_{iso}) due to tensile strain	• AC temperature: 4.1 °C • n_{AC} : 0.25-1.0 • AC temperature: 35.1 °C • n_{AC} : 0.25-1.0	• D_{anis}/D_{iso} is the maximum at *n*-value of 0.25 • D_{anis}/D_{iso} decreases as *n*-value increases towards isotropy (*n*=1.0) • D_{anis}/D_{iso} is high at low temperature	• Damage due to cross-anisotropy is greater than that due to isotropy • Damage due to cross-anisotropy is enhanced at low temperature
Vertical strain in AC	• AC temperature: 4.1 °C • n_{AC} : 0.25-1.0 • AC temperature: 4.1 °C • n_{AC} : 0.25-1.0	• Strain is the maximum at *n*-value of 0.25 • Strain decreases as *n*-value increases towards isotropy (*n*=1.0) • Strain is high at high temperature and small at low temperature	• Vertical strain in the AC layer is high whenever AC is cross-anisotropic • Strain is sensitive to AC temperature variation
Vertical strain in base	• AC temperature: 4.1 °C • n_{AC} : 0.25-1.0 • AC temperature: 4.1 °C • n_{AC} : 0.25-1.0	• Strain is the maximum at *n*-value of 0.25 • Strain decreases as *n*-value increases towards isotropy (*n*=1.0) • Strain is high at high temperature and small at low temperature	• Vertical strain in the base layer is high whenever AC is cross-anisotropic • Strain is sensitive to AC temperature variation
Vertical strain in subbase	• AC temperature: 4.1 °C • n_{AC} : 0.25-1.0 • AC temperature: 4.1 °C • n_{AC} : 0.25-1.0	• Strain is the maximum at *n*-value of 0.25 • Strain decreases as *n*-value increases towards isotropy (*n*=1.0) • Strain is high at high temperature and small at low temperature	• Vertical strain in the subbase layer is high whenever AC is cross-anisotropic • Strain is sensitive to AC temperature variation
Vertical strain in subgrade	• AC temperature: 4.1 °C • n_{AC} : 0.25-1.0 • AC temperature: 4.1 °C • n_{AC} : 0.25-1.0	• Strain is the maximum at *n*-value of 0.25 • Strain decreases as *n*-value increases towards isotropy (*n*=1.0) • Strain variation in subgrade is relatively small	• Vertical strain in the subbase layer is high whenever AC is cross-anisotropic • Strain variation is relatively small compared to base & subbase layers
Damage due to permanent deformation (AC, base, subbase & subgrade)	• AC temperature: 4.1 & 35.1 °C respectively • n_{AC} : 0.25-1.0	• Damage is the maximum at *n*-value of 0.25 • Damage decreases as *n*-value increases towards isotropy (*n*=1.0) • Damage varies with AC temperature	• Damage due to cross-anisotropy is greater than that due to isotropy • Damage due to cross-anisotropy is sensitive to temperature variation
Depth-temperature variation	• Differential temperature • Constant temperature	• Insignificant error	• Incorporation of depth-temperature profile does not enhance the level of accuracy

4.6 Summary

In the preliminary phase, the dynamic FEM is developed in ABAQUS/Explicit to investigate the effect of AC cross-anisotropy on pavement stress-strain. It is observed that the tensile strain at the bottom of the AC layer is sensitive to the AC cross-anisotropy variation. It is also observed that rectangle-semi-circle shaped loading area yields pavement stress-strain much closer to that measured in field. Based on the observation and recommendation, the next phase of this study is performed and the following conclusions are made based on the outcomes:

- The horizontal tensile strain at bottom of the AC layer decreases as the *n*-value increases, i.e., increase in horizontal AC modulus, towards the isotropy. It is also observed that the transverse tensile strain is greater than the longitudinal tensile strain. Both longitudinal and transverse strains are highly sensitive to the temperature variation.
- The vertical strains on top of the pavement layers such as AC, base, subbase, and subgrade also increases as the *n*-value increases, i.e., increase in horizontal AC modulus, towards the isotropy. These strains are also sensitive to the temperature variation.
- Damage ratio of cross-anisotropic and isotropic based on both fatigue and permanent deformation is calculated using the Miner's damage formula. It shows that damage ratio based on both of the criteria decreases as the *n*-value increases and it becomes very small at or above *n*-value of 0.75. Damage ratio is highly sensitive to temperature variation at *n*-value of 0.25 and diminishes rapidly towards the isotropy.
- Both horizontal and vertical strains are calculated from the FEM simulation considering varying as well as constant (average) temperature over the depth of the AC layer. It is observed that incorporation of constant temperature leads to very small amount of error.

Therefore, constant or averaged temperature can be used in pavement analysis with reasonable accuracy.

CHAPTER 5

UNBOUND LAYER CROSS-ANISOTROPY

5.1 General

Effect of the unbound layer cross-anisotropy on the pavement response is evaluated in this chapter. In addition to cross-anisotropy, the stress-dependency of the unbound layer is incorporated to the dynamic FEM. During this study, the AC cross-anisotropy is ignored.

5.2 Outline

This study focuses on the combined effect of cross-anisotropy of unbound layers, such as base, subbase, and subgrade, and AC temperature on pavement stress-strain. Figure 5.1 shows the outline of the study. In this stage of the study, AC cross-anisotropy is ignored which indicates that *n*-value of the AC is not be varied. Average AC temperature is incorporated to the model to address the temperature-dependency. A uniform vertical contact stress is applied for the FEM simulations. Finally, the simulations are performed at varying *n*-values of unbound layers one be one.

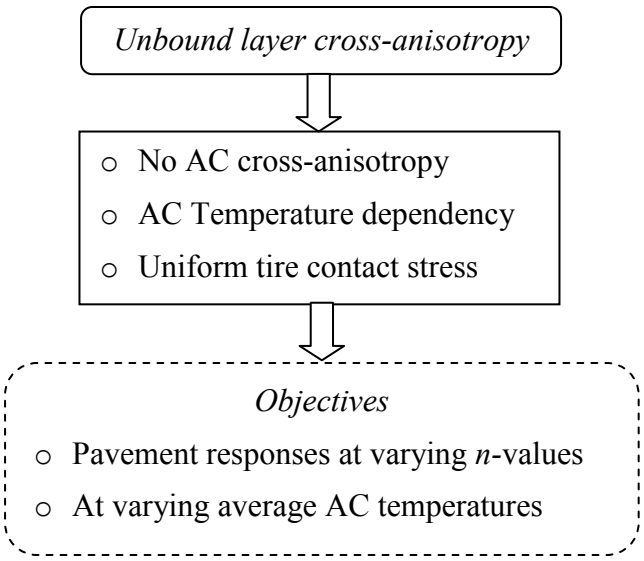

Figure 5.1 Outline of the study

5.3 Model Description

The model geometry is similar to the geometry in Figure 3.4. Preliminary boundary condition, i.e., BC 1 (see Figure 3.5), is also assigned where the bottom of the geometry is restrained to move along both vertical and horizontal directions. In addition, the vertical planes are restrained to move along horizontal direction. The layer interfaces are considered partially-bonded and coulomb friction law is used to model the contact between the interfaces. The friction coefficients along layer interfaces in AC are 0.7. Mesh is generated over the geometry according to the method as discussed in section 3.7. The minimum dimension of an element is 0.6 in. Assignment of layer materials to the model is described below:

The AC is assumed as isotropic and viscoelastic. Among the unbound layers, the base is considered as nonlinear elastic and stress-dependent. The dynamic modulus test was conducted to determine the Prony series parameters and instantaneous modulus**.** The instantaneous moduli

(*E*) at different temperatures are summarized in Table 5.1. Instantaneous moduli at different temperatures are incorporated to the dynamic FEM whenever stress-strain are determined form the simulations at these temperatures. The Poisson's ratio is 0.3 which is same in all directional planes.

Table 5.1 Instantaneous modulus at different temperatures

Temperature (°C)	Instantaneous modulus (ksi)
12.3	1134.8
25.3	825.1
33.3	543.6

The Prony series coefficients are determined from the relaxation modulus variation as converted from the dynamic values at different frequencies and temperatures (see Table 5.2).

Table 5.2 Prony series coefficient (unbound layer cross-anisotropy)

i	e_i	τ_i
1	0.2	1.1
2	0.2	4.7
3	0.15	9.75
4	0.15	100
5	0.1	250
6	0.1	470

The stress-dependency of the base layer was characterized by the laboratory resilient modulus test according to the AASHTO T307-99 as mentioned earlier. The generalized model as adopted in the newly developed Mechanistic Empirical Pavement Design Guide (MEPDG) is used in this study to incorporate base nonlinearity to the model. The model is as below:

$$M_r = k_1 p_a \left(\frac{\theta}{p_a} \right)^{k_2} \left(\frac{\tau_{oct}}{p_a} + 1 \right)^{k_3} \tag{5.1}$$

where $\theta =$ bulk stress, $\tau_{oct} =$ octahedral shear stress, $p_a =$ atmospheric pressure, and $k_1, k_2, k_3 =$ regression coefficients that need to be determined from laboratory resilient modulus test. The regression coefficients of base material were determined from laboratory measured resilient modulus at different loading sequences. The values of these coefficients are determined to be 5384, 0.15, and 0.75 respectively. This stress-dependency of the base layer is incorporated to the dynamic FEM using User Defined Material (UMAT) interface available in ABAQUS.

The moduli of elasticity of subbase and subgrade are predicted from the backcalculation of FWD test data. The FWD test was conducted on the instrumented pavement section at the selected locations where the sensors were installed. Table 5.3 summarizes the parameters of the unbound layers which are required for the dynamic FEM. Both of the density and Poisson's ratio are summarized in addition to the layer moduli.

Table 5.3 Backcalculated moduli of the unbound layers

Layer	E (ksi)	ρ (pcf)	ν_{vh}
Base	Nonlinear	135	0.4
Subbase	91	120	0.4
Subgrade	25	110	0.45

In this stage, depth-temperature variation over the depth of the AC layer is ignored. Instead, the average AC temperature is assigned to the model to evaluate the temperature-dependency on pavement response. The earlier mentioned two different types of loads applied to simulate the

dynamic FEM: FWD and wheel load. The wheel load is assigned by the application of uniform vertical contact stress over a rectangle-semi circle shape of tire imprint area. This shape is selected since it was observed that the load over this shape yields better prediction of stress-strain. Duration of the wheel load is shown and described in Figure 3.22 and related discussion.

The dynamic simulation is performed in the ABAQUS/Implicit to ensure unconditional stability. As mentioned earlier, another important issue related to a dynamic analysis is damping which is assigned to this model according to the method as described in section 3.9. For the parametric study, Table 5.4 is followed as an analysis matrix to perform the FEM simulations. A total of 27 simulations are performed under wheel load. In addition, simulation is performed under FWD test load at three different temperatures for comparison between simulated and measured pavement responses.

Table 5.4 Analysis matrix of FEM simulation under wheel load

n-value	Base			Subbase			Subgrade		
	12.3 ºC	25.3 ºC	33.3 ºC	12.3 ºC	25.3 ºC	33.3 ºC	12.3 ºC	25.3 ºC	33.3 ºC
0.5	X	X	X	X	X	X	X	X	X
0.75	X	X	X	X	X	X	X	X	X
1.0	X	X	X	X	X	X	X	X	X

5.4 Analysis and Discussion

5.4.1 Horizontal Strain

The time-history of the horizontal strain is determined at the bottom of AC layer from the dynamic FEM simulation at different temperatures by varying *n*-values of the unbound layers. A study by Garcia and Thompson (2008) shows that transverse strain is 1.5 times the longitudinal

strain. Therefore, this horizontal strain is determined along transverse to the traffic direction. The peak strain is obtained from the time-history of horizontal strain. In FEM simulations, whenever the *n*-value of an unbound layer is varied, the *n*-values of the other layers are kept constant. This type of variation is repeated for base, subbase, and subgrade. In addition to cross-anisotropy variation of individual layer, *n*-values are varied for all the unbound layers together. In this study, it is referred as combined cross-anisotropy variation.

Figure 5.2(a) shows the effect of base layer cross-anisotropy on the strain at the bottom of AC layer. At a specific temperature such as 12.3 °C, the AC strain increases gradually with increase in *n*-value. Similar trend is observed at the temperature of 25.3 °C. However, at the temperature of 33.3 °C, the rate of increase in strain is very low. The AC strain also increases with temperature. This is due to the reduction of AC stiffness at high temperatures. At n,b=1, the change in strain is about 26.5 microstrain increasing from 12.3 °C to 33.3 °C. This trend is fairly similar for the *n*-values of 0.5 and 0.75. In case of the subbase (PPC) cross-anisotropy, Figure 5.2(b) shows that the strain increases with temperature whereas the strain deceases with increase in *n*-value at a certain temperature. This is due to the increase in modulus of elasticity along the horizontal direction.

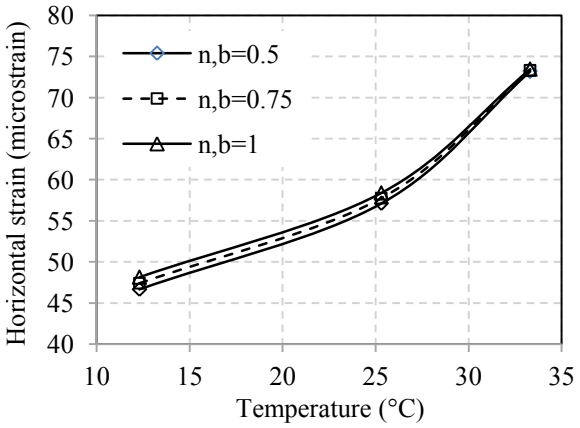

(a) Base cross-anisotropy

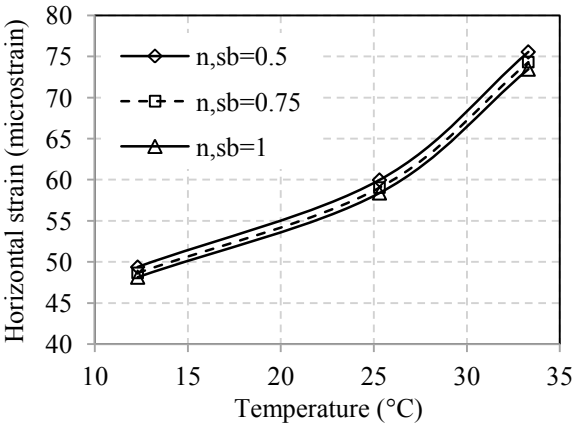

(b) Subbase cross-anisotropy

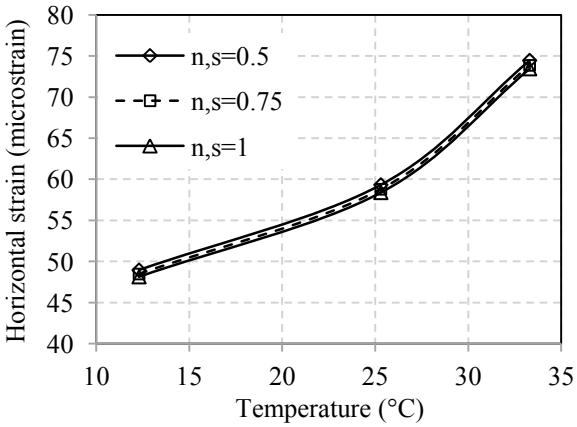

(c) Subgrade cross-anisotropy

Figure 5.2 Effect of cross-anisotropy on tensile strain at the bottom of AC

The effect of the subgrade cross-anisotropy on the AC layer transverse horizontal strain is shown in Figure 5.2(c). The strain slightly decreases with the increase in *n*-value. The variation of strain with change in temperature is still dominant.

The ratios of horizontal tensile strain considering cross-anisotropy to isotropy are calculated for both longitudinal and transverse directions. The strain ratio at varying cross-anisotropy and temperatures are plotted in Figure 5.3. Strain ratio increases as the *n*-value of the base layer

increases towards isotropy (see Figure 5.3(a)). Strain ratios of the other unbound layers are barely affected the *n*-value variation. Temperature shows very little effect on strain ratios at *n*-value of 0.25 and it diminishes as the *n*-value increases.

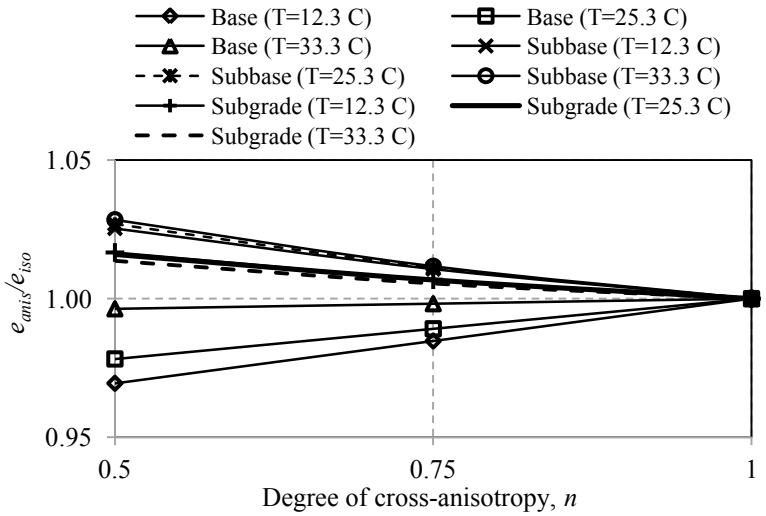

(a) Strain ratio

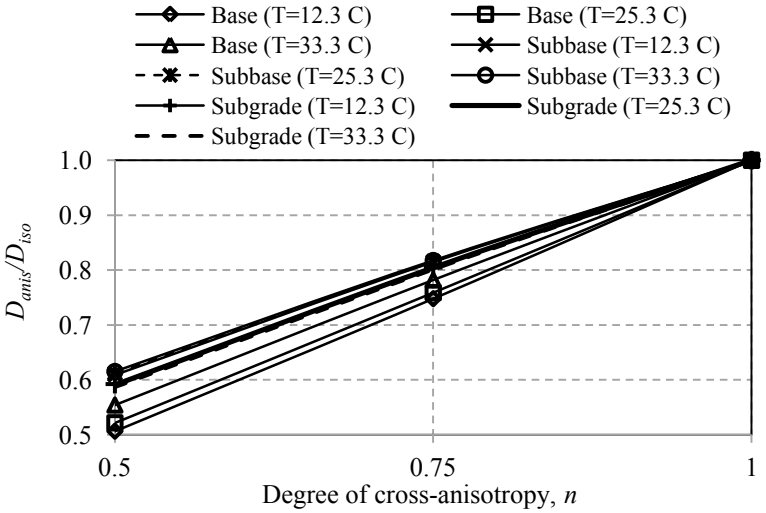

(b) Damage

Figure 5.3 Tensile strain ratios and damage in AC

Figure 5.3(b) shows the variation of damage at varying cross-anisotropy and temperatures (eqn. 4.12). It is evident that the damage is ratios are the minimum at the smallest *n*-value and it increases with increase in *n*-value. This trend is opposite to the AC cross-anisotropy. Damage ratios due to base and subbase cross-anisotropy are affected by temperature variation. However, this ratio due to subgrade cross-anisotropy is very little to not affect by temperature variation.

5.4.2 Vertical Strain

The vertical strains are determined at the middle of AC, base, and subbase layer. In the case of subgrade, it is determined at the top. The peak vertical strains are obtained from the time-histories. The *n*-values of the other layers are kept constant whenever the *n*-value of an unbound layer is varied.

Figure 5.4(a) through (c) show the effect of cross-anisotropy on vertical strain in AC layer. Figure 5.4(a) shows that the vertical strain in the AC layer increases rapidly with temperature. It is found to be insensitive to the variation of the *n*-value of the base layer at 12.3 °C and 25.3 °C. In Figure 5.4(b), the AC strain is fairly constant at all the *n*-values of the subbase layer at different temperatures. Figure 5.4(c) shows that this trend is also true for the subbase cross-anisotropy. In summary, it is observed that vertical strain of the AC layer is barely affected by the cross-anisotropy of unbound layers. It indicates that only temperature affects the permanent deformation in AC layer.

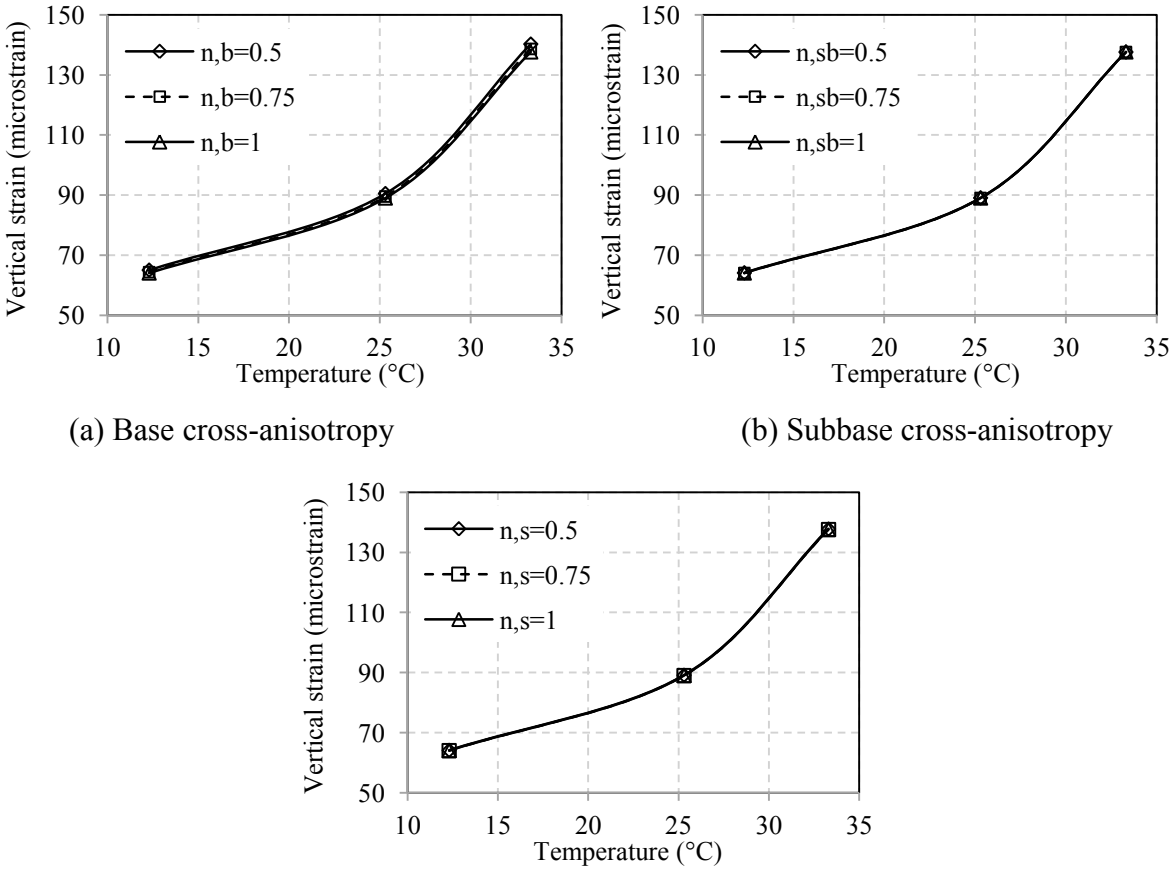

(a) Base cross-anisotropy

(b) Subbase cross-anisotropy

(c) Subgrade cross-anisotropy

Figure 5.4 Effect of cross-anisotropy on vertical strain in AC

The ratios of vertical strain in the AC layer, considering cross-anisotropy and that considering isotropy are calculated. The strain ratios at varying cross-anisotropy and temperatures are plotted in Figure 5.5. It is observed that these ratios are very little to not sensitive to variation in base layer cross-anisotropy (see Figure 5.5(a)). Temperature variation does not have any effect on these ratios.

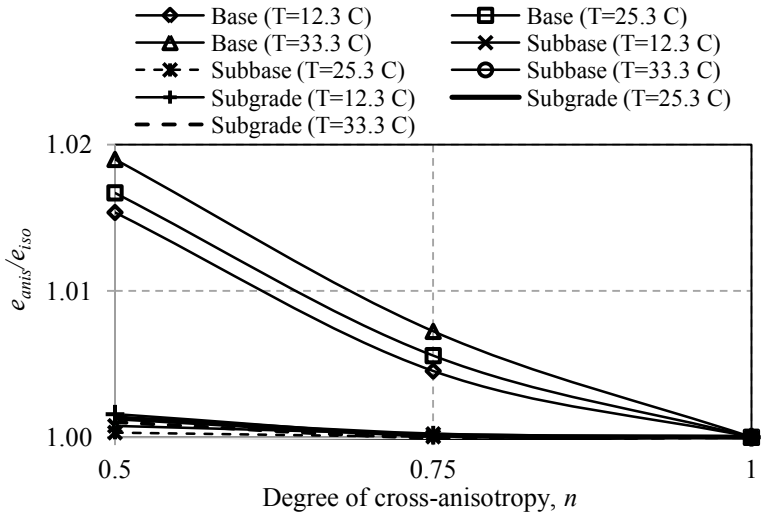

(a) Strain ratio

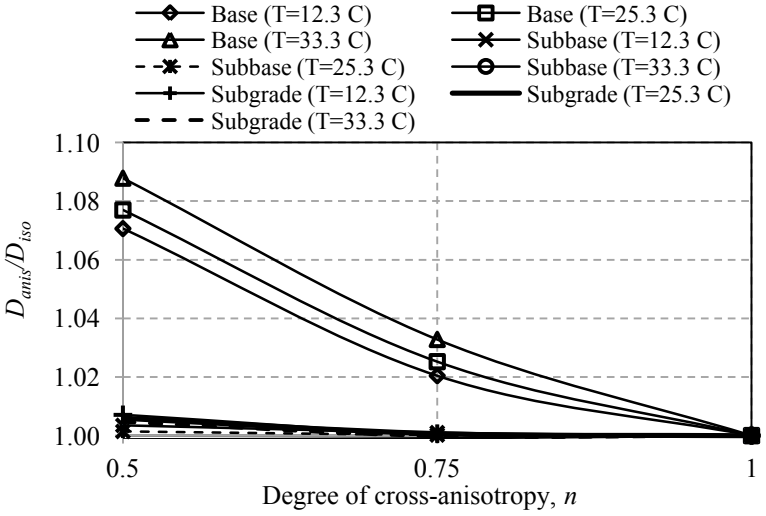

(b) Damage

Figure 5.5 Vertical strain ratios and damage in AC

Figure 5.5(b) shows the variation of damage based on permanent deformation in the AC layer at varying cross-anisotropy and temperatures (eqn. 4.13). It is observed that the damage ratio due to base layer cross-anisotropy decrease with increase in *n*-values. However, this ratio is not sensitive to cross-anisotropic variation in other unbound layers, such as subbase and subgrade.

This trend is opposite to the AC cross-anisotropy. Damage ratios due base and subbase cross-anisotropy are affected by temperature variation. However, this ratio due to subgrade cross-anisotropy is barely affected by temperature variation.

Figure 5.6(a) through (c) show the effect of cross-anisotropy on vertical strain in the base layer. In Figure 5.6(a), it is observed that the base vertical strain is significantly affected by the *n*-value variation of the base layer. Figure 5.6(b) shows that the base vertical strain is also affected by the subbase cross-anisotropy. In case of the subgrade cross-anisotropy, the base vertical strain is slightly influenced by *n*-values as shown in Figure 5.6(c). In all these cases, vertical strain is sensitive to temperature variation. Therefore, in addition to temperature, permanent deformation in base layer is highly sensitive to base layer cross-anisotropy.

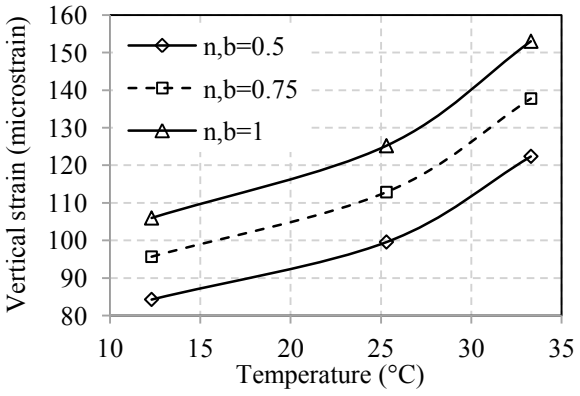

(a) Base cross-anisotropy

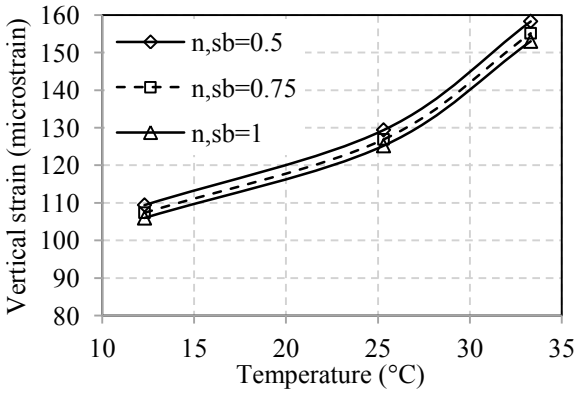

(b) Subbase cross-anisotropy

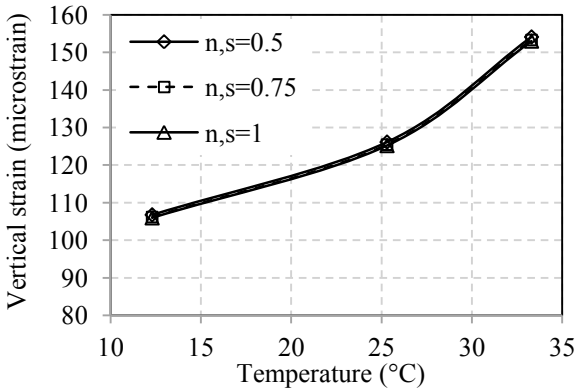

(c) Subgrade cross-anisotropy

Figure 5.6 Effect of cross-anisotropy on vertical strain in base

The ratios of vertical strain in the base layer, considering cross-anisotropy and that considering isotropy are calculated. The strain ratios at varying cross-anisotropy and temperatures are plotted in Figure 5.7. It is observed that strain ratios in base layer increase with increase in *n*-value of base layer (see Figure 5.7(a)). However, strain ratio decreases slightly with increase in *n*-value of base layer. It is also observed that temperature variation does not have any effect on these strain ratios.

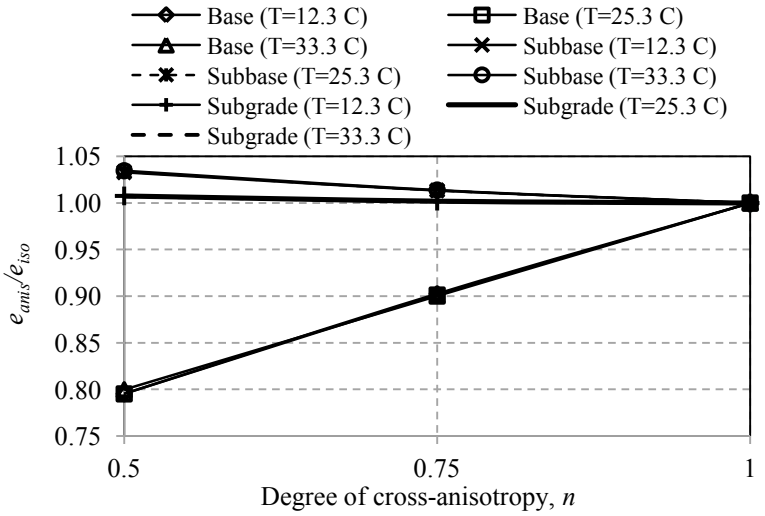

(a) Strain ratio

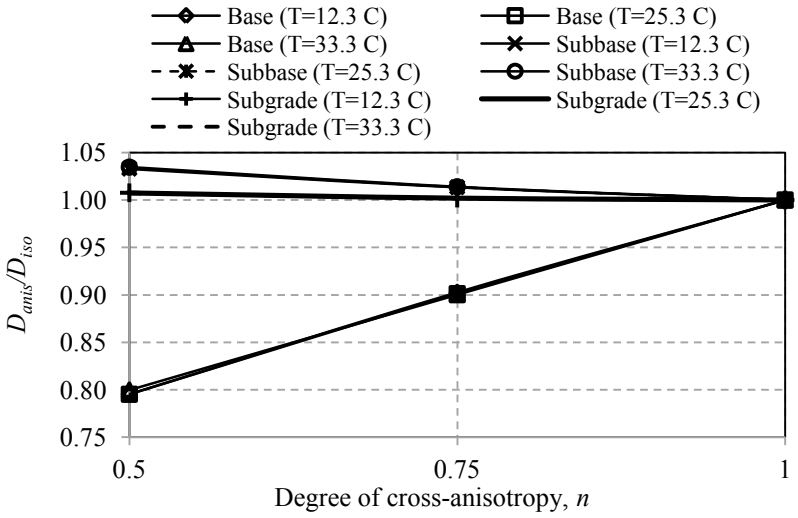

(b) Damage

Figure 5.7 Vertical strain ratios and damage in base

Figure 5.7(b) shows the variation of damage based on permanent deformation in the base layer at varying cross-anisotropy and temperatures (eqn. 4.13). It is observed that the damage ratio due to base layer cross-anisotropy decrease with increase in *n*-values. However, this trend is opposite in case of subbase. Damage ratios are nearly insensitive to the subgrade cross-anisotropy.

Figure 5.8(a) through (c) show the effect of cross-anisotropy on vertical strain in the subbase layer. Figure 5.8(a) shows that the vertical strain in the subbase layer is slightly affected by the cross-anisotropy of the base layer. Compared to the base cross-anisotropy, the subbase cross-anisotropy is more pronounced. The vertical subbase strain increases with an increase in *n*-value as shown in Figure 5.8(b). In case of subgrade cross-anisotropy, subbase strain varies with *n*-values as shown in Figure 5.8(c). Finally, it is observed that the vertical strain in subbase is mostly affected by the cross-anisotropy of subbase in addition to the temperature variation.

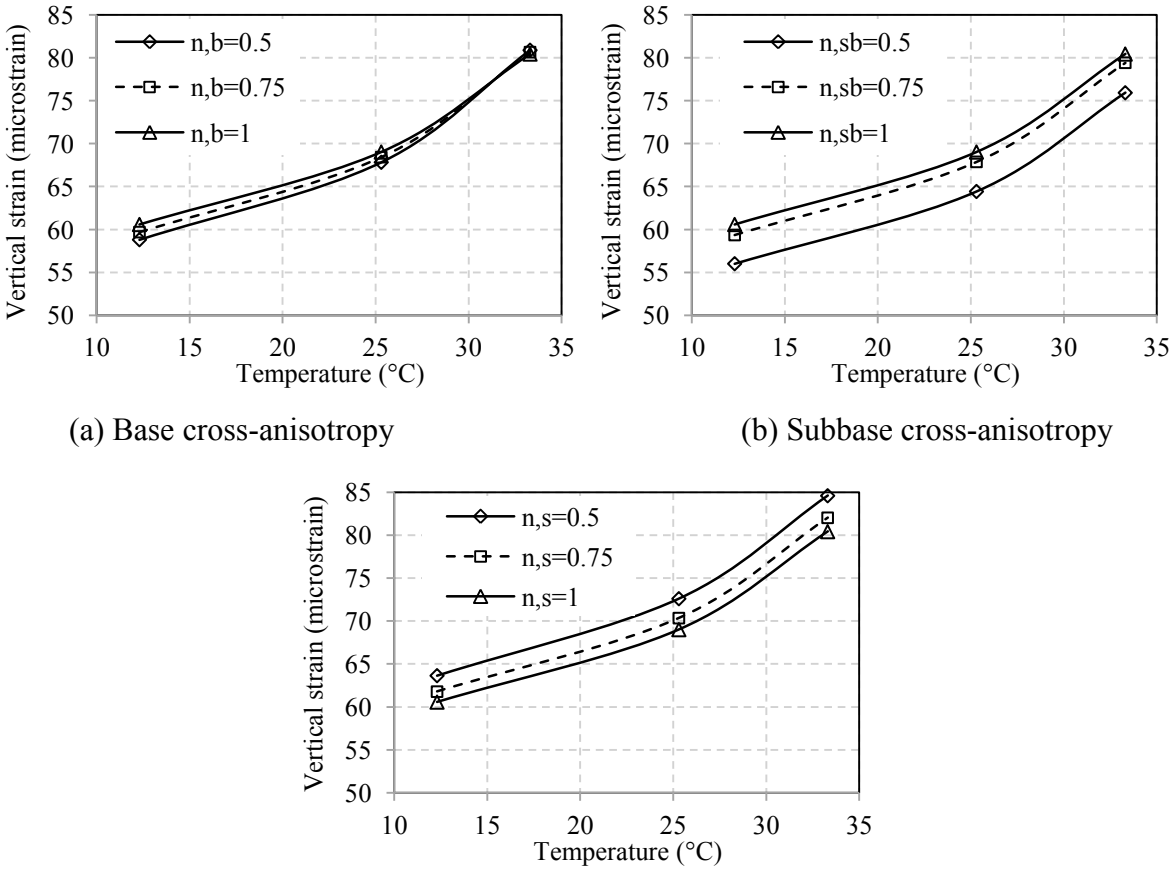

(a) Base cross-anisotropy

(b) Subbase cross-anisotropy

(c) Subgrade cross-anisotropy

Figure 5.8 Effect of cross-anisotropy on vertical strain in subbase

The ratios of vertical strain in the subbase, considering cross-anisotropy and that considering isotropy are calculated. The strain ratios at varying cross-anisotropy and temperatures are plotted in Figure 5.9. It is observed that strain ratios in subbase layer with increase in *n*-values of both of the base and base layers (see Figure 5.9(a)). However, strain ratio decreases slightly with increase in *n*-value of subgrade. It is also observed that temperature variation affects the strain ratios slightly in case of base and subbase cross-anisotropy.

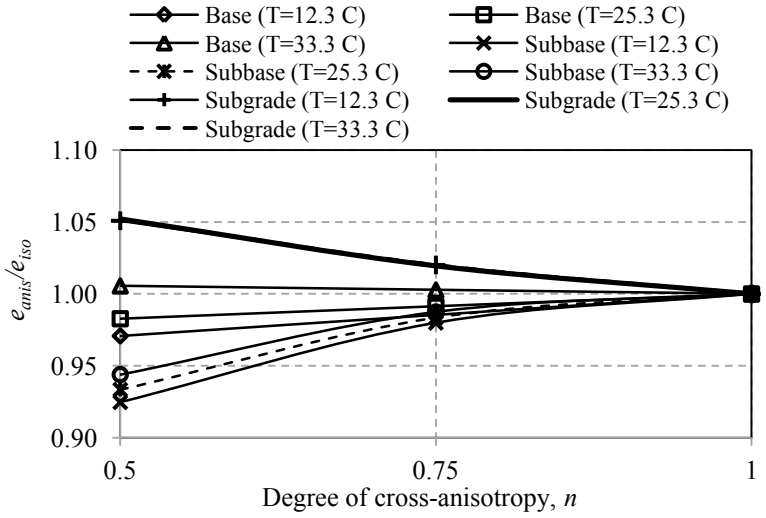

(a) Strain ratio

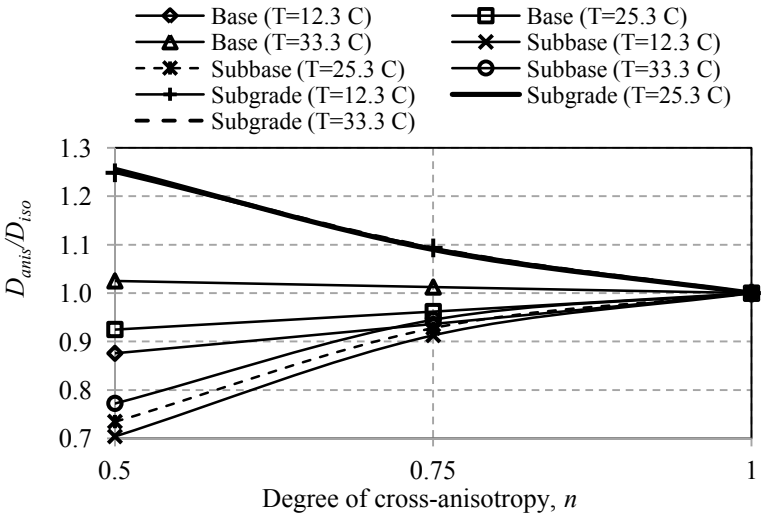

(b) Damage

Figure 5.9 Vertical strain ratios and damage in subbase

Figure 5.9(b) shows the variation of damage based on permanent deformation in the subbase at varying cross-anisotropy and temperatures (eqn. 4.13). It is observed that the damage ratio due to subbase layer cross-anisotropy increase with increase in *n*-values of base and subbase. However, this trend is opposite in case of subgrade cross-anisotropy variation. It is also observed that damage ratios due to base and subbase cross-anisotropy are sensitive to temperature variation.

Figure 5.10(a) through (c) show the effects of cross-anisotropy on vertical strain on top of the subgrade. Figure 5.10(a) shows that subgrade strain is highly sensitive to the *n*-values of base. The subgrade strain decreases abruptly as the *n*-value of subgrade approaches to isotropy, i.e., $n,s=1$. In Figure 5.10(b), it is observed that the subgrade strain is less sensitive to the subbase cross-anisotropy compared to the case of base cross-anisotropy. Figure 5.10(c) shows that the subgrade vertical strain is also affected by *n*-values of subgrade. In summary, it is obvious that the base cross-anisotropy has a dominant effect on the vertical strain on top of the subgrade. Temperature does not have a pronounced effect on this strain as compared to the earlier cases. Therefore, base layer cross-anisotropy may play an important role in the permanent deformation in subgrade.

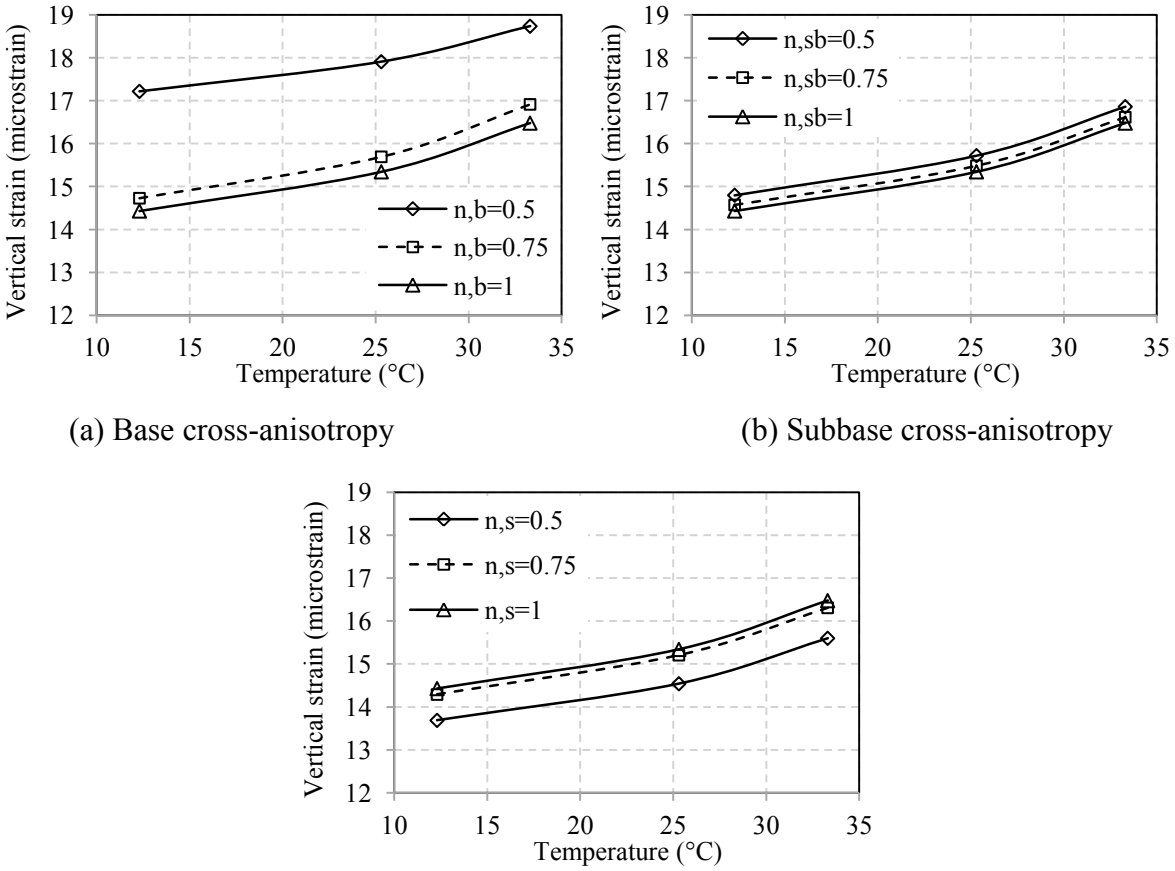

(a) Base cross-anisotropy

(b) Subbase cross-anisotropy

(c) Subgrade cross-anisotropy

Figure 5.10 Effect of cross-anisotropy on vertical strain in subgrade

The ratios of vertical strain in the subgrade considering cross-anisotropy to isotropy are calculated. The strain ratios at varying cross-anisotropy and temperatures are plotted in Figure 5.11. It is observed that strain ratios in subgrade decreases with increase in *n*-value of base layer which is opposite to that due to variation in *n*-value of subgrade (see Figure 5.11(a)). It is also observed that temperature variation has very little effect on the strain ratios whenever *n*-value of base is 0.5.

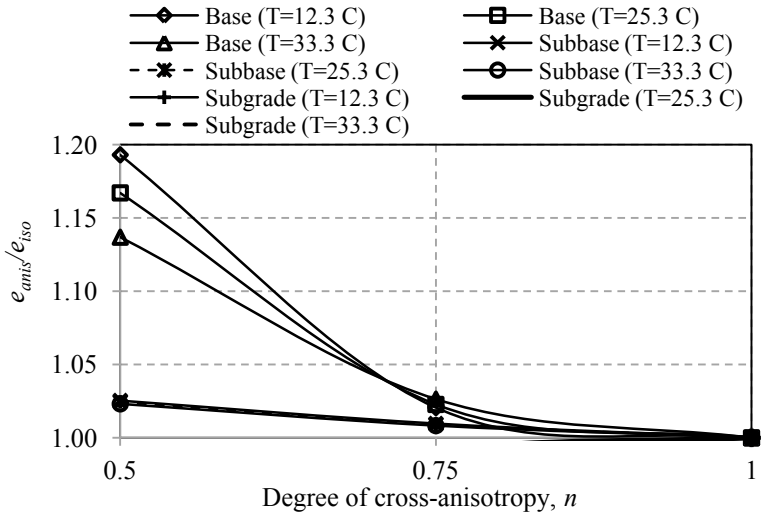

(a) Strain ratio

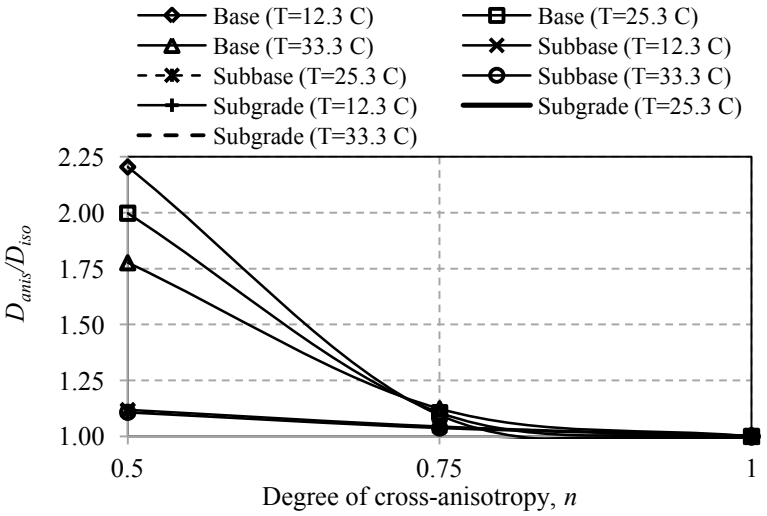

(b) Damage

Figure 5.11 Vertical strain ratios and damage in subgrade

Figure 5.11(b) shows the variation of damage based on permanent deformation in the subgrade at varying cross-anisotropy and temperatures (eqn. 4.13). It is observed that the damage ratio in subgrade decreases with increase in *n*-values base. However, this trend is opposite in case of subgrade cross-anisotropy variation. Damage ratios considering base cross-anisotropy are sensitive to temperature variation at *n*-value of 0.5.

5.5 Summary of parametric study

In the earlier steps, a parametric study is performed to investigate the effect of unbound cross-anisotropic variation, i.e., base, subbase, and subgrade respectively, on pavement responses and damage. Outcomes of the parametric study are summarized in Table 5.5.

Table 5.5: Summary of parametric study (Unbound layer cross-anisotropy)

Response	Parameter variation	Observation	Comment
Tensile strain at the bottom of the AC	• AC temperature: 12.3, 25.3 & 33.3 °C • n_{base} : 0.5-1.0 • $n_{subbase}$: 0.5-1.0 • $n_{subgrade}$: 0.5-1.0	• Strain barely varies as *n*-value increases • Strain is high at high temperature and small at low temperature	• Tensile strain at the bottom of the AC layer is not sensitive to unbound layer cross-anisotropy • Strain is sensitive to AC temperature variation
Fatigue damage (D_{anis}/D_{iso}) due to tensile strain	• AC temperature: 12.3, 25.3 & 33.3 °C • n_{base} : 0.5-1.0 • $n_{subbase}$: 0.5-1.0 • $n_{subgrade}$: 0.5-1.0	• D_{anis}/D_{iso} is smaller than 1.0 due to very small strain variation • D_{anis}/D_{iso} increases as *n*-value increases towards isotropy (n=1.0)	• Damage due to cross-anisotropy is smaller than that due to isotropy
Vertical strain in AC	• AC temperature: 12.3, 25.3 & 33.3 °C • n_{base} : 0.5-1.0 • $n_{subbase}$: 0.5-1.0 • $n_{subgrade}$: 0.5-1.0	• Strain does not vary as *n*-value increases • Strain is high at high temperature and small at low temperature	• Tensile strain at the bottom of the AC layer is not sensitive to unbound layer cross-anisotropy • Strain is sensitive to AC temperature variation
Vertical strain in base	• AC temperature: 12.3, 25.3 & 33.3 °C • n_{base} : 0.5-1.0 • $n_{subbase}$: 0.5-1.0 • $n_{subgrade}$: 0.5-1.0	• Strain is the minimum due to base cross-anisotropy • Strain in base is barely sensitive to subbase & subgrade cross-anisotropy • Strain is high at high temperature and small at low temperature	• Vertical strain in base layer is highly sensitive to base layer cross-anisotropy • Strain is sensitive to AC temperature variation
Vertical strain in subbase	• AC temperature: 12.3, 25.3 & 33.3 °C • n_{base} : 0.5-1.0 • $n_{subbase}$: 0.5-1.0 • $n_{subgrade}$: 0.5-1.0	• Strain is the minimum due to subbase cross-anisotropy • Strain in base is slight sensitive to subgrade cross-anisotropy • Strain is high at high temperature and small at low temperature	• Vertical strain in base layer is highly sensitive to subbase layer cross-anisotropy • Strain is sensitive to AC temperature variation
Vertical strain in subgrade	• AC temperature: 12.3, 25.3 & 33.3 °C • n_{base} : 0.5-1.0 • $n_{subbase}$: 0.5-1.0 • $n_{subgrade}$: 0.5-1.0	• Strain variation in subgrade due to unbound layer cross-anisotropy is very small • Strain is high at high temperature and small at low temperature	• Vertical strain in subgrade layer is barely affected by unbound layer cross-anisotropy • Strain variation is sensitive to temperature variation
Damage due to permanent deformation (AC, base, subbase & subgrade)	• AC temperature: 12.3, 25.3 & 33.3 °C • n_{base} : 0.5-1.0 • $n_{subbase}$: 0.5-1.0 • $n_{subgrade}$: 0.5-1.0	• Damage in AC is high due to base cross-anisotropy • Damage in base increases due to subbase cross-anisotropy • Damage in subbase increases due to subgrade cross-anisotropy • Damage is high due to unbound layer cross-anisotropy	• Damage in a specific layer is mostly sensitive to it's underneath layer's cross-anisotropy except subgrade

5.5 Summary

Based on the findings of this study, the following conclusions can be made:

- Both of the horizontal tensile strain at the bottom and vertical strain on top of the AC layer are not sensitive to the cross-anisotropy of unbound layers. However, incorporation of the cross-anisotropic strains into the Miner's damage formula shows that the fatigue damage is less compared to that incorporating isotropic strain.
- Vertical strains in the base, subbase, and subgrade layers are highly affected by cross-anisotropy. Damage ratio based on permanent deformation criterion incorporating these strains shows different trends with variation in *n*-value of unbound layers. The damage due to cross-anisotropic strain is considerably high at small *n*-value.
- Temperature influences both horizontal strain at the bottom of the AC layer as well as vertical strains in both of the AC and unbound layers.

CHAPTER 6

CROSS-ANISOTROPY AND STRESS-DEPENDENCY

6.1 General

The AC cross-anisotropy is combined with unbound layer stress-dependency in this chapter. The AC viscoelasticity and cross-anisotropy material model is also improved based on further laboratory testing. The boundary condition is also modified by the incorporation of the spring-dashpot boundaries. Finally, pavement responses as well as performance are evaluated at varying AC cross-anisotropy, temperatures, and vehicle speed, i.e., loading rate.

6.2 Outline

This study focuses on the evaluation of effect of mainly AC cross-anisotropy on both pavement response and performance in presence of varying unbound layer stress-dependency, depth-temperature variations, and loading rate using a modified dynamic FEM. Figure 6.1 shows the outline of this study. At the beginning, laboratory dynamic modulus tests were conducted on both field-compacted vertical and horizontal cores to improve the cross-anisotropic and viscoelastic model. Resilient modulus tests were conducted on unbound layer materials to develop the stress-dependent and nonlinear elastic material model. Both of these models are integrated into the same dynamic FEM. The boundary condition is modified by incorporation of spring-dashpot boundaries. A non-uniform vertical contact stress is applied over different ribs of a tire. Finally, the simulations are performed at varying *n*-values of AC, depth-temperature profiles, and vehicle speeds.

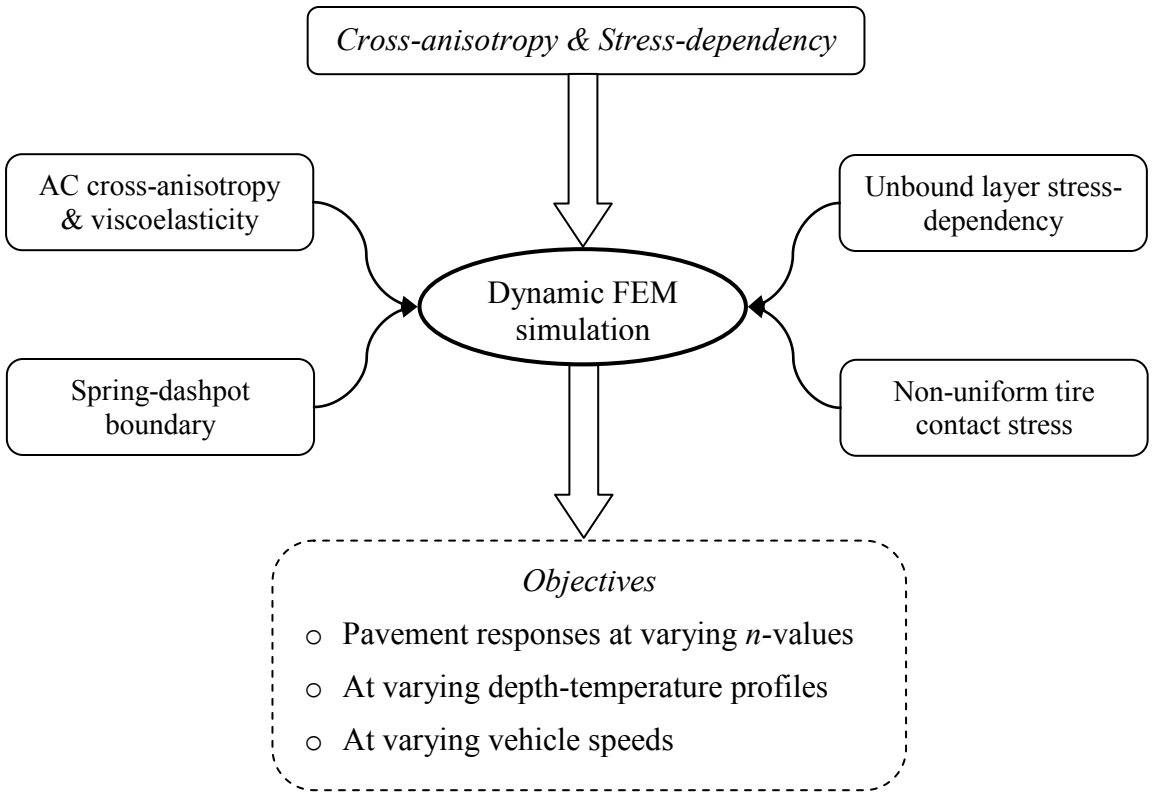

Figure 6.1 Outline of the study

6.3 Model Description

The model geometry is similar to the geometry in Figure 3.4. The modified boundary condition, i.e., BC 2 (see Figure 3.6), is assigned where the spring-dashpot boundaries are assigned along both vertical and horizontal planes. In this manner, reflection of stress wave can be avoided. The layer interfaces are considered partially-bonded and coulomb friction law is used to model the contact between the interfaces. The friction coefficients along layer interfaces in AC are 0.7. Mesh is generated over the geometry according to the method as discussed in section 3.7. The minimum dimension of an element is 0.6 in. Assignment of layer materials to the model is described below:

In this step, laboratory dynamic modulus tests were conducted on both OGFC and AC cores to determine the dynamic modulus at different frequencies and temperatures. In case of AC, cores were collected along both vertical and horizontal directions. Collection of cores from the instrumentation pavement section and details of laboratory tests are discussed in Chapter 3. Later, Prony series coefficients for the OGFC as well as AC along both vertical and horizontal directions were determined based on relaxation modulus variation over time which was converted from the dynamic modulus values. These values are summarized in Table 6.1. Instantaneous moduli of the OGFC, vertical and horizontal AC are 1500, 7037, and 3795 ksi respectively. for assigning vicoelasticity and cross-anisotropy to the dynamic FEM.

Table 6.1 Prony series coefficients (OGFC & AC)

i	$e_{OGFC,i}$	$\tau_{OGFC,i}$	$e_{AC,v,i}$	$\tau_{AC,v,i}$	$e_{AC,h,i}$	$\tau_{AC,h,i}$
1	0.2	1.1	0.277	1.04E-05	0.292	0.001
2	0.2	4.7	0.2	0.018	0.2	0.056
3	0.15	9.75	0.15	0.0011	0.15	15.64
4	0.15	100	0.13	0.00019	0.19	0.0001
5	0.1	250	0.13	0.68	0.1	0.61
6	0.1	470	0.09	22.99	0.054	0.02

The other required material parameters for the AC are documented in Chapter 3 (Section 3.7.2). It was mentioned earlier that the shear modulus in vertical plane (G_{vh}) was not determined by the laboratory testing since the required testing equipment is not available. In that case, this value can be obtained from the different studies by the researchers who conducted the shear test on the AC. It is known that the mechanical properties of the AC may vary in different regions even for the same mix and volumetric properties. This is due to the use of different types of aggregates and asphalt binders. It indicates that incorporation of shear modulus based on other studies may

not be the same as that of the field-compacted AC core from the instrumented section. Therefore, it is necessary to investigate the difference in pavement responses, such as deflection, stress and strain, at varying shear modulus of the AC. Pavement responses will be considered as the least sensitive to the shear modulus if the difference is very small. This situation leads to a need for parametric study of pavement responses, such as deflection, stress and strain, at varying shear modulus.

The parametric study is performed based on four different types of pavement responses, i.e., vertical surface deflection, vertical stress, horizontal tensile and vertical strain in the AC layer, simulated by the dynamic FEM by varying the shear modulus. These FEM simulations are performed under the FWD test load which generates a vertical stress of 79.6 psi. Figure 6.2(a) shows the surface deflections at six different radial distances, i.e., 0, 8, 12, 18, 24, and 36 inch. The shear modulus is varied from 0.3 to 0.5 times the vertical modulus (E_v). It is observed that the deflections at different shear moduli at the radial distance of 0 inch are not the equal. However, the differences are very small and even, these differences diminishes as the radial distance increases. Finally, these deflections overlap each other which indicate that the variation in shear modulus is barely affects the surface deflections.

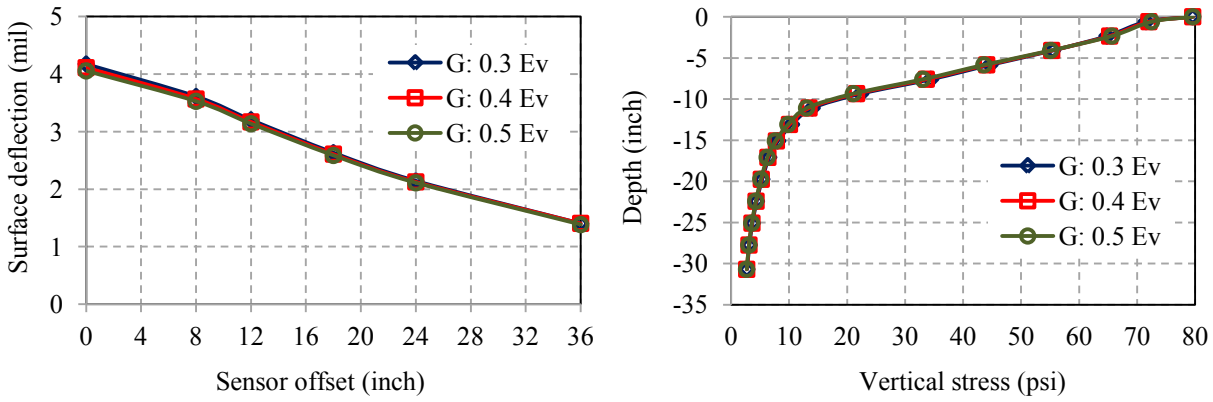

(a) Surface deflection (b) Vertical stress

Figure 6.2 Deflection and stress at varying shear modulus (G_{vh})

Vertical stresses over pavement depth at varying shear modulus are plotted in Figure 6.2(b). It is observed that the vertical stress profiles at the varying shear modulus are almost overlapping each other over the depth. Therefore, effect of shear modulus variation on vertical stress is negligible. The horizontal tensile strain at the bottom and vertical strain in mid-depth of the AC layer at varying shear modulus is summarized in Table 6.2. The differences in strain are also negligible which indicates that the effect of shear modulus variation on strains is also negligible.

Table 6.2 Strain at varying shear modulus

Shear Modulus	Tensile strain (micro-strain)	Vertical strain (micro-strain)
G: 0.3 E_v	29.8	30.6
G: 0.4 E_v	29.6	30.8
G: 0.5 E_v	29.4	30.9

Based on the above discussion, it is obvious that the shear modulus in vertical plane has the least effect on the specific pavement responses. Therefore, shear modulus based on the other studies

can be incorporated to the dynamic FEM. Finally, the shear modulus is assigned as 0.4 times vertical modulus (E_v) which was already mentioned in Chapter 3.

The depth-temperature variations in four different months are also incorporated to the AC layer. These variations are assigned based on temperature measurement by the temperature probes which were installed at different depths, i.e., 0, 2, and 12 inch from the pavement surface. These variations are plotted in Figure 6.3. Temperature is constant over top 0.6 inch in the OGFC layer and below this, it gradually decreases with depth. It is also observed that temperature is the maximum in July and minimum in January respectively. This variation is incorporated to the AC layer using the eqn. (3.7).

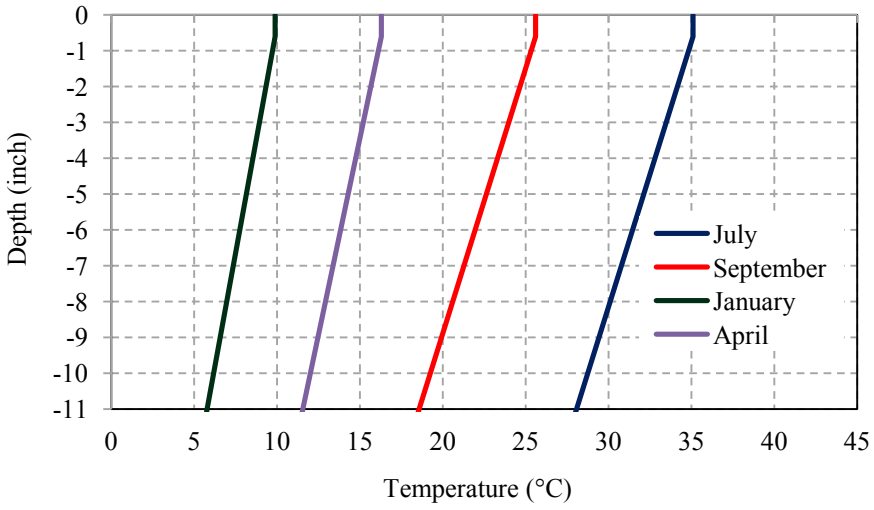

Figure 6.3 Flow chart of stress-dependency determination in different months

Once the depth-temperature variation is incorporated to the AC layer, temperature dependency is also incorporated to both vertical and horizontal AC modulus using the eqn. (3.6). As mentioned earlier in Chapter 3, a FORTRAN subroutine is developed to implement the temperature-

dependent and cross-anisotropic viscoelasticity to the dynamic FEM in ABAQUS through the UMAT.

Stress-dependency and nonlinear elasticity of the unbound layers, such as base and subbase, are assigned to the dynamic FEM using the eqn. (3.11). Coefficients of this equation are determined by regression analyses of the laboratory resilient modulus tests on aggregates collected from the field (see Chapter 3). As mentioned earlier, the resilient modulus tests were conducted at varying sequences of deviatoric and confining stresses. Coefficients of the eqn. (3.11) to assign the stress-dependency are summarized in Table 6.3. The nature of coefficients indicates that granular aggregate in the base layer shows only stress-hardening, i.e., modulus increases with increase in bulk stress and not decreases with increase in octahedral shear stress. This may be due to the use of RAP in the base layer which increases the inter-particle friction resistance. The subbase shows both stress-hardening and softening.

Table 6.3 Summary of regression coefficients

Layer	k_1	k_2	k_3
Base	5385	0.15	0.75
Subbase	1722	0.17	-0.27

The regression coefficients, summarized in Table 6.3, are based on the resilient modulus tests at a moisture content which matches with the field moisture content in the month of July. The FEM simulations, in this phase of the study, are also performed in three other months: January, April, and September respectively. The modulus of the unbound layers in those months may be not the same. Therefore, stress-dependencies in different months need to be determined to incorporate

these to the dynamic FEM. The methodology is shown in Figure 6.4. The FWD tests were conducted in January, April, July, and September to backcalculate unbound layer moduli.

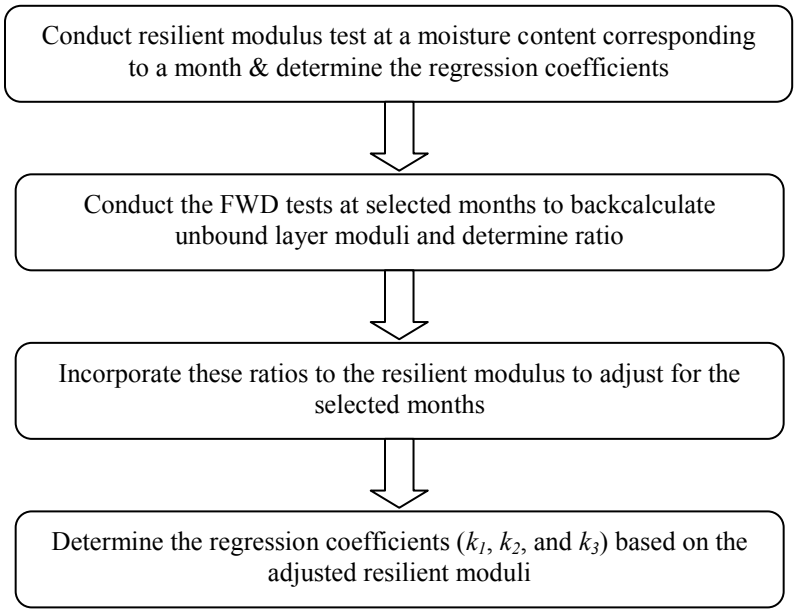

Figure 6.4 Flow chart of stress-dependency determination in different months

Ratios of the backcalulated moduli ($R = E_i / E_{July}$, where, $i =$ January, April, and September) in those months are determined. These ratios are shown in Figure 6.5. The ratios for both base and subbase in July are 1.0 since the moduli in this month are considered as reference. These ratios are the maximum in January since the moduli are the maximum in this month.

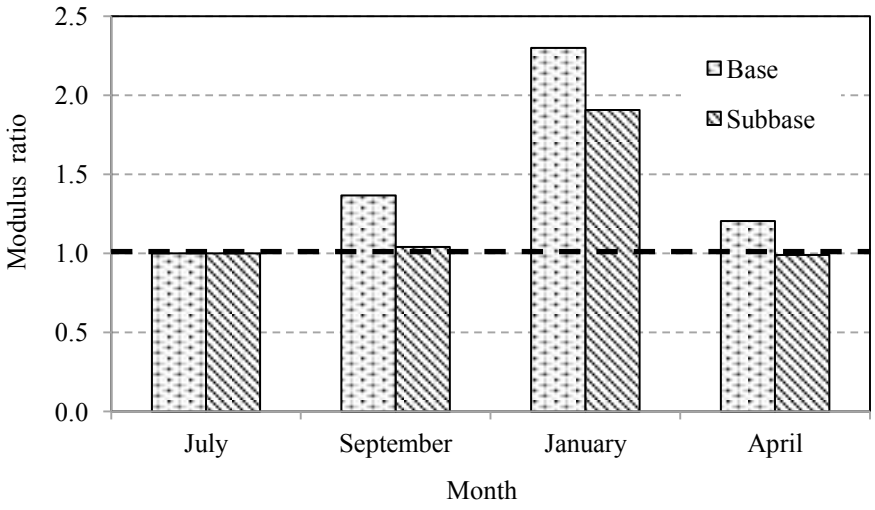

Figure 6.5 Base and subbase modular ratios in different months

These ratios (*R*-values) are then multiplied with the resilient modulus values corresponding to July. Finally, regression coefficients are determined based on the adjusted resilient modulus values. Regression coefficients of January, April, and September are summarized in Table 6.4. Here, only the k_1 varies whereas the other two factors, namely, k_2 and k_3 are same. It indicates that the nature/trend of stress-dependency will be the same even though the modulus values will vary. Finally, the stress-dependencies in different months are incorporated to the model in ABAQUS through the UMAT.

Table 6.4 Adjusted regression coefficients

Layer	Base			Subbase		
	k_1	k_2	k_3	k_1	k_2	k_3
January	12384	0.15	0.75	3285	0.17	-0.27
April	6490			1705		
July	5385			1722		
September	7358			1792		

The top of the subgrade is located at a depth of 25.1 inch where the overburden stress is high. However, this stress is constant over the time. The other source of load is traffic induced stress which is very low at that depth. It indicates that change of state of stresses in the subgrade is almost negligible for this specific pavement section. Based on the overall phenomenon, the stress-dependency is ignored in this layer and the subgrade is assumed as linear elastic. The modulus of elasticity of this layer was determined from the backcalculation of the FWD test data in the earlier mentioned months. The variation in subgrade modulus was small and therefore, an average of 25 ksi is assigned to this layer.

In this phase of the study, the dynamic FEM simulation requires two major types of material models for the OGFC, AC, base, and subbase which is not available in the material library of the ABAQUS. These are: a generalized temperature-dependent & cross-anisotropic viscoelastic model and a generalized stress-dependent, nonlinear elastic & cross-anisotropic model. Figure 6.6 shows the flow chart of the execution of the material models through UMAT in ABAQUS. For every single element of the model, ABAQUS main program provides the initial state of stresses and strain increments at zero-time step to the UMAT subroutine. The UMAT will determine where the element belongs, for instance, element in OGFC, AC or unbound layers. The cross-anisotropic viscoelastic model will be implemented if the element is in OGFC or AC, otherwise, the stress-dependent model will be implemented. Both of these models can incorporate both isotropy and cross-anisotropy based on material type.

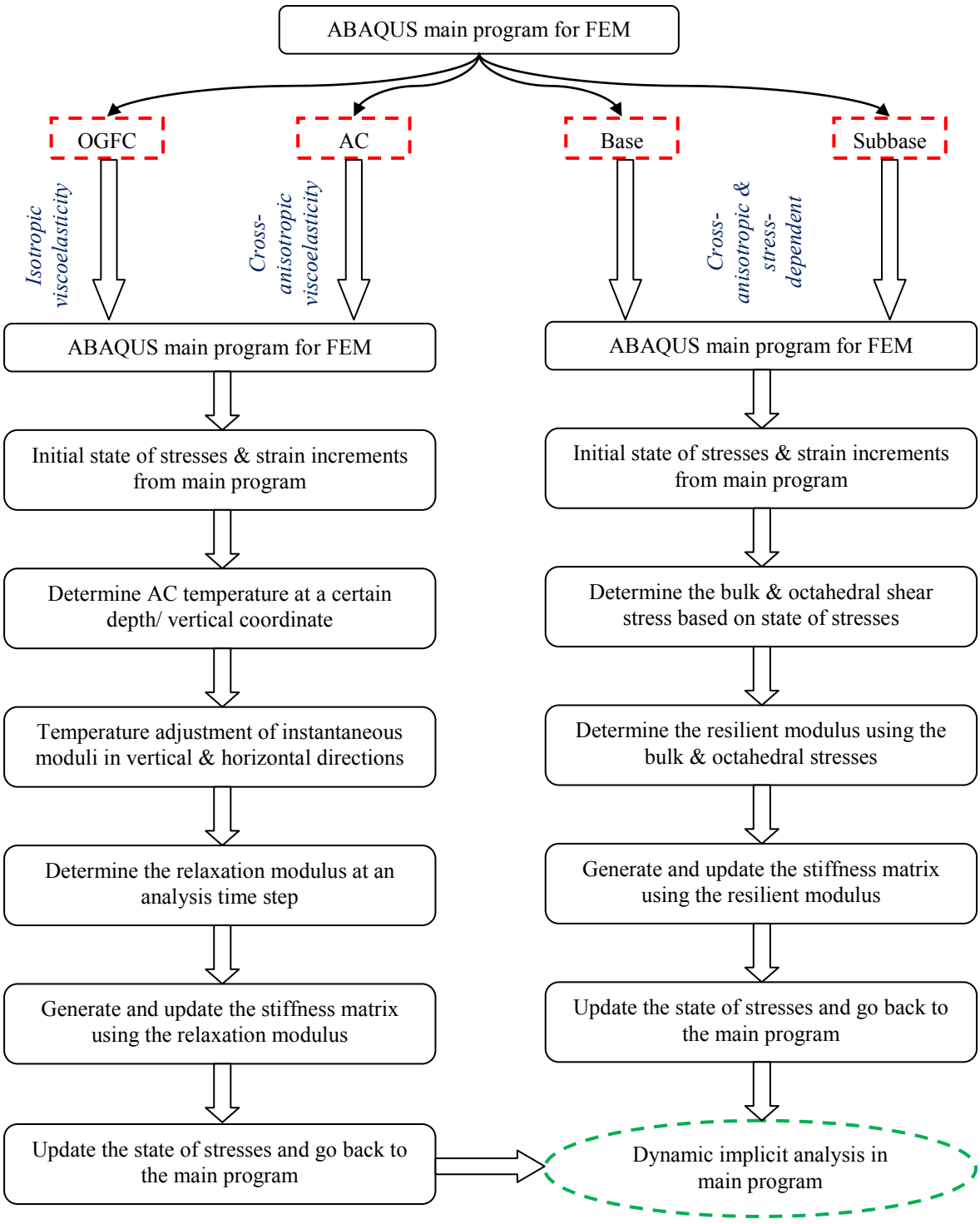

Figure 6.6 Flow chart of material models in UMAT, ABAQUS

The general scenario is that the subroutines determine the modulus, i.e., relaxation modulus for viscoelastic material or resilient modulus for unbound layers, and generate/update the stiffness matrix. Later, the stresses are updated based on the updated modulus and strain increments which were provided by the main program at the beginning of the execution of the subroutine. Finally, the subroutine provides the stiffness matrix and goes back to the main program to calculate strains for the next analysis/time step. In this phase, the implicit algorithm is again used to execute the dynamic simulation. Details of the other inputs, such as, damping and loading, are already discussed in Chapter 3.

6.4 Analysis and Discussion

6.4.1 Depth-Temperature Variation

Tensile Strain in the AC Layer

Horizontal tensile strains at bottom of the AC layer along two orthogonal directions, i.e., along and transverse to traffic directions, are determined at varying *n*-values. Figure 6.7(a) and (b) shows the variation of the longitudinal and transverse tensile strains. It is observed that the transverse tensile strain is greater than longitudinal tensile strain. This is resulted from the load distribution due to the shape of tire imprint area. The common observation is that the tensile strain decreases as *n*-value increases towards isotropy, i.e., n =1.0. In addition, tensile strain in July is greater than that in any other months due to high temperature in the AC layer. In July, difference in strain between *n*-value of 0.25 and 1.0 is more 40 microstrain whereas that is about 20 microstrain in January.

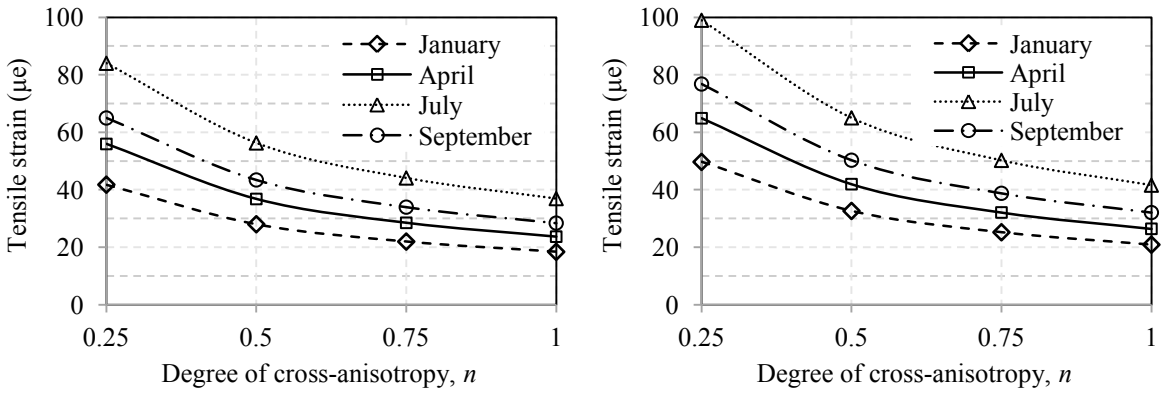

(a) Longitudinal tensile strain (b) Transverse tensile strain

Figure 6.7 Horizontal tensile strain in AC (Temperature variation)

The ratio of horizontal tensile strain considering cross-anisotropy and isotropy are calculated again for both longitudinal and transverse directions, i.e., e_{anis}/e_{iso}, where e_{anis} = cross-anisotropic strain and e_{iso} = isotropic strain. The strain ratio at varying cross-anisotropy and temperatures are plotted in Figure 6.8. The minimum and maximum pavement temperatures in January and July respectively are selected for this plot. Strain ratios along both longitudinal and transverse directions decrease as the *n*-value increases towards isotropy (see Figure 6.8(a)). The transverse strain ratio is greater than the longitudinal strain ratio. It is also observed that both of the strain ratios are not sensitive to the pavement temperatures. It indicates that the tensile strain at the bottom of the AC layer varies with *n*-values at the similar rates for different temperatures.

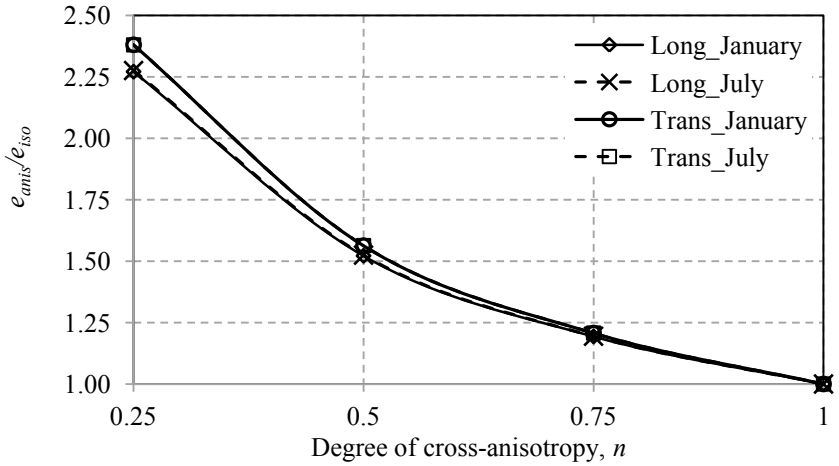

(a) Strain ratio

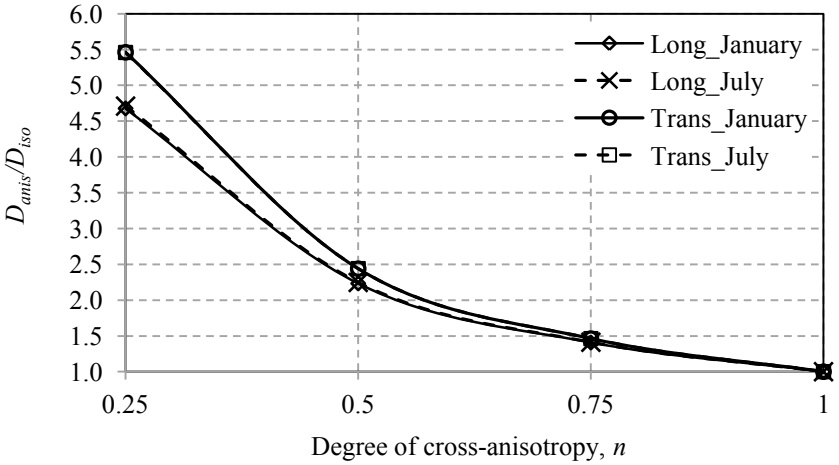

(b) Damage

Figure 6.8 Tensile strain ratio and damage in AC

Figure 6.8(b) shows the variation of relative damage at varying cross-anisotropy and temperatures (eqn. 4.12). The damage ratio follows the similar trend of the strain ratio where it decreases with increase in *n*-values. Damage ratio based on transverse strain is greater than that based on longitudinal strain as expected. In cases of both of the strains, damage ratios are barely affected by temperature variation.

In summary, decrease in horizontal stiffness causes an increase in tensile strains at the bottom of the AC layer. In addition, strain increases more rapidly with decrease in horizontal stiffness at higher pavement temperatures. The relative damage per loading repetition is the maximum due to the minimum horizontal stiffness. Damage due to cross-anisotropy is 1.5 times that due to isotropy whenever the horizontal stiffness is 0.75 times the vertical stiffness.

Vertical Strain in Pavement Layers

Vertical strains were determined at mid-depth of AC, base, subbase, and top of the subgrade at varying *n*-values. Figure 6.9(a) through (d) shows the variation of vertical strains in pavement layers at varying *n*-values in different months. The common observation is that the vertical strains are the maximum in July whereas those are the minimum in January due to the temperature variation. In addition, the strains decrease with increase in *n*-value towards 1.0 (isotropy). Differences in strains in AC, base, subbase, and subgrade are about 15.1, 44.3, 69.9, and 39.5 microstrain, respectively, in July and these are the maximum compared to those in other months. The minimum strain differences are observed in January and these are about 7.5, 18.7, 28.0, and 32.8 microstrain in AC, base, subbase, and subgrade respectively.

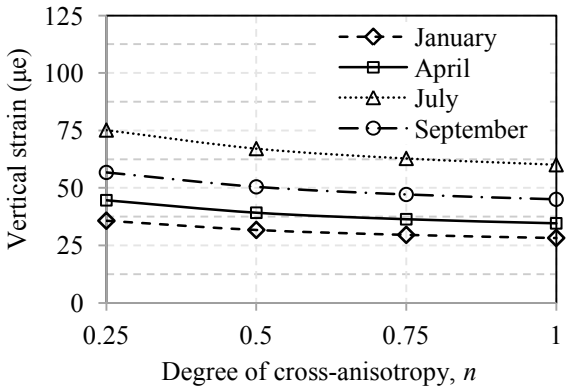

(a) AC

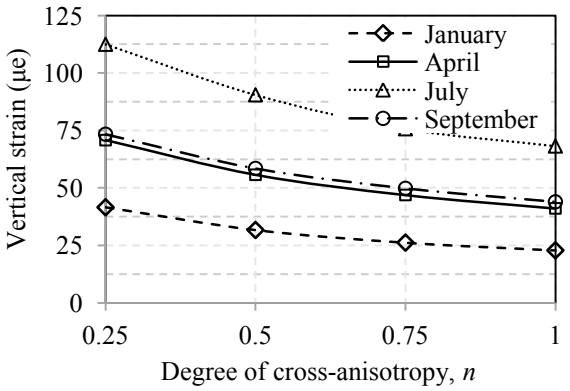

(b) Base

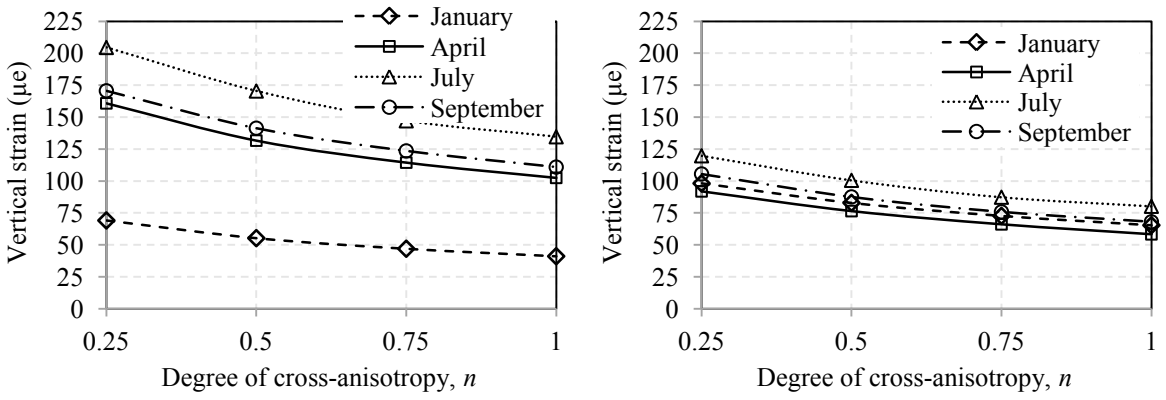

(c) Subbase (d) Subgrade

Figure 6.9 Vertical strain in pavement layers (Temperature variation)

It is observed that difference in the vertical strain due to cross-anisotropy variation is very high in both base and subbase. The reason may be due to the variation in stress-dependent modulus of unbound layers. Figure 6.10(a) and (b) show the variation of vertical stress with *n*-value of the AC in four different months. Stress decreases as the *n*-value increases in those months. In addition, stresses in both base and subbase are the maximum at high temperature in July due to the least stiffness of the AC. It indicates that the base and subbase moduli are expected to decrease with increase in *n*-value since the stress also decreases in those layers. The reason is that a decrease in vertical stress will lead to a decrease in both bulk and octahedral shear stresses. Finally, the unbound layer modulus will also decrease since it depends on the earlier mentioned stresses.

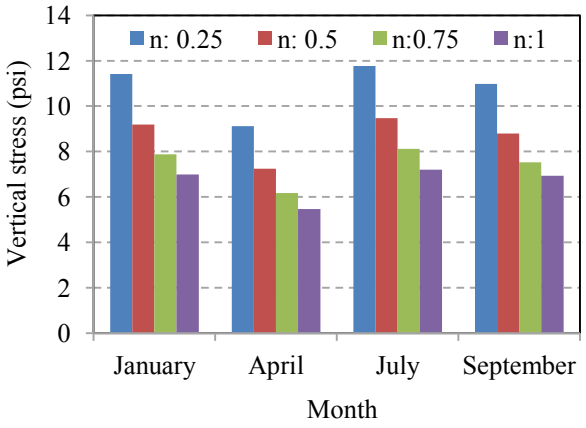

(a) Vertical stress in base

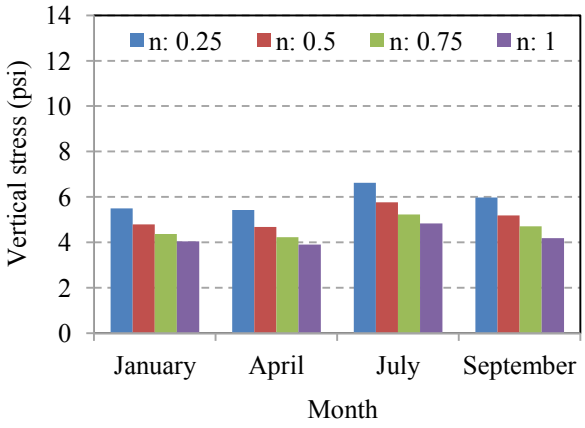

(b) Vertical stress in subbase

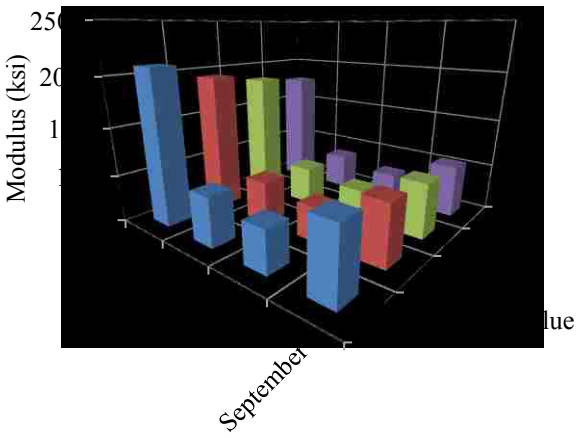

(c) Modulus in base

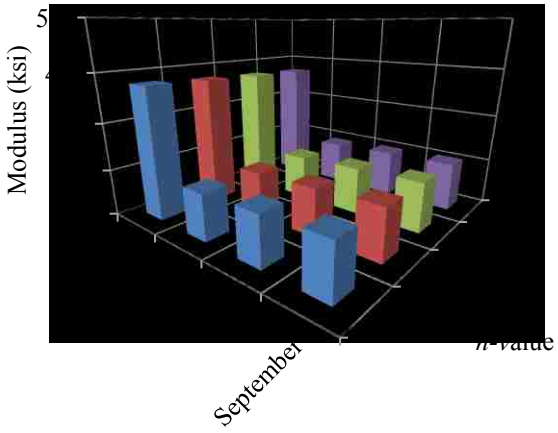

(d) Modulus in subbase

Figure 6.10 Vertical nonlinear modulus in unbound layers

Later, the expected trend is observed in Figure 6.10(c) and (d). Base modulus is greater than subbase modulus and the rate of modulus decrease is also high in base layer. Moduli in both of the layers are the maximum in January and minimum in July respectively. The main reason for this monthly variation of the modulus is the varying regression coefficient, k_1, which is the maximum in January. It was observed earlier that the vertical strain decreases with increase in *n*-value. The reason is that the rate stress decrease is higher than modulus decrease.

The vertical strain ratios in pavement layers at varying cross-anisotropy and temperatures are plotted in Figure 6.11. The minimum and maximum pavement temperatures in January and July respectively are selected for this plot. Strain ratios decrease as the *n*-value increases towards isotropy (see Figure 6.11(a)). The strain ratios in unbound layers are greater than that in the AC layer. It is also observed that both of the strain ratios are not sensitive to the pavement temperatures in case of the AC and subgrade. Strain ratios in base and subbase are highly sensitive to pavement temperatures. This ratio is high at low temperature and vice versa.

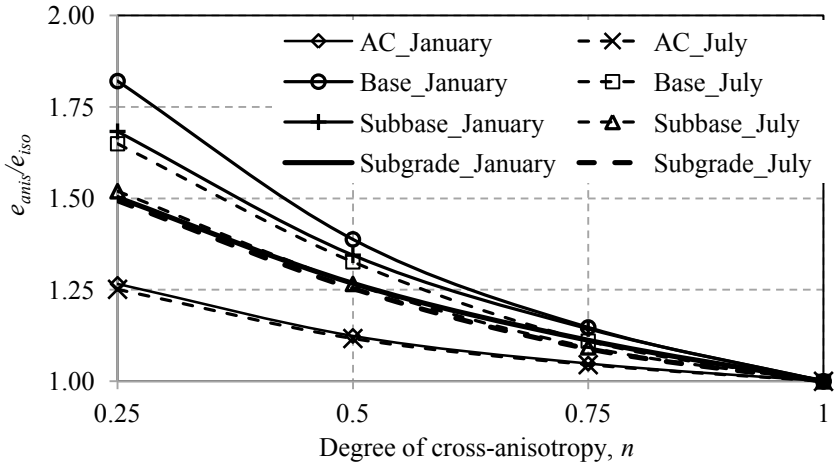

(a) Strain ratio

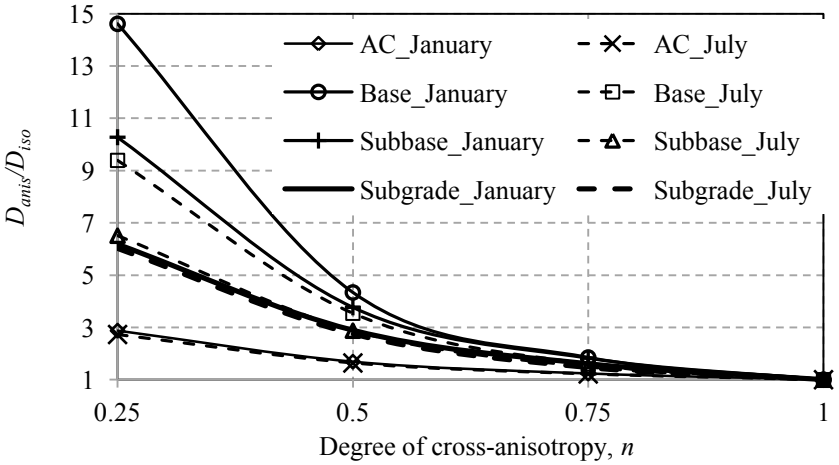

(b) Damage

Figure 6.11 Vertical strain ratio and damage in pavement layers

Figure 6.11(b) shows the variation of damage incorporating vertical strains at varying cross-anisotropy and temperatures (eqn. 4.13). The damage ratio follows the similar trend of the strain ratio where it decreases with increase in *n*-values. In addition, damage ratios in base and subbase are very high as well as sensitive to temperature variation.

In summary, vertical strains in pavement layers decrease with increase in *n*-value of the AC towards the isotropy. The strain variation at varying *n*-values is the maximum in July due to both higher temperature variation and lower values of unbound layer moduli in this month. The damage per loading repetition is the maximum due to the minimum horizontal stiffness.

6.4.2 Base Isotropy vs. Cross-anisotropy

Tensile Strain in the AC Layer

Figure 6.12(a) and (b) shows the variation of the longitudinal and transverse tensile strains with *n*-value of the AC in presence of both base isotropy and cross-anisotropy. It is observed that the transverse tensile strain is greater than longitudinal tensile strain similar to the earlier observation. In addition, tensile strain along both of the directions decreases as *n*-value increases towards isotropy, i.e., n =1.0. The strain values increase whenever the base cross-anisotropy is incorporated, i.e., n-value of the base is 0.25.

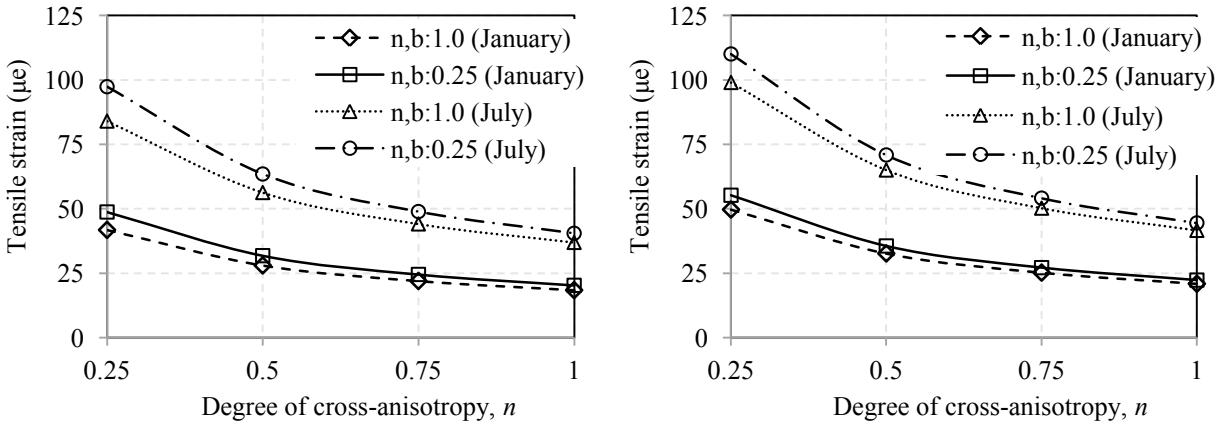

(a) Longitudinal strain (b) Transverse strain

Figure 6.12 Horizontal tensile strain in AC (isotropic vs. cross-anisotropic base)

In summary, reduction in horizontal stiffness of the base layer also causes an increase in tensile strains at the bottom of the AC layer.

The ratio of horizontal tensile strain considering cross-anisotropy and isotropy are calculated again for both longitudinal and transverse directions incorporating both base isotropy and cross-anisotropy. The strain ratios at varying cross-anisotropy and temperatures are plotted in Figure 6.13. The minimum and maximum pavement temperatures in January and July respectively are selected for this plot. Strain ratios along both longitudinal and transverse directions decrease as the *n*-value increases towards isotropy (see Figure 6.13(a)). The transverse strain ratios are greater than the longitudinal strain ratios. It is also observed that both of the strain ratios are enhanced due to incorporation of the base cross-anisotropy, i.e., $n,b=0.25$.

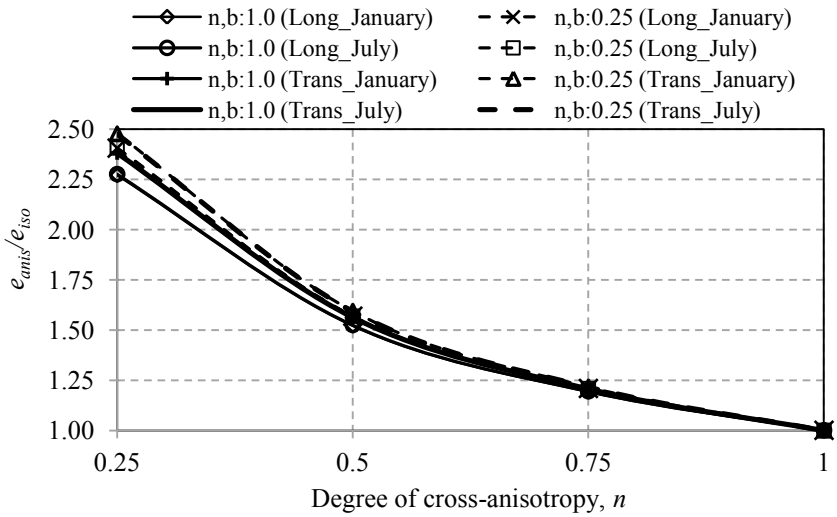

(a) Strain ratio

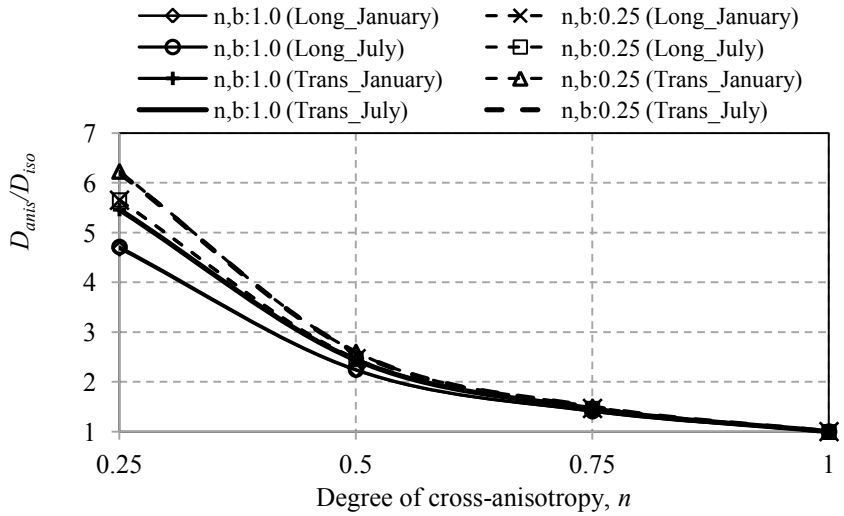

(b) Damage

Figure 6.13 Tensile strain ratio and damage in AC

Figure 6.13(b) shows the variation of damage for isotropic and cross-anisotropic base layer (eqn. 4.12). The damage ratio follows the similar trend of the strain ratio where it decreases with increase in *n*-values. Damage ratio based on transverse strain is greater than that based on longitudinal strain as expected. Finally, presence of base cross-anisotropy enhances the values of the damage ratios.

In summary, tensile strains at the bottom of the AC layer increases due to incorporation of the base cross-anisotropy. Later, it results the enhanced damage per loading repetition. Unlike to earlier observations, the damage ratio incorporating base cross-anisotropy is sensitive to pavement temperatures.

Vertical Strain in Pavement Layers

Figure 6.14(a) through (d) show the variation of vertical strains in pavement layers at varying *n*-values in presence of base isotropy and cross-anisotropy. In both cases, the vertical strains are

the maximum in July whereas those are the minimum in January. The reason is that both AC and unbound layer moduli are the minimum in July which is opposite to January. In addition, the strains decrease with increase in *n*-value towards 1.0 (isotropy) as before. Values of the vertical strains are enhanced whenever the *n*-value of the base layer is 0.25. In addition, amount of this strain increase is pronounced at high temperature. Strains in the pavement layers are highly sensitive to temperature, except, subgrade.

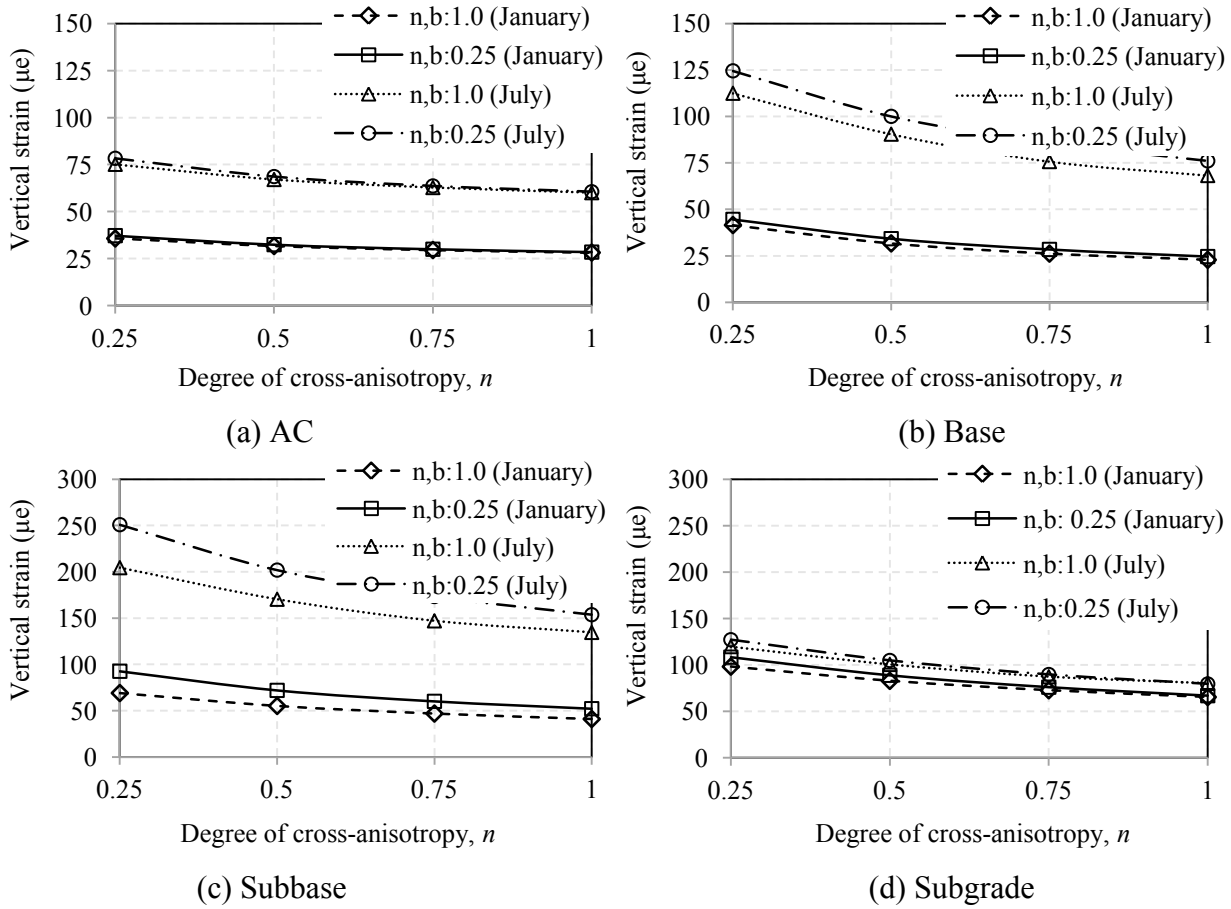

Figure 6.14 Vertical strain in pavement layers (isotropic vs. cross-anisotropic base)

It is observed that difference in the vertical strain due to cross-anisotropy variation is very high in both base and subbase due to the variation in stress-dependent modulus of unbound layers.

Figure 6.15(a) and (b) show the variation of vertical stress with *n*-value of the AC in January and July considering both base isotropy and cross-anisotropy. Stress decreases as the *n*-value of the AC increases in those months. In addition, stresses in both base and subbase are the maximum at high temperature in July due to the least stiffness of the AC. It indicates that the base and subbase moduli are expected to decrease with increase in *n*-value since the stress also decreases in those layers. The expected trend is evident in Figure 6.15(c) and (d). Moduli in both of the layers are the maximum in January and minimum in July respectively due to the similar trend of variation in regression coefficient, k_1, which is the maximum in January.

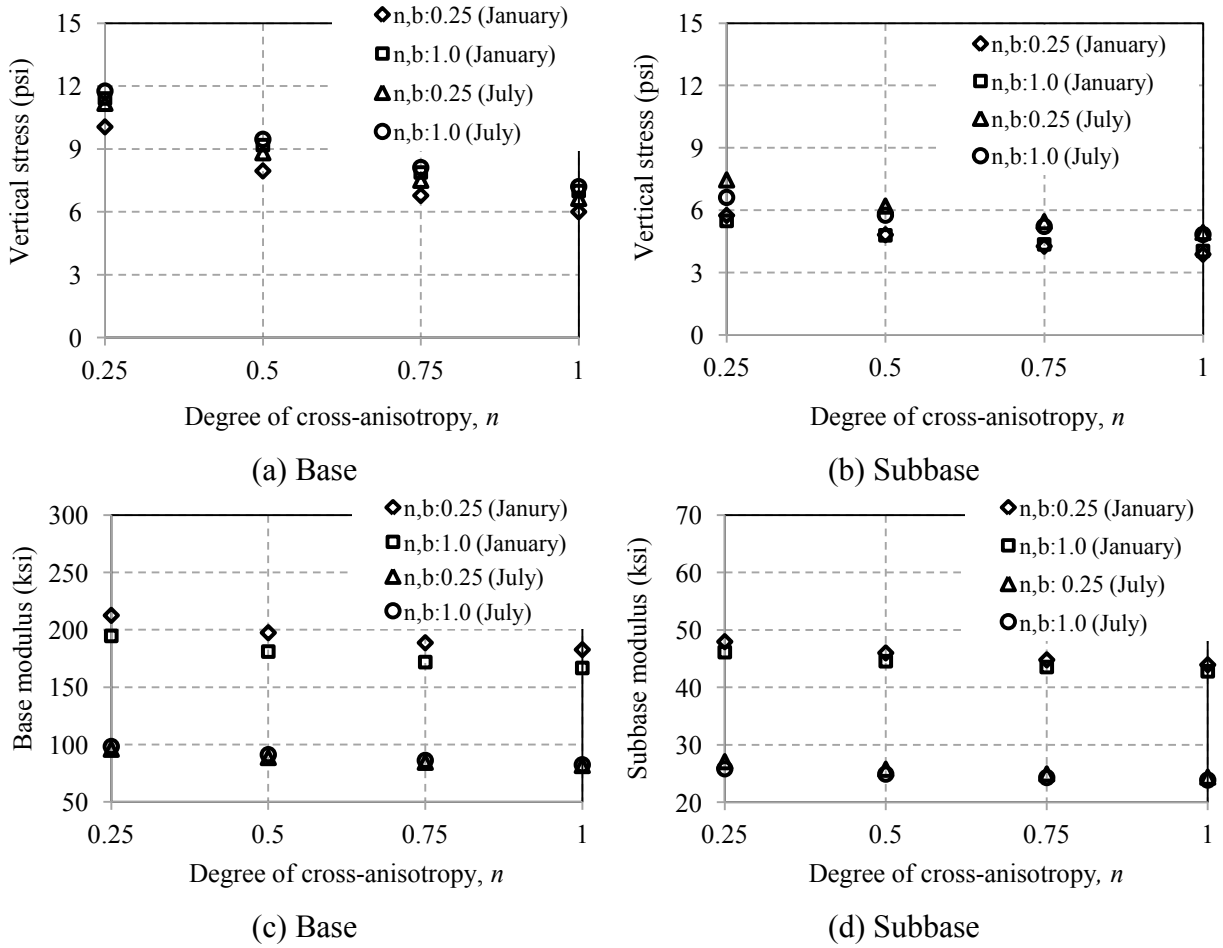

Figure 6.15 Vertical stress and modulus in unbound layers

Variations in stress and modulus due to incorporation of base cross-anisotropy are relatively small. However, the resulted vertical strains are high. This actually happens due to the decrease in stiffness/moduli (E_1 and E_3) in the horizontal plane which leads to smaller values of stresses (σ_1 and σ_3) in same plane. In summary, vertical strains in AC, and unbound layers will be enhanced in presence of the unbound layer cross-anisotropy due to decrease in stresses in the horizontal plane.

The vertical strain ratios in pavement layers at varying cross-anisotropy and temperatures are plotted in Figure 6.16. The minimum and maximum pavement temperatures in January and July respectively are selected for these plots. Strain ratios decrease as the *n*-value increases towards isotropy (see Figure 6.16(a) and (b)). The strain ratios in unbound layers are greater than that in the AC layer. It is also observed that the strain ratios are sensitive to the pavement temperatures. This ratio is high at low temperature and vice versa.

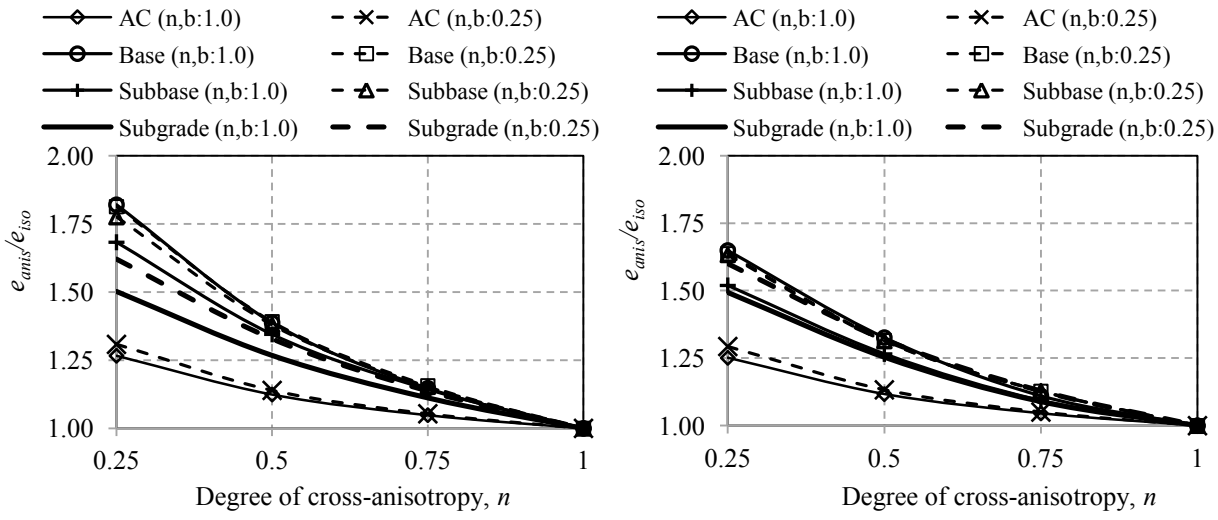

(a) Strain ratio (January)

(b) Strain ratio (July)

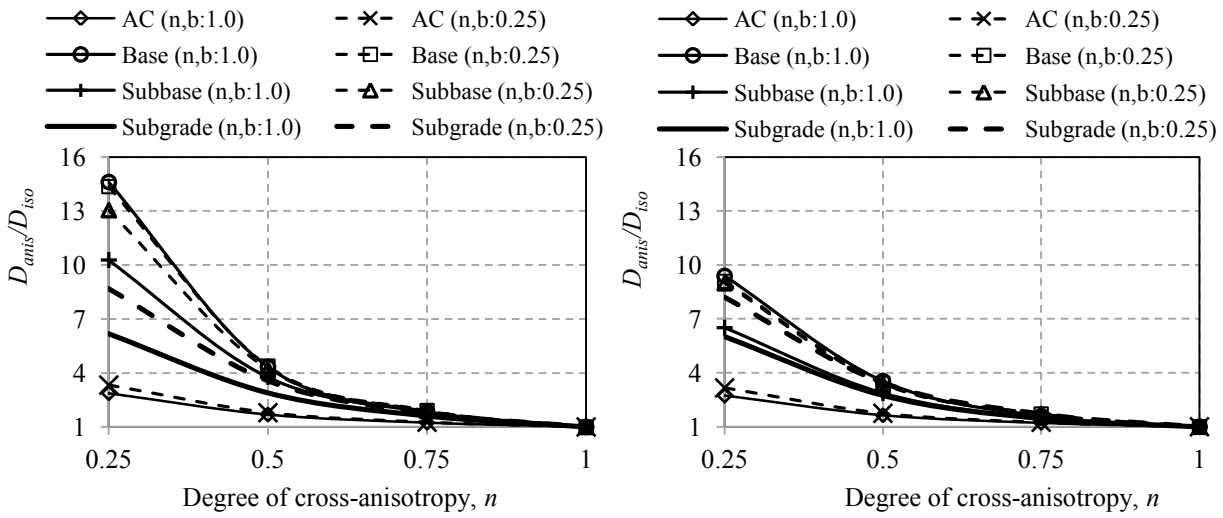

(c) Damage (January) (d) Damage (July)

Figure 6.16 Vertical strain ratio and damage in pavement layers

Figure 6.16(c) and (d) show the variation of damage based on vertical strain ratios incorporating base cross-anisotropy (eqn. 4.13). The damage ratio follows the similar trend of the vertical strain ratio where it decreases with increase in *n*-values. The damage ratios are sensitive to temperature variation. It is observed that this ratio is high at low temperature in January and vice versa.

In summary, vertical strains in pavement layers decrease with increase in *n*-value of the AC towards the isotropy. The strain variation at varying *n*-values is the maximum in July due to both higher temperature variation and lower values of unbound layer moduli in this month. However, the relative damage per loading repetition is the high in January whenever the pavement temperature is low.

6.4.3 Linear vs. Nonlinear Elastic

Tensile in the AC Layer

Figure 6.17(a) and (b) shows the variation of the longitudinal and transverse tensile strains for linear and nonlinear elastic unbound layers, i.e., base and subbase, at two different temperatures. The tensile strain decreases as *n*-value increases towards isotropy, i.e., n =1.0, which is similar to the earlier observations. In case of both longitudinal and transverse strains, incorporation of unbound layer nonlinearity enhances the values of tensile strain. Finally, the strains are sensitive to the temperature as expected.

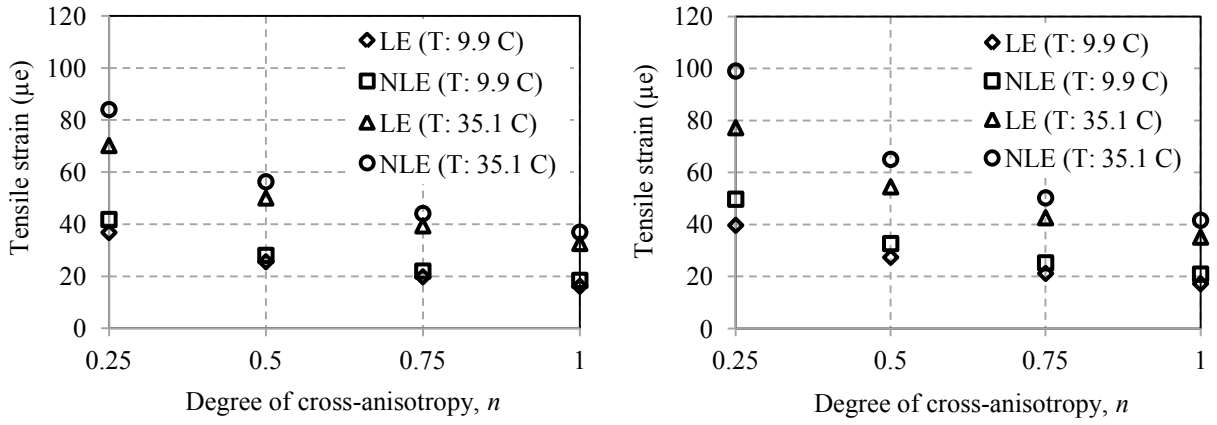

(a) Longitudinal strain (b) Transverse strain

Figure 6.17 Tensile strain in AC layer (Linear vs. nonlinear elastic)

The ratio of horizontal tensile strain ratios incorporating linear and nonlinear elastic base and subbase are calculated for both longitudinal and transverse. The strain ratios at varying cross-anisotropy and temperatures are plotted in Figure 6.18(a) and (b). The minimum and maximum pavement temperatures in January and July respectively are selected for this plot. Strain ratios along both longitudinal and transverse directions decrease as the *n*-value increases towards

isotropy. At high temperature, strain ratios considering nonlinear elasticity are greater than those considering linear elasticity. At and above *n*-value of 0.5, the ratios are same for both linear and nonlinear elasticity.

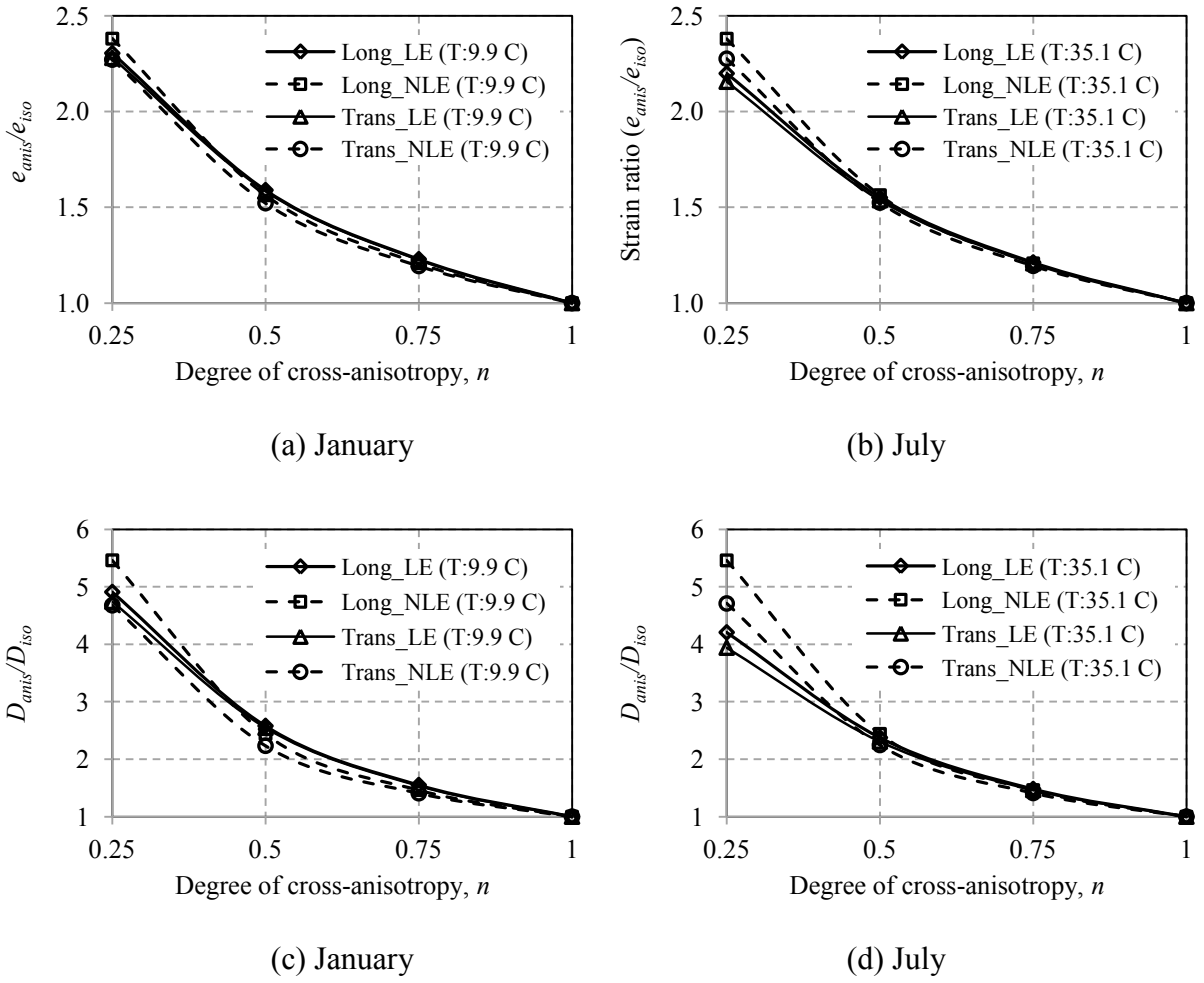

Figure 6.18 Tensile strain ratio and damage (Linear vs. nonlinear elastic)

Figure 4.18(c) and (d) show the variation of damage for linear and nonlinear elastic base and subbase (eqn. 4.12). The damage ratio follows the similar trend of the strain ratio where it decreases with increase in *n*-values. Damage ratio based on transverse strain is greater than that

based on longitudinal strain at high temperature. Finally, presence of unbound layer nonlinear elasticity enhances the values of the damage ratios.

In summary, tensile strains at the bottom of the AC layer increases due to incorporation of the base cross-anisotropy. Later, it results the enhanced damage per loading repetition. Unlike to earlier observations, the damage ratio incorporating base cross-anisotropy is sensitive to pavement temperatures.

Vertical Strain in Pavement Layers

Figure 6.19(a) through (d) shows the variation of vertical strains in pavement layers at varying *n*-values for linear and nonlinear elastic unbound layers at two different temperatures. The vertical strains in the layers decreases with increase in *n*-value which are also sensitive to temperature variation which agrees with the earlier trends. It is also observed that the incorporation of nonlinear unbound layer leads to increase in vertical strains. However, in case of subgrade, vertical strain due to linear base and subbase layer is greater than that due to nonlinearity.

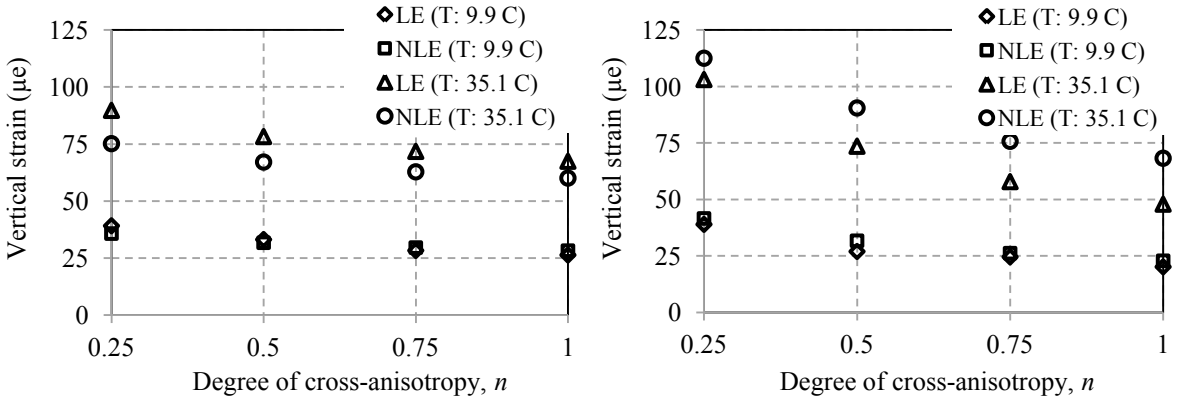

(a) AC (b) Base

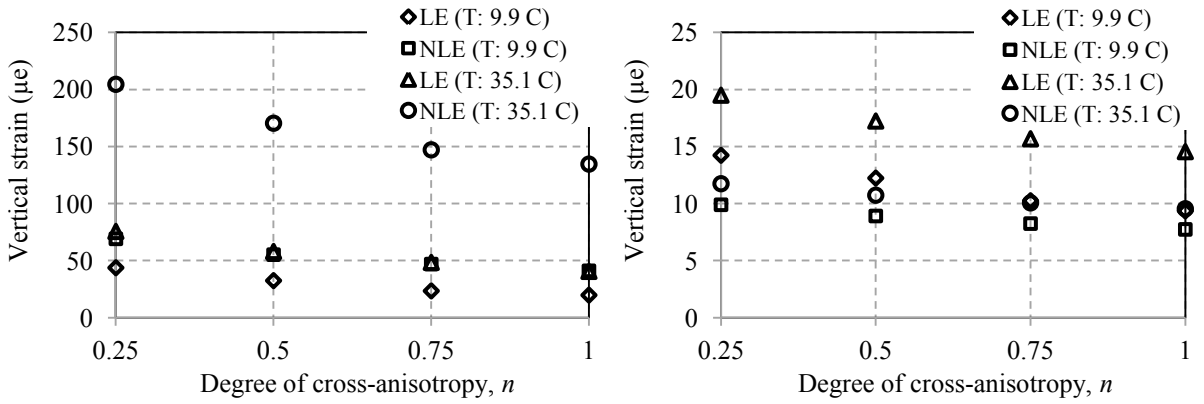

(c) Subbase (d) Subgrade

Figure 6.19 Vertical strains in pavement layers (Linear vs. nonlinear elastic)

The vertical strain ratios in pavement layers at varying cross-anisotropy incorporating unbound layer nonlinearity are plotted in Figure 6.20(a) through (d). Strain ratios decrease as the *n*-value increases towards isotropy as expected. The strain ratios in the base and subbase are greater than those in the AC and subgrade. Strain ratios are affected by temperature variations However, there is no regular trend. It is also observed that the strain ratios are high for linear elastic unbound layers.

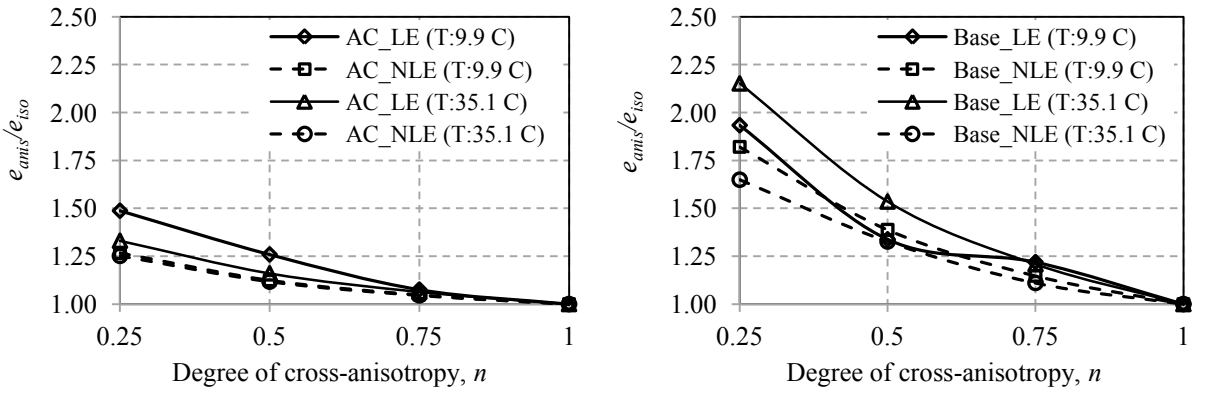

(a) AC (b) Base

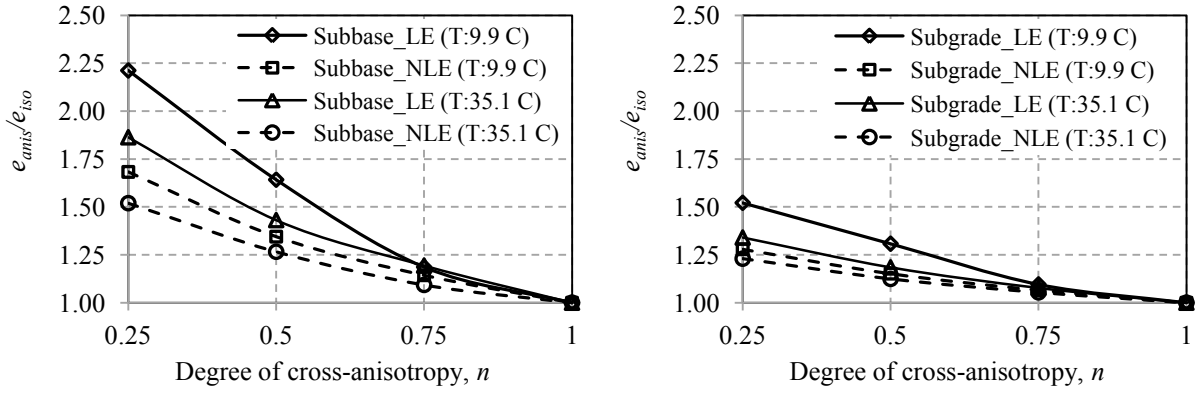

(c) Subbase (d) Subgrade

Figure 6.20 Vertical strain ratios in pavement layers (Linear vs. nonlinear elastic)

Figure 6.21(a) through (d) show the variation of damage based on vertical strain ratios incorporating unbound layer nonlinearity (eqn. 4.13). The damage ratio follows the similar trend of the vertical strain ratio where it decreases with increase in *n*-values. The damage ratios in the base and subbase are greater than those in the AC and subgrade. In addition, these ratios based on linear elasticity are greater than that based on nonlinear elasticity in unbound layer.

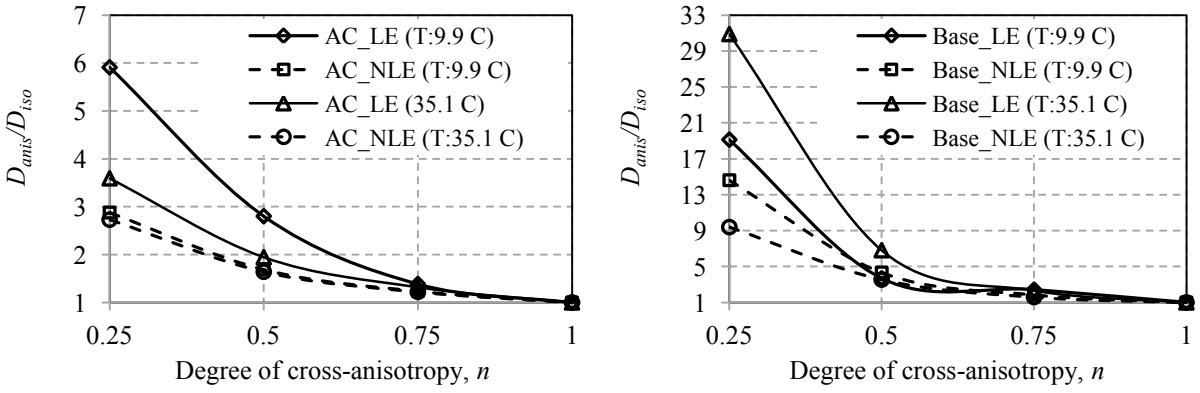

(a) AC (b) Base

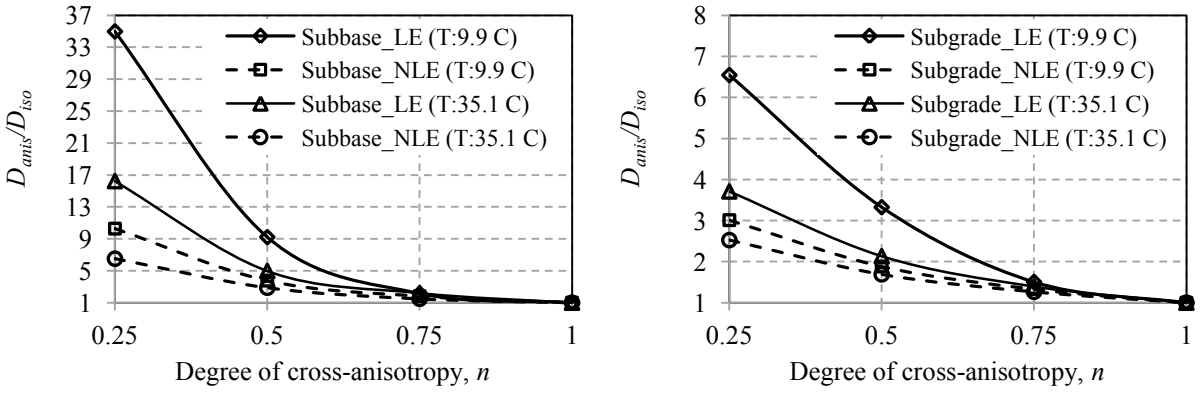

(c) Subbase (d) Subgrade

Figure 6.21 Damage in pavement layers (Linear vs. nonlinear elastic)

In summary, vertical strains in pavement layers decrease with increase in *n*-value of the AC towards the isotropy in both cases of linear and nonlinear elastic unbound layers. In addition, these strains are sensitive to temperature. In case of base and subbase, vertical strains based on nonlinear elasticity are greater than those based on linear elasticity. Finally, the damage based on cross-anisotropic and isotropic strain, per load repetition is high whenever the unbound layers are considered linear elastic.

6.4.4 Loading Duration

Tensile in the AC Layer

Figure 6.22 shows that the variation of the tensile strain with AC cross-anisotropy at different loading durations, i.e., resulted from different vehicle speed. The tensile strain decreases with increase in *n*-value of the AC as before. It is also observed that strain due to loading duration of 30 ms is slightly greater than due to 22.5 ms. This is due to the reduced relaxation modulus of the AC during the loading duration of 30 ms. The peaks of tire pressure are attained at 11.25 and 15 ms at loading durations of 22.5 and 30 ms respectively. At these specific time steps, the

relaxation modui are 2448 and 2301 ksi respectively. Therefore, strain is smaller at of loading duration of 2448 ksi and vice versa. The different the two relaxation moduli is very small which leads to a very small difference in tensile strain.

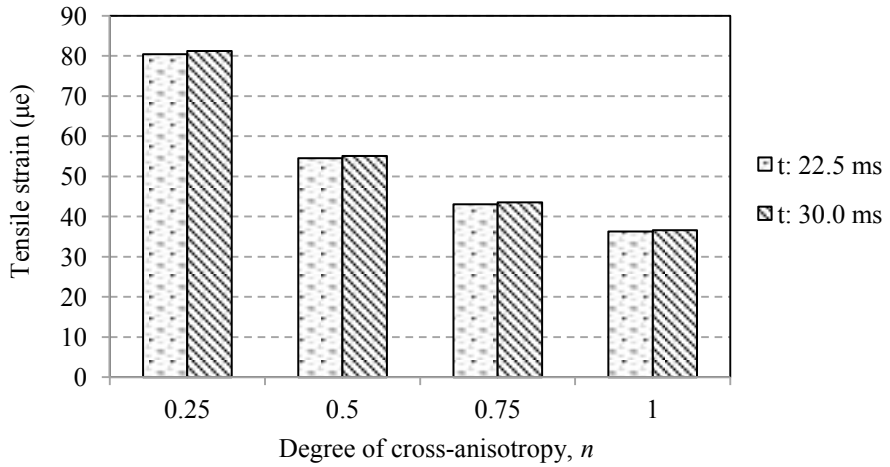

Figure 6.22 Tensile strain in AC layer at varying loading duration

The tensile strain ratios are calculated considering different loading durations along transverse directions since the strain along this direction is typically greater than that along longitudinal direction. The strain ratios are plotted in Figure 6.23(a). Strain ratios based on both loading durations decrease with *n*-value. In addition, both these trends are the same. Figure 6.23(b) shows the variation of the resulting damage (eqn. 4.12). The damage also follows the similar trend of the strain ratio where it decreases with increase in *n*-values. These ratios are not affected by the variation in loading durations.

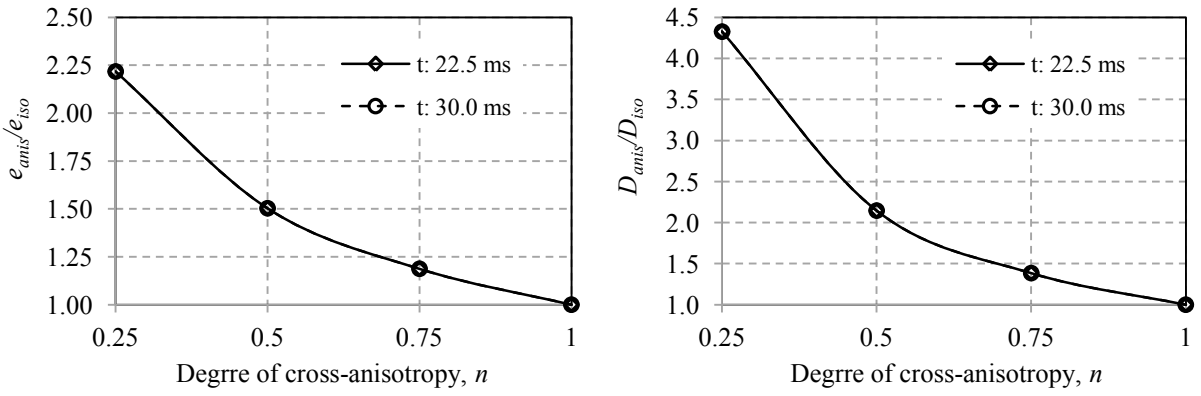

(a) Tensile strain ratio (b) Damage

Figure 6.23 Tensile strain ratio and damage at varying loading duration

Vertical Strain in Pavement Layers

Figure 6.24(a) through (d) shows the variation of vertical strains in pavement layers at varying *n*-values at the earlier mentioned loading durations. Difference in the vertical strains in the AC layer at two loading durations is very small since the difference between the relaxation moduli is also very small. However, in case of base and subbase, difference in vertical strain is high. The maximum difference is about 25 microstrain and it decreases with increase in *n*-value. This difference is resulted due to variation of vertical stresses in base and subbase, For instance, vertical stresses at mid-depth of base and subbase, i.e., 17.3 and 8.6 psi respectively, at loding duration of 30 ms which greater than those, i.e., 12.4 and 6.4 psi respectively, at loading duration of 22.5 ms. Later, the greater magnitude of stresses will lead to greater strains. In case of subgrade, vertical strain is still high due to loading duration of 30 ms. However, the difference is small which is due to very small difference in vertical stresses in this layer.

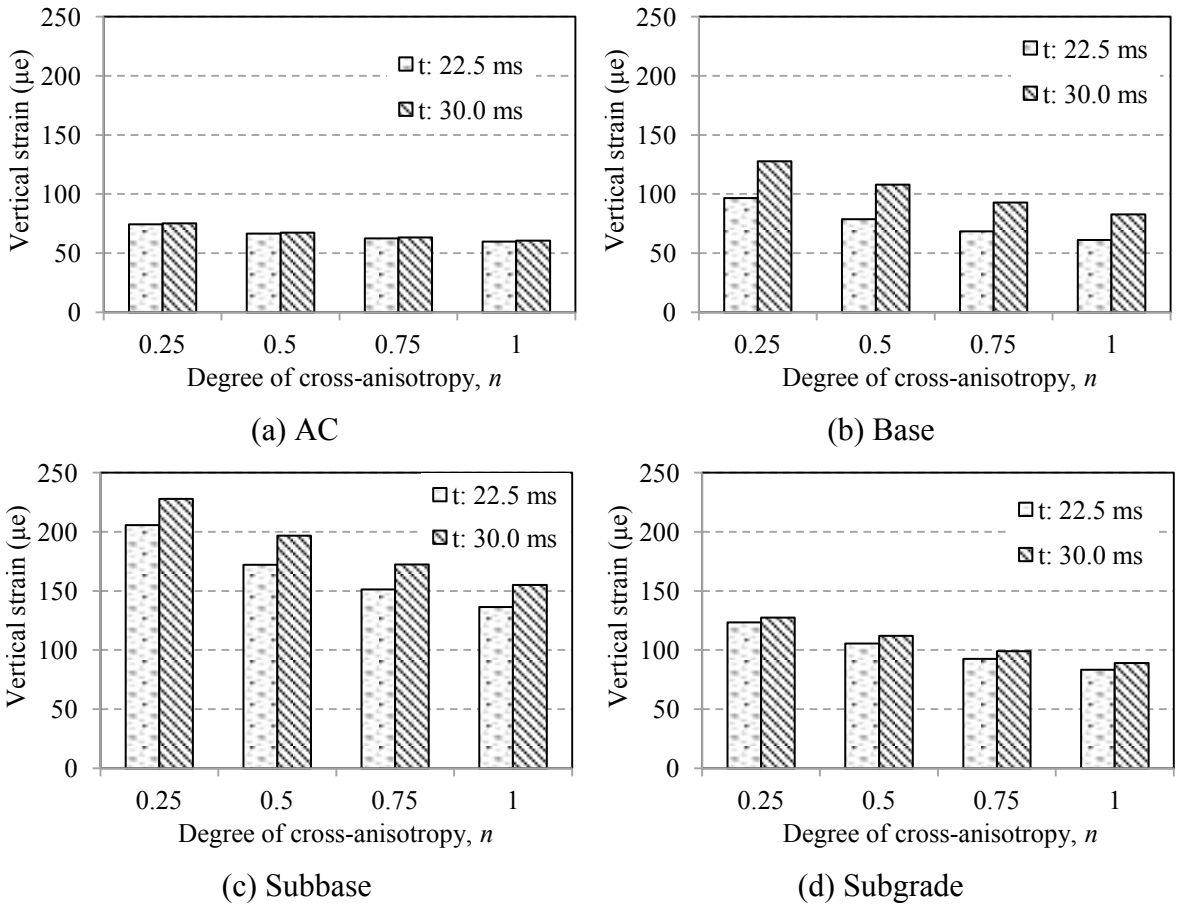

Figure 6.24 Vertical strain in pavement layers at varying loading duration

Figure 6.25(a) show the variation of vertical strain ratios in pavement layers incorporating two different loading durations. The strain ratios decrease with increase in *n*-values as expected. In case of base and subbase, the ratio for shorter loading duration (22.5 ms) is greater than that for longer duration (30.0 ms). Strain ratios in the AC layer are not affected by the loading durations. The resulting damage is plotted against the cross-anisotropic variation in Figure 6.25(b). The damage ratios in the unbound layers are mainly affected by the variation in loading durations.

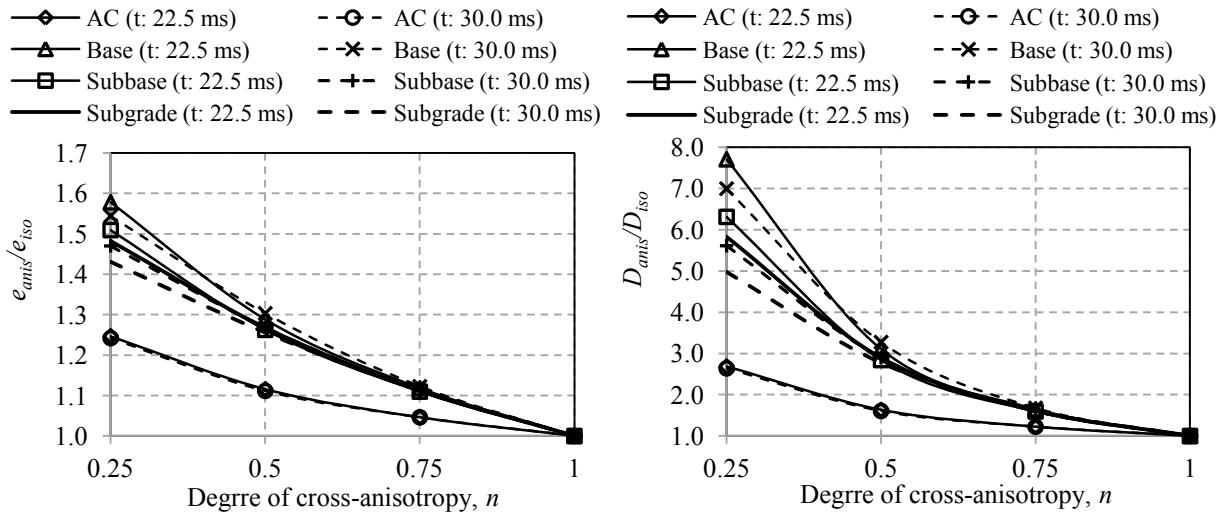

(a) Vertical strain ratio (b) Damage

Figure 6.25 Vertical strain ratio and damage at varying loading duration

In summary, vertical strains in the AC are barely affected by the variation in loading duration whereas these strains in unbound layers are affected by these durations. The damage ratio also follows the similar trend at the varying loading durations.

6.5 Summary of parametric study

In the earlier steps, a parametric study is performed to investigate the combined effect of AC cross-anisotropic variation in presence of unbound layer stress-dependency on pavement responses and damage. Outcomes of the parametric study are summarized in Table 6.5.

Table 6.5: Summary of parametric study (AC cross-anisotropy & stress-dependency)

Response	Parameter variation	Observation	Comment
Tensile strain at the bottom of the AC	• AC temperature: 9.9, 16.3, 25.6 & 35.1 °C • n_{AC} : 0.25-1.0	• Strain is the maximum at *n*-value of 0.25 • Strain decreases as *n*-value increases towards isotropy (*n*=1.0) • Transverse strain is greater than longitudinal strain • Strain is high at high temperature and small at low temperature	• Tensile strain at the bottom of the AC layer is high whenever AC is cross-anisotropic • Strain is sensitive to AC temperature variation
Fatigue damage (D_{anis}/D_{iso}) due to tensile strain	• AC temperature: 9.9, 16.3, 25.6 & 35.1 °C • n_{AC} : 0.25-1.0	• D_{anis}/D_{iso} is the maximum at *n*-value of 0.25 • D_{anis}/D_{iso} decreases as *n*-value increases towards isotropy (*n*=1.0) • D_{anis}/D_{iso} is high at low temperature	• Damage due to cross-anisotropy is greater than that due to isotropy • Damage is not sensitive to temperature variation • Damage due to transverse strain greater than due to longitudinal strain
Vertical strain in AC	• AC temperature: 9.9, 16.3, 25.6 & 35.1 °C • n_{AC} : 0.25-1.0	• Strain is the maximum at *n*-value of 0.25 • Strain decreases as *n*-value increases towards isotropy (*n*=1.0) • Strain is high at high temperature and small at low temperature	• Vertical strain in the AC layer is high whenever AC is cross-anisotropic • Strain is sensitive to AC temperature variation
Vertical strain in base	• AC temperature: 9.9, 16.3, 25.6 & 35.1 °C • n_{AC} : 0.25-1.0	• Strain is the maximum at *n*-value of 0.25 • Strain decreases as *n*-value increases towards isotropy (*n*=1.0) • Strain is high at high temperature and small at low temperature	• Vertical strain in the base layer is high whenever AC is cross-anisotropic • Strain is sensitive to AC temperature variation
Vertical strain in subbase	• AC temperature: 9.9, 16.3, 25.6 & 35.1 °C • n_{AC} : 0.25-1.0	• Strain is the maximum at *n*-value of 0.25 • Strain decreases as *n*-value increases towards isotropy (*n*=1.0) • Strain is high at high temperature and small at low temperature	• Vertical strain in the subbase layer is high whenever AC is cross-anisotropic • Strain is sensitive to AC temperature variation
Vertical strain in subgrade	• AC temperature: 9.9, 16.3, 25.6 & 35.1 °C • n_{AC} : 0.25-1.0	• Strain is the maximum at *n*-value of 0.25 • Strain decreases as *n*-value increases towards isotropy (*n*=1.0) • Strain variation in subgrade is relatively small	• Vertical strain in the subbase layer is high whenever AC is cross-anisotropic • Strain variation is relatively small compared to base & subbase layers
Damage due to permanent deformation (AC, base, subbase & subgrade)	• AC temperature: 9.9, 16.3, 25.6 & 35.1 °C • n_{AC} : 0.25-1.0	• Damage is the maximum at *n*-value of 0.25 • Damage decreases as *n*-value increases towards isotropy (*n*=1.0) • Damage varies with AC temperature	• Damage due to cross-anisotropy is greater than that due to isotropy • Damage in unbound layer is greater than that in AC layer

Table 6.5: Summary of parametric study (continued)

Response	Parameter variation	Observation	Comment
Tensile strain at the bottom of the AC due to AC & base cross-anisotropy	• AC temperature: 9.9 & 35.1 °C • n_{AC} : 0.25-1.0 • n_{base} : 0.25-1.0	• Strain decreases as *n*-value increases towards isotropy (n=1.0) • Strain increases due to incorporation of base cross-anisotropy	• Tensile strain is enhanced in presence of base cross-anisotropy
Fatigue damage due to AC & base cross-anisotropy	• AC temperature: 9.9 & 35.1 °C • n_{AC} : 0.25-1.0 • n_{base} : 0.25-1.0	• D_{anis}/D_{iso} decreases as *n*-value increases towards isotropy (n=1.0) • D_{anis}/D_{iso} increases in presence of base cross-anisotropy	• Damage is enhanced whenever base cross-anisotropy is incorporated
Vertical strains due to AC & base cross-anisotropy	• AC temperature: 9.9 & 35.1 °C • n_{AC} : 0.25-1.0 • n_{base} : 0.25-1.0	• Vertical strain in AC is barely affected by base cross-anisotropy • Vertical strains in unbound layers are increase due to incorporation of base layer cross-anisotropy	• Vertical strains only in unbound layer are highly sensitive to base layer cross-anisotropy
Damage based on permanent deformation due to AC & base cross-anisotropy	• AC temperature: 9.9 & 35.1 °C • n_{AC} : 0.25-1.0 • Nonlinear base	• Damage in base, subbase, and subgrade is greater than that in the AC layer	• Damages in unbound layers are highly sensitive to base layer cross-anisotropy
Tensile strain at the bottom of the AC (Linear vs. Nonlinear)	• AC temperature: 9.9 & 35.1 °C • n_{AC} : 0.25-1.0 • Nonlinear base	• Strain increases due to incorporation of nonlinear unbound layer • This trend is enhanced at high temperature	• Tensile strain is sensitive to unbound layer nonlinearity, specially, at high temperature
Fatigue damage (Linear vs. Nonlinear)	• AC temperature: 9.9 & 35.1 °C • n_{AC} : 0.25-1.0 • Nonlinear base	• D_{anis}/D_{iso} increases in presence of unbound layer nonlinearity • This trend is enhanced at high temperature	• Fatigue damage is sensitive to unbound layer nonlinearity, specially, at high temperature
Vertical strains (Linear vs. Nonlinear)	• AC temperature: 9.9 & 35.1 °C • n_{AC} : 0.25-1.0 • Nonlinear base	• Vertical strains in AC & linear elastic subgrade decreases due to unbound layer nonlinearity • Vertical strains in nonlinear unbound layer are enhanced due to unbound layer nonlinearity	• Vertical strains in base & subbase are enhanced due to incorporation of unbound layer nonlinearity
Damage based on permanent deformation (Linear vs. Nonlinear)	• AC temperature: 9.9 & 35.1 °C • n_{AC} : 0.25-1.0 • Nonlinear base	• Damages in AC & subgrade (VE & linear elastic layer) are smaller than those in base & subbase	• Damage in unbound layers are highly increases due to incorporation of nonlinearity in those specific layers
Strains (varying loading duration)	• n_{AC} : 0.25-1.0 • Loading duration (ms): 22.5 & 30.0	• Tensile strain in AC layer does not vary • Vertical strain in base & subbase vary	• Strain in AC layer is not affected by loading variation within this specific range • Vertical strains in base & subbase layer are sensitive to loading duration
Damages (varying loading duration)	• n_{AC} : 0.25-1.0 • Loading duration (ms): 22.5 & 30.0	• Fatigue damage in AC layer does not vary • Damage based on permanent deformation varies with loading durations	• Damages based on permanent deformation are sensitive to loading duration variation

6.5 Summary

In this phase of the study, the dynamic FEM is updated by combining the temperature dependent and cross-anisotropic viscoelasticity of the bound layers, such as OGFC and AC, as well as stress-dependencies of the unbound layers, such as base and subbase, to investigate the effect of cross-anisotropy on pavement responses. This investigation is performed at varying pavement temperatures, base layer cross-anisotropy, unbound layer nonlinearity, and loading durations resulted from vehicle speed. The findings are summarized below:

- The horizontal tensile strains at the bottom of the AC along both longitudinal and transverse directions increase with decrease in horizontal stiffness. Later, similar trend was also evident in case of the damage based on fatigue per loading repetition which indicates both strain and resulting damage increase due to presence of AC cross-anisotropy .
- The vertical strains in pavement layers also increase with decrease in horizontal stiffness. This trend is also evident in case of the damage based on permanent deformation or rutting per loading repetition. It indicates that incorporation of the AC cross-anisotropy leads to increase in pavement responses and thereby, permanent deformation.
- Both of the tensile strain at the bottom of the AC layer and vertical strains in pavement layers are highly sensitive to temperature variations. At high temperature, strains are high whereas these are small at low temperature. These strains based on both isotropic and cross-anisotropic stiffness are incorporated into the damage at different temperatures which shows that the damage per loading repetition is sensitive to the temperature variation.
- Cross-anisotropy is also incorporated to the base layer which leads to increase in both tensile strain at the bottom of the AC layer and vertical strains in pavement layers. The damage per loading repetition due to these strains also increases. Based on these observations, it

can be said that the pavement responses in a cross-anisotropic asphalt pavement increases due to incorporation of unbound layer cross-anisotropy which expedites the damage.

- The dynamic FEM is simulated for both linear and nonlinear elastic unbound layers which show that tensile strains at the bottom of the AC layer are enhanced due to incorporation of nonlinear unbound layers which leads to the damage based on fatigue. This trend is opposite in case of the vertical strains. The vertical strains as well as the relative damages in pavement layers are high during the incorporation of linear elastic unbound layers.

- The loading durations are also varied during the dynamic FEM simulations. The horizontal tensile and vertical strains slightly increase due to longer loading duration. In case of the unbound layers, vertical strains at longer duration are considerably greater than those at shorter loading durations. Later, it is observed that the damage in the unbound layers is mostly sensitive to the loading duration variation.

- Shear modulus in vertical plane is varied to investigate the necessity of the accuracy of this parameter on specific pavement responses, such as tensile strain at the bottom of the AC and vertical strains in pavement layers, which are typically required to calculate the damage based on fatigue and permanent deformation. It is observed that it barely affects the strains and thereby, the damage.

CHAPTER 7

CONCLUSIONS AND RECOMMENDATIONS

7.1 General

This study is performed to investigate the cross-anisotropy of pavement layers, especially AC layer, on pavement stress-strain using the dynamic FEM of an instrumented pavement section. To facilitate this study, the entire model is developed in ABAQUS 6.9-EF-2. Two different material models, namely cross-anisotropic and temperature-dependent viscoelastic model for the AC and cross-anisotropic and stress-dependent nonlinear elastic models for the unbound layers, are developed in FORTRAN since these models are not available in the material library of ABAQUS. Findings of different phases of this study and related conclusions are summarized in this chapter.

7.2 Conclusions

Findings of this study are summarized as below:

AC Cross-anisotropy

- The horizontal tensile strain at bottom of the AC layer decreases as the *n*-value increases, i.e., increase in horizontal AC modulus, towards the isotropy. It is also observed that the transverse tensile strain is greater than the longitudinal tensile strain. Both longitudinal and transverse strains are highly sensitive to the temperature variation.

- The vertical strains on top of the pavement layers such as AC, base, subbase, and subgrade also increases as the *n*-value increases towards the isotropy. These strains are also sensitive to the temperature variation.

- Damage (cross-anisotropy vs. isotropy) is calculated using the Miner's damage formula based on both fatigue and permanent deformation. Damage ratio is high whenever the AC is cross-anisotropic and this value decreases as the horizontal AC stiffness increases, i.e., *n*-values increases towards isotropy. It is observed that damage is very small at or above *n*-value of 0.75. In addition, this ratio is sensitive to temperature variation.

- Both horizontal and vertical strains are calculated from the FEM simulation considering varying as well as constant (average) temperature over the depth of the AC layer. It is observed that incorporation of constant temperature leads to very small amount of error. Therefore, constant or averaged temperature can be reasonably used in pavement analysis.

Unbound Layer Cross-anisotropy

- Both of the horizontal tensile strain at the bottom and vertical strain on top of the AC layer are not sensitive to the cross-anisotropy of unbound layers. However, incorporation of the cross-anisotropic strains into the Miner's damage formula shows that the fatigue damage is less compared to that incorporating isotropic strain.

- Vertical strains in the base, subbase, and subgrade layers are highly affected by unbound layer cross-anisotropy. Damage ratio based on permanent deformation criterion incorporating these strains shows different trends with variation in *n*-value of unbound layers. The damage due to cross-anisotropic strain is considerably high at small *n*-value.

- Temperature influences both horizontal strain at the bottom of the AC layer as well as vertical strains in both of the AC and unbound layers.

Cross-anisotropy & Stress-dependency

- The horizontal tensile strains at the bottom of the AC along both longitudinal and transverse directions increase with decrease in horizontal stiffness. Later, similar trend was also evident in case of the damage based on fatigue per loading repetition which indicates both strain and resulting damage increase due to presence of AC cross-anisotropy .
- The vertical strains in pavement layers also increase with decrease in horizontal stiffness. This trend is also evident in case of the damage based on permanent deformation or rutting per loading repetition. It indicates that incorporation of the AC cross-anisotropy leads to increase in pavement responses and thereby, permanent deformation.
- Both of the tensile strain at the bottom of the AC layer and vertical strains in pavement layers are highly sensitive to temperature variations. At high temperature, strains are high whereas these are small at low temperature. These strains based on both isotropic and cross-anisotropic stiffness are incorporated into the relative damage at different temperatures which shows that the damage per loading repetition is sensitive to the temperature variation.
- Cross-anisotropy is also incorporated to the base layer which leads to increase in both tensile strain at the bottom of the AC layer and vertical strains in pavement layers. The damage per loading repetition due to these strains also increases. Based on these observations, it can be said that the pavement responses in a cross-anisotropic asphalt pavement increases due to incorporation of unbound layer cross-anisotropy which expedites the damage.

- The dynamic FEM is simulated for both linear and nonlinear elastic unbound layers which show that tensile strains at the bottom of the AC layer are enhanced due to incorporation of nonlinear unbound layers which leads to the damage based on fatigue. This trend is opposite in case of the vertical strains. The vertical strains as well as the damages in pavement layers are high during the incorporation of linear elastic unbound layers.
- The loading durations are also varied during the dynamic FEM simulations. The horizontal tensile and vertical strains slightly increase due to longer loading duration. In case of the unbound layers, vertical strains at longer duration are considerably greater than those at shorter loading durations. Later, it is observed that the damage in the unbound layers is mostly sensitive to the loading duration variation.
- Shear modulus in vertical plane is varied to investigate the necessity of the accuracy of this parameter on specific pavement responses, such as tensile strain at the bottom of the AC and vertical strains in pavement layers, which are typically required to calculate the damage based on fatigue and permanent deformation. It is observed that it barely affects the strains and thereby, the damage.

Finally, the above mentioned findings lead to this conclusion that the AC cross-anisotropy has significant effect on the pavement responses, such as stress-strain. An earlier damage will be evident in a pavement section due to presence of the AC cross-anisotropy. Ignoring this material property in a pavement mechanistic model will lead to an under-design of a pavement section.

7.3 Recommendations

The following recommendations are made for the future study:

- This study has addressed mainly the inherent AC cross-anisotropy which is developed due to compaction during construction. There is one more phenomenon, called stress-induced anisotropy which may result due to particle re-arrangement in an AC layer under wheel load at high temperature. This phenomenon is recommended to investigate through small-scale FEM.

- The permanent deformation or rutting in the AC layer cannot be directly determined using the current FEM since it incorporates linear viscoelasticity. A cross-anisotropic viscoelastic-viscoplastic model is recommended to develop for the AC so that the permanent deformation under repeated load can be determined using this dynamic FEM.

- The scope of this study needs to be extended in the next phase to determine the fatigue damage at a varying AC cross-anisotropy under repeated cycles of wheel load. A viscoelastic continuum damage model is recommended to integrate to the developed cross-anisotropic and viscoelastic AC model for this purpose.

REFERENCES

AASHTO (American Association of State Highway and Transportation Officials). (2007). "Standard Method of Test for Determining Dynamic Modulus of Hot Mix Asphalt Concrete Mixtures." *AASHTO TP 62-07*, Washington, D.C.

AASHTO (American Association of State Highway and Transportation Officials). (2003). "Standard Method of Test for Determining the Resilient Modulus of Soils and Aggregate Materials." *AASHTO T307-99*, Washington, D.C.

Abu-Farsakh, M. Y., Nazzal, M. D., and Mohammad, L. N. (2007). "2D Finite Element Analysis to Evaluate the Performance of Geogrid Base Reinforcement in Weak Flexible Pavement Structure." *Intl. J. of Pavements*, 6(1), 146-157.

Al-Qadi, I. L., Wang, H., and Tutumluer, E. (2010). "Dynamic Analysis of Thin Asphalt Pavements Utilizing Cross-Anisotropic Stress-Dependent Properties for Granular Layer." *Trans. Res. Rec.: J. of the Trans. Res. Board*, 10-1553, 1-17.

Al-Qadi, I. L., and Wang, H. (2009). *Pavement Damage due to Different Tire and Loading Configurations on Secondary Roads*. Final Report: 0081Y01, NEXTRANS Center, Indiana, USA.

Appea, A. K. (2003). *Validation of FWD Testing Results at the Virginia Smart Road: Theoretically and by Instrument Response*. Ph.D Dissertation, Virginia Polytechnic Institute and State University, Virginia, USA.

ARA (Applied Research Associates). (2004). *Guide for Mechanistic-Empirical Design of New and Rehabilitated Pavement Structures*. Final Report: I-37A, Transportation Research Board, National Research Council, Washington, D. C.

Asphalt Institute. (1982). *Research and Development of the Asphalt Institute's Thickness Design Manual (MS-1)*. 9th Edition, Report: 82-2, Lexington, KY, USA.

El-Ayadi, A., Picoux, B., Lefeuve-Mesqouez, G., Mesqouez , A., and Petit, C. (2012). "An Improved Dynamic Model for the Study of a Flexible Pavement." *Adv. in Eng. Software*, Elsevier, 44(1), 44-53.

Barksdale, R. D., Brown, S. F., and Chan, F. (1989). *Potential Benefits of Geosynthetics in Flexible Pavements*. NCHRP Report. 315, Transportation Research Board, National Research Council, Washington D. C.

Bayat, A., Kasani, H. A., and Soleymani, H. R. (2011). "Investigation of Temperature Dependency of Asphalt Concrete Using Laboratory Dynamic Modulus and Field Deflection Testing." *Proc., 90th Annual Meeting of Trans. Res. Board*, 1–14.

Buechlar, M. A. (2012). *Viscoelastic-Viscoplastic Combined Hardening Constitutive Model based on the Drucker-Prager Yield and Flow Potentials*. Technical Report: LA-UR-12-24895, Los Alamos National Laboratory, NM, USA.

Chapuis, R. P., and Gatien, A. (1995). *Temperature Dependent Tensile Strength of Asphalt Mixtures in Relation to Field Cracking Data*. Engineering Properties of Asphalt Mixtures and the Relationship to their Performance, American Society for Testing and Materials, ASTM STP 1265, Philadelphia, USA.

Clyne, T. R., Li, X., Marasteanu, M. o., and Skok, E. L. (2003). *Dynamic and Resilient Modulus of MNDOT Asphalt Mixtures*. Report No: MN/RC-2003-09, Minnesota Department of Transportation (MNDOT), St. Paul, Minnesota, USA.

Cook, R. D., Malkus, D. S., Plesha, M. E., and Witt, R. J. (2002). *Concepts and Applications of Finite Element Analysis*. 4th Edition, John Wiley & Sons, New York, USA.

Dave, E. V., Paulino, G. H., and Buttlar, W. G. (2011). "Viscoelastic Functionally Graded Finite-Element Method Using Correspondence Principle." *J. of Mat. in Civil Eng.*, ASCE, 23(1), 39-38.

Dealy, J., and Plazek, D. (2009). "Time-Temperature Superposition: A User's Guide." *Rheology Bulletin*, 78(2), 16-31.

Diefenderfer, B. K. (2002). *Moisture Content Determination and Temperature Profile Modeling of Flexible Pavement Structures*. PhD Dissertation, Civil and Environmental Engineering, Virginia Polytechnic Institute and State University, VA, USA.

Duncan, J. M., Monismith, C. L., and Wilson, E. L. (1968). "Finite Element Analyses of Pavements." *Highway Res. Rec.: J. of Highway Res. Board*, 228, 18-23.

Fekadu, P. (2010). *Simulating the Dynamic Response of a Soil-Pile System using ABAQUS*. M.Sc. Thesis, Royal Institute of Technology, Department of Mechanics, Stockholm, Sweden.

Garcia, G., and Thompson, M. (2008). "Strain and Pulse Duration Considerations for Extended Life of Hot-Mix Asphalt Pavement Design." *Trans. Res. Rec.: J. of Trans. Res. Board*, 2087, 3-11.

Gazetas, G. (1991). "Formulas and Charts for Impedances of Surface and Embedded Foundations." *J. of Geo. Eng.*, ASCE, 117(9), 1363-1381.

Gurp, V., and Palmen, J. (1998). "Time-Temperature Superposition for Polymer Blends." *Rheology Bulletin*, 67, 5-8.

Haddad, Y. M. "Viscoelasticity of Engineering Materials." 1st Edition, Chapman & Hall, New York, USA.

Herb, W., Marasteanu, M., and Stefan, H. G. (2006). *Simulation and Characterization of Asphalt Pavement Temperatures*. Project Report: 480, Minnesota Department of Transportation, MN, USA.

Hicks, R. G., and Monismith, C. L. (1971). "Factors Influencing the Resilient Properties of Granular Materials." *Trans. Res. Rec.: J. of Trans. Res. Board,* 345, 15–31.

Huang, Y. H. (2004). *Pavement Analysis and Design*. 2nd Edition, Pearson Education Inc., New Jersey, USA.

Huber, G. (2000). *Performance Survey on Open-Graded Friction Course Mixes*. NCHRP Synthesis of Highway Practice 284, Transportation Research Board, Washington, D.C.

Islam, M. R. (2015). *Thermal Fatigue Damage of Asphalt Pavement*. Ph.D. Dissertation, University of New Mexico, Albuquerque, USA.

Jurado, M. C. (2008). *Quantifying Anisotropy in Asphalt Pavement Concrete Pavements using an Ultrasonic Method*. M.Sc. Thesis, University of Texas-El Paso, El Paso, USA.

Kaloush, K. (2001). *Simple Performance Test for Permanent Deformation of Asphalt Mixtures*. PhD Dissertation, Arizona State University, Tempe, AZ, USA.

Kim, S. H. (2004). *Determination of Aggregate Physical Properties and its Effect on Cross-Anisotropic Behavior of Unbound Aggregate Materials*. Ph.D. Dissertation, Texas A&M University, College Station, TX, USA.

King, S., and Richards, T. (2013). "Solving Contact Problems with ABAQUS." <http://moodle.insatoulouse.fr/pluginfile.php/42654/mod_resource/content/3/CONTACT_Imulia.pdf> (Last accessed: 02/23/2016).

Kuo, C. M., and Chou, F. J. (2004). "Development of 3-D Finite Element Model for Flexible Pavements." *J. of the Chinese Inst. of Eng.*, 27(5), 707-717.

Lee, H. J. (1996). *Uniaxial Modeling of Asphalt Concrete using Viscoelasticity and Continuum Damage Theory*. PhD Dissertation, Civil Engineering Department, North Carolina State University, Raleigh, NC, USA.

Lee, H. S., and Kim, J. (2009). "Determination of Viscoelastic Poisson's Ratio and Creep Compliance from the Indirect Tension Test." *J. of Mat. in Civil Eng.*, ASCE, 21(8), 416-425.

Lo, S-C. R., and Lee, I. K. (1990). "Response of Granular Soil along Constant Stress Increment Ratio Path." *J. of Geo. Eng.*, ASCE. 116(3), 355-376.

Lysmer, J., and Kuhlemeyer, R. L. (1969). "Finite Element Model for Infinite Media." *J. of Eng. Mech.*, ASCE, 95(EM4), 859-877.

Mamlouk, M. S., Witczak, M. W., Kaloush, K. E., and Ho, Y-S. (2002). "Effect of Anisotropy on Compressive and Tensile Properties of Asphalt Mixtures." *J. of Test. and Eval.,* ASTM*,* 30(5), 1-7.

Masad, E., Tashman, L., Somedavan, N., and Little, D. (2002). "Micromechanics-Based Analysis of Stiffness Anisotropy in Asphalt Mixtures." *J. of Mat. in Civil Eng., ASCE,* 14(5), 374-383.

Masad, S., Little, D., and Masad, E. (2006). "Analysis of Flexible Pavement Response and Performance Using Isotropic and Anisotropic Material Properties." *J. of Trans. Eng.*, ASCE, 132(4), 342-349.

Mase, G. T., and Mase, G. E. (1999). *Continuum Mechanics for Engineers*. 2nd Edition, CRC Press, USA.

Mehta, Y. (2007). *Evaluation of Interlayer Bonding in HMA Pavements*. Report No: WHRP 07-07, Wisonsin Department of Transportation, WI, USA.

MEPDG. (2008). "Mechanistic-Empirical Pavement Design Guide: A Manual of Practice." *Interim Edition by AASHTO* (American Association of State Highway and Officials).

Molinari, A., Cheriguene, R., and Miguelez, H. (2012). "Contact Variables and Thermal Effects at the Tool-Chip Interface in Orthogonal Cutting." *Int. J. of Solids and Structures*, Elsevier, 49(26), 3774-3796.

Motola, Y., and Uzan, J. (2007). "Anisotropy of Field-Compacted Asphalt Concrete Material." *J. of Test. and Eval.*, ASTM.

Novak, M., Aboul-Ella, F., and Nogami, T. (1978). "Dynamic Soil Reactions for Plane Strain Case." *J. of Eng. Mech. Div.*, ASCE, 104(4), 953-959.

Oh, J. H., Lytton, R. L., and Fernando, E. G. (2006). "Modeling of Pavement Response Using Nonlinear Cross-Anisotropy Approach." *J. of Trans. Eng.*, ASCE, 132(6), 458-468.

Papazian, H. S. (1962). "The Response of Linear Viscoelastic Materials in the Frequency Domain with Emphasis on Asphalt Concrete." *Proc., 1st Int. Conf. on the Structural Design of Asphalt Pavements*, 454-463.

Park, S. W., and Schapery, R. A. (1999). "Methods of Interconvertion between between Linear Viscoelastic Material Functions. Part I-A Numerical Method Based on Prony Series*." Int. J. of Solids and Structures*, 36, 1653-1675.

Pellinen, T. K., Xiao, S., and Raval, S. Y. (2006). "Dynamic Modulus Testing of Thin Pavement Cores." *J. of ASTM Int.*, 3(4), 1–14.

Petyt, M. (1990). *Introduction to Finite Element Vibration Analysis*. 1st Edition, Cambridge University Press, Cambridge, UK.

Putman, B. J. (2012). *Evaluation of Open-Graded Friction Courses: Construction, Maintenance, and Performance*. Report No: FHWA-SC-12-04, South Carolina Department of Transportation, South Carolina, USA.

Rajbongshi, P. (1997). "A Critical Discussion on Mechanistic-Empirical Fatigue Evaluation of Asphalt Pavements." *Int. J. of Pavement Res. Technol.*, 2(5), 223-226.

Robbins, M. M. (2009). *An Investigation into Dynamic Modulus of Hot-mix Asphalt and its Contributing Factors*. M.Sc. Thesis, Auburn University, Auburn.

Romanoschi, S. A., and Metcalf, J. B. (2001). "Characterization of Asphalt Concrete Layer Interfaces." *Trans. Res. Rec.: J. of Trans. Res. Board*, 1778, 132-139.

Roque, R., Myers, L. A., and Birgisson, B. (2000). "Evaluating Measured Tire Contact Stresses to Predict Pavement Response and Performance." *Trans. Res. Rec.: J. of Trans. Res. Board*, 1716, 73-81.

Sadd, M. H. (2009). *Elasticity: Theory, Applications, and Numerics*. Elsevier Inc., Burlington, MA, USA.

Samali, B., and Kwok, K. C. S. (1995). "Use of Viscoelastic Dampers in Reducing Wind- and Earthquake-Induced Motion of Building Structures." *J. of Eng. Str., Elsevier Science Ltd.*, 17(p), 639-654.

Schwartz, C. W., Gibson, N., and Schapery, R. A. (2002). "Time-Temperature Superposition for Asphalt Concrete at Large Compressive Strains." *Trans. Res. Rec.: J. of Trans. Res. Board*, 1789, 101-112.

Serdaroglu, M. S. (2010). *Nonlinear Analysis of Pile Driving and Ground Vibrations in Saturated Cohesive Soils using the Finite Element Method*. Ph.D. Dissertation, Iowa University, Iowa, USA.

Shahin, M. Y., Kirchner, K., Blackmon, E. W., and Tomita, H. (1986). "Effect of Layer Slippage on Performance of Asphalt-Concrete Pavements." *Trans. Res. Rec.: J. of Trans. Res. Board*, 1095, 79-85.

Siddharthan, R.V., Krishnamenon, N., El-Mously, M., and Seabaaly, P. E. (2002). "Investigation of Tire Contact Stress Distribution on Pavement Response." *J. of Trans. Eng.*, ASCE, 128(2), 136-144.

Spears, R. E., and Jensen, S. R. (2009). "Approach for Selection of Rayleigh Damping Parameters used for Time History Analysis." *Proc., of ASME Pres. Vessels and Piping Div. Conf.*, Prague, Czeck Republic.

Stempihar, J. J., and Kaloush, K. E. (2010). "Failure Investigation for an AR Open-Graded Friction Course in Sweden." *Report of Swedish Road Administration*, Sweden.

Tarefder, R. A., and Ahmed, M. U. (2013). "Modeling of the FWD Deflection Basin to Evaluate Airport Pavements." *Int. J. of Geomechanics*, ASCE, 14(2), 205-213.

Tarefder, R. A., Ahsan, S., and Ahmed, M. U. (2014). "A Neural Network based Thickness Determination Model to Improve the Backcalculation of Layer Moduli without Coring." *Int. J. of Geomechanics*, ASCE, 1-12.

Tarefder, R. A., and Islam, M. R. (2015). *Study and Evaluation of Material Response in Hot Mix Asphalt based on Field Instrumentation*. Report No. NM11MSC-03, New Mexico Department of Transportation, NM, USA.

Tschoegl, N. W. (1989). *The Phenomenological Theory of Linear Viscoelastic Behavior: An Introduction*. Springer-Verlag, New York, USA.

Tutumluer, E., and Barksdale, R. D. (1995). "Behavior of Pavements with Granular Bases-Prediction and Performance." *Proc., UNBAR4 Sym.*, Nottingham, UK, 173-183.

Tutumluer, E. (1998). "Anisotropic Behavior of Unbound Aggregate Bases-State of the Art Summary." *Proc., 6th Annual Sym. of the Int. Cent. for Aggregate Res.*, St. Louis, Missouri, 11-33.

Tutumluer, E. and Seyhan, U. (1999). "Laboratory Determination of Anisotropic Aggregate Resilient Moduli Using an Innovative Testing Device." *Trans. Res. Rec.: J. of Trans. Res. Board*, 1687, 13-21.

Tutumluer, E., Adu-Osei, A., Little, D. N., and Lytton, R. L. (2001). *Field Validation of the Cross-Anisotropic Behavior of Unbound Aggregate Bases*. Report No. ICAR/502-2, Texas Transportation Institute, TX, USA.

Uddin, W., and Garza, S. (2010). "3D-FE Simulation Study of Structural Response Analysis for Pavement-subgrade Systems Subjected to Dynamic Loads." *Pavements and Materials: Testing and Modeling in Multiple Length Scales*, ASCE, 170-181.

Ulloa, A., Hajj, Y. E., Siddharthan, R. V., and Sebaaly, P. E. (2013). "Equivalent Loading Frequencies for Dynamic Analysis of Asphalt Pavements." *J. of Mater. in Civ. Eng.*, ASCE, 25(9), 1162-1170.

Underwood, B. S., and Kim, Y. R. (2009). "Determination of the Appropriate Representative Elastic Modulus of Asphalt Concrete." *Int. J. of Pavement Engineering*, 10(2), 77-86.

Uzan, J. (1985). "Characterization of Granular Materials." *Trans. Res. Rec.: J. of Trans. Res. Board, 1022*, 52–59.

Wang, L., Hoyos, L., R., Wang, J., Voyiadjis, G., and Abadie, C. (2005). "Anisotropic Properties of Asphalt Concrete: Characterization and Implications for Pavement Design and Analysis." *J. of Mat. in Civil Eng., ASCE,* 17(5), 535–543.

Wang, Y., Leng, Z., and Wang, G. (2013). "Structural Contribution of Open-Graded Friction Course Mixes in Mechanistic-Empirical Pavement Design." *Int. J. of Pavement Eng.*, 15(8), 731-741.

Wang, H., and Al-Qadi, I. L. (2013). "Importance of Nonlinear Anisotropic Modeling of Granular Base for Predicting Maximum Viscoelastic Pavement Responses under Moving Vehicular Loading." *J. of Eng. Mech.*, 139(29), 29–38.

Williams, M. L., Landel, R. F., and Ferry, J. D. (1955). "The Temperature Dependence of Relaxation Mechanisms in Amorphous Polymers and other Glass-forming Liquids." *J. of the American Chem. Society*, 77, 3701-3706.

Witczack, M. W., and Root, R. E. (1974). "Summary of Complex Modulus Laboratory Test Procedures and Results." *J. of American Soc. for Test. and Mat.*, STP 561, 67-94.

Witczack, M. W., and Fonseca, O. A. (1996). "Revised Predictive Model for Dynamic (Complex) Modulus of Asphalt Mixtures." *Trans. Res. Rec.: J. of Trans. Res. Board*, 1540, 125-132.

Witczak, M. W., and J. Uzan. (1988). *The Universal Airport Pavement Design System, Report I of V: Granular Material Characterization*. Department of Civil Engineering, University of Maryland, College Park, MD.

Witczack, M. W., and El-Basyouny, M. M. (2004). *Guide for mechanistic-empirical design of new and rehabilitated pavement structures*. Final Report, NCHRP 1-37A, Transportation Research Board, Washington, D.C.

APPENDIX A

Table A1: OGFC dynamic modulus

Frequency (Hz)	Temperature (°C)				
	-10	4	21	37	54
25	1976.3	1208.9	484.8	149.0	50.3
10	1833.0	1082.6	387.1	122.3	46.9
5	1679.7	939.9	330.8	105.0	44.4
1	1492.8	691.4	206.9	73.5	46.1
0.5	1284.7	639.2	169.8	63.9	40.1
0.1	1125.3	415.7	107.3	56.0	39.1

*Dynamic modulus values are in 'ksi'

Table A2: Phase angle of OGFC during dynamic modulus test

Frequency (Hz)	Temperature (°C)				
	-10	4	21	37	54
25	12.8	16.5	24.7	27.3	30.4
10	12.9	19.2	28.1	28	24.3
5	14.1	18.7	28.9	27.1	22.8
1	15.2	23.1	31.1	23	17.8
0.5	17.3	23.3	31.9	22.2	17.6
0.1	18.7	27.4	31.6	18.3	17.4

*Phase angle values are in 'degree'

Table A3: Vertical AC dynamic modulus

Frequency (Hz)	Temperature (°C)				
	-10	4	21	37	54
25	7723.4	3172.2	2026.3	1202.6	325.3
10	7498.4	2917.4	1790.7	797.4	276.0
5	7239.9	2596.8	1665.3	660.8	220.9
1	5699.6	2006.3	1169.6	404.0	141.4
0.5	5536.4	1775.4	1141.3	324.3	122.0
0.1	4886.9	1356.8	749.7	206.3	85.1

*Dynamic modulus values are in 'ksi'

Table A4: Phase angle of vertical AC during dynamic modulus test

Frequency (Hz)	Temperature (°C)				
	-10	4	21	37	54
25	7.3	18.5	22.2	25.1	33.9
10	7.5	20.2	13.5	25.1	28.7
5	6.8	18.8	13.4	26.7	28.5
1	15.7	19.4	19.1	29.7	29.2
0.5	18.8	18.5	20.5	30.4	27.2
0.1	16.5	20.7	21.8	29.2	23.7

*Phase angle values are in 'degree'

Table A5: Horizontal AC dynamic modulus

Frequency (Hz)	Temperature (°C)				
	-10	4	21	37	54
25	4265.4	3016.8	1506.7	362.3	130.4
10	4138.0	2671.6	1263.9	275.6	91.7
5	3997.8	2453.0	1077.0	219.9	74.9
1	3572.6	2037.2	718.0	126.7	47.3
0.5	3161.9	1788.2	598.9	98.5	34.9
0.1	2909.0	1451.4	424.2	62.4	25.1

*Dynamic modulus values are in 'ksi'

Table A6: Phase angle of horizontal AC during dynamic modulus test

Frequency (Hz)	Temperature (°C)				
	-10	4	21	37	54
25	25	20.1	18.4	30.4	35.9
10	7.2	10.7	17.8	28.7	32.9
5	8.1	11.9	19.4	29.1	32
1	7.9	11.7	24.2	30.5	28.7
0.5	9.2	10.7	24.3	31.1	28.2
0.1	7.4	15.8	25.5	29.1	23.2

*Phase angle values are in 'degree'